OXIDATION BEHAVIOR OF ZIRCONIUM DIBORIDE-SILICON CARBIDE COMPOSITES AT HIGH TEMPERATURES

by

Sigrun N. Karlsdottir

A dissertation submitted in partial fulfillment
of the requirements for the degree of
Doctor of Philosophy
(Materials Science and Engineering)
in the University of Michigan
2007

Doctoral Committee:

Professor John W. Halloran, Chair
Professor Tresa M. Pollock
Associate Professor Margaret S. Wooldridge
Assistant Professor Anton Van der Ven

Stoltur má hver er stendur sig
í starfi og leik - og nýtur sín,
en mörg er leið um lífsins stig
og lán æ valt – svo gættu þín:
Svíktu aldrei sjálfa þig;
Sigrún Nanna, stúlkan mín.
Karl Helgason ‘96

Til þín núna hugsum hlýtt,
heiðurskona í “fjarri-stað”.
Það er auðvitað ekkert nýtt,
oft samt viljum nefna það!
Karl Helgason ‘07

To my parents, family and husband –

Your love, support and encouragement made this possible.

ACKNOWLEDGEMENTS

Firstly, and foremost, I would like to thank my advisor John W. Halloran for his endless support and an opportunity of a lifetime. Without his advice and great knowledge this journey would not have been possible. Also, his great enthusiasm for his work and science, inspirited and encouraged me in my work.

I would also like to thank our collaborator; Dr. Alida Bellosi and Dr. Frederic Monteverde from the Institute of Science and Technology for Ceramics in Italy, and Dr. William G. Fahrenholtz and Dr. Gregory E. Hilmas from The University of Missouri-Rolla, for supplying the material used for this study and for great discussion and collaboration. I must also thank Dr. Nicholas A. Grundy for extremely valuable collaboration related to this work. I would also like to thank Dr. Inna G. Talmy from the Naval Surface Warfare Center Carderock Division for helpful discussion on topics related to this dissertation.

Thank you to my committee members – Prof. Tresa Pollock, Prof. Margaret Wooldridge and Prof. Anton Van Der Ven for your time and advice.

Also, I would like to thank my colleagues from Prof. Halloran’s research group, for a great time and support throughout the last four years.

Finally, and most importantly, I would like to thank my friends, family and my parents, for their support and encouragement, and my husband Magnus, for his endless support, whose own academic pursuit is inspiring.

TABLE OF CONTENTS

CHAPTER

6. COMPARISON OF RIBBON METHOD TO CURRENT HIGH TEMPERATURE TESTING FACILITIES 119

7. INTERPRETATION OF OXIDE SCALES OF ZIRCONIUM DIBORIDE AND HAFNIUM DIBORIDE-SILICON CARBIDE COMPOSITES............................140

LIST OF FIGURES

LIST OF TABLES

ABSTRACT

OXIDATION BEHAVIOR OF ZIRCONIUM DIBORIDE-SILICON CARBIDE COMPOSITES AT HIGH TEMPERATURES

by

Sigrun N. Karlsdottir

Chair: John W. Halloran

The ZrB_2-SiC composite is a prominent member of Ultra-High Temperature Ceramics (UHTCs). Here the oxidation behavior of ZrB_2-SiC composites at temperatures between 1500-1900ºC is studied. The structure and composition of complex oxide scales, formed at these temperatures, are characterized using microstructural and elemental analysis.

A novel method, called the Ribbon Method, was developed for testing UHTCs at high temperatures, rapidly at low cost. Self-supported UHTC ribbon specimens are resistively heated with a table-top apparatus to achieve temperatures from 900-2000ºC. The Ribbon Method is a novel method for rapid oxidation characterization of UHTC at high temperatures and a valuable alternative to the current high temperature facilities for UHTCs. Oxidation studies with the Ribbon Method showed that a SiO_2 rich borosilicate surface layer forms during the oxidation of the ZrB_2-SiC composite and acts as a protective barrier at lower temperatures by hindering oxygen diffusion through the surface layer. The SiO_2-rich surface layer starts to volatilize extensively at temperatures above 1700ºC resulting in a decreases in the oxidation resistance of the composite.

A novel mechanism is proposed for the high temperature oxidation of ZrB_2-SiC based composites. This mechanism is based on liquid transport of oxide liquid solution formed during oxidation at temperatures around 1550ºC. Patterns in borosilicate surface layer of oxidized ZrB_2-SiC composites were discovered, showing evidence of liquid flow in the oxide film. These patterns, called here convection cells, are formed when a fluid B_2O_3-rich borosilicate liquid containing dissolved ZrO_2 is transported to the surface where the B_2O_3 is lost by evaporation, depositing ZrO_2 in a viscous SiO_2-rich liquid. The driving force for the liquid transport is proposed to be the large volume increase upon oxidation. Liquid transport of the oxide liquid solution is claimed to play a significant role in the formation of oxide scales of ZrB_2-SiC composites and other boride-SiC based UTHC composites. Mass transport by liquid flow has not yet been reported for the high temperature oxidation of ZrB_2-SiC composites thus a novel mechanism for the high temperature oxidation of these materials is presented.

CHAPTER 1

INTRODUCTION

1.0 Ultra-High Temperature Ceramics

Recently interest in Ultra-High Temperature Ceramics (UHTC) has increased significantly due to 21st century technology and the drive to produce a reusable thermal protection system (TPS) and other components for future generations of hypersonic aerospace vehicles[1]. Most modern designs of hypersonic vehicles incorporate sharp aero-surfaces to increase aerodynamic performance. These designs require materials capable of operating in extreme reentering environment, such as oxidizing atmosphere at high temperatures (above 1500ºC) and corrosive gases at high velocities[2]. Today there are few, if any fully developed materials that meet these needs. Due to this problem UTHC are receiving more attention as the solution due to their attractive material properties.

UHTC are a class of refractory materials including transition metal borides, carbides and nitrides e.g.: ZrB_2, HfB_2, ZrC, HfC, TaC, HfN and ZrN. The refractory borides i.e. ZrB_2 and HfB_2 have extremely high melting temperatures, greater than 3000ºC, as well as high thermal conductivity, high hardness, retained strength and chemical stability at elevated temperatures[3]. The high melting temperature of borides results from a unique interaction of metallic, covalent and ionic types of bonding[3]. Their unique properties also make them promising for variety of other high-temperature structural applications such as plasma arc electrodes, cutting tools, furnace elements, molten metal crucibles, thermo-well tubes for steel refining, and parts of electrical devices such as heaters and igniters [4-5]. The UHTC material ZrB_2 has been considered as a very attractive candidate for components used in aerospace applications due to its low theoretical density (6.09 g/cm^3) compared to HfB_2 (11.2 g/cm^3) [3]. It also has an excellent thermal shock resistance due to its high thermal conductivity, ranging from 65-135 W/m·K [6] which is an important quality for aerospace applications. The high conductivity reduces temperature gradients and thermal stresses in the material and thus improves the thermal shock resistance. A higher conductivity also allows more energy to be conducted away from lower temperature regions, e.g. along the outer surface of the wing leading edge component. ZrB_2 composite are also less expensive than HfB_2 so they are often preferred over HfB_2[18]. Material properties of ZrB_2 are given in Table 1.1

2.0 Background: Oxidation Behavior of the UHTCs; ZrB_2-SiC

Among the earliest studies on the oxidation behavior of UHTC were the studies done by Hoffman [7] at the Lewis Flight Propulsion Labs in 1953 on thermal shock resistance of ZrB_2 for gas turbine blade application. Other early studies include work done by Berkowitz-Mattuck [8] in 1966 and by Kaufman et al. [9] in 1967 on the oxidation behavior of ZrB_2- and HfB_2 materials. In the 1970's Kaufman et al. [10-11] showed that by the addition of SiC to ZrB_2- and HfB_2 the oxidation resistance could be greatly improved and identified ZrB_2 and HfB_2 based composites to be the most promising material for hypersonic applications. Tripp and Graham [12-13] confirmed Kaufman's results and contributed additional information such as microstructural studies of the oxide scale.

During the last 30 years, development of UHTC materials and the development of processing methods for UHTCs have been scarce, but in recent years increased number of groups around the world have picked up where researchers in the 1970's left off to answer the increasing need for highly oxidation-resistant materials for extreme environments [14-36, 40]. NASA Ames research group led the way by starting to work on UTHCs in the 1990's and became the first to demonstrate the possibility of using UHTCs for sharp leading edges, during their Sharp Hypersonic Aero-thermodynamic Research Probe-Ballistic experiments 1 and 2 (SHARP-B1 and SHARP-B2) in 1997 and 2000 [22, 30]. Recent studies by Opila et al.,[18, 21, 23] Bellosi and Monteverde et al.,[16, 19-20, 24-26, 28, 31] and Fahrenholtz and Hilmas et al.,[14, 29] and Talmy and Opeka et al.[1, 15, 34-35] have verified the results from the earlier studies; that the addition of SiC to ZrB_2 and HfB_2 increases oxidation resistance as well as increasing densification and thermal shock resistance of the composites.

Researchers in the field have discovered that ZrB_2- and HfB_2-SiC based composites form a multi-layer and multi-component oxide scale after oxidation at elevated temperatures. The oxide scale of ZrB_2-SiC and HfB_2-SiC composites have similar structures; composed of refractory oxide skeleton and amorphous (glass) oxide components which are believed to provide the oxidation resistance of the composites at higher temperatures [13-15, 17-18, 20-22, 24-26, 28-29, 34-35]. The complex multi-layer oxide scale of oxidized ZrB_2-SiC composites, depending on the oxidation conditions features some or all of the following [13, 18, 20, 36:] 1) a silica (SiO_2)-rich outer layer; 2) a subscale of crystalline zirconia (ZrO_2), often with a columnar microstructure with silica between the zirconia grains, and; 3) a zirconium diboride region depleted in SiC (the "SiC-depleted region") [18, 29, 36]. This is reported to be due to the preferred oxidation of the SiC particles in the composites which results in a layer of a porous bulk material depleted of SiC particles [18, 29, 36]. Figure 1.1 shows a typical structure of a multi-layer oxide scale of ZrB_2-SiC composite.

Significant studies have been done on the oxidation behavior of monolithic ZrB_2 and ZrB_2-SiC composites at oxidizing temperatures. At around 600ºC the monolithic zirconium diboride (ZrB_2) starts to oxidize and forms an oxide scale composed of crystalline zirconia (ZrO_2) and boron oxide (B_2O_3) liquid ($T_m = 450$ºC): [9,12, 20, 27]

$$ZrB_2(s) + 5/2 O_2(g) \rightarrow ZrO_2(s) + B_2O_3(l) \tag{1.1}$$

Below about 1100ºC, the B_2O_3 liquid forms a continuous passive layer acting as a barrier to oxygen diffusion which results in passive oxidation of ZrB_2 and a reported parabolic (diffusion controlled) oxidation kinetics. [8, 14, 37] For this temperature range the activation energies have been reported to be in the range of 80-120 kJ/mole [8, 37-38] The oxidation rate at these temperatures has been reported to be dependant on the partial pressure of oxygen (p_{O_2}), and the rate of oxidation has been presumed to be controlled by the transport of oxygen through $B_2O_3(l)$ [8-9, 12, 37]. Between 1100ºC and 1400ºC, the oxidation rate of ZrB_2 increases due to volatilization of the B_2O_3 liquid, because of the high vapor pressure of B_2O_3 at these temperatures. The kinetics are then controlled by the competition between mass gain ($ZrO_2(s)$ and $B_2O_3(l)$ formation) and mass loss ($B_2O_3(l)$ evaporation), and has been described by para-linear kinetics [12, 14, 20, 35] . Above ca. 1400ºC, for monolithic ZrB_2, the oxidation rate increases due to the rate of evaporation of the B_2O_3 liquid is greater than its rate of formation, resulting in porous non-protective ZrO_2 and is described with rapid linear kinetics [12, 14, 29].

With the addition of SiC to ZrB_2 the oxidation resistance of the composite above ca. 1200ºC increases due to the formation of a silica (SiO_2) rich layer on the exposed surface when SiC part of the composite starts oxidizing: [1, 13-15, 18-20, 29, 35-36]

$$SiC(s) + 3/2O_2(g) \rightarrow SiO_2(l) + CO(g) \tag{1.2}$$

The surface layer forms when the SiO_2 dissolves with the B_2O_3 forming a borosilicate surface layer (B_2O_3-SiO_2). But at these oxidizing temperatures, the B_2O_3 is much more volatile than SiO_2[1, 25, 27, 29], e.g. B_2O_3 has a vapor pressure of 233 Pa at 1500ºC[39], compared to SiO_2 that has a vapor pressure of 3×10^{-4} Pa [27]. Thus during oxidation at temperatures above ca. 1200ºC much of the B_2O_3 formed presumably evaporates from the borosilicate layer, leaving a SiO_2-rich borosilicate layer as the external layer. The SiO_2-rich borosilicate layer has been reported to provide increased oxidation resistance to at least 1500°C [13, 35-36] due to its lower vapor pressure, higher melting temperature and viscosity, which can decrease the oxygen diffusion rate through the layer and suppress B_2O_3 evaporation at these temperatures. Adding just 20vol% of SiO_2 to a pure B_2O_3 system results in raising the liquidus temperature from 450ºC to 700ºC. The binary phase diagram of the B_2O_3-SiO_2 system is shown in Figure 1.2.

In general researchers have reported that relatively little B_2O_3 is found in the oxide scale. Some controversy exists though about the amount of B_2O_3 in the oxide scale for both monolithic ZrB_2 and ZrB_2-SiC at temperatures above 1200ºC. Opeka et al.[15]

reported that there still existed 10wt% of B_2O_3 in the oxidation product of a monolithic ZrB_2 after oxidation testing from 1200 to 1400ºC, while Rezaie et al.[40] reported, that for a ZrB_2-SiC specimen oxidized at 1200ºC for 30 min, calculations from SIMS (Secondary Ion Mass Spectroscopy) showed that the silica rich outermost scale contained less than 1wt% boron (B) content. It should be noted here that there exist some challenges in the detecting Boron (B) especially if it exists in low amounts in material, e.g. in the oxide scale of ZrB_2-SiC composites. For light elements (low atomic number) like Boron (B) it can be difficult to detect it with typical elemental analysis equipment like X-ray Energy Dispersive Spectroscopy (XEDS). XEDS has a low sensitivity to light elements like Boron thus the detection of B is difficult. Also, mapping of B within matrices containing zirconium (Zr) is out of the potentiality of an XEDS detector due to the overlapping of the M x-ray line peaks for Zr and the K lines for B. Another difficulty exists in analyzing the microstructure of the oxide scale of ZrB_2-SiC composites; B_2O_3(l) is very sensitive to hydration thus oxidized specimen need to be prepared for analysis carefully, such as being stored in moisture free desiccators to avoid any reaction of a B_2O_3 on the surface of the specimens. Cross-section of the oxidized specimen also needs to be prepared for microstructural analysis by non-aqueous polishing procedures to avoid hydration.

In recent years there has been some significant amount of work done towards improving processing techniques for ZrB_2 composites [16, 19, 26, 28, 31] as well as efforts in improving the oxidation resistance of ZrB_2-SiC systems with compositional variations [23, 32]. Current researchers in the field have also tried to deepen the understanding of the oxidation behavior of ZrB_2 and its composites with thermodynamic analysis and vapor phase equilibrium such as with construction and interpretation of volatility diagrams.

This includes recent work done by Fahrenholtz [27, 29] on volatility diagrams for monolithic ZrB_2, and ZrB_2-SiC composites. Fahrenholtz explains the formation of so called SiC-depleted layer during ZrB_2-SiC oxidation in air at 1500ºC by construction and interpretation of a ZrB_2-SiC volatility diagram. In published work done by Opeka et al.[1] volatility diagrams were constructed and discussed for the following systems at 2227ºC: Si-SiO_2; B-B_2O_3; Zr-ZrO_2; Al- Al_2O_3; Cr_2O_3; Be-BeO; and a combined Si-SiO_2; B-B_2O_3; Zr-ZrO_2 system. This was done in effort to shed light on the interfacial vapor pressure for systems which forms oxide scale of SiO_2, Al_2O_3, Cr_2O_3, and BeO, which are known to experience slow oxidation rate at high temperatures. Their interpretation was that materials that form pure oxide scales of SiO_2, Al_2O_3, Cr_2O_3, and BeO, cannot be utilized at temperatures of 1800ºC (or above) due to a disruptively high vapor pressures which arises at the interface of the base material and the oxide scale.

Recent work at the Naval Surface Warfare Center (NSWCCD), on improving the oxidation resistance of ZrB2-SiC systems with compositional variations was done by Opeka and Talmy and their associates [1, 34.] Their focus was on modifying the chemical composition of the borosilicate surface layer that forms during oxidation of ZrB_2-SiC composites to increase its melting temperature and viscosity and thus decrease inward diffusion of oxygen. The oxidation resistance of ZrB_2-SiC composite was improved for the temperature range 1200-1400ºC with the introduction of TiB_2, NbB_2, TaB_2, VB_2, and CrB_2 as partial substitution (up to 20 mole%) for ZrB_2. A presence of Ti, Zr, Nb, V, and Cr oxides was reported to exist in the borosilicate glass layer and to cause phase separation (immiscibility) in the glass at temperatures ranging from 1200-1400ºC. The improvement in the oxidation resistance was reported to be due to an increased liquidus temperature and viscosity of the immiscible glasses. The oxidation behavior was characterized by measuring mass changes of test bars during furnace heating in air at 1000-1500ºC for 2 hours as well as evaluated by thermogravimetric analysis (TGA). No significant effect of the additives on the oxidation behavior of the ZrB_2-SiC composites were observed for testing at 1500ºC, explained to be due to exceeding the miscibility gap in these multi-component glass systems[34].

Other recent studies have used the additive Ta_5Si_3 to try to improve the oxidation resistance of the ZrB_2 based systems [23, 32]. For example, Opila et al.[23] found that the ZrB_2-20vol% SiC-20vol% Ta_5Si_3 composite showed the lowest oxidation rate at 1627ºC, but then it performed poorly under the more extreme tests such as in furnace test at 1927ºC for 1, 5 and 10 ten-min cycles and arc jet test at ca. 1890ºC for ten minutes. This was due to the formation of a liquid oxide phase, called phase V, which did not increase the oxidation resistance of the composite but reacted to supports and did not act as a protective layer. Phase V was described to be of a variable composition, e.g. to be $Ta_2O_5 \cdot 6ZrO_2$.

3.0 Motivation and Outline of Dissertation

There exist some challenges in studying the oxidation behavior of the ZrB_2-SiC system. Much of the oxidation experiments that have been done on ZrB_2-SiC materials have been oxidation kinetics measurements based on weight change or scale thickness changes with time upon exposures to a known temperature and oxidizing atmosphere. The weight change measurements, usually done by thermogravimetric analysis (TGA), are somewhat limited because of the simultaneous oxidation and vaporization of the B_2O_3 phase. Also, to explore the performance of these UHTC materials in extreme environments they need to be tested at very high temperatures (>1500ºC) [1-2]. This follows some challenges, such as difficulties in achieving the necessary high temperatures in conventional laboratory furnaces, making experiments at temperatures above 1600ºC difficult and expensive. Thus the majority of the recent oxidation studies have been at temperatures below 1600ºC [1, 12-13, 15, 20-21, 24-25, 27, 29, 31-32, 34-36, 40].

The oxidation mechanism(s) of the UHTC material ZrB_2-SiC are only partially understood despite significant research the last 50 years [1]. This has been explained by Opeka[33], a leading researcher in the field, to be due to the complexity of the oxide scale that forms at high temperatures; "The multiphase scale containing multiple crystalline and glassy phases has a complex microstructure that makes the determination of the rate-limiting transport exceedingly difficult " [33].The composition gradient of the glass phase through the scale has also been acknowledged not to be well understood at this time [33] as well as the role of oxygen transport through the crystalline ZrO_2 skeleton of the ZrB_2-SiC oxide scale [1].

In general, the chemical composition and structure of an oxide scale defines the oxidation stability of a ceramic material. Deeper understanding of the formation and structure of the oxide scale of ZrB_2-SiC at temperatures at and above 1500ºC would further advance our knowledge on the oxidation mechanism(s) of this system and perhaps aid in future materials development for reusable materials in extreme condition. For this dissertation the oxidation behavior of ZrB_2-SiC composites at temperatures at and above 1500ºC is studied. First half of the thesis will focus on a novel method for rapid oxidation characterization of UHTC. The second half will introduce and discuss a novel mechanism for the high temperature oxidation of UHTC borides with SiC addition; convection of boron oxide rich liquid oxide.

Chapter 2 introduces the Ribbon Method; a novel method for testing UHTC at high temperature, rapidly at low cost. Self-supported UHTC ribbon specimens are resistively heated with a table-top apparatus to achieve temperatures from 900-2000ºC. The function and design of the Ribbon Method are discussed in detail and presented. The method enables a large temperature-time-composition parameter space to be covered by rapidly producing a large set of post-oxidation samples for analysis.

In Chapter 3 the complex oxide scale known to form during oxidation of UHTC materials is shown to be easily reproduced by using the Ribbon Method. Sets of experiments were performed on a ZrB_2-15vol%SiC-2vol%$MoSi_2$ composite at temperatures from 1500-1900ºC in ambient air and pressure. The structure and composition of the oxide scale formed at these conditions and the oxidation behavior of the composite is reported and discussed.

Chapter 4 introduces a novel mechanism for the high temperature oxidation of ZrB_2-SiC composites; a convection of boron oxide liquid. The following is proposed; during the high temperature oxidation of ZrB_2-SiC composites, boron oxide rich liquid forms at the ZrB_2-ZrO_2 interface and is transported through an overlying layer of viscous silica liquid by liquid flow, forming patterns resembling convection cell patterns. The driving force is proposed to be the large volume increase that occurs upon oxidation of boride-SiC based materials at high temperatures (≥1500ºC).

In Chapter 5 the mass transport of zirconium oxide (ZrO_2) by liquid flow of boron oxide rich liquid is introduced. The formation of ZrO_2 deposits found in the center of the convection cells during high temperature oxidation is proposed to be the consequence of liquid transport. The nature and deposition mechanism of the zirconia is reported in detail, using calculated phase equilibrium diagrams and microstructure observations of a ZrB_2-15vol%SiC composite tested at 1550ºC and 1700ºC in ambient air for various times. The calculated phase equilibrium diagrams for the binary ZrO_2-B_2O_3 system as well as the ternary B_2O_3-SiO_2-ZrO_2 system at 1500ºC are reported here to interpret these results.

Chapter 6 compares the applicability of Ribbon Method is verified further by comparing it to a conventional high temperature furnaces and arc jet facilities. Firstly, the ribbon method is compared to a high-temperature furnace by testing the same ZrB_2-SiC based composite with the two methods at same conditions. Secondly ZrB_2-SiC-$MoSi_2$ specimens tested with the ribbon method are compared to ZrB_2-SiC based composites tested with Arc Jet facilities and high-temperature furnaces, previously reported in the literature.

In Chapter 7 interpretations of oxide scale features on boride-SiC composites are discussed. Close examination of cross-sectional micrographs from the literature suggest that convection cell features reported here in earlier chapters might have been observed previously, but not interpreted. In this chapter, interpretation of these oxide scale features on ZrB_2- and HfB_2-SiC composites and their possible significance is discussed and analyzed.

In Chapter 8 the evolution of the convection cells with time, temperature and SiC concentration is investigated. Sets of oxidation tests were performed at temperatures between 1500 and 1600ºC for various dwelling times. The effect of SiC concentration on the oxide thickness and the population of the convection cells was investigated by testing three different compositions; 15 vol%, 20 vol% and 30 vol% SiC- ZrB_2. Distribution, morphology and population of the convection cells are discussed and analyzed for the different oxidation conditions and SiC concentration. The microstructure and the chemical composition of the oxide scales are also analyzed for the different composition and oxidation conditions. The oxide thicknesses of specimens with different SiC concentration are then compared and the relationship between oxide thickness and the number of convection cells is discussed.

Chapter 9 summarizes the main results of the oxidation behavior studies on ZrB_2-SiC based composites at temperatures at and above 1500ºC conducted for this dissertation. The last part of this chapter includes discussion and suggestions of future work related to this dissertation.

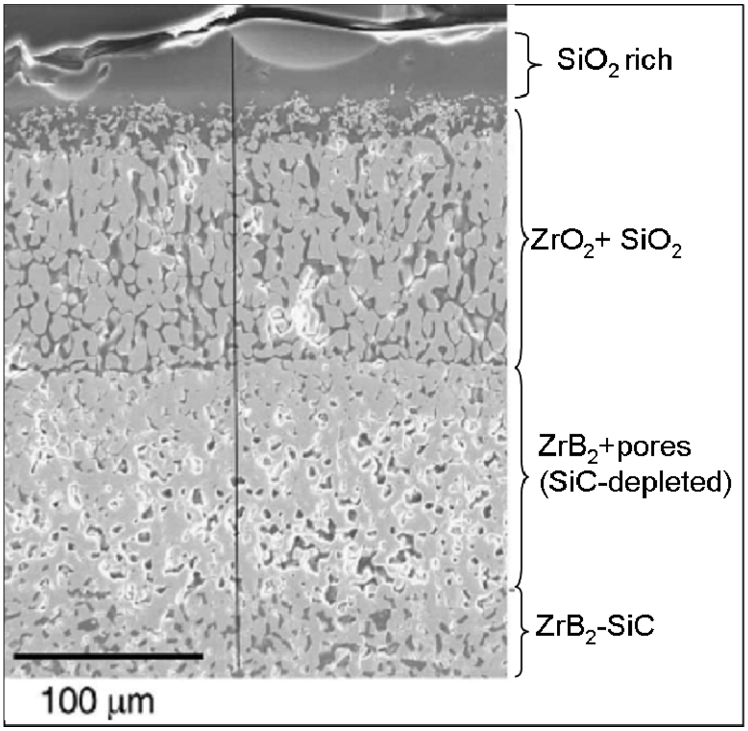

Figure 1.1: An example of an multilayer oxide scale of a ZrB2-20vol%SiC composite tested at 1627ºC for ten 10 min cycles (total 100 min) (SEM image)[18].

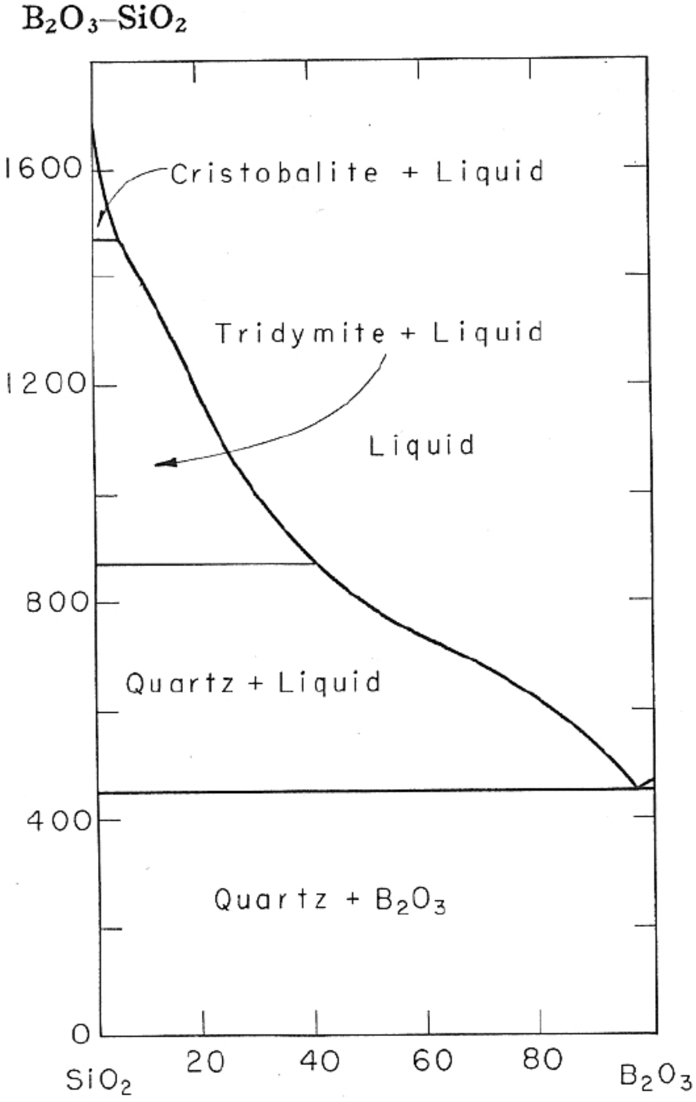

Figure 1.2: Binary phase diagram of the B_2O_3-SiO_2 system[42].

Table 1.1: Physical Properties of ZrB_2[3]

Property	Unit	ZrB_2
Density	(g/cm^3)	6.09-6.17
Lattice constants a, c	nm	0.3167, 0.3529
Crystal Structure	Space Group	C_6/mmm (Hexagonal)
Modulus of Elasticity	(GPa)	490
Hardness	(GPa)	12-22
Melting Point	ºC	3200
Electrical Resistivity at 25ºC	ΩW-cm	6-9
Thermal Conductivity	W/m·K	23-24
Oxidation resistant up to temperature	ºC	1100

References

1. M. M. Opeka, I.G. Talmy, and J.A. Zaykoski, “Oxidation-Based Materials Selection for 2000ºC + Hypersonic Aerosurface: Theoretical Considerations and Historical Experience,” J. of Mater. Sci., 39 [19] 5887-5904 (2004).

2. P. Kolodziej, “Aerothermal Performance Constraints for Hypervelocity Small Radius Unswept Leading Edges and Nosetips,” NASA Technical Memorandum 112204, July (1997).

3. R. Telle, L. S. Sigl, and K. Takagi, “Transition Metal Boride Ceramics”; pp. 803-945 in Handbook of Ceramic Hard Materials, Vol. 2. Edited by R. Reidel R. Wiley-VCH, Germany, Weinheim, (2000).

4. C. Morz. “Annual Mineral Review: Zirconium Diboride,” Am. Ceram. Soc. Bull., 74 [6] 165-166 (1995).

5. R. Tanaka, “Research and Development of Ultra-High Temperature Materials in Japan,” Materials at High Temperature, 17 [4] 457-464 (2000).

6. R.A. Cutler, “Engineering Properties of Borides,” pp.787-803 In Ceramics and Glasses, Engineering Materials Handbook, Vol. 4, ed. S.J. Schneider. ASM International, Materials Park, OH, (1992).

7. C. A. Hoffman, “Preliminary Investigation of Zirconium Boride Caramels for Gas-Turbine Blade Applicatons,” NASA Technical Memorandum E52L15a, Lewis Flight Propulsion Laboratory, Cleveland, OH (1953).

8. J.B. Berkowitz-Mattuck, “High-Temperature Oxidation, III. Zirconium and Hafnium Diborides,” J. Electrochem. Soc., 113 908-914 (1966).

9. L. Kaufman, E.V. Clougherty, and J.B. Berkowitz-Mattuck, “Oxidation Characteristics of Hafnium and Zirconium Diboride,” Trans. Metall. Soc. Of AIME, 239 [4] 458-466 (1967).

10. L. Kaufman and H. Nesor, “Stability Characterization of Refractory Materials under High Velocity Atmospheric Flight Conditions, Part I, Vol. I, Summary,” Technical Report no. AMFL-TR-69-84, Air Force Materials Laboratory, Wright-Patterson Air Base, OH (1970).

11. L. Kaufman, “Boride Composites – A New Generation of Nose Cap and Leading Edge Materials for Reusable Lifting Reentry Systems,” AIAA Advanced Space

Transportation Meeting. American Institute of Aeronautics and Astronautics, AIAA 270-278 (1970).

12. W.C. Tripp and H.C. Graham, "Thermogravimetric Study of Oxidation of ZrB_2 in Temperature Range of 800 Degrees to 1500 Degrees," Journal of the Electrochemical Society, 118, 1195-1971 (1971).

13. W.C. Tripp, H.H. Davis, and H.C. Graham, "Effect of SiC Addition on the Oxidation of ZrB_2," Am. Ceram. Soc. Bull., 52 [8] 612-616 (1973).

14. Chamberlain, W. Fahrenholtz, G. Hilmas and D. Ellerby. "Oxidation of ZrB_2-SiC Ceramics under Atmospheric and Reentry Conditions," Refractories Applications Transactions, 1 [2] 1-8 (2005).

15. M. M. Opeka, I.G. Talmy, E.J. Wuchina, J.A. Zaykoski and S.J. Causey. "Mechanical, Thermal, and Oxidation Properties of Refractory Hafnium and Zirconium Compounds," J. Eur. Ceram. Soc., 19 2405-2414 (1999).

16. F. Monteverde, A. Bellosi and S. Guicciardi, "Processing and Properties of Zirconium Diboride-Based Composites," J. Eur. Ceram. Soc., 22 279-288 (2002).

17. C.R. Wang, J.M Yang, and W. Hoffmann. "Thermal Stability of Refractory Carbide/Boride Composites," Materials Chemistry and Physics, 74 272-281 (2002).

18. S. R. Levine, E.J. Opila, M. C. Halbig, J. D. Kiser, M. Singh and J. A. Salem. "Evaluation of Ultra-High Temperature Ceramics for Aeropropulsion Use," J. Eur. Ceram. Soc., 22 2757-2767 (2002).

19. F. Monteverde, S. Guicciardi, and A. Bellosi. "Advances in Microstructure and Mechanical Properties of Zirconium Diboride Based Ceramics," Materials Science and Engineering, A346 310-319 (2003).

20. F. Monteverde and A. Bellosi. "Oxidation of ZrB_2-Based Ceramics in Dry Air," Journal of the Electrochemical Society, 150 [11] B-552-B559 (2003).

21. Q.N. Nguyen, E.J. Opila, and R.C. Robinson. "Oxidation of Ultrahigh Temperature Ceramics in Water Vapor," Journal of the Electrochemical Society, 151 [10] B558-B562 (2004).

22. M. Gash, D. Ellerby, E. Irby, S. Beckman, M.Gusman, and S. Johnson. "Processing, Properties and Arc Jet Oxidation of Hafnium Diboride/Silicon Carbide Ultra High Temperature Ceramics," Journal of Materials Science, 39 5925-5937 (2004).

23. E.J. Opila, S.R. Levine and J. Lorincz. "Oxidation of ZrB_2-and HfB_2 based Ultra-High Temperature Ceramics: Effect of Ta Additions," Journal of Materials Science, 39 5969-5977 (2004).

[24] F. Monteverde and A. Bellosi, "The Resistance to Oxidation of HfB_2-SiC Composite," J. Eur. Ceram. Soc., 25 1025-1031 (2005).

[25] F. Monteverde, "The Thermal Stability in Air of Hot Pressed Diboride Matrix Composites for Uses at Ultra-High Temperatures," Corrosion Science 47 2020-2033 (2005).

[26] L. Scatteia, R. Borelli, G. Marino, A. Bellosi, F. Monteverde, "Characterization and Process of New Metal Diboride Compound for TPS Applications," AIAA/CIRA 13th International Space Planes and Hypersonic Systems and Technology Proceedings. American Institute of Aeronautics and Astronautics, AIAA 2005-3267 (2005).

[27] W.G. Fahrenholtz, "The ZrB_2 Volatility Diagram," J. Am. Ceram. Soc., 88 [12] 3509–3512 (2005).

[28] F. Monteverde and A. Bellosi, "Development and Characterization of Metal-Diboride-Based Composites Toughened with Ultra-Fine SiC Particulates," Solid State Sciences, 7 [5] 622-630 (2005).

[29] W.G. Fahrenholtz, "Thermodynamics of ZrB_2-SiC oxidation: the formation of a SiC-depleted region," J. Am. Ceram. Soc., 90 [1] 143-148 (2007).

[30] P. Kolodziej, J. Salute, and D.L. Keese, "First Flight Demonstration of a Sharp Ultra-High Temperature Ceramic Nosetip," NASA Technical Memorandum 112215 (1997).

[31] F. Monteverde, "Beneficial Effects of an Ultra-fine α-SiC Incorporation on the Sinterability and Mechanical Properties of ZrB_2," Appl. Phys. A, 82 329-337 (2006).

[32] I.G. Talmy, J.A. Zaykoski, M.M. Opeka, and A.H. Smith, "Properties of ceramics in the system ZrB_2-Ta_5Si_3," J. Mater. Res., 21 [10] 2593-2599 (2006).

[33] A. Bongiorno, C.J. Först, R.K. Kalia, J. Li, J. Marschall, A. Nakano, M.M. Opeka, I.G. Talmy, P. Vashishta, and S. Yip. "A Perspective on Modeling Material in Extreme Environments: Oxidation of Ultra-High Temperature Ceramics." Materials Research Society Bulletin, 31 410-418 (2006).

[34] I.G. Talmy, J.A. Zaykoski, M.M. Opeka, S. Dallek, "Oxidation of ZrB_2 ceramics modified with SiC and Group IV-VI Transition Metal Diborides," Proceedings of the International Symposium on "High Temperature Corrosion and Materials Chemistry III," edited by M. McNallan and E. Opila, The Electrochemical Society, 12, p.144. (2001).

[35] I.G. Talmy, J.A. Zaykoski, and M.M. Opeka, "Properties of Ceramics in the ZrB_2/ZrC/SiC System Prepared by Reactive Processing," Ceramic Engineering and Science Proceedings, 19 [3] 105-112 (1998).

36. A. Rezaie, W.G. Fahrenholtz, and G.E. Hilmas, "Evolution of Structure during the oxidation of Zirconium Diboride-Silicon Carbide in Air up to 1500ºC," Journal of the European Ceramic Society, 27 [6] 2495-2501 (2007).

37. A.K. Kuriakose and J.L. Margrave, "The Oxidation Kinetics of Zirconium Diboride and Zirconium Carbide at High Temperatues," J. Electrochem. Soc., 111 [7] 827-831 (1964).

38. R.J. Irving and I.G. Worsley, "Oxidation of Titanium Diboride and Zirconium diboride at high temperatures," J. Less-Common Metals, 16 [2] 102-112 (1968).

39. P.C. Setze, "A Review of the Physical and Thermodynamic Properties of Boric Oxide," Lewis Flight Propulsion Laboratory, Cleveland, OH. NACA-RM-E57B14, April 24, (1957).

40. A.R. Rezaie, W.G. Fahrenholtz, and G.E. Hilmas, "Oxidation of Zirconium Diboride-Silicon Carbide at 1500ºC a low partial pressure of oxygen," J. Am. Soc., 89 [10] 3240-3245 (2006).

41. Terrazas-Salinas and C. Cornelison. Test Planning Guide for ASF Facilities. A029-9701-XM3 Rev. B. Thermophysics Facilities Branch, Space Technology Division, NASA Ames Research Center, CA, March (1999).

42. T.J. Rockett and W.R. Foster, J. Am. Soc., 48 [2] 78 (1965).

CHAPTER 2

RAPID OXIDATION CHARACTERIZATION OF ULTRA-HIGH TEMPERATURE CERAMICS*

1.0 Introduction

UTHC are receiving more attention and interest due to their potential ability as the material for the reusable thermal protection system and other components for the next generation of hypersonic aerospace vehicles. These new designs of hypersonic vehicles incorporate sharp aero-surfaces i.e. nose caps, engine cowl inlets, and leading edges (LE's), to increase aerodynamic performance. These components will experience extreme re-entering environment such as oxidizing atmosphere, high velocities and pressures, and temperatures from 1500ºC-2400ºC [1-4].

Currently the oxidation behavior of UHTC materials at higher temperatures (≥1600ºC) is not well understood. This is primarily due to the complexity of the oxide scale and limited information of the oxidation mechanism at higher temperatures. Also, there exist challenges in achieving the necessary high temperatures in conventional laboratory furnaces, making experiments at temperatures above 1600ºC difficult and

---

[*] Parts of this chapter were presented in the manuscript "Rapid Oxidation Characterization of Ultra-High Temperature Ceramics" by S.N. Karlsdottir, and J.W. Halloran, in the Journal of American Ceramic Society, 90 [10] 3233–3238 (2007).

expensive. Thus the majority of the oxidation tests being done are in furnace at temperatures below 1600ºC.

Exceptions from this are tests at the Arc Jet Facilities, which simulates reentering environment; the NASA Glenn Torch Facility; and high temperature furnaces with Zirconia (ZrO_2) heating elements (max. T= 2000ºC). The high temperature furnaces have $MoSi_2$ heating elements in an outer chamber that are used to heat the Zirconia elements in the hot-zone of the furnace to their conductive temperature of 1200ºC [5-6]. These furnaces do not seem to be very common in laboratories studying high temperature oxidation, possible due to the high cost of the Zirconia heating elements. The NASA Glenn Torch Test facility was designed to simulate a rocket motor combustion environment, where the specimen is exposed to a flame of an oxy-acetylene torch, T_{max} = 3037°C (5500 °F), representative of the 3037°C solid rocket motor combustion temperatures [7-8]. The Arc Jet facilities are located in the NASA Ames Arc Jet Complex at NASA Ames Research Center, CA, and at the Aerospace Testing Alliance, Arnold Engineering Development Center, Arnold AFB, TN. The Arc Jet facility is used to simulate the aerodynamic heating that occurs on nose caps, wing leading edges and other areas of spacecrafts requiring thermal protection. It is capable of reaching temperatures on the range of 1700-2500ºC [1, 6, 9-10]. Arc jet testing is expensive due to the high power used during testing (40-75 MW) and the application process, which is both time consuming and complicated. The Ames Arc Jet facilities are operated primarily to support the government aerospace research and developmental testing (particular NASA) and if outsiders want to use it a proposal has to be submitted on their behalf. If the proposal is accepted, a test development process begins which can take weeks or months, all depending on the complexity of the test and the amount of fabrication or facility modification required [11].

Deeper understanding of the oxidation mechanism of UTHC at temperatures at and above 1500ºC is crucial for assessing the suitability of these materials as a structural component at high temperatures. Better knowledge of the oxidation behavior of these systems will be useful in materials development for future reusable components for extreme re-entering environment. To be able to understand the oxidation mechanisms of UHTCs such as the ZrB_2 based composites and the formation of its multi-component oxide scale, we must characterize the oxidation behavior and physical properties at very high temperatures. But as described above that can be difficult and expensive with the oxidation facilities and techniques available today. Thus we have designed and built a table-top apparatus used with a self-supported, UHTC ribbon specimen to achieve the necessary high temperatures for oxidation experiments from 900-2000ºC. This is a novel method for testing UHTC materials at high temperatures, rapidly at low cost. It enables a large temperature-time-composition parameter space to be covered by rapidly producing a large set of post-oxidation samples for analysis. Herein it will be referred to as the Ribbon Method. This chapter introduces the Ribbon Method and explains its design in detail. The design of the table-top apparatus and the ribbon specimen is described, as well as the function and performance of the system.

2.0 The Ribbon Method

2.1 The Ribbon Specimen

UHTC materials are metallic conductors, thus are able to resistively heat when a current is past through the material. The design of the Ribbon Method is based on this fact; a ribbon specimen is resistively heated by passing modest current through it. A table-top apparatus supplies the ribbon specimen with the current and controls the temperature of the specimen. The specimen is fabricated by reducing the thickness of matchstick size specimens in the center with machining to make a ribbon region with a thickness of 400-500 µm. The ribbon, herein called the hot-zone, can reach very high temperatures when a current is passed into the thicker ends of the specimen. The thicker ends of the specimen will stay relatively cool, while the hot-zone can reach the desired temperature. With this geometry the specimen is self-supportive. Figure 2.1 shows the geometry and a digital image of a ribbon specimen. The hot-zone is thus not in contact with foreign material. This is important, because at these high temperatures the specimen would react to materials it contacts.

2.2 The Table-Top Apparatus

2.2.1 Validation of Design Concept

Before building the final design of the table-top apparatus, a demo design of the apparatus was built from available material from the laboratory to verify that the design concept would work. Figure 2.2 shows the first version (demo design) of the apparatus with a self-supported ribbon sample. In the demo design a UHTC ribbon specimen sits on a simple copper holder fixed on a plexi-glass plate and connected to current leads with alligator clips; see Figure 2.2 (a)-(b). For the verification test the current leads were connected to a power supplier of a conventional furnace which passed a current into the thick ends of a ribbon specimen. The hot-zone of the sample would then start to glow and reach high temperatures quickly. This experiment verified that the self-supporting, ribbon specimen would heat up to high temperatures in the reduced center of the matchstick in the ribbon hot-zone, without failure and without creating a difficult-to-manage heat load in the surroundings. After verifying that the demo designed worked, i.e. the design concept was applicable, the final version of the table-top apparatus with the ribbon specimen was designed and built.

2.2.2. Design and Function

The table-top apparatus provides the current and controls the temperature of the specimen. The control unit of the apparatus consists of a control panel (MHI BPAN-O^{TM}, Micropyretics Heaters Int., Cincinnati, OH, USA), and a programmable temperature controller (Model 2416, Eurotherm, Leesburg, VA, USA). The power controller is a single phase silicon controlled rectifier (SCR) with an advanced current limit and a soft start feature. A step down transformer is a part of the apparatus and is connected to the controller to give us a desired secondary current on the range of 0-125 Amps. The power input used to heat the ribbon specimen to temperatures from 900ºC to 2000ºC is around 90-125 W, where the voltage across the specimen is on the order of 1 V and the current ranges from 90-125 Amps.

The temperature sensor of the apparatus is a micro optical infrared pyrometer that can measure temperature from 900°C to 3300°C with a fast response time (minimum 1 ms). The micro pyrometer is a single color pyrometer with a wavelength of 1 μm and a bandwidth of 0.7-1.1 μm. It is focused on the hot-zone of the specimen and provides the temperature signal to the temperature controller. The amount of current passed through the sample is controlled with the power controller to obtain the desired temperature-time schedule. The fast response time is crucial here because during the oxidation testing the specimen will oxidize and form an insulating oxide scale which will result in smaller cross-sectional area of the conducting material with time. This means that the current needed to maintain the set temperature will also decrease with time, because of this the temperature and the current signal will have to be translated to the temperature controller constantly and frequently to be able to control the temperature. The UHTC specimen can also be quickly heated and cooled due to a fast response of the temperature controller and the pyrometer and the small size of the ribbon specimen. Any time-temperature profile, cyclic or static oxidation, can be conducted using the pyrometer signal as the control variable. With the table-top apparatus and the ribbon specimen oxidation experiments at temperatures in the range of 900ºC-2000ºC can be performed, without creating a difficult-to-manage heat load in the surroundings due to the small size of the specimen. A similar approach was used by Cabrera et al.[12] for the design of a cyclic metal-oxidation apparatus. Cabrera et al. resistively heated thin Si-coated steel foils, 50 μm thick, but were only capable of reaching temperatures on the range of 400-1000ºC [12].

Figure 2.3(a) shows the self-supported ribbon specimen connected to the table-top apparatus. Figure 2.3(b) shows the specimen sitting on a simple Cu/Ag bridge fixed with alligator clips, which can serve as voltage probes. The bridge consists of copper (Cu) plates that hold up silver (Ag) sheets where the thicker ends of the specimen sits. The Cu plates are connected to the current leads and fixed to a thermal insulation base plate (Transite® HT, Monaco, MI, USA). Silver was used for connecting the specimen to the Cu plates due to its high conductivity and oxidation resistance (copper was not suitable due to its poor oxidation resistance). Thin alumina (Al_2O_3) sheets are used between the alligator clips and the sample as heat shields, to avoid over-heating of the alligator clips.

2.2.3 Trouble Shooting

The demo design used for the verification tests gave valuable information how the final design should look like. During the verification tests few problems occurred e.g. for tests run for longer than 10 min. the Plexiglas base and the glue, used for attaching the copper (Cu) sheet supports to the base, started to melt. Thus the final design had a thermal insulation base plate instead of the Plexiglas base and a high temperature epoxy polymer was used instead of the glue. For the demo design the ribbon specimen sat on a Cu supports and current was conducted from the leads connected to the Cu supports to the specimen (see Figure. 2.2). This was not suitable for high temperature testing due to the low oxidation resistance of the copper, which started to oxidize during testing and forming an insulating oxide on the surface. This would stop the current from being conducted from the current leads through the Cu supports to the specimen. For this sake thin silver (Ag) sheets were used for conducting the current to the thicker ends of the specimen in the final design. In the final design the Ag sheets are attached to Cu supports which are connected to the current leads, this is shown in Figure 2.3. Also, the plastic covered Cu current leads used for the demo design (see Fig. 2.2) were replaced by heavy duty electric cables due to overheating of the Cu leads for longer testing times.

Due to variable electrical resistance of the ribbon specimen (dependant on the cross-sectional area of the hot-zone and the materials resistivity) the proportional-integral-derivative (PID) control variables of the temperature controller have to be adjusted accordantly so the desired temperature is reached without overshooting. This can be done by using the automatic tuning (Atun) option of the Eurotherm temperature controller (Model 2416). Before using the Atun, higher and lower power percentage output (oP %) limits have to be set accordantly which can range from 0-100%. An appropriate value will depend on the cross-sectional area of the hot-zone and the materials resistivity, to high or low value of the higher and lower oP% limit will result in the specimen reaching to high temperatures or not reaching the set temperature at all. When appropriate values are chosen for the lower and higher oP% limit, the set temperature maintained within ± 10ºC.

2.2.4 Data Sampling and Processing

An AC clamp-on-adapter is clamped on the secondary wire in the circuit to detect the current going through the specimen and then transfers it to a data acquisition card (DAQ) (NI USB-6009, National Instruments Corporation, Austin, TX, USA) connected to a computer. The temperature of the hot-zone measured with the micro pyrometer is transferred to a computer through a RS-232 cable. To process the data from the DAQ and the RS-232 cable LabVIEW from National Instruments Inc. is used. A LabVIEW program was designed to collect and save the temperature, current and voltage data recorded during testing. The LabVIEW program records the signal from the DAQ and the RS-232 cable (connected to the pyrometer) and plots the Root Mean Square (RMS) value of the alternating current (A.C.) vs. time, and the temperature vs. time. The data is collected at sampling frequency of 4 Hz, i.e. a sampling time of 250 ms. Figure 2.4 shows an example of a temperature and a current profile of a ribbon specimen tested in the apparatus at 1600ºC for 15 min.

2.2.5 Temperature Calibration

The MI-S 140 infrared pyrometer is a single color pyrometer where emittance from the heated material has to be a fixed input of the pyrometer. For UTHC there is limited information available of the emissivity at elevated temperatures. For ZrB_2-SiC and HfB_2-SiC composites it is known that the emissivity changes with temperatures. The few reported emissivities of ZrB_2 and ZrB_2-SiC composites at elevated temperatures range from 0.8 to 0.5, and for oxidized SiC-Si composites the emissivity has been reported as high as 0.93 [13-15].

For our experiments the emissivity was set to 0.9 (which is a more conservative setting, in effort to never underestimate the temperature). Calibration of the pyrometer with emissivity value of 0.9 was done by using a conventional furnace with a calibrated Type B thermocouple situated in the middle of a tube furnace close to a ZrB_2-15vol%SiC-2vol%$MoSi_2$ specimen that the pyrometer was focused on; a schematic of the setup is shown in Figure 2.5. The tube furnace was open at one end so the pyrometer could focus on the sample. The furnace was ramped up to 1550ºC with a holding time of 1 hour. The temperature measurement from the pyrometer with emissivity equal to 0.9 agrees well with the temperature measured with the thermocouple, see Figure 2.6. This suggests that the emissivity does not change dramatically at temperatures around 1500-1600ºC. Thus the emissivity of 0.9 was used for the pyrometer for experiments at temperatures from 1500-2000ºC. Some change in the emissivity is though expected at temperatures above 1700ºC. This will have to be taken as an insignificant error in the temperature signal, due to measurements of the true value of the emissivity for these materials are beyond the scope of this dissertation and thus not a subject here.

3.0 Temperature Gradients in the Ribbon Specimen

3.1 Temperature Gradient Measurements and Modeling along the Hot-zone of the Ribbon Specimen

Micro-structural studies of the surface of the ribbon specimen show evidence of a thermal gradient along the x-axis of the hot-zone of the ribbon specimen in the form of a non-uniform microstructure, as shown in Figure 2.7. This is not surprising since the geometry of the ribbon specimen, specifically the chamfered edges shown in Figure 2.1., should induce some thermal gradient (dT/dx) in the thin ribbon section (hot-zone). The image shown in Figure 2.7 is a secondary electron image (SEM) of a surface of a ZrB_2-15vol%SiC-2vol%$MoSi_2$ ribbon specimen tested in the apparatus by heating it from room temperature to 1917ºC in ca. 1.5 min. A ca. 4 mm^2 region of the hot-zone, shown in Figure 2.7, has a rather uniform microstructure while the region close to the chamfered edges has a gradual change in the microstructure.

Temperature characterization along the x-axis of the hot-zone of a ZrB_2-15vol%SiC-2vol%$MoSi_2$ ribbon specimens were conducted by measuring temperatures along the hot-zone of the specimens with a MI-S 140 infrared micro-pyrometer with a spot size of ca. 1 mm (0.9 mm). For a comparison, a finite element modeling (FEM) of the temperature distribution along a ribbon section of a specimen was done by using a software called FEMlab (recently changed to COMSOL Multiphysics™) [16]. The simulations with COMSOL were done partially in collaboration with Andrew Koltonow, an undergraduate student in the Materials Science and Engineering department at University of Michigan.

Five temperature distributions were measured along the hot-zone with different peak temperatures, from 1310-1570ºC. The peak temperature is the temperature in the middle of the hot-zone, indicated by x = 0 in Figure 2.8. Two ZrB_2-SiC-$MoSi_2$ specimens were used for the measurements with a cross-sectional area of the hot-zone as 1.23 mm^2 (specimen no.1; width =2.28 mm, thickness = 0.54 mm, length = 7.0 mm) and, 1.16 mm^2 (no. 2; w=2.28 mm, t = 0.51 mm, l = 7.0 mm). The arrows in Figure 2.8(a) indicate where the measurements were taken along the hot-zones of the ribbon specimens. The measurements were taken at nine locations on the ribbon specimen; these are indicated with white circles on the ribbon specimen shown in Figure 2.8(a). The radiation from each location was measured by the pyrometer with a spot-size of ~1 mm. Five measurements were taken on average for each location in effort to get a good estimation of the temperature distribution.

The Finite Element Method (FEM) is a numerical approach to solve problems governed by differential equations. With FEM modeling sets of differential equations are solved by splitting the part that is being modeled into finite number of elements, connected at their nodes and along hypothetical interelement boundaries[17]. The elements are typically in the shape of triangles that form a grid over the object as shown in Figure 2.8(b). So called Multiphysics application, available in the FEMlab software, was used to model the temperature distribution in the ribbon specimen three dimensionally. The Multiphysics application is a finite element based program which allows the user to combine more then one physical model to describe the system. For our case a so called Conductive Media was used to describe how the specimen resistively heats up when the current is applied. Another model called Convection and Conduction was used with the Conductive Media model to describe the heat transfer in the system, i.e. conduction and convection. The radiation part of the heat transfer mechanism which is a dominant part for this system is included in the boundary conditions. The system can be solved either as a steady-state non-linear equation or as a time-dependant equation. The time-dependant approach predicted correctly that the ribbon heats up rapidly, reaching 99% of its steady-state temperature in 7.5 sec. The objective of the experiment described in this section was in determining the temperature gradient and distribution in the ribbon specimen after it reaches the steady-state temperature. Thus steady-state temperature solution will only be used here. The experiment performed on specimen no. 1 with an average peak temperature of 1431ºC was modeled with FEMlab for a comparison to the experimental data. The boundary conditions used were heat loss due to radiation and convection, using emissivity $\varepsilon = 0.9$[*]; view factor $F_{12} = 1$ (for a small radiating surface enclosed in large cavity, i.e. larger room)[18]; and convection heat transfer coefficient in air $h_{air} = 25$ W/m² (commonly used for free convection)[18]. The physical properties and dimensions used for the modeling are shown in Table 2.1[20-22].

The experimental results are compared to the results from the FEM modeling in Figure 2.9 and 2.10. In Figure 2.9, simulated temperatures along x-axis of the hot-zone of specimen no. 1, for a current of 104 Amps, is compared to the experimental values. The diamonds in the graph represents the experimental data and the boxes represent the computational results. For these conditions (shown in Table 2.1) the experimental and computational data agree quite well. The simulated temperature in center of the ribbon is within the standard deviation and gives a good estimation of the temperature that can be reached with a corresponding current. The simulated temperatures at the end of the hot-zone (at x = – 4 and 4 mm) are slightly higher and not within the standard deviation. This

---

[*] This is considered a reasonable value from the temperature calibrations from Section 2.2.5.

could be due to an error from the computation by under estimating heat loss to the surrounding by having the silver supports in air or an overestimation in the experimental values due to radiation effect from the hotter part of the specimen. Figure 2.10 shows the FEM simulated temperature distribution for specimen no.1 (shown in Figure 2.9) and the measured temperature distribution of all the experiments. The measured temperatures along the hot-zone of the ZrB_2-SiC-$MoSi_2$ specimens are shown with solid lines while the temperature distribution modeled with FEMlab is indicated by circles and slashed line. An average temperature gradient for each measurement (each peak temperature) was calculated by subtracting the peak temperature (at x = 0) from an average temperature of the two end points (at x = – 4 and 4 mm) and dividing it by the distance; 4 mm. These values are shown in Table 2.2 along with the computed value from the FEM analysis. The gradient from the FEM modeling agrees quite well with the gradient calculated from the measured values, especially for the experiments closer to the peak temperature estimated from the FEM modeling. Figure 2.11 shows a graph of the calculated temperature gradients for the lower peak temperature experiments and from the FEM modeling, vs. the corresponding location on the ribbon specimen. The graph illustrates that the temperature gradient agrees rather well close to the center of the hot-zone whereas to the sides the FEM model differs from the experimental values. A possible reason for this could be a discrepancy in the curvature of the chamfered edges in the drawn 3D model of the ribbon specimen and the actual curvature, which would induce an error in the temperature distribution and gradient close to the chamfered edges. Figure 2.11 also shows how the temperature gradient is small close the center, indicating that there exists a relatively uniform temperature distribution in the center with a length of ca.

2.0 mm. Figure 2.7 also supports this, showing a uniform microstructure, in the center of the hot-zone of a ZrB_2-SiC-$MoSi_2$ specimen, of ca, 2.0 mm in length (x-direction).

The characterization of the temperature distribution along the hot-zone of the ribbon specimen is important, primarily as a part of characterizing the function and performance of the Ribbon Method. Additionally, it shows how the FEM modeling can be used to gain valuable information of how the Ribbon method works for different UHTC systems. Information such as how much current is needed to reach a particular temperature for a particular specimen with different dimensions and physical properties.

3.2 Temperature Gradient through the thickness of the Hot-zone

Because the ribbon specimen is being heated internally with a flowing current a thermal gradient is also possible in the z-direction, i.e. from the inside of the ribbon section to the outer surface. It is however not possible in our case to measure this gradient, but a very rough estimate of the gradient can be made by assuming steady-state conditions and a one-dimensional heat transfer. The heat transfer is assumed to be by conduction q''_{cond} through the half thickness of the ribbon specimen (in the z-direction) to the surface and then from the surface by radiation q''_{rad} and convection q''_{conv}. Then for an infinitely long and wide slab of ZrB_2-SiC material the conservation of energy gives[18],

$$\begin{aligned} \dot{E}_{in} - \dot{E}_{out} &= 0 \\ q''_{cond} - q''_{conv} - q''_{rad} &= 0 \\ k\frac{T_1 - T_2}{t} &= h(T_2 - T_\infty) + \varepsilon\sigma_B(T_2^4 - T_{sur}^4) \end{aligned} \tag{2.1}$$

were k is the thermal conductivity (66 W/m·K)[22], t is the half thickness of the ribbon section of the specimen (250 μm) and h is the convection coefficient (25 $W/m^2 \cdot K$)[18], ε is the surface emissivity (0.9), σ_B is the Stefan-Boltzmann constant (5.67×10^{-8} W/m^2·K^4), T_2 is the known surface temperature, T_{sur} is the temperature of the surroundings (25ºC) and T_∞ is the temperature of the ambient air (25ºC).

If we substitute these values into equation (2.1) as well as a surface temperature of 1600ºC the interior temperature T_1 is equal to 1603ºC, which would give a temperature gradient of 12ºC/mm in the z-direction. This is a very small thermal gradient compared to the high temperatures involved, it is likely that it results from the relatively high thermal conductivity of the ZrB_2-SiC material and the small thickness of the ribbon section (where t is the half thickness of the ribbon). The author acknowledges that this is a rough estimation and that with a growing insulating oxide scale the temperature gradient presumably will increase somewhat, nevertheless this suggests that the thermal gradient in the z-direction is not a crucial factor so this will not be pursued further.

4.0 Discussion: Comparison of Ribbon Method with Current High Temperature Facilities for UTHC

The table-top-apparatus with the ribbon specimen allows rapid and inexpensive oxidation experiments on UHTC due to the fast heating rate and the low power (~100 W) required to resistively heat the hot-zone of the specimen. The UHTC specimen can be quickly heated and cooled by varying the current due to the fast response of the temperature controller and the small size of the hot-zone of the specimen. This allows a very fast heating rate which minimizes the oxidation effect during heating (before reaching the dwelling temperature). That is not so easy with conventional furnaces where the heating and cooling rates are often limited (very fast heating rate damages the heating elements). Also, with the fast heating and cooling of the ribbon specimen cyclic oxidation is easy and quick. Another advantage of the Ribbon Method is that the oxidizing part of the sample is not touching any foreign materials, thus contamination is not a problem. That is known to be a problem for high temperature furnaces and arc jet testing. For these facilities a specimen holder has to be specifically designed and used in the oxidation tests to minimize contamination. This is not easily done, for example for oxidation tests done in zirconium heating element furnaces at high temperatures, above 1500ºC and up to 1900ºC, the UHTC specimen was shown to be easily contaminated by its supports [6]. At these high temperatures the specimen reacts with everything that it touches. This can be avoided by using the ribbon method. The operation cost of the table-top apparatus is very low due to the small power used during testing. For example only c.a. 120 Watts (120 Amp and ca 1.0 Volt) are needed to reach a temperature of 2000ºC, which is very small compared to the 60 MW used during an Arc Jet testing. With the table-top apparatus and the ribbon specimen UHTC oxidation experiments can be done rapidly at low cost enabling a much larger range of temperature-time-composition parameter space to be covered by easily producing a large set of post-oxidation samples for analysis.

With many high temperature experiments, the sample is hidden inside a furnace, making direct observation and real time diagnostics difficult. One of the advantages of the Ribbon Method is that the ribbon specimen is unobstructed and can be directly observed during oxidation. Also, the heat load is small due to the small size of the specimen so optics can be focused on the hot ribbon to obtain images or observe spectra. To be able to achieve high temperatures with the Ribbon Method, the cross-sectional area of the hot-zone of the specimen has to be small; $A = 0.7\text{-}0.15\ \text{mm}^2$ ($t = 0.35\text{-}0.5$ mm and $w = 2.00\text{-}2.30$ mm). This means that the testing time can be limited by how fast the sample oxidizes. For example, at very high temperatures, around 1900ºC, the duration of the oxidation test is limited by the size of the sample i.e. how fast it oxidizes away (through the cross-section of the specimen). The most advanced facilities also have limitations i.e. for the Arc Jet facilities the duration time of the tests are limited by the input power levels used. For example, to achieve temperatures in the range of at 1700-2400ºC[10] the power needed is 20-60 MW for which the maximum duration time is 30 min. Table 2.3 summarizes the comparison of current UHTC testing facilities and the Ribbon Method. The grey boxes represent the desired qualities for high temperature facility for testing UHTC materials for sharp-surface reentering vehicles. The reentering conditions for a sharp-surface space vehicle includes temperatures up to 2400ºC, low air pressures (0.005-0.010 atm) and relatively short times (15 min) [1-4, 19]. From Table 2.4 we can see that the ribbon method fulfills the desirable qualities quite well and thus should be considered as a valuable addition to the current high temperature facilities for UHTC.

5.0 Summary

The Ribbon Method, consisting of the table-top apparatus and its ribbon specimen, enables us to perform oxidation experiments at temperatures above 900ºC and as high as 2000ºC, with a power input of only around 100 watts. With the Ribbon Method there is no difficult-to-manage heat load in the surroundings due to the small size of the specimen. It also allows a large temperature-time-composition parameter space to be covered by rapidly producing a large set of post-oxidation samples for analysis. The Ribbon Method is a novel method for rapid oxidation characterization of UHTCs at high temperatures and a valuable alternative to the current high temperature facilities for UHTC.

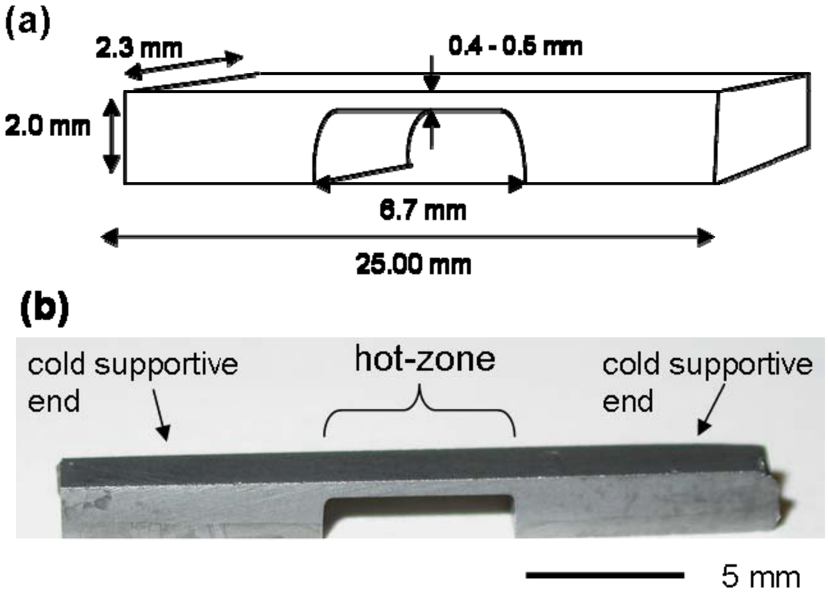

Figure 2.1: (a) Schematic of the dimensions and geometry of a ribbon specimen (b) Digital image of a machined ribbon specimen.

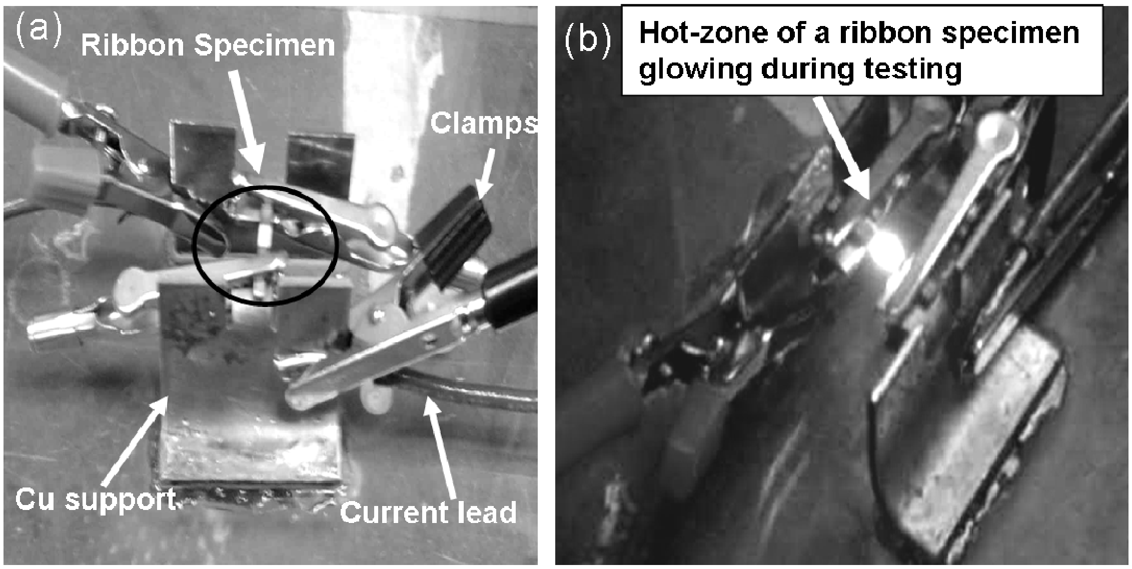

Figure 2.2: The first version of the table-top apparatus; (a) Image of the ribbon specimen sitting on the copper supports of the table-top apparatus after testing, the white oxide on the middle of the ribbon specimen is the oxide grown in the hot-zone during oxidation, (b) a glowing specimen during oxidation testing in the apparatus.

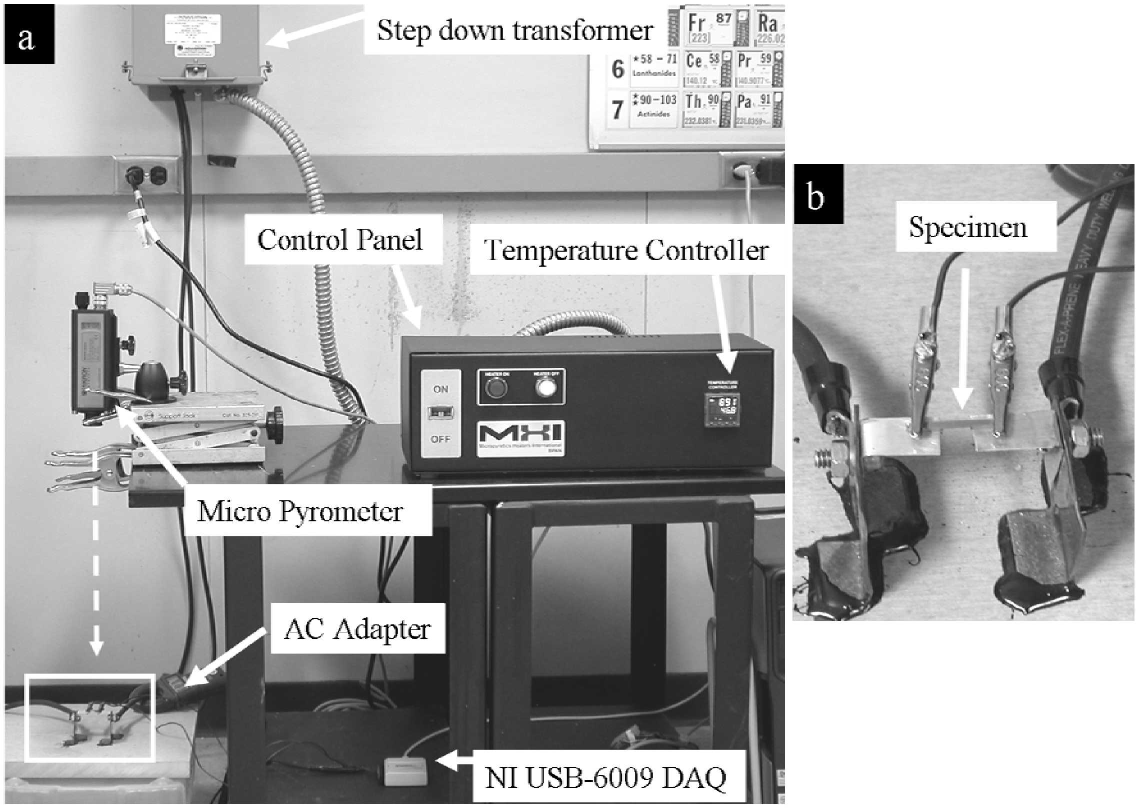

Figure 2.3: Digital image of the final design of the table-top apparatus (a) The self-supported ribbon specimen (white box) and its table top apparatus (b) the ribbon specimen sitting on the Cu/Ag holder (higher magnification of the white box in the lower left corner of (a)).

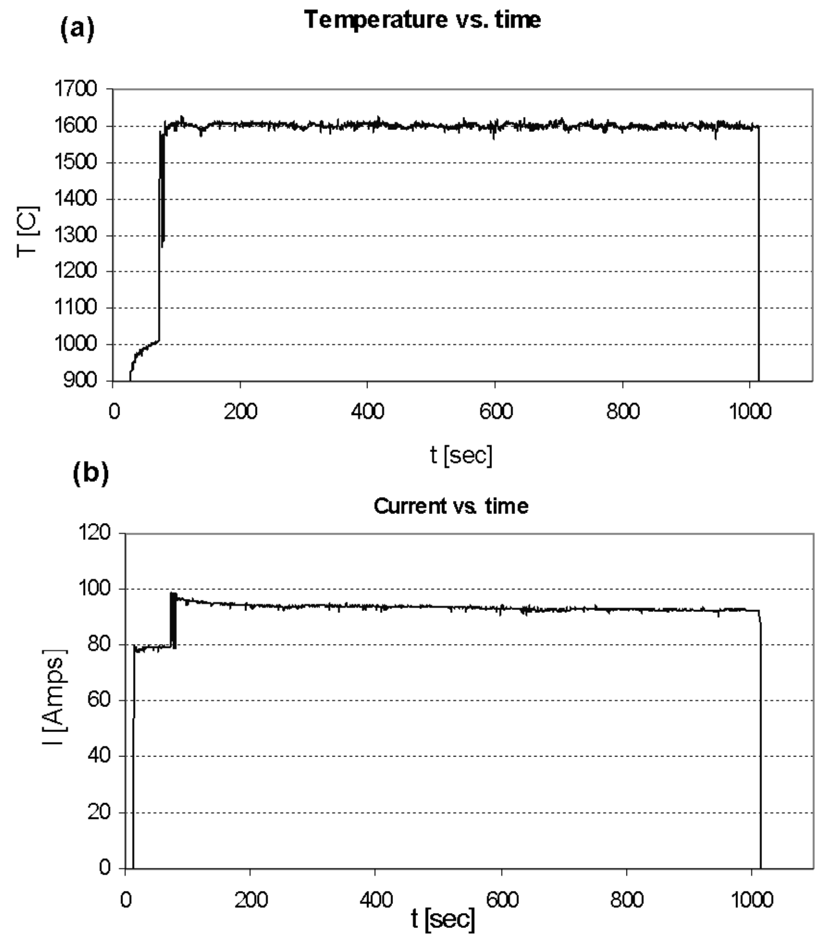

Figure 2.4: (a) Temperature profile (b) and a current profile of a specimen tested at 1600°C for 15 min.

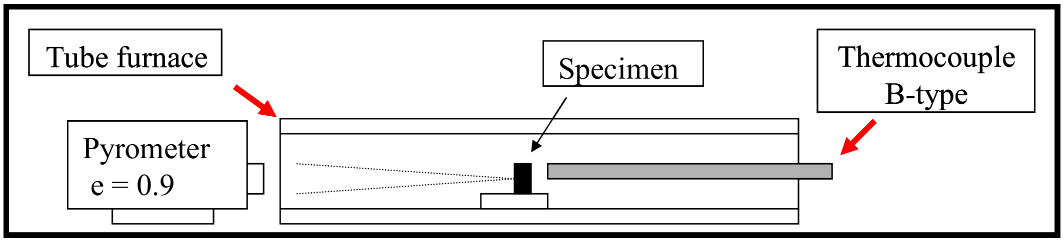

Figure 2.5: Schematic of the setup of the experiment for the temperature calibration. Showing the pyrometer with an emissivity value of 0.9 focused on a ZrB_2-SiC-$MoSi_2$ specimen and a B-type calibrated thermocouple measuring the temperature of the air close to the specimen.

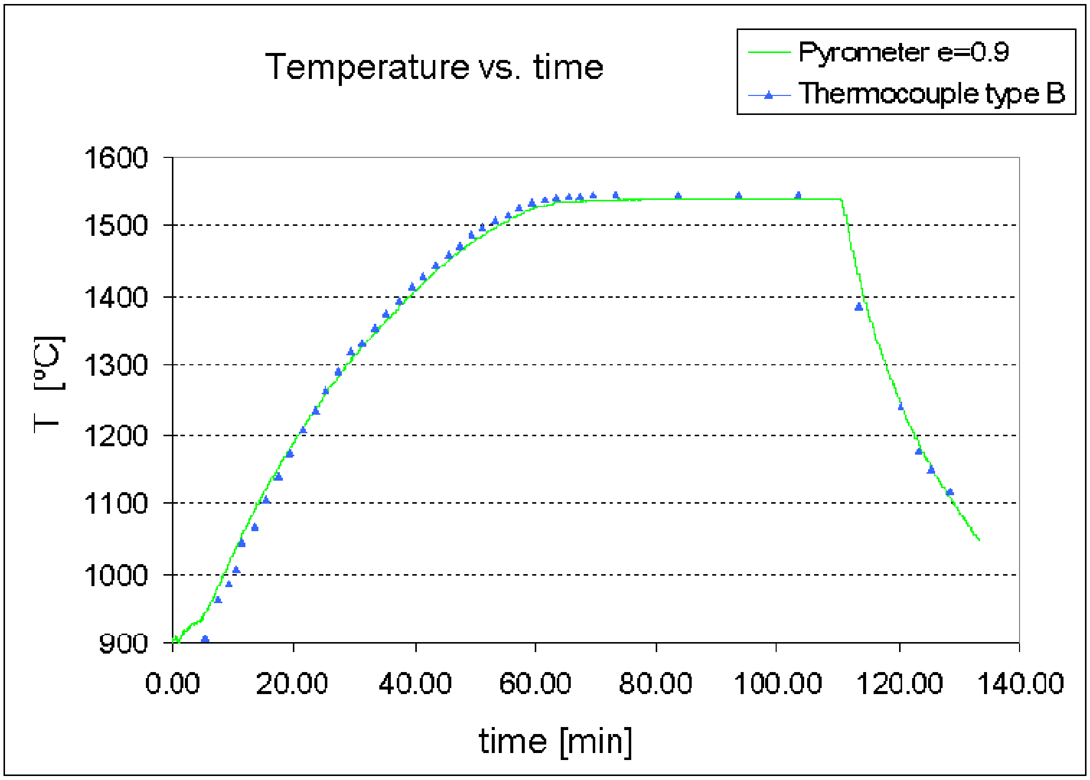

Figure 2.6: The measured temperature of a ZrB_2-SiC-$MoSi_2$ specimen tested at 1550° for 1 hr. with the micro-pyrometer set to a emissivity of 0.9 (solid line) and with a calibrated B-type thermocouple (triangles).

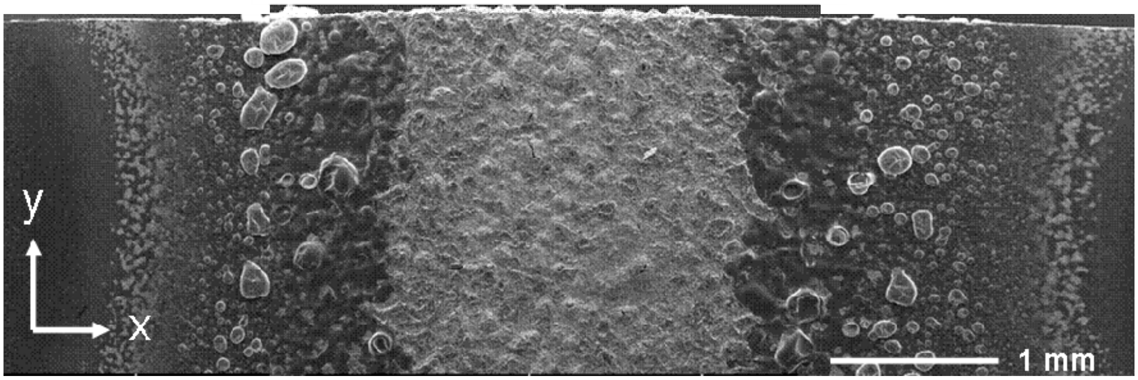

Figure 2.7: SEM picture of the surface of a ZrB_2-SiC-$MoSi_2$ specimen, showing evidence of a temperature gradient along the x-direction of ribbon specimen tested in the table-top apparatus.

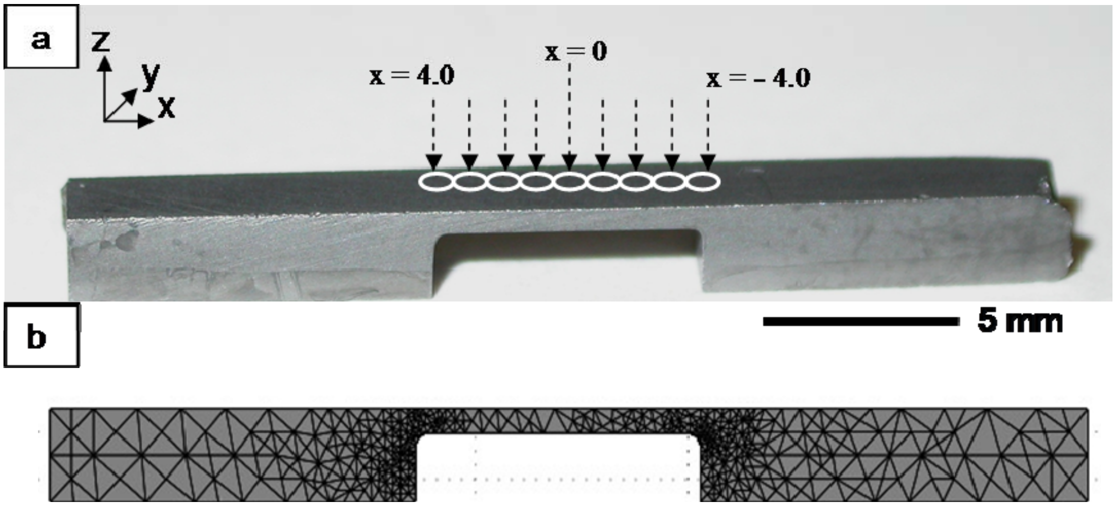

Figure 2.8: (a) A digital image of a ribbon specimen; the white circles indicate the locations where the measurements were taken (b) A 2D view of a 3D drawing of the ribbon specimen, showing the FEM grid.

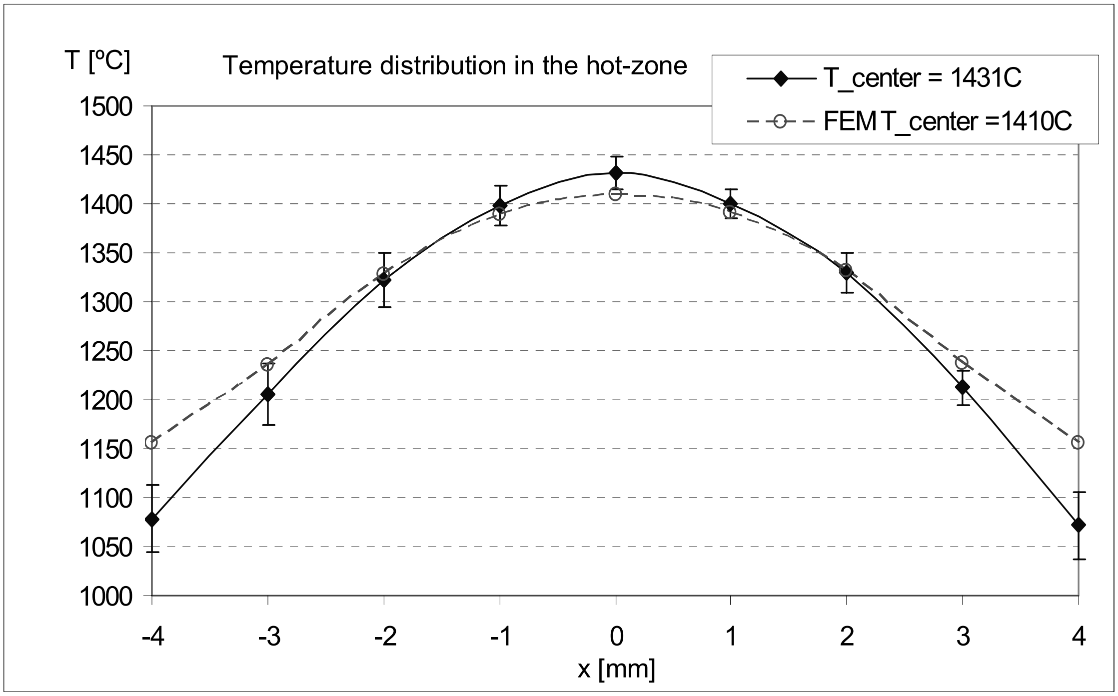

Figure 2.9: Temperature distribution along the x-axis of the hot-zone; the solid diamonds are the measured values and the open circles are the FEM simulated temperatures for specimen no. 1 and the parameters and properties given in Table 2.1.

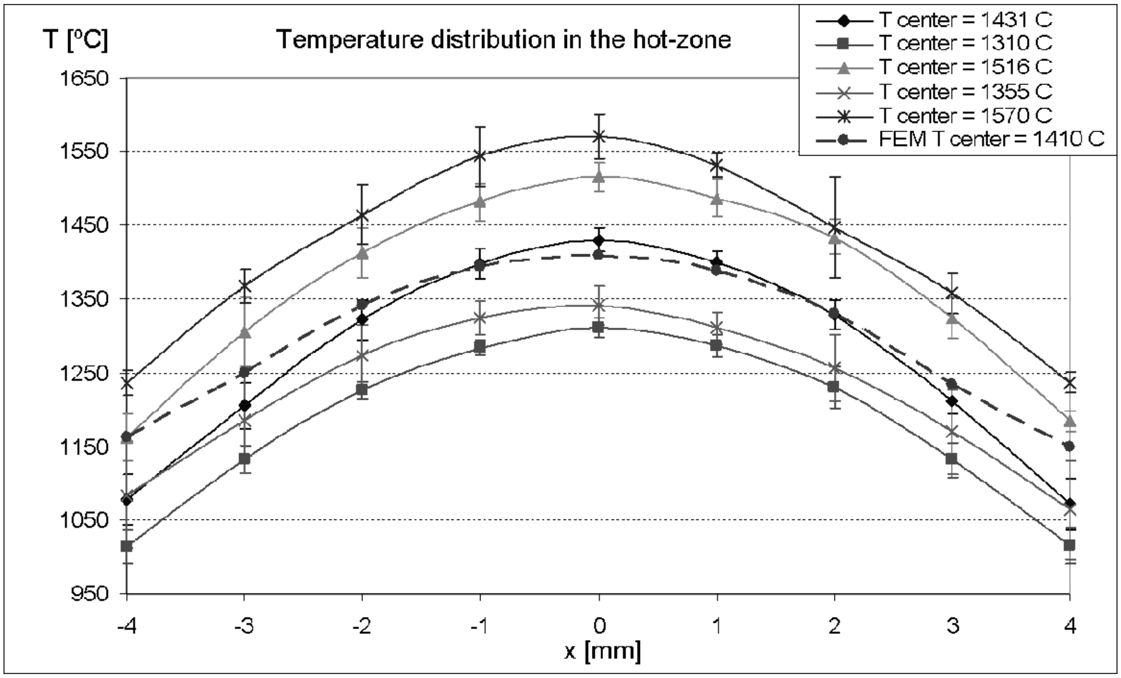

Figure 2.10: Measured temperatures along the hot-zone of the ZrB_2-SiC-$MoSi_2$ specimens and the simulated temperature distribution of specimen no.1 for I = 104 Amps. The solid lines are the measured values and the slashed line with circles is the temperature distribution modeled with FEMlab.

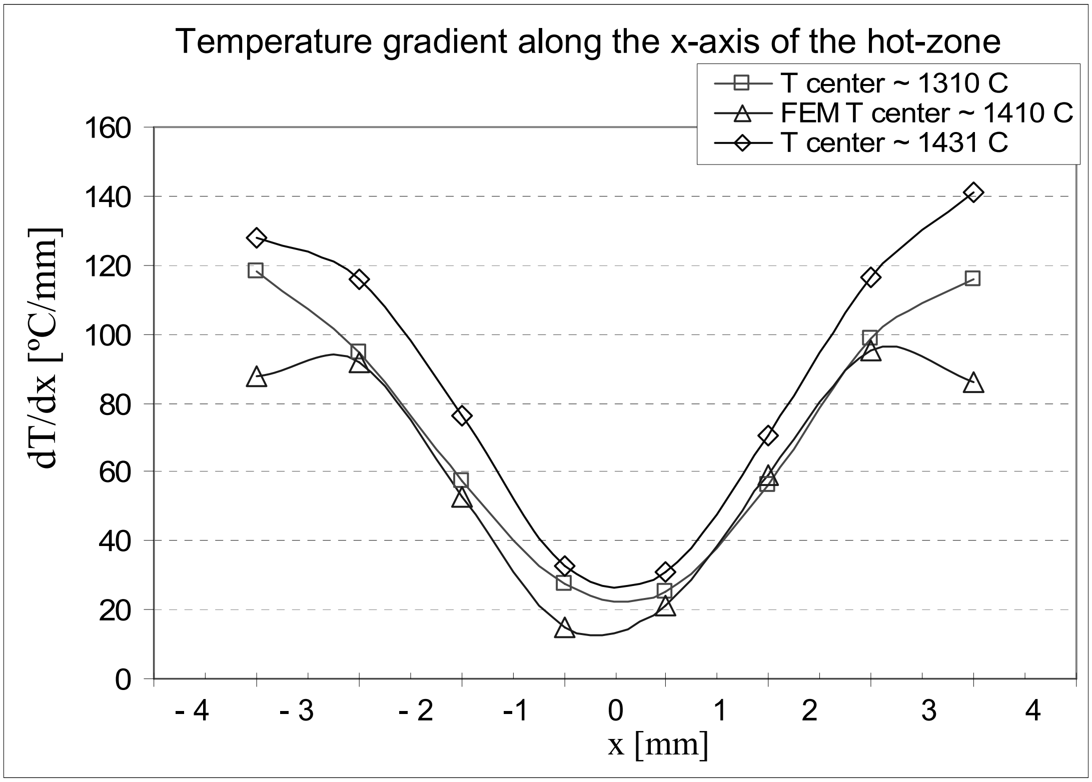

Figure 2.11: Temperature gradient calculated from the measured values (open box and diamond) and the FEM modeling (open triangle) vs. the location in the hot zone, x = 0 represents the center.

Table 2.1: Properties and parameters used for FEM modeling [20-22]

Properties and parameters	Symbol	ZrB_2-SiC	Ag Supports
Thermal conductivity	k [W/m·K]	66	429
Density	ρ [kg/m³]	5560	10500
Heat Capacity	Cp [J·kg/K]	717	235
Resistivity	ρ_e [Ω-m]	$9.2\cdot10^{-8}$	$1.59\cdot10^{-8}$
Thickness of hot-zone	t [m]	$0.53\cdot10^{-3}$	$0.5\cdot10^{-3}$
Current	I [Amps]	104	104

Table 2.2: Temperature gradient in the hot-zone of the ribbon specimen, calculated from the measured (no. 1 and 2) and simulated (FEM) temperatures.

ZrB_2-SiC Specimen	T_{center} [C]	dT/dx [ºC/mm]
no.1	1310	74
no. 2	1355	67
no.1	1431	89
no.1	1516	86
no. 2	1570	84
FEM simulation	1410	64

Table 2.3: Comparison of the current UHTC facilities and the Ribbon Method. The grey boxes represent the desired quality of high temperature testing facility for studying UHTC for re-entering vehicles.

Facility:	Simulates	Temperature	Atmosphere	Cost	In-situ analysis	Contamination
Conventional Furnace	Temperature	1700°C<	Any	modest	not accessible	Possible
Zirconia Furnace	Temperature	1700-2000°C	Any	expensive	not accessible	Possible
Burner Rig	Pressures and gas velocities	700-1650°C	combustion gases	Relatively inexpensive	difficult	Not likely
Arc Jet Heater	Temperature, momentum and enthalpy	>1700°C	limited	Very expensive	difficult	Not likely
Ribbon Method	Temperature	900-2000°C	Any	Relatively cheap	accessible	not possible

References

1. M. M. Opeka, I.G. Talmy, and J.A. Zaykoski, "Oxidation-Based Materials Selection for 2000ºC + Hypersonic Aerosurface: Theoretical Considerations and Historical Experience," J. of Mater. Sci., 39 [19] 5887-5904 (2004).

2. P. Kolodziej, "Aerothermal Performance Constraints for Hypervelocity Small Radius Unswept Leading Edges and Nosetips," NASA Technical Memorandum 112204, July (1997).

3. L. Scatteia, A. Riccio, G. Rufolo, F. De Filippis, A. Del Vecchio, G. Marino, "PRORA-USV SHS: Ultra High Temperature Ceramic Materials for Sharp Hot Structures". AIAA/CIRA 13th International Space Planes and Hypersonics Systems and Technologies. The American Institute of Aeronautics and Astronautics, AIAA 2005-3266, 1-16 (2005).

4. R. Monti, and D. Paterna, "A Low Risk Reentry: Looking Backward To Step Forward," AIAA/CIRA 13th International Space Planes and Hypersonics Systems and Technologies. The American Institute of Aeronautics and Astronautics, AIAA 2005-3365, 1-11 (2005).

5. S. R. Levine, E.J. Opila, M. C. Halbig, J. D. Kiser, M. Singh and J. A. Salem. "Evaluation of Ultra-High Temperature Ceramics for Aeropropulsion Use," J. Eur. Ceram. Soc., 22 2757-2767 (2002).

6. E.J. Opila, S.R. Levine and J. Lorincz. "Oxidation of ZrB_2-and HfB_2 based Ultra-High Temperature Ceramics: Effect of Ta Additions," Journal of Materials Science, 39 5969-5977 (2004).

7. B.M. Steinetz and P.H. Dunlap. "Development of Thermal Barriers for Solid Rocket Motor Nozzle Joints." Journal of Propulsion and Power, 17 [5] 1023-1034 (2001).

8. S. R. Levine, E. J. Opila, R. C. Robinson, and J.A. Lorincz. "Charecterization of an Ultra-High Temperature Ceramic Composite." NASA/TM-2004-213085. National Aeronautics and Space Administration, Glenn Research Center, Ohio, (2004).

9. Chamberlain, W. Fahrenholtz, G. Hilmas and D. Ellerby. "Oxidation of ZrB_2-SiC Ceramics under Atmospheric and Reentry Conditions," Refractories Applications Transactions, 1 [2] 1-8 (2005).

10. M. Gash, D. Ellerby, E. Irby, S. Beckman, M.Gusman, and S. Johnson. "Processing, Properties and Arc Jet Oxidation of Hafnium Diboride/Silicon

Carbide Ultra High Temperature Ceramics," Journal of Materials Science, 39 5925-5937 (2004).

11. Terrazas-Salinas and C. Cornelison. Test Planning Guide for ASF Facilities. A029-9701-XM3 Rev. B. Thermophysics Facilities Branch, Space Technology Division, NASA Ames Research Center, CA, March (1999).

12. A.L. Cabrera and J.F. Kirner. "A Rapid-Temperature-Cycling Apparatus for Oxidation Testing." Oxidation of Metals, 35 [5/6] 471-479 (1991).

13. P.C. Saxton, A.L. Moran, M. J. Harper, and K.W. Lindler. "Thermophotovoltaic Emitter Material Selection and Design." United States Naval Academy, Annapolis, MD. Pentagon Report. Storming Media. Washington, DC. (1997).

14. D. J. Thomas. "Design and Analysis of UHTC Leading Edge Attachment." NASA/CR—2002-211505. National Aeronautics and Space Administration, Glenn Research Center, Ohio, (2002).

15. R. Savino, M.D.S. Fumo, D. Paterna, and M. Serpico "Aerothermodynamic Study of UHTC-based Thermal Protection Systems." Aerospace Science and Technology, 9 151–160 (2005).

16. COMSOL, Inc. http://www.comsol.com/products/

17. A.C. Ugural, and S.K. Fenster. Advanced Strength and Applied Elasticity 3rd Edition, Chapter 7.0 Numerical Methods; Section 7.9 Finite Element Method: Preliminaries, Prentice-Hall Inc. Upper Saddle River, NJ, USA, pp. 279-301 (1995).

18. F.P. Incropera, and D.P. DeWitt. Fundamental of Heat and Mass Transfer 2nd Edition. John Wiley & Sons, Inc. Toronto, Canada, pp. 12-19 (1985).

19. Q.N. Nguyen, E.J. Opila, and R.C. Robinson. "Oxidation of Ultrahigh Temperature Ceramics in Water Vapor," Journal of the Electrochemical Society, 151 [10] B558-B562 (2004).

20. C.C. Wang, S.A. Akbar, W. Chen, and V.D. Patton, "Electrical Properties of high-temperature Oxides, Borides, Carbides, and Nitrides," J. Mat. Sci. 30 [7] 1627-1641 (1995).

21. NASA Ames Research Center. TPSX Material Properties Database, "Zirconium Diboride, ZrB2-SiC," http://tpsx.arc.nasa.gov/ Assessed December 2006.

22. S.N. Karlsdottir, J.W. Halloran, A. Bellosi, and F. Monteverde, "Oxidation of ZrB_2-SiC: Comparison of Furnace Heated Coupons and Self-Heated Ribbon Specimens," *Proceedings of the International Conference on Advanced Ceramics and Composites, Daytona Beach FL*, January 21-26, 2007 (accepted, May 2007).

CHAPTER 3

HIGH TEMPERATURE TESTING OF UHTC WITH THE RIBBON METHOD

1.0 Introduction

To verify that the Ribbon Method is applicable as a valuable addition to the current UHTC high temperature facilities it has to reproduce the complex oxide scale that forms on UHTC during high temperature oxidation. This complex multi-layer oxide scale is reported to feature some or all of the following [1-2]: 1) a silica (SiO_2)-rich borosilicate surface layer, which is believed to act as a protective scale; 2) a subscale of crystalline zirconia (ZrO_2), often with a columnar microstructure with some SiO_2 between the zirconia grains, and; 3) a zirconium diboride region depleted in SiC (the “SiC-depleted region”) [3].

This chapter shows the applicability of the Ribbon Method. To study the oxidation behavior of a ZrB_2-SiC based material and to verify the applicability of the Ribbon Method, sets of experiments were performed at temperatures from 1500-1900ºC in ambient air and pressure. Oxidation behavior of the composite and formation of the oxide scale is reported and discussed in this chapter.

2.0 Experimental Procedure

2.1 Material Fabrication

The material was fabricated by our collaborators at the Institute of Science and Technology for Ceramics (ISTEC-CNR) in Faenza, Italy. A ZrB_2-15vol% SiC-2vol% $MoSi_2$ mixture of commercial powders was ball-milled in absolute ethyl alcohol for 1 day, using zirconia milling media. The $MoSi_2$ (2 vol%) was added as a sintering aid. After drying in a rotating evaporator, the powder mixture was sieved through a mesh screen with 250 μm openings. The powder mixture was then uniaxially hot-pressed in vacuum using an inductively heated graphite die. Peak temperatures, dwell times and applied pressures were 1820°C, 15 min. and 30 MPa, with an average heating rate of 20°C/min. The temperature was measured by means of an optical pyrometer focused on the graphite die. Table 3.1 shows some basic properties of the composite measured by our collaborators at CNR-ISTEC.

The fabrication of the ribbon specimens was done in two steps at The University of Michigan. Firstly, the bulk material is cut with a wire-EDM machine into 2.3×2.0×25 mm bars. The bars are then reduced in thickness in the center with a mechanical grinder (220 grit –diamond wheel) to make the thin ribbon hot-zones, with thickness of 400-500 μm. Herein the ZrB_2-15vol% SiC-2vol% $MoSi_2$ specimens will be referred to as ZrB_2-SiC or ZrB_2-15vol%SiC specimens.

2.2 Oxidation Testing

To verify that the ribbon specimen method could reproduce the complex oxide scale that forms during high temperature experiments on UHTC, ZrB_2-SiC specimens were tested with the Ribbon Method. The design of the Ribbon method is described thoroughly in Chapter 2. Specimens were tested isothermally at 1500, 1600, 1650, and 1700ºC in stagnant ambient air each for 15 min. Two specimens were also tested isothermally at 1550ºC for 1 hour and 1600ºC for 30 min. The heating rate was ca. 480ºC/min and the specimen experienced a free cooling (767ºC/sec). Additionally, a specimen was continuously heated up to 1900ºC in 1 ½ min. and then freely cooled.

The fast cooling rate is due to the fast thermal response time of the specimen, for example a ribbon specimen with a hot-zone thickness of 420 μm and a thermal diffusivity of $1.61 \cdot 10^{-5}$ m^2/s (at 1700ºC) has a thermal response time of 2.74 ms at 1700ºC. The fast heating rate minimizes the oxidation prior to the isothermal runs.

The tested specimens were stored in moisture free desiccators. Cross-sections of oxidized specimens were prepared for microstructural analysis by non-aqueous polishing procedures down to 1 μm finish. The composition and morphology of the multilayer oxide scale formed after the oxidation test was characterized by Scanning Electron Microscopy (SEM), Backscattering Electron Microscopy (BSE), X-ray Energy Dispersive Spectroscopy (XEDS), and Electron Microprobe Analyzer (EPMA). Analyses were done on the surface of the specimens and cross-sections.

3.0 Results and Discussion

3.1 Structure and Composition of the Oxide Scale

SEM/XEDS analyses were done on the surfaces of the specimen to examine the microstructure and the elemental distribution. Figures 3.1(a)-3.4(a) show SEM images of the surfaces of specimens tested at 1500, 1600, 1650, and 1700ºC in stagnant ambient air for 15 min. Figures 3.1(b)-3.4(b) show higher magnification SEM images of the surfaces shown in Figures 3.1(a)-3.4(a). The surface layer of the specimens tested at 1500ºC for

15 min shown in Figure 3.1(a)-(b) is covered with continuous silica (SiO_2) rich layer with small zirconia (ZrO_2) particles spread evenly in the SiO_2 rich matrix. The SiO_2 rich layer is believed to be a SiO_2-rich borosilicate layer which is known to form at temperatures around 1200°C for ZrB_2-SiC composites. At higher temperatures (>1200ºC) the B_2O_3(l) in the borosilicate is presumed to start evaporating from the borosilicate surface layer, leaving a SiO_2 rich borosilicate as the external layer, due to the much higher vapor pressure of B_2O_3 at these temperatures compared to SiO_2 [1-6]. The XEDS equipment used does not have the ability to detect as light element as Boron (B) thus the existence of B_2O_3 in the surface layer of the oxide scale could not be verified for these specimens. Because of an irregular shape and surface roughness of the specimens' elemental analysis of the surfaces were not done by EPMA.

The surface of the specimen tested at 1600ºC for 15 min (Figure 3.2(a)-(b)) is also covered with continuous SiO_2 (silica) rich layer but it has additionally large zirconium (Zr) and oxygen (O) rich features distributed randomly with small ZrO_2 particles around it. The small ZrO_2 are arranged in non-randomly fashion around the Zr, O, rich features which could be interpreted as a flow pattern. These features could possibly be connected to a liquid flow of boron oxide rich liquid, introduced in Chapter 4 and 5, in borosilicate surface layer of oxidized ZrB_2-SiC composites at temperatures around 1550ºC.

The surface layer of the specimen that underwent oxidation at 1650ºC for 15 min consists of small ZrO_2 protuberances in a SiO_2 rich matrix, openings are also evident in the silica layer and formation of blisters are apparent. Also some Zr, O, rich features, seen for the specimen oxidized at 1600ºC, were found on the surface, this is shown in Figure 3.3(a)-(b).

The specimen tested at 1700ºC for 15 min has a SiO_2 rich surface layer that has in some places disrupted and left behind bare ZrO_2 regions, this is shown in Figure 3.4(a). ZrO_2 protuberances, larger than for the specimen tested at 1650ºC, are also evident in the SiO_2 rich surface layer (Figure 3.4(b)).

SEM/XEDS and BSE/EMPA analyses were done on cross-sections of the tested specimens to examine the microstructure and the elemental distribution of the oxide scales. BSE images of the cross-sections of the specimens tested at 1500, 1600, 1650, and 1700ºC for 15 min are shown in Figures 3.5-3.7, and 3.9.

The specimens tested at 1500 and 1600ºC formed a similar two layer oxide scale. Consisting of an outer SiO_2 rich layer and an inner ZrO_2 layer, see Figure 3.5-3.6. For the specimen tested at 1500ºC, the average thicknesses of the SiO_2 and the ZrO_2 layers were 6 μm, and 8 μm, respectively, thus the total average thickness of the oxide scale was measured to be 14 μm. The oxide thickness of the specimen tested at 1600ºC was slightly larger, as expected; 21 μm. For this specimen, the measured thicknesses of the SiO_2-rich and the ZrO_2 layers was on average 9 μm, and 12 μm, respectively.

There is a dramatic difference in the appearance and the thickness of the oxide scale formed on the specimen tested at 1650ºC (Figure 3.7) compared to the specimen tested at 1600ºC (Figure 3.6). For the specimen tested at 1650CºC, a three layer structure formed during oxidation; (1) an outermost SiO_2 rich layer, (2) columnar ZrO_2 layer, and (3) a SiC-depleted layer. Thus an additional layer, a SiC-depleted layer underneath the ZrO_2 layer, formed in the oxide scale for this specimen compared the two layer oxide scale of the specimen tested at 1600ºC. Also the average total thickness of the oxide scale increased dramatically. The average thicknesses of the SiO_2 and ZrO_2 layers were; 27 μm, and 58 μm, respectively. The average thickness of the SiC-depleted region was measured to be 87 μm.

EPMA analyses were performed on the cross-section. The analyses were done to verify results from XEDS/SEM analysis on the distribution off the following elements: silicon (Si), oxygen (O), zirconium (Zr), and boron (B). Also, boron (B) cannot be detected with the SEM/XEDS machine used, thus EPMA analysis were performed to see if any borosilicate glass or boron oxide (B_2O_3) could be detected in the oxide scale. B_2O_3 could not be detected in the SiO_2 rich scale or in the ZrO_2 columnar region. This could be due to the small amount of the B_2O_3 existing in the oxide scale which could not be detected with the scanning speed (20 ms) used for the EPMA analysis. A small amount of B_2O_3 if any is expected due to the high testing temperature (1650ºC). But B_2O_3 is believed to start volatilizing extensively at temperatures above 1200°C for monolithic material [12-14]. Figure 3.8 shows the elemental maps from the EPMA analysis for the following elements; silicon (Si), oxygen (O), zirconium (Zr), and boron (B). From these maps a distinct three layer structure of the specimen tested at 1650ºC can be seen. The O, Zr, and Si maps indicate the thickness of the ZrO_2 and SiO_2 layers while from the B and Si maps a region of a bulk material depleted of SiC (the SiC-depleted region) is evident underneath the ZrO_2 layer. Existence of a SiC-depleted layer in oxidized ZrB_2/HfB_2 – SiC composites have been reported by other researcher in the field [1, 3, 6-7].

The oxide scale of the specimen tested at 1700ºC for 15 min. consisted of a thin outermost SiO_2 layer and a ZrO_2 columnar layer with small amounts of SiO_2 rich glass embedded between the ZrO_2 columns, see Figure 3.9. The thickness of the oxide scale was measured to be on average 102 μm. The thicknesses of the SiO_2 and the ZrO_2 layers were on average 12 μm and 90 μm respectively. A SiC-depleted region was also observed for this specimen, between the un-reacted core and the ZrO_2 layer. The SiC-depleted region is large c.a. 120 μm, which results in a small region of un-reacted material (core). This is evident from the elemental maps from the EPMA analysis (Figure 3.11). The EPMA analysis were done by same procedure as described for the specimen tested at 1650ºC. As for the specimen tested at 1650ºC, B_2O_3 was not detected in the oxide scale, this is explained as before due to the small amount of the B_2O_3 existing in the oxide scale which could likely not be detected with the scanning speed (20ms) used for the EPMA analysis. Figure 3.11(a)-(e) shows a BSE image of the cross-section that the EPMA analysis was done on and the corresponding elemental maps. From the oxygen (O), zirconium (Zr) and silicon (Si) maps the small amount of the interstitial SiO_2 glass in the ZrO_2 columnar layer can be identified. These maps also show clearly the thin outermost SiO_2 rich layer; these are shown in Fig. 3.11(b)-(d). The silica (SiO_2) scale contains small amounts of particulate zirconia (ZrO_2). Higher magnification of the SiO_2 rich scale and the particulate ZrO_2 is shown in Figure 3.10; small protuberances of the particulate ZrO_2 can be readily seen at the higher magnification. These protuberances were also observed in the surface layer of the specimen (Fig. 3.4(a)). The nature of the particulate ZrO_2 protuberances and a speculated mechanism about their formation is discussed in detail in Chapter 5. Figure 3.12 shows a graph of the oxide thickness of the specimens vs. the testing temperature (with fixed dwelling time of 15 min). The sharp increase between the oxide thickness of the specimens tested at 1600ºC and 1650ºC is apparent. Figure 3.18 shows a graph of the total affected thickness (oxide thickness + SiC-depleted layer) of the specimens vs. temperatures (1500-1700ºC). This graph summarizes the effect of the testing temperature on the oxidation of the specimens (the dwelling time was fixed (15 min.)), showing the large increase in the total affected thickness of the specimens tested at 1650ºC compared to the specimen tested at 1600ºC.

Additional tests were done to gain further insight in the protectiveness of the SiO_2-rich borosilicate scale for longer dwelling time at temperatures at and around 1600ºC and also for a short period of time above 1750ºC. Thus specimens were tested at 1600ºC for 30 min., and at 1550ºC for 60 min, as well as one specimen was continuously heated from 900ºC to 1900ºC in ca. 1 ½ min.

The specimens tested at 1550ºC for 60 min. and at 1600ºC for 30 min, have similar oxide scale structure as the ones that were tested at 1500 and 1600ºC for 15 min.; consisting of a continuous outer SiO_2-rich surface layer with an inner ZrO_2 layer. The thickness of the oxide scale for the specimen tested at 1550ºC for 1 hour was measured to be on average 25 μm, while thickness for the specimen tested at 1600ºC for 30 min was 37 μm. For the specimen tested at 1600ºC for 30 min, the SiO_2 layer was measured to be on average 8 μm which is slightly less then for the specimen tested at the same temperature for 15 min. This could suggest more rapid evaporation of B_2O_3 from the oxide scale, resulting in a thinner borosilicate layer. Additionally, a SiC-depleted region was observed with a thickness of ca 12 μm which further suggest an increase in the oxidation rate.

The additional tests, as mentioned above, included a specimen tested by rapid heating from 900ºC to 1900ºC in just 1 ½ min. This test was performed to explore if the SiO_2-rich outer scale would withstand higher temperatures than 1750ºC for short period of time. Figure 3.13 shows SEM images of the surface of the specimen which is covered with a porous ZrO_2 layer, verified with XEDS analysis. The cross-section shown in Figure 3.14 shows the outermost porous ZrO_2 layer and a thin SiC depleted region below. This elemental composition was verified with EPMA and XEDS analyses.

Table 3.2 lists the measured thickness of the oxide scale; the SiC-depleted layer; and the overall affected thickness of all the tested specimens. Figures 3.15-3.17 show graphs of the thickness of each layer vs. temperature for the specimens tested at 1500; 1600; 1650; and 1700ºC, for 15 min.

3.2 Oxidation Behavior

The small thickness of the oxide scale of the specimen tested at 1500-1600°C indicates that the continuous SiO_2 rich layer formed acts as a protective barrier at these temperatures by hindering oxygen diffusion through the surface layer. This is consistent with literature where SiO_2-rich borosilicate layer formed on ZrB_2-SiC composites has been reported to provide increased oxidation resistance to at least 1500°C compared to pure boron oxide that forms on monolithic ZrB_2 [4, 8-9]. This is believed to be due to a lower vapor pressure, higher melting temperature and viscosity of the SiO_2-rich borosilicate layer which can decrease the oxygen diffusion rate through the layer and possible suppress B_2O_3 evaporation at these temperatures [4].

The outer SiO_2 rich borosilicate layer that formed during the oxidation of the ZrB_2-SiC composites does not seem to have the same effective role in limiting oxygen diffusion at temperatures above 1650ºC as at lower temperatures (1600ºC). This is interpreted from the increased thickness of the oxide scale (SiO_2 + ZrO_2 layers) and the formation of a large SiC depleted layer at temperatures at and above 1650ºC. Also the decreased thickness of the SiO_2-rich borosilicate layer for the specimen tested above 1700ºC indicates an increase in the volatilization of B_2O_3 and SiO_2. At 1700ºC B_2O_3 is reported to have a vapour pressure of 1500 Pa (0.015 atm) [10]. Jacobsen reported that the use of silica (SiO_2) forming ceramics at high temperatures would be limited to max. 1725ºC because of rapid oxidation, potential volatility, scale-melting, and scale/substrate reactions of the SiO_2 formed [11].

The additional tests verified these conclusion, i.e.; the specimen tested at 1550ºC for 60 min, had relatively thin oxide scale (SiO_2 + ZrO_2; 25 μm) indicating the effectiveness of the SiO_2-rich scale in limiting oxygen diffusion through the scale; and the specimen that experienced oxidation at 1600ºC for 30 min. showed decrease in the protectiveness of the outer SiO_2-rich layer. This was interpreted from a formation of a thin SiC depleted layer and a small decrease in the thickness of the SiO_2-rich layer, compared to the specimen tested at 1550ºC for 60 min and at 1600ºC for 15 min. The outer porous ZrO_2 surface layer of the specimen tested up to 1900ºC supports the author's suggestion of an increased volatilization of the SiO_2-rich layer at temperatures above 1700ºC.

Our results are consistent to results reported by other researchers in field; Levine and Opila et al.[2] found that a ZrB_2-SiC (20vol%) composite, tested in air at 1627ºC for ten 10-min cycles (total 100 min), formed an oxide scale composed of two layers; an outer SiO_2 layer, and a inner ZrO_2 + SiO_2 layer. A porous SiC-depleted layer was also observed beneath the oxide scale. Also, Gasch et al.[6] performed tests on HfB_2-SiC (20vol %) composite in a simulated re-entry environment using the NASA Ames Arc Jet Facility. The specimen was tested at a reported steady state surface temperature of ~

1750ºC for two 10-min. cycles. The oxide scale of the specimen consisted of a porous HfO_2 surface layer with a thickness of 70 μm. An underlying thin SiC-depleted layer (2 μm) was also observed.

4.0 Summary

Here the complex oxide scale known to form during oxidation of UHTC materials is shown to be easily reproduced by using the Ribbon Method. Sets of experiments were performed on a ZrB_2-15vol%SiC based composite at temperatures from 1500-1900ºC in ambient air and pressure. The oxide scale of the specimens tested at and below 1700ºC consisted of an outer SiO_2-rich borosilicate layer with an underlying ZrO_2 layer. Additionally, for the specimens that were tested above 1600ºC and at 1600ºC for longer time period (30 min.) a SiC-depleted layer formed underneath the ZrO_2 layer.

The continuous SiO_2-rich borosilicate surface layer, formed during the oxidation of the ZrB_2-SiC-$MoSi_2$ composites, acts as a protective barrier between 1500-1600ºC by hindering oxygen diffusion through the layer. The SiO_2 rich surface layer does not have the same effective role in limiting oxygen diffusion at temperatures above 1650ºC as at lower temperatures (i.e. 1500 and 1600ºC). This is likely to be due to the higher vapor pressure, lower melting temperature and viscosity of the SiO_2-rich surface layer at higher temperatures (>1600ºC). The SiO_2-rich surface layer starts to volatilize extensively above 1700ºC, resulting in a porous ZrO_2 surface layer at 1900ºC.

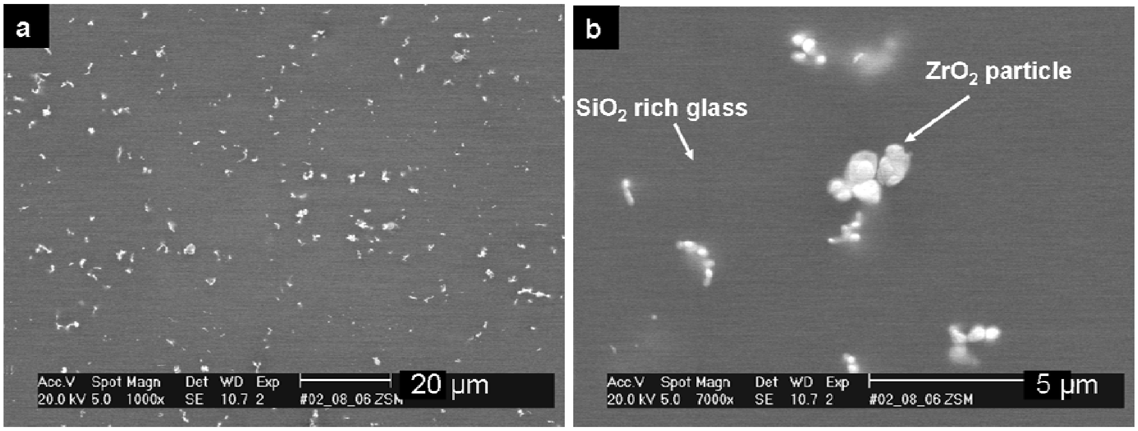

Figure 3.1: SEM images of the surface of the ZrB_2-SiC specimen tested at 1500ºC for 15 min. (a) Small ZrO_2 particles (white spots) in a SiO_2-rich glass matrix (grey area) (b) Higher magnification of the ZrO_2 particles.

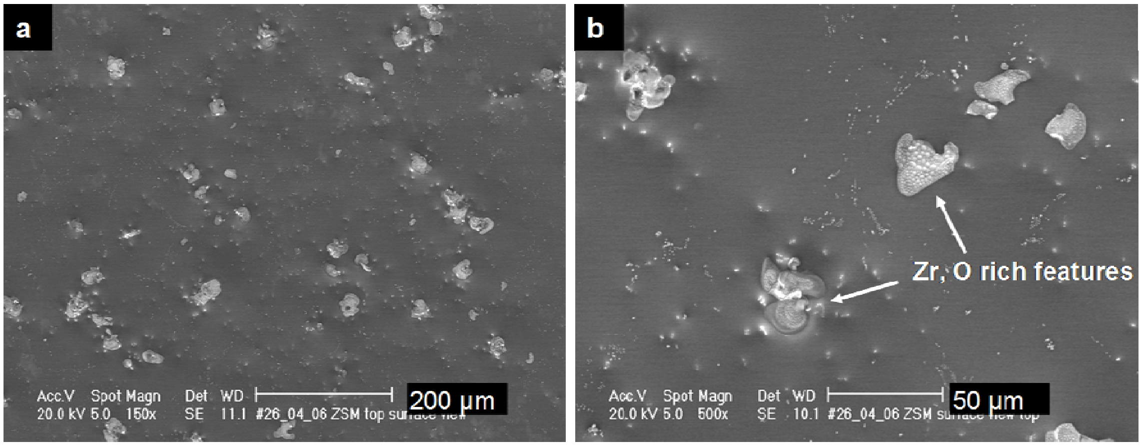

Figure 3.2: SEM images of the surface of the ZrB_2-SiC specimen tested at 1600ºC for 15 min. (a) Zr, and O rich features decorating (white region) a SiO_2-rich glass matrix (grey region) (b) Higher magnification of the Zr, and O features surrounded by small ZrO_2 particles.

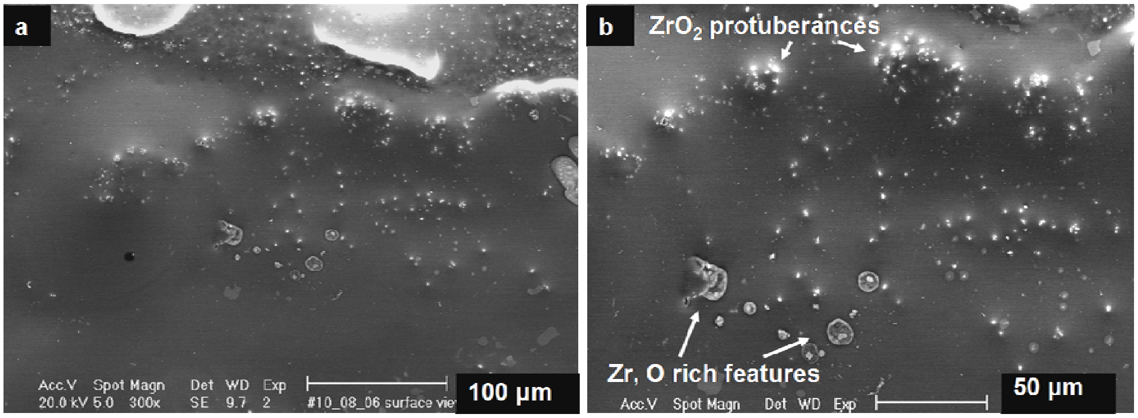

Figure 3.3: SEM images of the surface of the ZrB_2-SiC specimen tested at 1650ºC for 15 min. (a) Openings in the SiO_2 rich surface layer and small ZrO_2 protuberances in the SiO_2-rich surface layer (b) Higher magnification of (a) revealing Zr, and O rich features in the SiO_2 matrix.

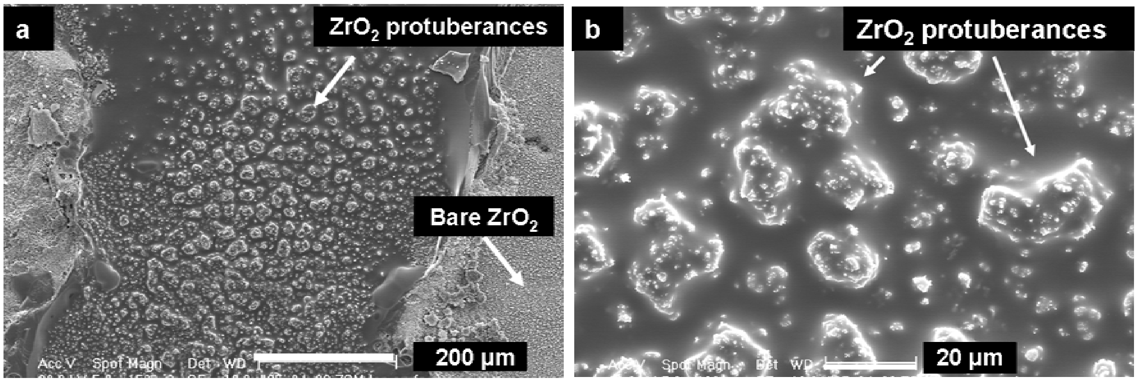

Figure 3.4: SEM images of the surface of the ZrB_2-SiC specimen tested at 1700ºC for 15 min. (a) Showing openings in the SiO_2 rich surface layer (bare ZrO_2 regions) and small ZrO_2 protuberances in the SiO_2-rich surface layer (b) Higher magnification of the ZrO_2 protuberances in the SiO_2 rich matrix.

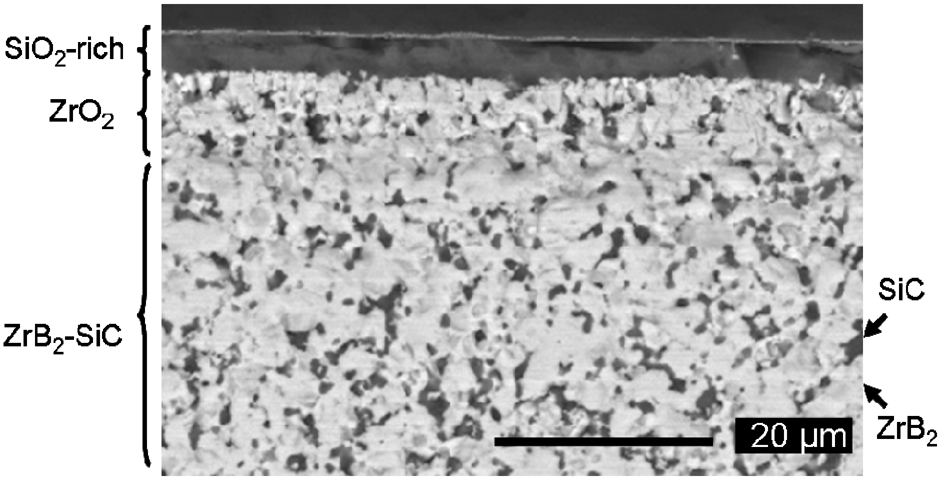

Figure 3.5: BSE image of the cross-section of a ZrB_2-SiC specimen tested at 1500°C for 15 min., showing a two layer structure of the oxide scale, consisting of an outer SiO_2-rich layer and an inner ZrO_2 layer with small SiO_2-rich glass embedded between the ZrO_2 grains. The dark grey regions in the un-reacted bulk material (ZrB_2-SiC) are the SiC grains, while the bright areas are the ZrB_2 grains, this is indicated by the arrows to the right in the image.

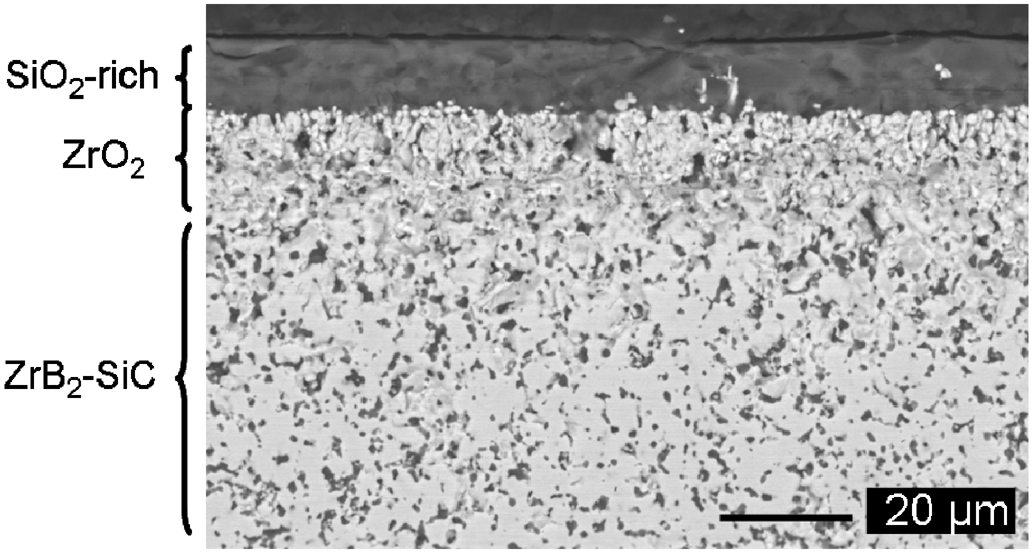

Figure 3.6: BSE image of the cross-section of a ZrB_2-SiC specimen tested at 1600°C for 15 min., showing a two layer structure of the oxide scale, consisting of a outer SiO_2-rich layer and in inner ZrO_2 layer, and the underlying bulk material (ZrB_2-SiC).

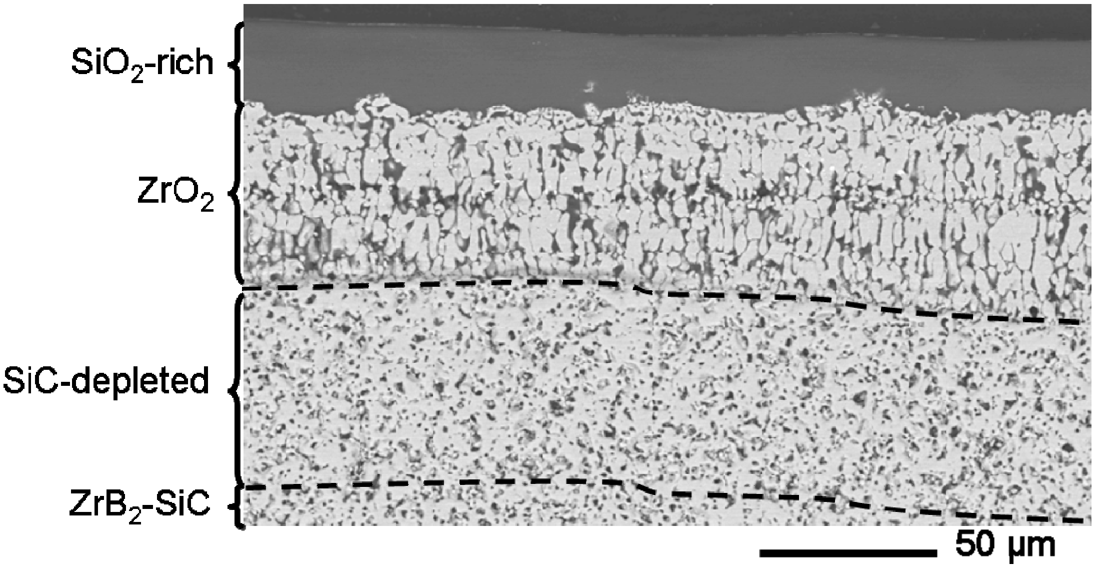

Figure 3.7: BSE image of the cross-section of a ZrB_2-SiC specimen tested at 1650ºC for 15 min., showing a three layers structure consisting of; an outer SiO_2-rich layer, an inner ZrO_2 layer with SiO_2-rich glass embedded between the grains, and a SiC-depleted layer.

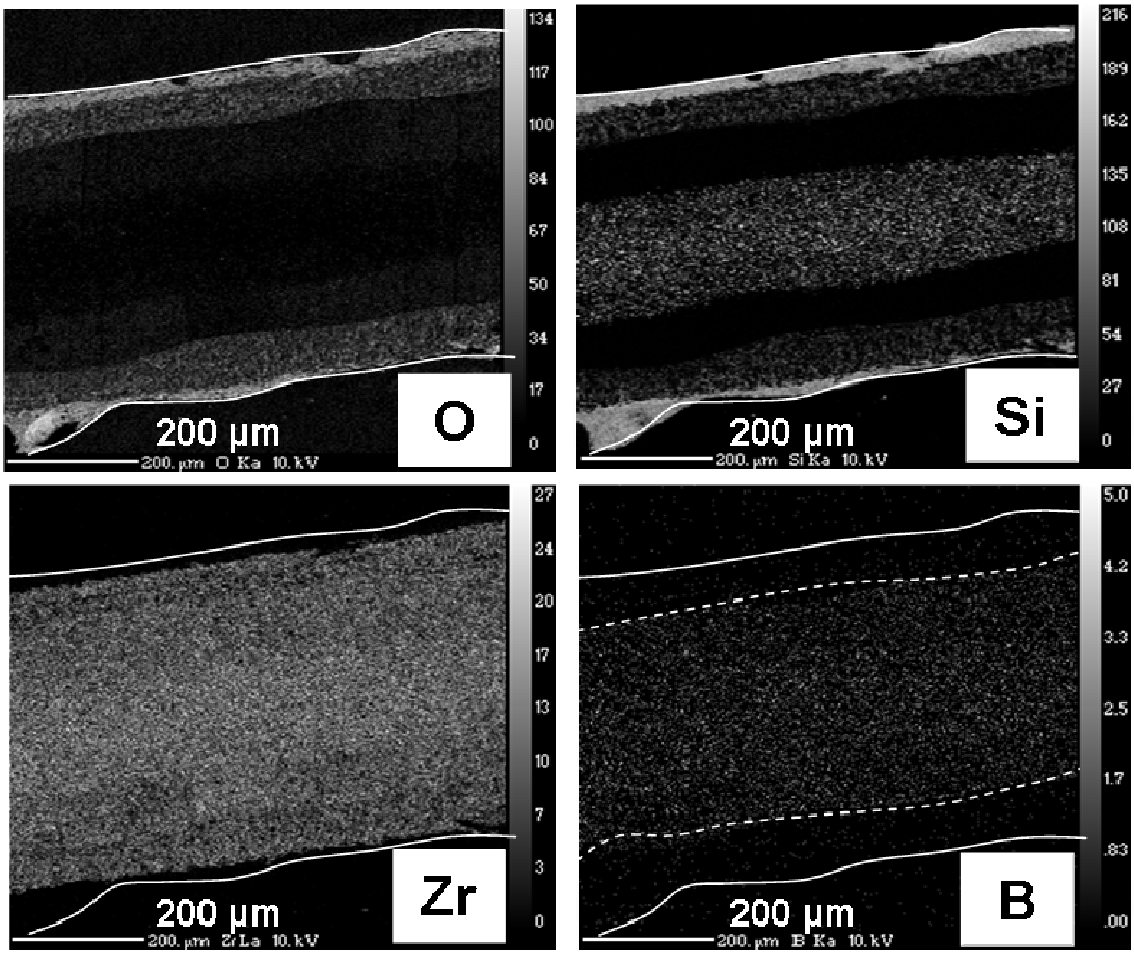

Figure 3.8: EPMA maps of the cross-section of the ZrB_2/SiC specimen tested at 1650°C for 15 min. The O map shows the oxygen distribution in the SiO_2 and ZrO_2 scales and the Si, Zr, and B maps indicate the SiC depleted region and the un-reacted core. The white solid line on the maps outlines the thickness of the specimen, while the white dashed line on the B map outlines the interface between the oxide scale and the SiC-depleted zone.

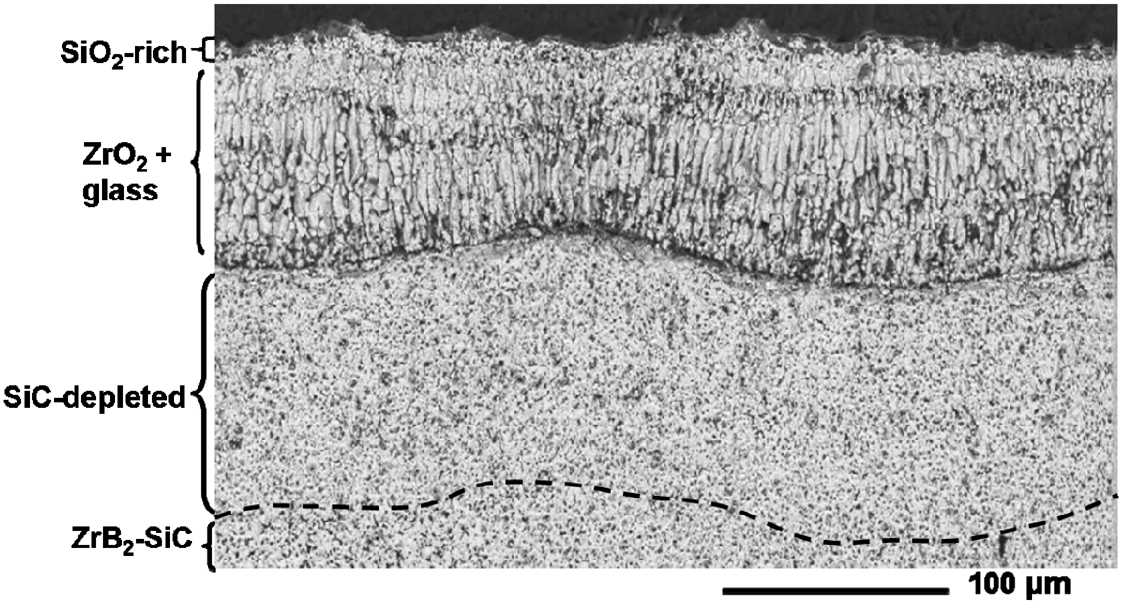

Figure 3.9: BSE image of the cross-section of a ZrB_2-SiC specimen tested at 1700ºC for 15 min, showing a three layers structure consisting of; a outer SiO_2-rich layer, an inner ZrO_2 layer with SiO_2-rich glass embedded between the grains, and a SiC-depleted layer.

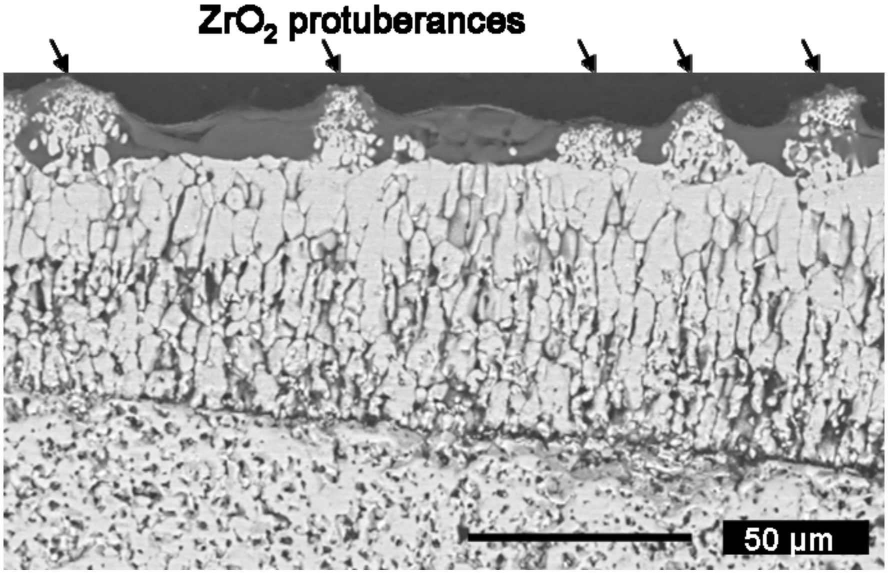

Figure 3.10: BSE image of the cross-section of a ZrB_2-SiC specimen tested at 1700ºC for 15 min showing the SiO_2 outermost layer containing protuberances of ZrO_2 particulate.

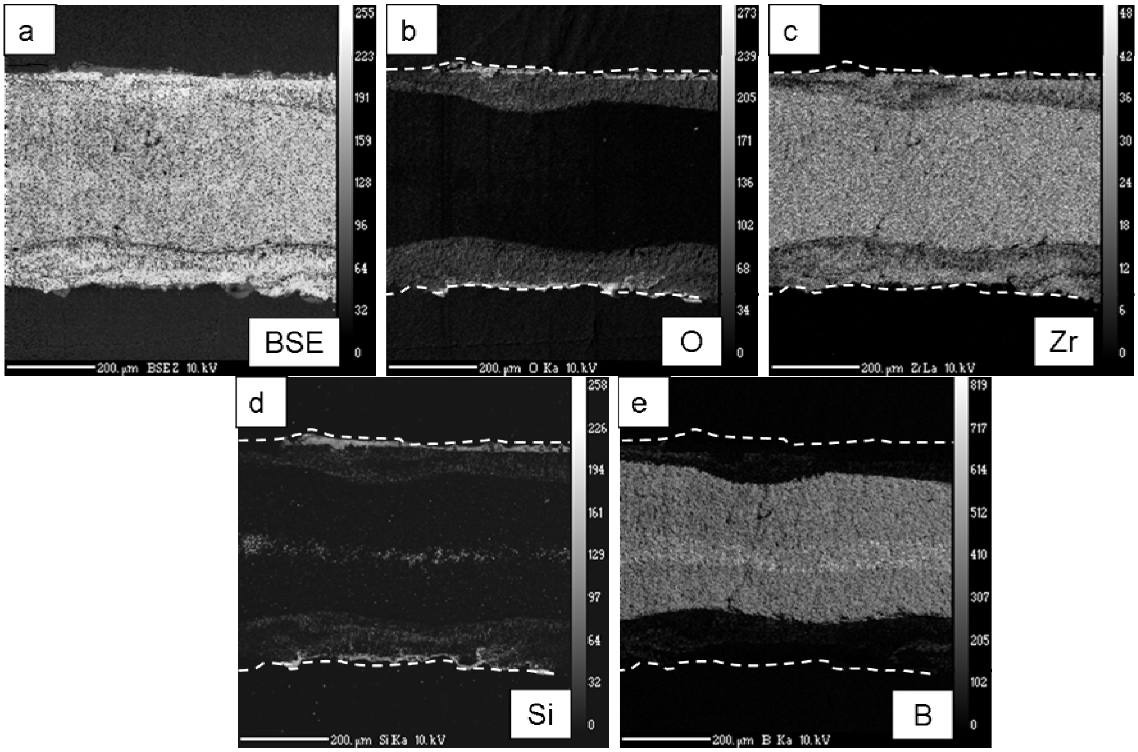

Figure 3.11: (a) BSE image of the cross-section of the ZrB_2/SiC specimen tested at 1700ºC for 15 min b) O map, shows the oxygen distribution in the SiO_2 and ZrO_2 scales (c) Zr map (d) Si map, shows the large SiC depleted region and the thin strip of the un-reacted core (e) B map, showing the thickness of the oxide scale and the un-reacted ZrB_2 in the SiC depleted zone. The white dashed line in b-e outlines the thickness of the specimen.

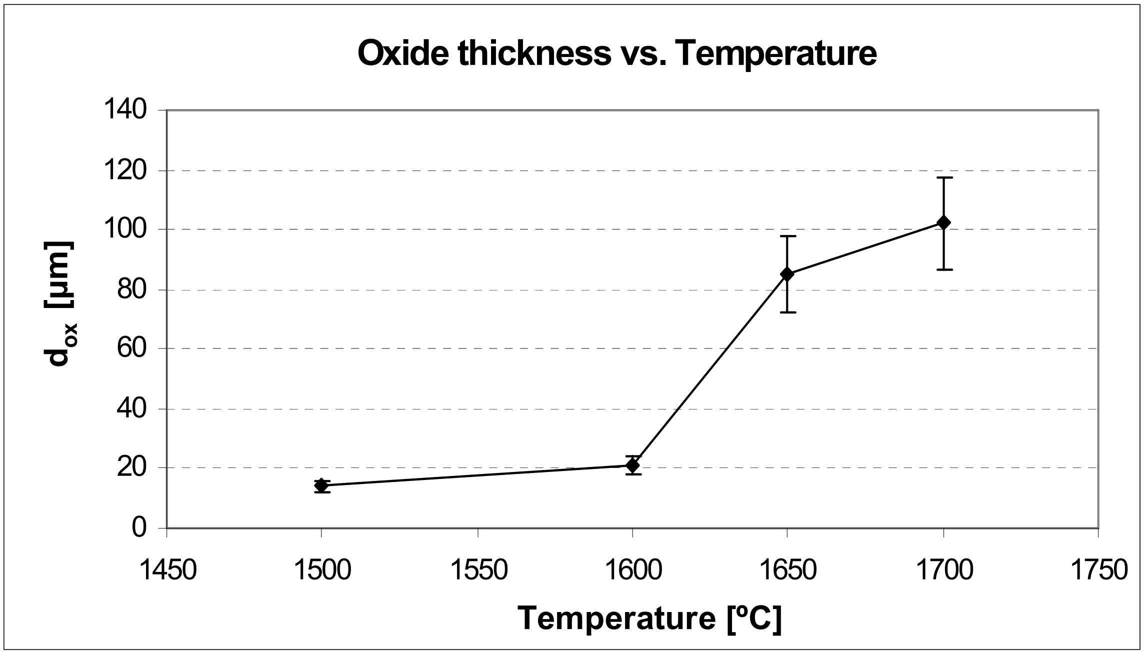

Figure 3.12: A graph showing the oxide thickness (SiO_2 +ZrO_2) for the specimen tested at temperatures from 1500-1700ºC, each for 15 min. Showing the large increase in the oxide thickness is between 1600 and 1650ºC.

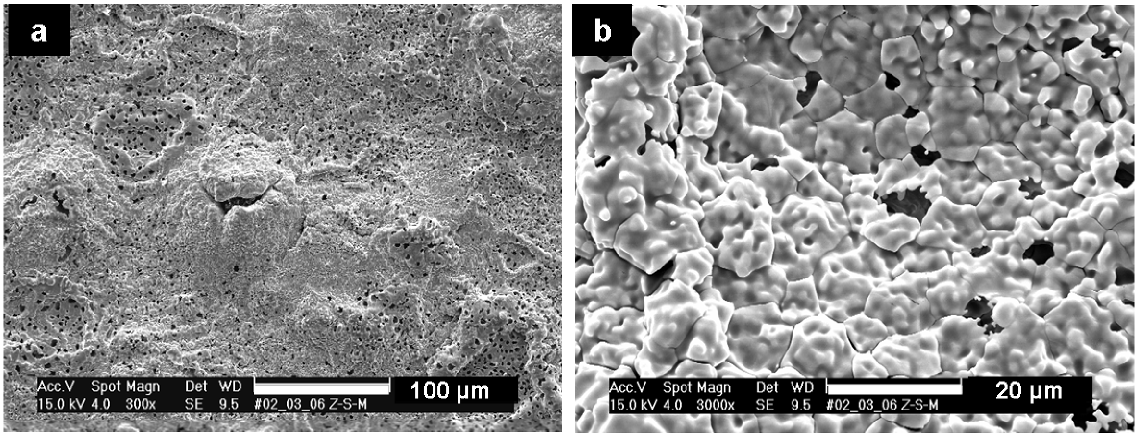

Figure 3.13: SEM images of the surface of the ZrB_2-SiC specimen tested up to 1900ºC in 1 ½ min. (a) The surface layer consist of a porous ZrO_2 (b) Higher magnification of (a) revealing the ZrO_2 particles forming the surface layer.

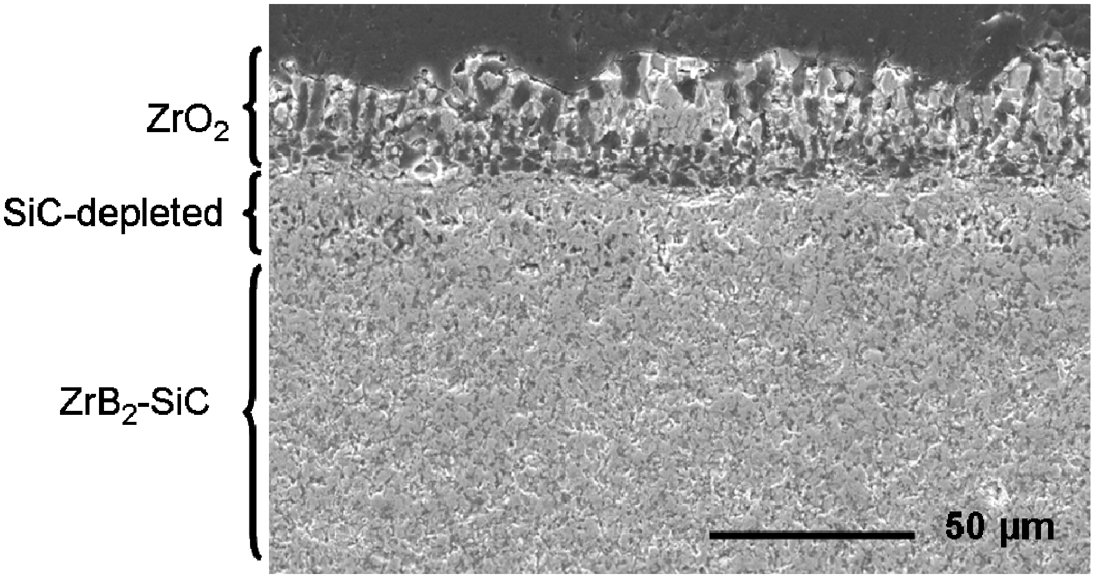

Figure 3.14: SEM image of the cross-section of the ZrB_2-SiC specimen tested up to 1900ºC in 1 ½ min. Showing the two layer structure; porous ZrO_2 surface layer, and an underlying SiC-depleted layer.

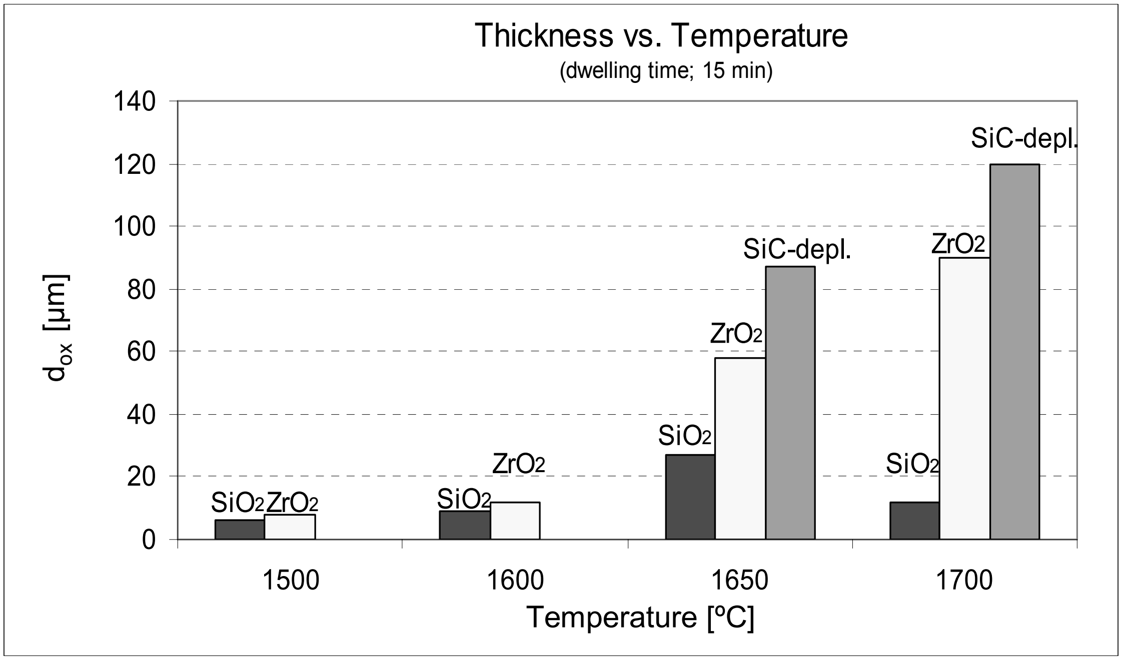

Figure 3.15: A graph showing the thickness of each layer of the oxide scale and the SiC-depleted layer for the specimens tested at temperatures from 1500-1700ºC, each for 15 min. The decrease in the thickness of the SiO_2 scale of the specimen tested at 1700ºC compared to 1650ºC is apparent as well as the formation of the SiC-depl. layer at 1650ºC and above.

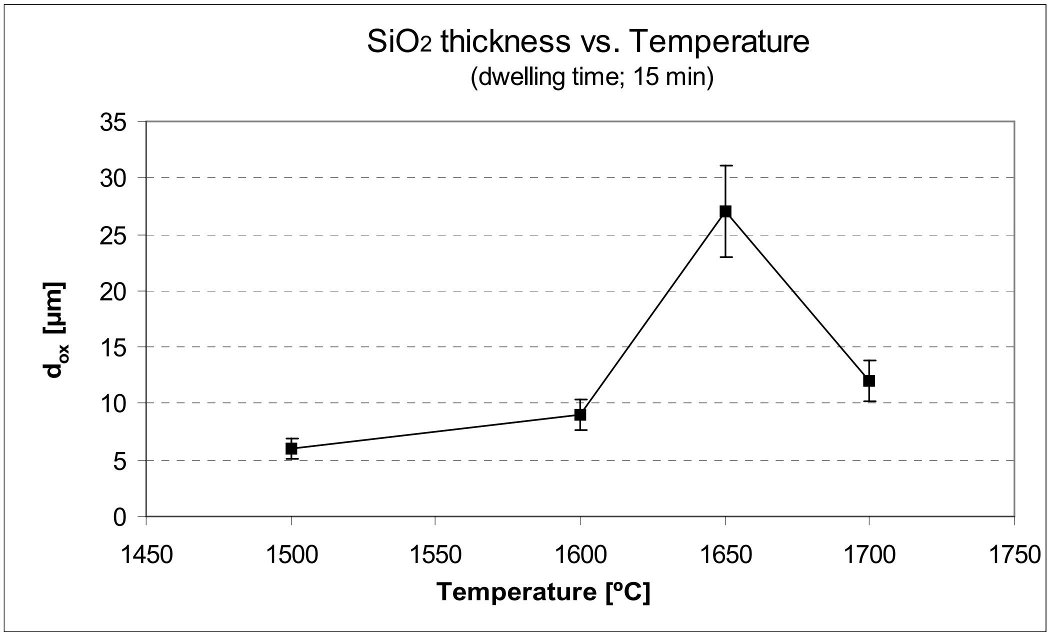

Figure 3.16: The measured thickness of the SiO_2 rich layer for the specimens tested at temperatures from 1500-1700ºC, each for 15 min. The decrease in the thickness of the SiO_2 scale of the specimen tested at 1700ºC compared to 1650ºC is apparent.

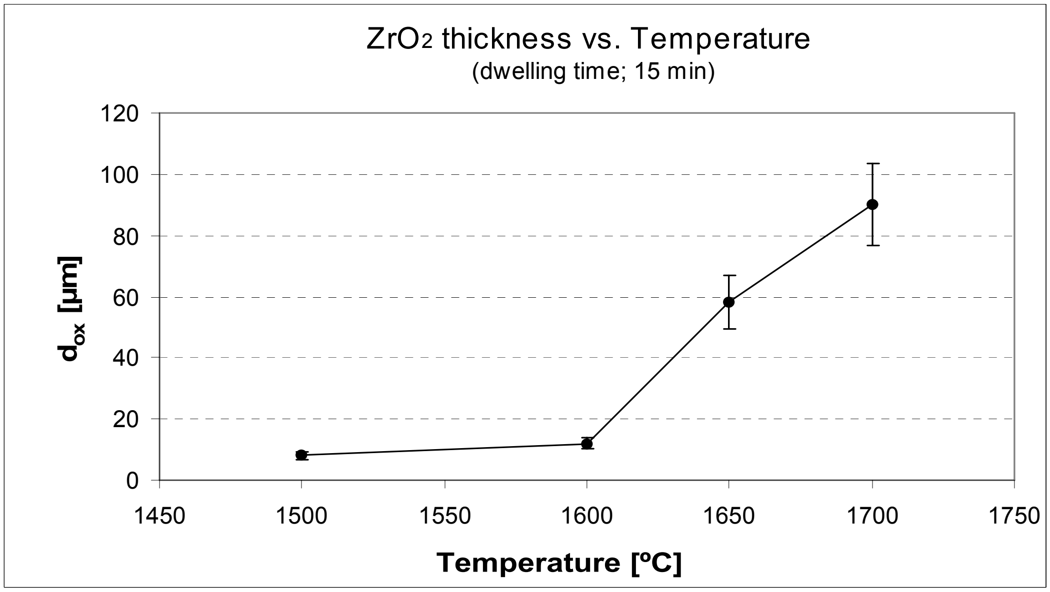

Figure 3.17: The measured thickness of the ZrO_2 layer for the specimens tested at temperatures from 1500-1700ºC, each for 15 min, showing the increase in the thickness of the ZrO_2 layer from 1600ºC to 1700ºC.

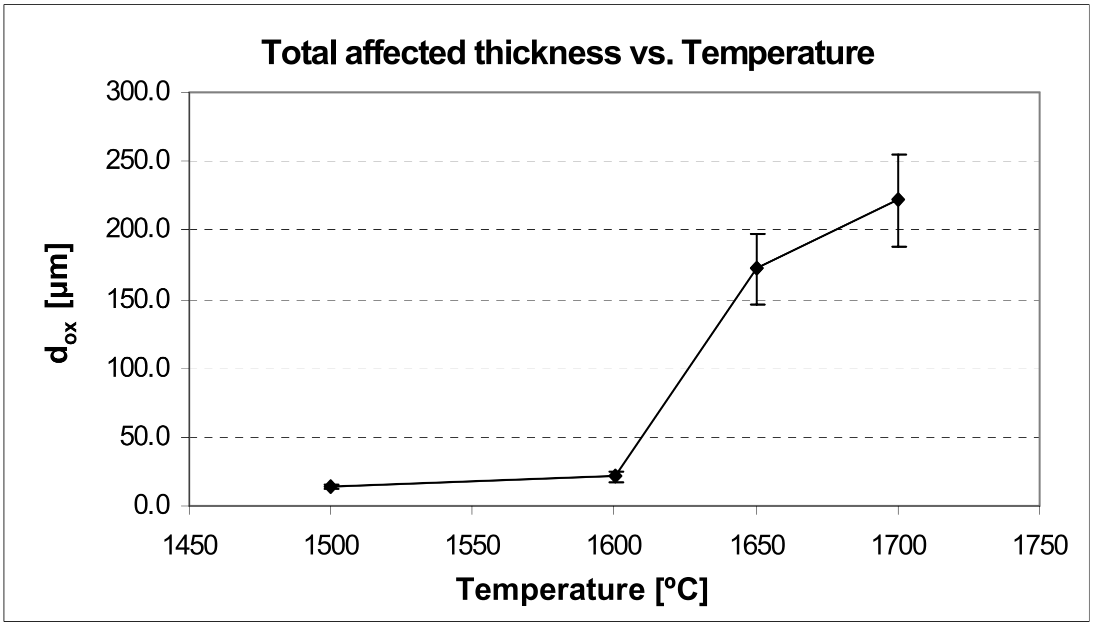

Figure 3.18: The measured total affected thickness (oxide thickness + SiC-depleted layer) of the specimens tested at temperatures from 1500-1700ºC, each for 15 min. The graph shows the large increase in the total affected thickness between 1600 and 1650ºC.

Table 3.1: Physical and mechanical properties of a ZrB_2-15vol%SiC-2vol%$MoSi_2$ composite[12].

ρ (g/cm^3)	E (GPa)	HV1.0 (GPa)	CTE (10^{-6}/K)	σ (MPa)		K_{TH} (W/m K)	
			(25-1300°C)	25°C	1500°C	25°C	1300°C
5.6	480	17.7 ± 04	7.1	795 ±105	255 ±25	62.5	66.2

Table 3.2: Summary of the oxide thickness of the specimens tested.

Temperature [ºC]	time [min]	d_{ox} (SiO_2 +ZrO_2) [μm]	d_{ox} (SiO_2) [μm]	d_{ox} (ZrO_2) [μm]	SiC-depleted [μm]	Total affected zone [μm]
1500	15	14	6	8	0	14
1550	60	25	9	16	0	25
1600	15	21	9	12	0	21
1600	30	37	8	17	12	49
1650	15	85	27	58	87	172
1700	15	102	12	90	120	222
T_{max} = 1900	1.5	34	0	34	12	46

References

1. F. Monteverde and A. Bellosi. "Oxidation of ZrB_2-Based Ceramics in Dry Air," Journal of the Electrochemical Society, 150 [11] B-552-B559 (2003).

2. E.J. Opila, S.R. Levine and J. Lorincz. "Oxidation of ZrB_2-and HfB_2 based Ultra-High Temperature Ceramics: Effect of Ta Additions," J. of Materials Science, 39 5969-5977 (2004).

3. W.G. Fahrenholtz, "Thermodynamics of ZrB_2-SiC oxidation: the formation of a SiC-depleted region," J. Am. Ceram. Soc. 90 [1] 143-148 (2007).

4. I.G. Talmy, J.A. Zaykoski, and M.M. Opeka, "Properties of Ceramics in the ZrB_2/ZrC/SiC System Prepared by Reactive Processing," Ceramic Engineering and Science Proceedings, 19 [3] 105-112 (1998).

5. W.G. Fahrenholtz, "The ZrB_2 Volatility Diagram," J. Am. Ceram. Soc., 88 [12] 3509–3512 (2005).

6. M. Gash, D. Ellerby, E. Irby, S. Beckman, M.Gusman, and S. Johnson. "Processing, Properties and Arc Jet Oxidation of Hafnium Diboride/Silicon Carbide Ultra High Temperature Ceramics," Journal of Materials Science, 39 5925-5937 (2004).

7. S. R. Levine, E.J. Opila, M. C. Halbig, J. D. Kiser, M. Singh and J. A. Salem. "Evaluation of Ultra-High Temperature Ceramics for Aeropropulsion Use," J. Eur. Ceram. Soc., 22 2757-2767 (2002).

8. W.C. Tripp, H.H. Davis, and H.C. Graham, "Effect of SiC Addition on the Oxidation of ZrB_2," Am. Ceram. Soc. Bull., 52 [8] 612-616 (1973).

9. A. Rezaie, W.G. Fahrenholtz, and G.E. Hilmas, "Evolution of Structure during the oxidation of Zirconium Diboride-Silicon Carbide in Air up to 1500ºC," Journal of the European Ceramic Society, 27 [6] 2495-2501 (2007).

10. P.C. Setze, "A Review of the Physical and Thermodynamic Properties of Boric Oxide," Lewis Flight Propulsion Laboratory, Cleveland, OH. NACA-RM-E57B14, April 24, (1957).

11. N.S. Jacobson. "Corrosion of Silicon-Based Ceramics in Combustion Environments." J. Am. Ceram. Soc., 76 [1] 3-28 (1993).

12. S.N. Karlsdottir, J.W. Halloran, A. Bellosi, and F. Monteverde, "Oxidation of ZrB_2-SiC: Comparison of Furnace Heated Coupons and Self-Heated Ribbon

Specimens," *Proceedings of the International Conference on Advanced Ceramics and Composites, Daytona Beach FL*, January 21-26, 2007 (accepted, May 2007).

CHAPTER 4

CONVECTION PATTERNS IN LIQUID OXIDE FILMS ON ZIRCONIUM DIBORIDE -SILICON CARBIDE COMPOSITES AT HIGH TEMPERATURE*

1.0 Introduction

When exposed to air at very high temperatures, zirconium diboride reacts to form crystalline zirconium oxide (ZrO_2) and boron oxide (boria (B_2O_3)), [1-2] which is a quite fluid liquid (T_m = 450ºC). The silicon carbide reacts to form silicon oxide (silica (SiO_2)), a very viscous liquid. Typically a two-layer oxide film forms, with a ZrO_2 inner film and a SiO_2 rich outer film [2-7]. Here our attention is directed to the outer film. The SiO_2 formed can dissolve with the B_2O_3 to form a SiO_2-B_2O_3 liquid solution of intermediate viscosity. At the temperature of oxidation, B_2O_3 is much more volatile than SiO_2 [1, 3, 6-7]. At the outer surface of the oxide, the B_2O_3 is then preferentially evaporated, so that the liquid film at the outer surface becomes predominantly viscous SiO_2 rich liquid. Microstructural evidence suggests that oxygen is transported inward through the oxide film, to react at the interface between the oxide and the boride. In this chapter horizontal pattern in oxide surface films on oxidized ZrB_2-SiC composites are reported and investigated.

---

* Parts of this chapter were presented in the manuscript "Convection Patterns in Liquid Oxide Films on ZrB_2–SiC Composites Oxidized at a High Temperature" by S.N. Karlsdottir, J.W. Halloran and C.E. Henderson, published in the Journal of American Ceramic Society; 90 [9] 2863-2867 (2007). Results from Electron Microprobe Analysis presented here were done with the help from Carl E. Henderson from the Department of Geological Sciences, University of Michigan, Ann Arbor, Michigan.

Interestingly, these patterns resemble convection patterns commonly reported in liquid layers in fluid dynamics. These patterns are suggested here to be an evidence of liquid flow in the oxide films formed during the oxidation of ZrB_2-SiC materials at high temperatures. A novel mechanism involving mass transport by liquid flow is proposed here for the high temperature oxidation of these materials for the first time.

2.0 Experimental Procedure

The UHTC material, ZrB_2-15vol%SiC-2vol%$MoSi_2$, used in this work was fabricated and provided by CNR-ISTEC (The Institute of Science and Technology for Ceramics, National Research Council, Faenza, Italy). Details of the properties and processing are presented in more detail in Chapter 3, Section 2.1 and elsewhere[8]. Specimens tested were rectangular coupons with average surface area of 1 cm^2. Oxidation was conducted in ambient laboratory air by heating to 1550ºC at dwelling times of 1.5 hr., 2 hrs. and 4 hrs. in a conventional tube furnace (Lindberg, Watertown, WI, USA) in ambient air with heating and cooling rate of 13ºC/min and free cooling. The specimens were supported on pieces of the same material. Prior to testing the specimen was ultrasonically cleaned in acetone and dried. The specimen was stored in moisture free desiccators after testing. Cross-sections of the oxidized specimens were prepared for microstructural analysis by non-aqueous polishing procedures down to 0.5 μm finish. The composition and morphology of the oxide scale formed after the oxidation test was characterized by Scanning Electron Microscopy (SEM), Backscattering Electron Microscopy (BSE), and X-ray Energy Dispersive Spectroscopy (XEDS). Electron Microprobe Analyzing (EMPA) was performed on the surfaces of the specimen by using well characterized mineral standards for qualitative analysis of boron (B), oxygen (O), zirconium (Zr), and silicon (Si) with Cameca SX100, which was also used for imaging in the BSE and cathodoluminscence (CL) modes. The standards used for each element are the following; PC3 (200Å) for B, LPC0 (46Å) for O, PET (8.75Å) for Zr, and TAP (25.7Å) for Si. The CL detector used is panchromatic, which collects visible light (~400-700nm) given off by the sample when impacted by the electron beam. The EMPA X-ray maps were acquired using a 10keV, 40nA electron beam with a 40μs pixel dwell time. The maps were background-corrected by image subtraction of a second map acquired with the spectrometer set to a nearby off-peak position to avoid any false counts for boron (B) due to the high x-ray background in the zirconium (Zr) mapping. Specimens were coated with carbon before microstructural and elemental analysis. Analyses were done on the surface of the specimens and cross-sections.

3.0 Result and Discussion

3.1 Microstructure Observations

Mass transport by liquid flow has not yet been reported for high temperature oxidation, but the microstructure of the oxide films on this material show clear evidence of liquid flow. Figure 4.1(a) is a backscattered electron image (BSE) of the surface of a sample oxidized for 2 hrs at 1550ºC. Notice how the pattern on the surface, resembling convection cell pattern, looks like many small islands surrounded by lagoons. Electron probe microanalysis (EMPA) showed that the bright "island"-like features consist of zirconium oxide (ZrO_2), while the dark grey "lagoon"-like regions are mostly silicon dioxide (SiO_2). The medium grey regions outside of the "lagoons" are SiO_2 rich glass decorated with many small particles of ZrO_2. Figure 4.1(b), is imaged using cathodoluminescence (CL) imaging. The flower-like patterns revealed by CL have lobes in dark contrast which are shown by electron probe microanalysis to be rich in boron oxide (B_2O_3), while the area in light gray contrast are SiO_2 rich regions. The SiO_2 rich “lagoons” and their ZrO_2 cores, with surrounding B_2O_3 lobes, will be referred to herein as convection cells and convection cell patterns.

Figure 4.2 shows EPMA line analysis performed on one of the convection cells on a specimen oxidized for 4 hrs at 1550ºC. The X-ray intensity (counts per second (cps)) vs. location in the oxide scale (μm) is shown for boron (B), oxygen (O), zirconium (Zr), and silicon (Si). The start of the line is labeled with A (i.e. 0 μm) and the end with B (i.e. 300 μm). From Figure 4.2 the increase in boron where the line crosses the petal is evident. The line analysis also verifies that the middle part of the cell mainly contains zirconia (ZrO_2). The silica rich regions outside of the convection cell features are decorated with many small particles of ZrO_2, as previously mentioned. This is shown in Figure 4.3(a), where the black arrows point out flow patterns formed by small ZrO_2 particles on a surface of a specimen oxidized for 4 hrs at 1550ºC. This is shown in more detail in Figure 4.3(b), where the swirling arrangement of the small particles suggests they were carried by a flowing liquid.

Figure 4.4 shows a BSE image of a cross-section through the middle of a convection cell on the specimen oxidized for 4 hrs at 1550ºC. The image shows the emergent ZrO_2 column in the middle of the convection cell surrounded by borosilicate glass as well as having some more B_2O_3-rich liquid in the middle of the ZrO_2 column (verified with EPMA and shown in Chapter 5).

The convection cells are associated with surface topography. Figure 4.5(a) is an SEM image of a surface oxidized for 1.5 hr. at 1550ºC tilted at an angle to emphasize topography. This area has four neighboring convection cells, where the ZrO_2 islands are obvious in the backscattered electron image in Figure 4.5(b). The secondary electron image in Figure 4.5(a), which does not have contrast for the zirconia or the boron-rich lobes, shows the central zirconia column rising above the film surface, with what appears to be elevated regions between the convection cells. Many bumps on the silicate surface are obvious, which could be convection cells that have yet to emerge on the surface.

3.2 Convection Cell Pattern Formation

Here the author proposes that during the high temperature oxidation of the ZrB_2-SiC composite, B_2O_3 rich borosilicate liquid is formed at the zirconium diboride-zirconium oxide interface and transported through the overlying layer of silica liquid. The B_2O_3 rich liquid then moves radially across the surface, forming dark flower petal patterns, where it subsequently evaporates. The upwelling B_2O_3 rich liquid is proposed to contain some dissolved zirconia (ZrO_2), which deposits in center of the flower-like patterns as the B_2O_3 evaporates, forming the ZrO_2 cores (islands), and leaving SiO_2 rich liquid behind in the form of SiO_2 rich cells (lagoons).

The formation of the ZrO_2 precipitated cores, found in the center of the convection cells, is explained in detail in Chapter 5, where calculated phase equilibrium diagrams and microstructure observations are used for interpretation.

Now let us focus our attention on the formation of the B_2O_3 flower petals pattern. In general, patterns can form when a less viscous liquid displaces a more viscous liquid, a phenomenon known as viscous fingering[9]. The viscous fingers form due to instability of the moving interface[10] between two liquids with a large viscosity contrast[11]. Viscous fingering is an important phenomenon in the formation of patterns at the nanoscale[12], the microscale[13], as well as macroscopic features in magma intrusions[14]. The B_2O_3 rich side lobes (flower pattern) shown in Figure 4.1- 4.3 are believed to be a lateral finger pattern. The viscosity variation with boron/silicon ratio in borosilicate liquids is extreme. At 1500ºC, the viscosity of SiO_2 is on the order of 10^{10} Pa-s, while B_2O_3 has a viscosity of only about 10 Pa-s[15]. Extrapolating from the data of Jabra et al.[16], we can roughly estimate the dependence of viscosity with mole fraction boron oxide (X_{B2O3}) at temperatures around 1500ºC as:

$$\log_{10}\eta = 11-9X_{B2O3} \qquad (4.1)$$

We assume that at steady state the composition of the freshly formed oxides (crystalline ZrO_2 and liquid B_2O_3-SiO_2 solution), at the boride/oxide interface is roughly in the ratio expected for oxidation of 85 vol% ZrB_2- 15 vol% SiC (or 79 mole% ZrB_2)., The composition of the fresh oxide liquid solution is then around $X_{B2O3} = 0.79$ B_2O_3., The viscosity at this composition should be on the order of 10^3 Pa-s. Boron oxide is much more volatile than silica, it has a vapor pressure of 233 Pa at 1500ºC[15], compared to vapor pressure of 3×10^{-4} Pa for silica [2-3]. At the surface, where the boron oxide can evaporate, there should be a silica rich liquid surface layer with very small or essentially no remaining boron oxide in the solution. From equation 4.1 the viscosity of the silica-rich surface layer is estimated to be around 10^9-10^{10} Pa-s. The viscosity ratio V_R between the viscous surface layer and the fluid fresh oxide liquid would then be very large indeed, ca, $V_R = 10^6$-10^7. This large viscosity ratio could enable viscous fingers to form, such as in the form of dark petals of a flower.

3.3 Driving Force for Liquid Flow and Convection Cell Formation

In this section the possible driving force for the flow of the liquid oxide layer on the ZrB_2-SiC composites and for the formation of the convection cell pattern is discussed. Four possible driving forces are suggested, i.e. convection driven flows; (1) density difference driven flow, (2) surface tension driven flow, (3) evaporation driven flow or (4) volumetric driven by chemical reaction, due to the large volume increase of the formed oxides.

The horizontal patterns previously shown (Fig. 4.1- 4.3) do indeed resemble convection patterns that are known to form in liquid layers when convective motion of the liquid occurs due to instability in the liquid. Convection patterns that form what appears to be spontaneously in liquid layers were first discovered around 1900 by Bénard[17] and Thomson[18]. The formation of convection patterns and the source of the instability that drives them has been the subject of thousands of publications the last hundred years [17-26]. Today researchers make the distinction primarily between three different mechanisms that drives convective flow of liquids in liquid layers: (1) density difference driven flow so called Rayleigh-Bénard convection [17, 19]; (2) surface tension driven flow, so called Bénard-Marangoni convection [20-21, 23, 25]; and (3) evaporation driven flow [22, 24]. The density difference in the liquid that drives the Rayleigh-Bénard convection can form due to a thermal gradient that exists through the liquid or a concentration gradient (solutal). The same applies for the surface tension difference that drives the Bénard-Marangoni convection, where gradients in the surface tension over the surface can form due to a thermal or a concentration gradient effect[23]. The evaporation driven flow can be thermo-capillary if the latent heat of vaporization of an evaporating component in the liquid cools the surface, or it could be solutal if the evaporation changes the surface tension thus leading to Bénard-Marangoni convection [22]. The ratio of convective forces to resisting forces (viscous and inertial forces) of the liquid is usually formulated as a dimensionless numbers, i.e. the Bénard-Marangoni convection can be described by a few dimensionless parameters, the most important of which is the Marangoni number (*Ma*) giving the ratio between surface tension and viscous forces[23] as:

$$Ma = \frac{\sigma_C \Delta C d}{\eta\kappa} = \frac{d\Delta\sigma}{\eta\kappa} \tag{4.2}$$

where η is the viscosity of the liquid, κ is the molecular diffusivity, d is the thickness of the liquid layer, ΔC is the change in concentration across the convecting layer, and $\sigma_C = \partial\sigma/\partial C$ is the derivative of the surface tension σ with concentration. Now $\sigma_C \Delta C = \Delta\sigma$, thus Equation (4.2) can be simplified as shown.

Similar, the Rayleigh-Bénard convection can be described by the Rayleigh number (*Ra*) giving the ratio between the buoyancy and viscous forces[23],

$$Ra = \frac{\rho g \beta_c \Delta C d^3}{\eta\kappa} = \frac{g d^3 \Delta\rho}{\eta\kappa} \tag{4.3}$$

where g is the acceleration due to gravity, β_c is the volume expansion coefficient, ΔC is the change in concentration across the convecting layer, and $\beta_c \Delta C = (\Delta\rho/\rho)$ where ρ is the fluid density and $\Delta\rho$ the density difference that arises from concentration gradients. Equation (4.3) can then be simplified as shown. The equations are shown in terms of concentration dependency (solutal, ΔC) instead of thermal dependency (ΔT).

For *Ma* and *Ra* greater than a critical value the steady diffusive state becomes unstable as the concentration difference overcomes dissipative effects, and the fluid begins to convect. The critical values of *Ma* and *Ra* reported vary somewhat which can be related with the boundary conditions that exist for each system. In general it can be said that if the *Ma* number is large and the *Ra* is relatively small then Bénard-Marangoni convection dominates while for the opposite the Rayleigh-Bénard convection dominates [23, 25]. A number of different studies have considered a more general case in which both density and surface-tension mechanisms act simultaneously. Nield [26] obtained the following relationship between *Ra* number and the *Ma* number,

$$\frac{Ra}{Ra_{0c}} + \frac{Ma}{Ma_{0c}} \cong 1 + \varepsilon \tag{4.4}$$

where $Ra_{0c} = 680$ is the critical value of Rayleigh number when there is no surface tension gradient ($\gamma = 0$), and $Ma_{0c} = 81$ is the critical value of the Marangoni number in weightlessness ($g=0$). The parameter ε is a dimensionless parameter that can take different values, where it characterizes the distance to the threshold of instability [26]. Moroto et al.[25] discussed an interesting relationship that can be obtained by dividing the Ma number with the *Ra* number,

$$\frac{Ra}{Ma} = \left(\frac{\rho \alpha g}{\sigma} \right) d^2 \tag{4.5}$$

where ρ is the fluid density, g is the acceleration due to gravity, α is the thermal diffusivity, σ is the surface tension and d is the thickness of the liquid layer. In typical convection experiment, the parameters between the brackets (which depend on the liquid used) take constant values. Thus for liquid layers of small thicknesses the convection is controlled by surface-tension forces (high *Ma* number), while for thicker liquid layers the convection is likely controlled by the density gradient (high *Ra* number) [25].

The fact that the oxide surface layer on the ZrB_2-SiC composites, where the patterns form, is very thin (~20-50 μm) and that they are observed on the upward-facing, side-facing, and downward-facing surfaces of the samples (shown in Figure 5.6 in Chapter 5), suggests that the formation of the so called convection cell patterns are not due to a density difference (buoyancy dominant), i.e. Rayleigh-Bénard convection. Thus density difference was excluded as the main driving force for the liquid flow and the pattern formation. To gain more information about whether the Bénard-Marangoni convection (or evaporation driven convection) were the driving force for the formation of the convection cells found on the specimens, the *Ma* and *Ra* numbers were estimated. Because the *Ma* number can be much larger in solutal convection than in the thermal case, because the molecular diffusivities are generally much smaller than thermal diffusivities, the solutal *Ma* and *Ra* numbers were calculated instead of thermal. The *Ma* and *Ra* numbers were calculated by using the available physical properties of borosilicate based melts at temperatures around 1500ºC, which are very scarce. The surface tension difference was estimated, from a known value for pure B_2O_3 and SiO_2, to be $\Delta\sigma$ = 0.2 N/m[27]. The thickness, *d*, of the liquid layer used was 20 μm[*] and the viscosity of the liquid, η, was estimated from Equation (4.1) for an intermediate composition (B_2O_3:SiO_2; 50:50). Table 4.1 shows the physical properties and parameters used and the corresponding solutal *Ma* and *Ra* values. As we can see from the table the *Ra* number ($1.1\cdot10^{-3}$) is very small which supports our theory that the driving force for the liquid flow and the pattern formation is not driven by Rayleigh-Bénard convection. The *Ma* number calculated, by using the molecular diffusivity of boron in SiO_2 rich halogranitic

---

[*] Microstructural analysis revealed that the thicknesses of the oxide films when the convection patterns start forming at these temperatures were around 20 μm, this is discussed in Chapter 8.

melts (wt%SiO_2/(B_2O_3+SiO_2)=0.951, 1600ºC) reported by Chakraborty et al.[28] to be $2.37 \cdot 10^{-13}$ m^2/s, is 53 which is below the critical Ma number (Ma_{0c}= 81) mentioned earlier. This indicates that Bénard-Marangoni convection, induced by a surface tension gradient, is not the dominant driving force. Chakraborty et al [28] reported that by adding small wt% of B_2O_3 to the melt the activation energy dropped from ~100 kCal to ~70 kCal and that the diffusivity increased with increasing amount of B_2O_3 (i.e. decrease in SiO_2). This indicates that the diffusivity of a B_2O_3 rich melt should be much larger than $2.37 \cdot 10^{-13}$ m^2/s (for 5 wt% B_2O_3), which would result in much smaller *Ma* number. This suggests further that the formation of the convection cell patterns are not due to Bénard-Marangoni convection. Additionally, because an evaporation driven flow is connected to Bénard-Marangoni convection (dependant on concentration and the surface tension difference) and thus dependant on the *Ma* number, we conclude that it is also not the driving force.

Instead we suggest that the driving force for the liquid flow is the very large volume increase upon oxidation of ZrB_2-SiC bulk material. The molar volume of the condensed oxides is different than the molar volume of the substrate. In the literature for oxidation of metals, the oxide/metal volume ratio is known as the Pillings-Bedworth Ratio (PBR). When the silicon carbide (SiC) is oxidized to silicon dioxide (SiO_2), the molar volume of SiC (12.47 cm^3/mole) is much smaller than the molar volume of SiO_2 (27.43 cm^3/mole). The carbon oxidizes to CO gas. The ratio of the molar volume of SiO_2 to the molar volume of SiC is the Pillings-Bedworth ratio of SiO_2; PBR_{SiO2} which is 2.2. For ZrB_2, we can define partial PBRs for B_2O_3 and for ZrO_2, and a total PBR, using the molar volumes of ZrB_2 (18.54 cm^3/mole), B_2O_3 (55.2 cm^3/mole) [27] and ZrO_2 (20.92

cm^3/mole). The B_2O_3 partial PBR_{B2O3} is 2.98, forming a liquid which can flow. The ZrO_2 partial PBR_{ZrO2} is 1.13, with the ZrO_2 being a solid. Combining the liquids formed from the 85 vol% ZrB_2 -15 vol% SiC, one unit volume of ZrB_2-15vol%SiC upon oxidation produces 0.96 unit volumes of solid oxide (ZrO_2) and 2.8 unit volumes of liquid oxide (B_2O_3-SiO_2), for an overall 380% volume increase. The liquid oxide must be squeezed up away from the interface. It is likely that the volume increase upon oxidation is the driving force for liquid flow and thus the formation of the convection cell patterns. The microstructural and elemental analyses support this hypothesis; a schematic of the proposed mechanism is shown in Figure 4.6. The proposed mechanism for the development of the viscous fingering of the boron oxide rich liquid going through the viscous outer silica during oxidation is demonstrated in Figure 4.6(d). BSE and CL images (Figure 4.6(a)-(b)) of a surface of a sample oxidized for 2 hours at 1550ºC is also shown in Figure 6 as well as EMPA elemental map showing the distribution of boron, B (Figure 4.6(c)). The white areas on the map indicate higher intensity of K_α X-rays detected for boron while black region present zero detected intensity of boron. Figure 4.6(e) shows backscattering electron images (BSE) of the cross-section of specimens tested at 1550ºC for 4 hrs showing the corresponding microstructure for the proposed mechanisms illustrated in Figure 4.6(d) of the formation of the convection cells shown in Figure 4.6(a).

The schematic shows the formation of a B_2O_3 rich + SiO_2 + ZrO_2 (BSZ) liquid between a “premature” oxide scale (consisting of a thin outer SiO_2-rich borosilicate surface layer and an inner porous ZrO_2 layer) and the bulk material (ZrB_2-SiC). This schematic was based on the microstructure of the oxide scale of specimens containing convection cell patterns, as shown from a cross-sectional view in Figure 4.6(e) and also in Chapter 7 (Figure 7.3-6). As indicated in the schematic; when the BSZ liquid forms the "premature" oxide scales becomes deformed and a "blister" forms, note that the convection cells do not form until these "blisters" rupture and the BSZ liquid is squeezed out, as described previously. Here it is hypothesized that the "blisters" form because of the large volume increase, induced by the formation of the oxides during oxidation. There are mainly two questions that arose when these deformations or "blisters" were observed: (1) why does the "blisters" filled with BSZ liquid form at a particular time during the oxidation of the material; and (2) why does the BSZ liquid filled "blisters" form after the formation of the premature oxide scale? Our hypothesis is based on Darcy's law[31] which is a mathematical description of liquid flow in porous media based on original work of Henry Darcy (1803-1858) a French scientist known for his hydraulic experiments. Darcy's law states that the volumetric flow rate Q of a liquid through a specimen of porous material is proportional to the length L [m] of the specimen; the cross-sectional are A [m^2]; and the hydrostatic pressure difference ΔP [Pa] [31]:

$$Q = -\frac{\kappa A \Delta P}{\mu L} \tag{4.6}$$

where Q [cm^3/s] is the total discharge; μ [Pa-s] is the viscosity of the liquid, and κ [m^2] is the permeability of the medium (the porous material). The permeability can then be described by [32]:

$$\kappa = d_f^2 \frac{\varepsilon^3}{(1-\varepsilon)^2} \tag{4.7}$$

where d_f is the diameter of the pore (or the diameter of the pore channel); and ε is the porosity; $\varepsilon = (1-V_f)$ where V_f is the volume fraction of the solid part of the material. More general notation can be produced by dividing both sides of Equation (4.6) by the area A:

$$q = -\frac{\kappa \Delta P}{\mu} \tag{4.8}$$

where q is the flux (discharge per unit area (m/s)); μ is the viscosity of the liquid; κ is the permeability of the medium; and ΔP is the hydrostatic pressure difference as before.

The two questions asked above can be answered now by considering Darcy's law. Firstly, our hypothesis is that in the beginning of the oxidation B_2O_3-rich BSZ liquid and a solid ZrO_2 are formed. The fluid BSZ liquid is formed in channels in the porous ZrO_2(s), but because of the high vapor pressure of B_2O_3 at these temperatures (ca. 1550ºC) [1-3] and the large volume increase from the formation of the condensed oxides, the BSZ liquid is squeezed to the surface and the B_2O_3 starts vaporizing away, leaving a SiO_2-rich surface layer covering porous ZrO_2 behind (filled with channels of SiO_2-rich liquid), forming the "premature" oxide scale. At this stage the channels (pores) are blocked by viscous SiO_2-rich liquid and the pressure gradient now needed to drive this SiO_2-rich liquid to the surface becomes much larger than for the BSZ liquid. This is evident from Darcy's law, i.e. the SiO_2 rich liquid in the channels has much higher viscosity thus much higher pressure gradient is needed than previously needed for the fluid B_2O_3-rich BSZ liquid. Now new BSZ liquid, forming at the interface of the premature oxide scale and the bulk material, is trapped and will start building up underneath the premature oxide scale. Then the large volume increase due the formation of the oxides (BSZ liquid + ZrO_2(s)) causes deformation of the premature scale, resulting in blisters filled with BSZ liquid.

3.4 Role on ZrB_2-SiC Composite Oxidation

As mentioned earlier, when ZrB_2-SiC composites oxidizes at higher temperatures a solid ZrO_2 and liquid B_2O_3 form in direct contact with the diboride, while SiO_2 (and CO) forms by oxidation of SiC deeper into the material (forming a SiC-depleted layer). Over the ZrB_2 grows a layer of zirconium oxide, with glass between the layers, which is covered with a glassy surface layer consisting of silicon oxide (SiO_2) and boron oxide (B_2O_3). Depending on the temperature and oxidation conditions, some or all of these features are commonly observed and reported in the UHTC literature [1-8]. This was also demonstrated for various oxidation temperatures and times in Chapter 3. It has been well appreciated that the glass at the oxidation temperature is liquid, and is depleted in boron oxide (B_2O_3) because much of the volatile B_2O_3 evaporates during oxidation [2-3, 6]. Lateral flow of liquid has been described for some B_2O_3- forming materials [29, 30]. However, liquid flow of B_2O_3-SiO_2 liquids has not been recognized as a major transport mechanism. Here we argue that formation of the SiO_2- rich surface layer is the result of the upwelling of B_2O_3 rich borosilicate liquid through convection cells, with subsequent lateral flow over the outer surface. The outer SiO_2- rich layer forms as a residue of this liquid, after evaporation of the B_2O_3. This outer SiO_2-rich layer is believed to be very important for oxidation resistance, as it forms a passive layer that slows oxidation. The loss of the silica layer at higher temperatures (where silica itself is volatile) results in much faster active oxidation[7]. Maintaining a passivating layer of silica liquid requires a balance of processes which diminish the layer, such as silica vaporization, with processes that replenish the layer. If replenishment indeed occurs by flow of B_2O_3-rich liquid, the convection cell patterns reported here play a critical role in the oxidation behavior of these composites at high temperatures.

4.0 Conclusion

An island-in-lagoon patterns on oxide scales is observed, formed by oxidation of a ZrB_2-SiC composite exposed to air at 1550^oC, consisting of a central zirconia “island” in a silica-rich “lagoon”. Within the latter is a pattern of boron-oxide rich lobes, arranged like flower petals. These features, called here convection cells, are proposed to form when a fluid B_2O_3-rich borosilicate liquid containing some dissolved ZrO_2, formed by oxidation, is transported to the surface where the B_2O_3 is lost by evaporation, depositing ZrO_2 in a viscous SiO_2-rich liquid, i.e. the convection cells. The driving force for the liquid transport is the large volume increase upon oxidation. The B_2O_3-rich flower patterns are suggested here to form by a viscous fingering process as the fluid B_2O_3-rich borosilicate liquid displaces a more viscous SiO_2-rich liquid at the surface. The process of liquid transport of the oxide liquid solution, with evaporation of boron oxide and deposition of zirconia in viscous silica liquid, is proposed here to play a significant role in the formation of external silica rich scales frequently observed on oxidized ZrB_2-SiC composites. Mass transport by liquid flow has not yet been reported for the high temperature oxidation of ZrB_2-SiC composites thus a novel mechanism for the high temperature oxidation of these materials is presented.

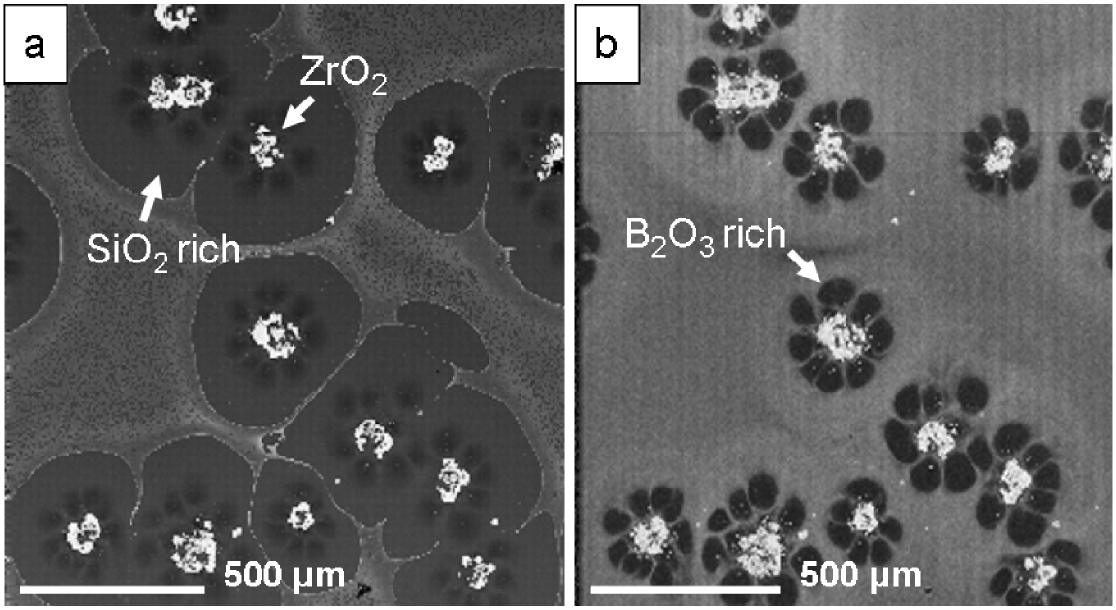

Figure 4.1: (a) Features on the surface of sample oxidized 2 hours at 1550ºC, imaged in backscattered electrons (BSE). Bright features are zirconium oxide (ZrO_2), surrounded by a c. 300 micron region in darker contrast, which is silica (SiO_2) rich glass (which was liquid at 1550ºC). The areas of light grey contrast, around the SiO_2 rich regions, consist of micron-size ZrO_2 particles, (b) same area showed in (a) imaged by cathodolumenscence imaging. The flower-like patterns with the lobes in dark contrast are shown by electron probe microanalysis to be rich in boron oxide (B_2O_3), while the area in light gray contrast is rich in SiO_2.

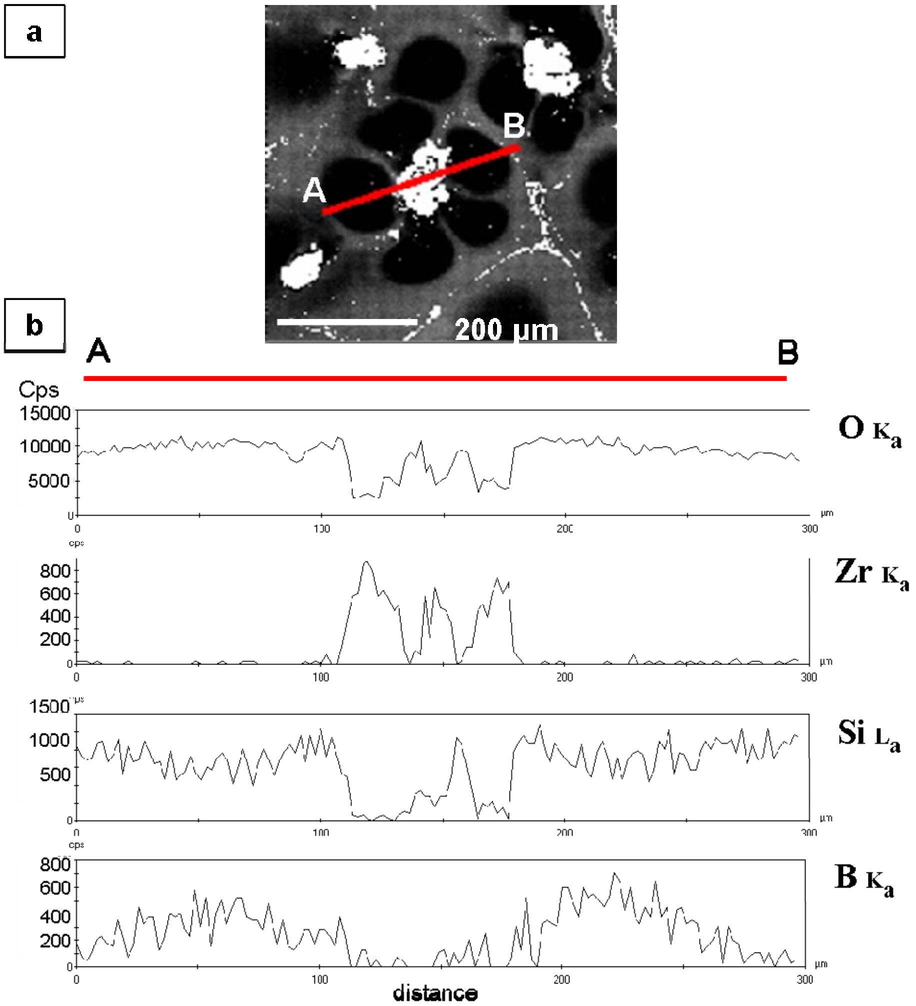

Figure 4.2: Line Analysis on EPMA maps (a) BSE image of a cell on surface of a ZrB$_2$-15vol%SiC composite tested at 1550°C for 4 hrs. The line through the cell indicates where the intensity of the elements was recorded, where letter A indicates the start of the line scan and B the end (b) graphs of the recorded intensity (counts per second (Cps)) vs. distance (µm) of the line scan shown in (a).

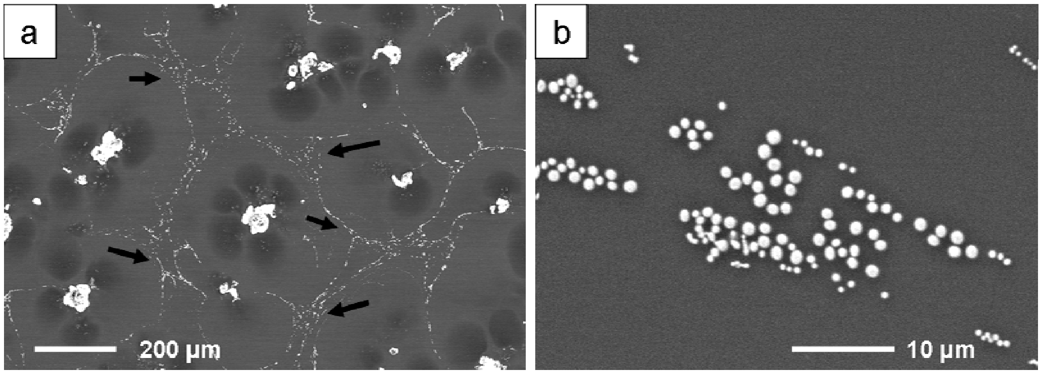

Figure 4.3: Surface of a sample oxidized at 1550°C for 4 hours (a) BSE image of clusters of particles in pattern suggestive of flow; the black arrows indicate the clusters of the zirconium oxide particles (b) Detail of the 0.5-2 µm zirconium oxide particles.

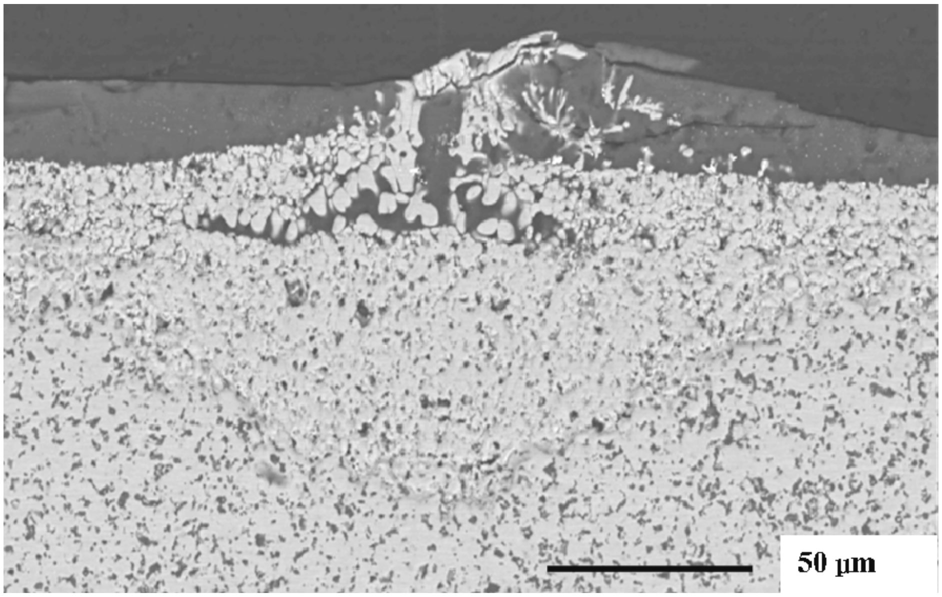

Figure 4.4: BSE image of a cross-section through the middle of a convection cell on a specimen oxidized for 4 hrs at 1550ºC. The image shows the emergent zirconium oxide column in the middle of the convection cell surrounded by borosilicate glass as well as having some more boron oxide-rich liquid in the middle of the ZrO_2 column.

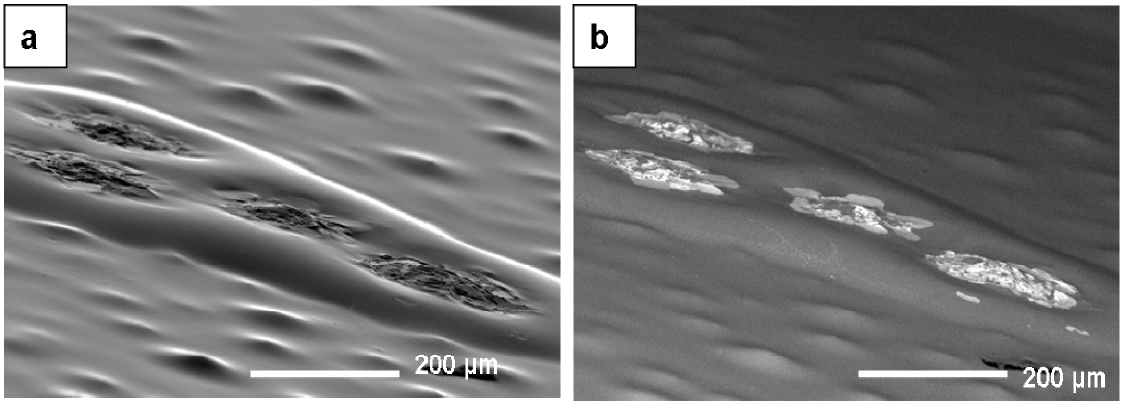

Figure 4.5: Surface of sample oxidized 1550ºC for 1.5 hour, viewed from an angle to reveal surface topography (a) SEM image where surface topography is more obvious, (b) BSE image of the same surface area where the boron–rich lobes are imaged.

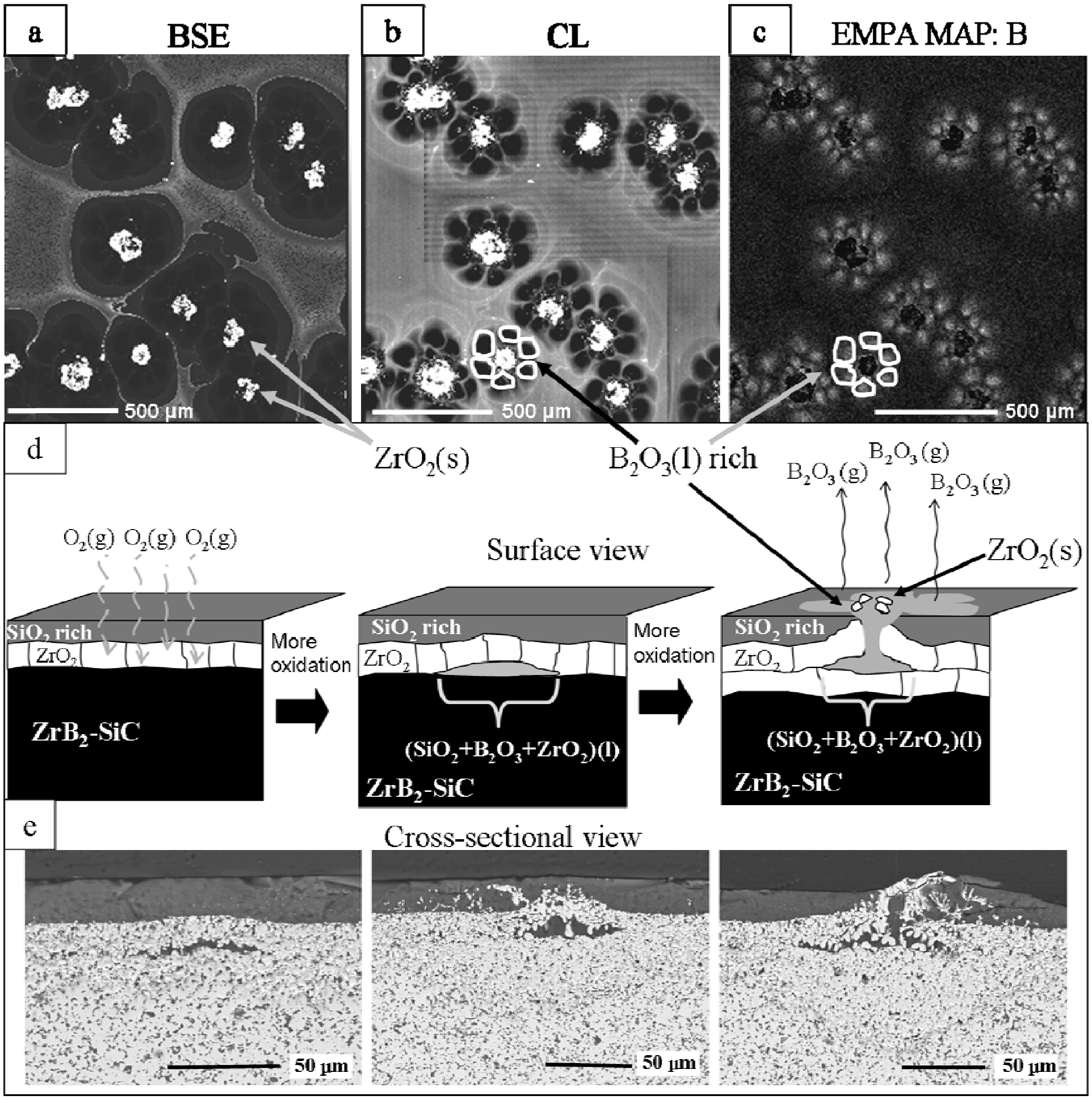

Figure 4.6: (a) BSE and (b) CL images of a sample oxidized for 2 hours at 1550ºC (c) EMPA elemental map of the same area as in (a) and (b), showing the distribution of boron (B). White color indicates higher intensity of K_α X-rays detected for boron while black region present zero intensity, (d) schematic of the proposed mechanism showing the development of the viscous fingering of the boron oxide rich liquid going through the viscous outer silica liquid oxide during oxidation (e) BSE images of cross-sections of a specimen tested for 4 hrs at 1550ºC.

Table 4.1: Properties of a B_2O_3, SiO_2 and borosilicate liquids[27-28] at temperatures around 1500°C and the corresponding calculated solutal Marangoni (Ma_s) and Reyleigh number (Ra_s).

Properties	Parameters	Values
Molecular Diffusivity	κ [m^2/s]	$2.37\cdot10^{-13}$
Dynamic viscosity	η [Pa-s]	$3.16\cdot10^{5}$
Surface tension of B_2O_3	σ_{B2O3} [N/m]	0.10
Surface tension of SiO_2	σ_{B2O3} [N/m]	0.30
Density of B_2O_3	ρ_{B2O3}[kg/m^3]	1200
Density of SiO_2	ρ_{SiO2}[kg/m^3]	2200
Solutal Marangoni number	Ma_s	53
Solutal Rayleigh number	Ra_s	$1.10\cdot10^{-3}$

References

[1] W.G. Fahrenholtz, “The ZrB_2 Volatility Diagram”. J. Am. Ceram. Soc. 88 [12] 3509–3512 (2005).

[2] F. Monteverde, and A. Bellosi, “Oxidation of ZrB_2-Based Ceramics in Dry Air”, Journal of the Electrochemical Society, 150 [11] B552-B559 (2003).

[3] W.G. Fahrenholtz, “Thermodynamics of ZrB_2-SiC oxidation: the formation of a SiC-depleted region”, J. Am. Ceram. Soc. 90 [1] 142-148 (2007).

[4] S.R. Levine, E.J. Opila, M.C. Halbig, J.D. Kiser, M. Singh, and J.A. Salem, “Evaluation of Ultra-High Temperature Ceramics for Aeropropulsion Use”. J. Eur. Ceram. Soc., 22 2757-2767 (2002).

[5] E.J. Opila, S.R. Levine, and J. Lorincz, “Oxidation of ZrB_2-and HfB_2 based Ultra-High Temperature Ceramics: Effect of Ta Additions” Journal of Materials Science 39 5969-5977 (2004).

[6] F. Monteverde, “The Thermal Stability in Air of Hot Pressed Diboride Matrix Composites for Uses at Ultra-High Temperatures”, Corrosion Science 47 2020-2033 (2005).

[7] M.M Opeka, I.G. Talmy, and J.A. Zaykoski, “Oxidation-Based Materials Selection for 2000ºC + Hypersonic Aerosurface: Theoretical Considerations and Historical Experience,” J. of Mater. Sci. 39, 5887-5904 (2004).

[8] S.N. Karlsdottir, J.W. Halloran, F. Monteverde, and A. Bellosi, “Oxidation of ZrB_2-SiC: Comparison of Furnace Heated Coupons and Self-Heated Ribbon Specimens” Proceedings of the International Conference on Advanced Ceramics and Composites, Daytona Beach FL, January 21-26, 2007 (accepted, May 2007).

[9] P.G. Saffman and G. Taylor, “Penetration of a fluid into a porous medium or Hele-Shaw cell containing a more viscous liquid”, Royal Society [London] Proceedings, Ser. A 245 [1242] 312-329 (1958).

[10] J.S. Langer, “ Dendrites, Viscous Fingers, and the Theory of Pattern Formation” Science 243 No. 4895 p. 1150-1156 (1989).

[11] D. Bonn, H. Kellay, and J. Meunier, “Viscous fingering and related instabilities in complex fluids”, Philosophical Magazine B 78 [2] 131-142 (1998)

[12] D. Rautaray, R. Kavathekar, and M. Sastry, “Using the dynamic, expanding liquid-liquid interface in a Hele-Shaw cell in crystal growth and nanoparticle assembly”, Faraday Discussions 129 205 (2005)

[13] H. Schift, L.J. Heyderman, M. Auf der Maur, and J.Gobrecht, “Pattern formation in hot embossing of thin polymer films”, Nanotechnology 12 173-177 (2001)

[14] D. Perugini and G. Poli, ‘Viscous fingering during replenishment of felsic magma chambers by continuous inputs of mafic magmas: Field evidence and fluid-mechanics experiments”, Geology 33 [1] 5-8 (2005).

[15] P.C. Setze, “A Review of the Physical and Thermodynamic Properties of Boric Oxide,” Lewis Flight Propulsion Laboratory, Cleveland, OH. NACA-RM-E57B14, April 24, (1957).

[16] R. Jabra, J. Phalippau, and J. Zarzicki, “Synthesis of binary glass-forming oxide glasses by hot-pressing”, J. Non-crystalline Solids 42 489-498 (1980).

[17] H. Bénard, “Les Tourbillons Cellulaires Dans une Nappe Liquide,” Rev. Gen. Sci. Pure Appl. 11 1261-1271 (1900).

[18] J. Thomson, “On Certain Curious Motions Observable at the Surfaces of Wine and other Alcoholic Liquors”, Phil. Mag. 10 330-333 (1855).

[19] L. Rayleigh, “On Convection Currents in a Horizontal Layer of Fluid when the Higher Temperature is on the under side,” Phil. Mag. 32 529-546 (1916).

[20] I. Langmuir, and D.B. Langmuir, “The Effect of Monomolecular Films on the Evaporation of Ether Solutions,” J. Phys. Chem. 31 1719-1731 (1927).

[21] J.C. Berg, and A. Acrivos, “The Effect of Surface Agents on Convection Cells Induced by Surface Tension,” Chemical Eng. Sci. 20 734-745 (1965).

[22] G.T. Barnes, “The Effects of Monolayers on the Evaporation of Liquids,” Advances in Colloid and Interface Science 25 89-200 (1986).

[23] J.H.E. Cartwright, O. Piro, and A.I. Villacampa, “Pattern Formation in Solutal Convection: Vermiculated Rolls and Isolated Cells,” Physica A 314 291-298 (2002).

[24] Dunbar P. Birnie, III, “Rational Solvent Selection Strategies to Combat Striation Formation during Spin Coating of Thin Films,” J. Mater. Res. 16, [4] 1145-1154 (2001).

[25] J.A. Maroto, V. Pérez-Munuzuri, and M.S. Romero-Cano, “Introductory Analysis of Bénard-Marangoni Convection,” Eur. J. Phys. 28 311-320 (2007).

[26] D.A. Nield, “Surface Tension and Buoyancy Effects in Cellular Convection,” J. Fluid Mech. 19 341-352 (1964).

[27] S. Fujino, C. Hwang, and R. Morinaga, “Density, Surface Tension, and Viscosity of PbO-B_2O_3-SiO_2 Glass Melts”, J. Am. Ceram. Soc 87 [1] 10-16 (2004)

[28] S. Chakraborty, D.B. Dingwell, and M. Chaussidon. “Chemical diffusivity of boron in melts of haplogranitic composition,” Geochimica et Cosmochimica Acta, 57 1741-1751 (1993).

[29] D.M. Sciti, A. Brach, A. Bellosi, “Long term oxidation behavior and mechanical strength degradation of a Pressureless sintered ZrB_2-$MoSi_2$ ceramic”, Scripta Materialia, 53 1297-1302 (2005).

[30] Y.G. Gogotsi, Y.P Yaroshenko, and F. Porz, “Oxidation resistance of boron carbide ceramics”, J. Mater, Sci Letters, 11, 308 (1992).

[31] Biswas A. History of Hydrology. North-Holland Publishing Co., Amsterdam-London, pp. 288-319 (1970).

[32] C. Lekakou, and M.G. Bader, “Mathematical Modeling of Macro-and Micro Infiltration in Resin Transfer Molding (RTM),” Composites Part A, 29A 29-37 (1998).

CHAPTER 5

ZIRCONIA TRANSPORT BY LIQUID CONVECTION DURING OXIDATION OF ZIRCONIUM DIBORIDE-SILICON CARBIDE COMPOSITES[*]

1.0 Introduction

In this chapter a novel mechanism for the high temperature oxidation of ZrB_2-SiC composites, proposed in Chapter 4, is further investigated and verified. This mechanism involves the formation of convection cells patterns in a silica-rich surface layer, containing zirconia (ZrO_2) deposits in the center of the convection cells[1]. B_2O_3-rich liquid, with dissolved ZrO_2, was proposed to be transported through the convection cells to the surface, where it evaporates leaving precipitated ZrO_2 behind. This chapter reports in detail the nature and deposition mechanism of the ZrO_2, using calculated phase equilibrium diagrams and microstructure observations of a ZrB_2-15vol%SiC composite tested at 1550ºC and 1700ºC in ambient air for various times.

---

[*] Parts of this chapter have been presented in the manuscript “Zirconia Transport by Liquid Convection during oxidation of Zirconium Diboride-Silicon Carbide Composite” by S.N. Karlsdottir, J.W. Halloran and A.N. Grundy, accepted for publication in the Journal of American Ceramic Society, July 2007. Results from Electron Microprobe Analysis presented here were done with help from Carl E. Henderson from the Department of Geological Sciences, University of Michigan, Ann Arbor, Michigan. Phase diagrams presented in this chapter were produced for the manuscript and done by Anthony N. Grundy from the Departement de Genie Chimique Ecole Polytechnique de Montreal, Quebec, Canada.

2.0 Experimental Procedure

The material used for this study was a ZrB_2-15vol%SiC-2vol%$MoSi_2$ composite fabricated and provided by The Institute of Science and Technology for Ceramics, National Research Council (ISTEC-CNR), Italy. Details of the properties and processing techniques are presented in more detail in Chapter 3 section 2.1. Specimens tested were rectangular coupons of average surface area of 1 cm^2. Oxidation was conducted in ambient laboratory air either by heating specimens to 1550ºC with a heating rate of 13ºC/min and a free cooling in a conventional tube furnace (Lindberg, Watertown, WI, USA), or by the using the Ribbon Method described in detail in Chapter 2 and elsewhere [2]. Briefly, the ribbon apparatus employs self-supported ribbon specimens which are self-heated by electrical resistance. In the conventional furnace, the specimens were supported on pieces of the same material, and heated in stagnant ambient air. Specimens were ultrasonically cleaned in acetone and dried before oxidation. After oxidation, specimens were stored in moisture free desiccators to avoid any reaction of a B_2O_3 on the surface of the specimens. Cross-section of the oxidized specimen was prepared for microstructural analysis by non-aqueous polishing procedures down to 0.5 μm finish. The composition and morphology of the oxide scales were characterized by Scanning Electron Microscopy (SEM), Backscattering Electron Microscopy (BSE) and X-ray Energy Dispersive Spectroscopy (XEDS) using a Philips XL30 FEG. A Cameca SX100 was used for Electron Microprobe Analysis (EMPA), using well characterized mineral standards for quantitative analysis of boron, zirconium, and silicon, and for imaging in the BSE and cathodoluminscence (CL) modes. The EPMA standards and technique used here is described in more detail in Chapter 4 section 2.0 and elsewhere [1].

3.0 Equilibrium Phase Diagram Calculations

The calculated phase equilibrium diagrams reported and used in this chapter were provided by our collaborator Dr. Anthony N. Grundy from the Chemical Engineering Department at the Ecole Polytechnique de Montreal, Canada. The phase diagrams of the ternary SiO_2-B_2O_3-ZrO_2 system were calculated using the commercial FACT-Sage software package and the FToxide thermodynamic database [3]. The ternary liquid phase was calculated using the modified quasichemical model [4]. The SiO_2-B_2O_3 and SiO_2-ZrO_2 binary systems were optimized based on experimental phase diagrams and thermochemical data [5-7]. The liquidus of the SiO_2-B_2O_3-ZrO_2 ternary system is predicted by symmetrically extrapolating [4] the binary interaction parameters to the ternary system. Due to the lack of experimental data the calculated phase diagrams must be regarded as somewhat speculative however the general features of the system can be expected to be qualitatively correct.

4.0 Results and Discussion

Figure 5.1 shows the surface of the oxide film on a sample oxidized for 2 hrs at 1550ºC in a conventional furnace, sufficient to grow an oxide with about 40 μm of zirconia covered with ca. 25 μm of silica rich glass. Figure 5.1(a) is an image taken with backscattered electrons showing the notable convection cell features, where ca. 100 μm diameter ZrO_2 islands, in bright contrast, are surrounded by ca. 500 μm diameter SiO_2-

rich cells, in darker contrast. Note that the width of these features is several times larger than the oxide scale thickness. The convection cells are separated by SiO_2 rich areas with small ZrO_2 particles (light grey contrast). The chemical composition of the convection cell features was analyzed by EPMA. The same area imaged by cathodoluminescence (CL) is presented in Figure 5.1(b). The CL image reveals a flower-like pattern in the middle of the SiO_2 cells, with B_2O_3-rich petal-like lobes in dark CL contrast surrounding central ZrO_2 island. These flower patterns resemble the Islandic soley *Ranuculus Acris*, or common Buttercup, so they will be referred herein as soleys or flower petals. Figure 5.2 shows a soley feature in a sample oxidized at $1550^{o}C$ for four hours, imaged in CL and by x-rays excited from oxygen (O), zirconium (Zr), silicon (Si), and boron (B). This confirms that the lobes in dark contrast in CL are rich in boria (B_2O_3) but relatively poor in silica (SiO_2) compared to the surroundings, and that the central island feature is zirconia (ZrO_2). In Chapter 4 the author argued that the soleys are part of convection cells that are formed when a fluid boria-silica-zirconia (BSZ) oxide liquid is transport to the surface, where it flows laterally creating the convection cell features. Evaporation of the volatile B_2O_3 from the soley petals at the surface deposits viscous SiO_2-rich liquid cells, and solid ZrO_2 island in the middle of the cell.

Zirconia is also present on the surface as discrete particles, about one micron in diameter. These are shown in Figure 5.3, where we see that the small zirconia particles are located primarily between the lagoon features forming a pattern which resembles a flow pattern. The fine scale arrangement of the particles, Figure 5.3(b), also suggests that particles have been moved by a flowing liquid. These fine zirconia particles can also be seen inside the glassy silica layer, often arranged in horizontal layers. An example is shown in Figure 5.4, a fracture surface of the cross section of the glassy scale. Note the repeated layers of fine zirconia particles separated by thin layers of particle-free silica glass. We suggest that these layers of zirconia particles were once decorating the surface (as in Figure 5.3), but were subsequently covered by silica-rich liquid, and this process was repeated several times. The thickness of the particle-free silica layers vary from about 5 microns near the bottom of the scale to about 2 microns near the middle of the scale, which might suggest that the extent of the lateral flow of liquid changes with oxidation time.

Figure 5.5 presents a fractured cross section of ZrB_2-15 vol% SiC specimen oxidized for 15 minutes at 1700°C in a the ribbon apparatus, showing (from the interior): un-oxidized ZrB_2-SiC interior; SiC-depleted zone of ZrB_2; a layer with columnar zirconia; and an outer glassy layer. The surface of the sample shows many protuberances, which consist of a core of zirconia surrounded by glass. These cores are elevated 5-10 μm above the silicate glass surface. We suggest that the protuberances have been formed by precipitation of ZrO_2 from a BSZ liquid associated with the convection cells.

The ZrB_2-15vol% SiC specimens tested are rectangular coupons. During oxidation the top surface (y-z plane) is horizontal while the side surface (x-z plane) is vertical. Figure 5.6 shows a corner of a ZrB_2-SiC composite oxidized for 3 hours at 1550°C in a conventional furnace. The horizontal top (y-z) surface is on the left, with the vertical (x-z) side surface to the right. Convection cells decorate the side and top surface of the specimen. Note that the structure is similar on top and side, demonstrating that the direction of gravity does not influence the shape of convection features. This suggests that the liquid flow is not density driven, for if it were density driven the shape of the features would be different on the top and side, or normal to and perpendicular to the gravity vector.

In Chapter 4 it was suggested that the liquid flow is mechanically driven by the large molar volume increase due to the formation of the oxides (ZrO_2, B_2O_3, and SiO2) during oxidation; leading to breakage in the oxide scale where liquid oxides then flows out. Figure 5.7(a) shows a BSE image of a cross-section through a convection cell, showing the emergent columnar ZrO_2 island, surrounded by borosilicate glass. The ZrB_2-15vol%SiC specimen shown in Figure 5.7(a) was oxidized for 4 hrs. at 1550ºC (the same image was shown in Chapter 4.). The columnar ZrO_2 island contains more B_2O_3-rich liquid in the middle of the ZrO_2 compared to the surrounding glass. This is shown by Figure 5.7(b) which shows the results from EPMA line analysis performed on the cross-section of the convection cell shown in Figure 5.7(a). The line through the convection cell (in Figure 5.7(a)) shows where the corresponding line analysis was done. The start of the line is labeled with A (30 μm) and the end with B (225 μm). The X-ray intensity ((cps) counts per second) vs. location in the oxide scale (μm) is shown for boron (B), oxygen (O), zirconium (Zr), and silicon (Si). The increase in B_2O_3 inside the columnar ZrO_2 island in the center of the convection cell, compared to the outside is evident. This supports the hypothesis that a B_2O_3 rich-SiO_2-ZrO_2 liquid is transported to the surface; playing a part in the formation of the convection cells. The different morphology of the columnar ZrO_2 islands also suggests a different mechanism controlling the formation of the zirconia islands than for the underlying ZrO_2 layer.

Details of the growth of the protuberances shown in Figure 5.5 might be also inferred from Figure 5.8(a), which is a fracture surface of the sample oxidized at 1700ºC for 15 min. with the Ribbon Method. Here the fracture plane has intersected two zirconia protuberances. The summits of both protuberances are decorated with fine zirconia particles. Beneath the protuberances are what appear to be columns of discrete zirconia particles in a glassy matrix. Figure 5.8(b) is a higher magnification of the columns of the zirconia particles showing the structure in details. We suggest that each of these zirconia particles was formed when the ZrO_2 dissolved in the BSZ liquid precipitated at the surface. Subsequently the zirconia particles were buried by fresh deposits from BSZ liquid which continued to be transported to the surface during oxidation.

The existence of a boria-silica-zirconia liquid (BSZ) is essential for the proposed mechanism of liquid convection of zirconia. The system B_2O_3-SiO_2 is known to form liquid solutions, but the available experimental data of the solubility of ZrO_2 in B_2O_3-SiO_2 liquids has not been reported. The only experimental data of the solubility of ZrO_2 in B_2O_3 liquid for the ZrO_2-B_2O_3 system was published by Beard et al. They found that the solubility of ZrO_2 in B_2O_3 liquid was 0.9 mole% at 1200°C. The only published report of phase equilibrium in the B_2O_3-SiO_2-ZrO_2 system is by Butterman [8] but his emphasis was on the geological conditions for zircon formation. Our collaborator, A.N. Grundy optimized the SiO_2-B_2O_3 and SiO_2-ZrO_2 binary systems based on experimental phase diagrams and thermochemical data [5-7]. He then predicted the liquidus of the SiO_2-B_2O_3-ZrO_2 ternary system by symmetrically extrapolating [4] the binary interaction parameters to the ternary system.

Figure 5.9 shows the calculated ternary B_2O_3-SiO_2-ZrO_2 phase diagram by Grundy, showing the isothermal section of the B_2O_3-SiO_2-ZrO_2 system at 1500ºC. The ternary phase diagram shows equilibrium between a boria-silica-zirconia (BSZ) liquid solution (liquid) and crystalline phases of zirconia (ZrO_2), zircon ($ZrSiO_4$), and silica (SiO_2). This phase diagram is used in the following section to interpret the phase behavior and microstructure of the oxides. The solubility of zirconia in a boron oxide (B_2O_3) liquid for the binary system ZrO_2-B_2O_3 is shown in Figure 5.10 along with the experimental data point from Beard et. al.[7]. Notice that a transient B_2O_3 liquid can dissolve much more zirconia at higher temperatures. The mole fraction zirconia, X_{ZrO2}, in the zirconia-saturated liquid at 1550ºC is about 0.2 in the binary but at 1800ºC the boron oxide liquid can dissolve up to 40 mol.% zirconia. This suggests that a transient boron oxide liquid would be a more potent transport medium for zirconia at higher temperatures, at least for conditions below the boiling point of boron oxide (about 1680ºC in air). Agents which promote boron oxide vaporization, such as water [9] decrease the temperature range where boron oxide liquids can exist, and should retard transport of dissolved zirconia and silica by the transient boron oxide rich liquid.

4.1 Analysis of Oxide Scale Microstructure Development

Some assumptions are necessary to estimate the composition and amounts of the phases produced by oxidation. It appears that relative thickness of the SiC depleted zone and thickness of zirconia layer after it forms does not change much with time (seen in Figure 3.15 in Chapter 3 and elsewhere [10]). This suggests that the diboride and the SiC oxidize in the same ratio as they are present (no marked preferred oxidation). This implies that in the ratio expected for oxidation of 85 vol% ZrB_2- 15 vol% SiC (or 79 mole% ZrB_2), the composition of fresh liquid oxide should have a boron to silica ratio $X_{B2O3} : X_{SiO2}$ of 0.79 : 0.21. Solid zirconia (ZrO_2) is also produced, and some of this will dissolve in the liquid. According to the calculated phase diagram a ZrO_2-saturated borosilicate (BSZ) liquid with this B/Si ratio dissolves about 11 mole% ZrO_2. The phase assemblage for the complete oxidation of the ZrB_2-15vol% SiC at 1500ºC can be expected to be, on a molar basis, 0.33 moles solid ZrO_2 and 0.67 moles of a BSZ liquid (liquid composition: 71 mole% Boria + 18 mole% silica + 11 mole% zirconia), the location of this composition is indicated on the ternary phase diagram in Figure 5.9 by arrows and labels. We presume that the solid undissolved zirconia remains at the interface with ZrB_2 as "primary zirconia", while the BSZ liquid flows out to the surface, carrying dissolved zirconia.

Boria, and to a lesser extent, silica, can evaporate from the BSZ liquid at the external surface, changing the composition of the remaining liquid. Boria is much more volatile, with a vapor pressure of 233 Pa at 1500°C [11]. The vapor pressure of silica is only 3×10^{-4} Pa at 1500°C[12]. At the surface, majority of the boria from the BSZ liquid will evaporate. Depending on the temperature and atmosphere, some of the silica might also evaporate, but none of the zirconia will be removed by evaporation. Consider the case where only the boria is volatile. As the boria evaporates, the remaining liquid moves into the two phase region BSZ liquid + solid ZrO_2, as defined by the tie lines in the phase diagram and indicated by the broken arrow in Figure 5.9. As boria is evaporated, the remaining BSZ liquid becomes richer in silica, and zirconia must precipitate from the BSZ liquid. Thus we expect the formation of so called "secondary" zirconia precipitates, located near the site of boria evaporation. The secondary zirconia, precipitated from the BSZ liquid, might have a different morphology from the primary zirconia, suggesting that it might be possible to distinguish secondary zirconia within the microstructure. Figure 5.4 showed a difference in the morphology of the primary zirconia in the inner scale from the zirconia islands of the convection cell (vertical feature), supporting our theory of the precipitation of the secondary zirconia.

The zirconia precipitates will either remain at the location where they formed (as zirconia islands), or be carried as a dispersed particle with the flowing BSZ liquid where they could serve as markers of the liquid flow. Figure 5.3 shows evidence of this, showing a flow pattern formed from small ZrO_2 particles, around and from the ZrO_2 islands. Figure 5.4 also suggests this showing a fracture surface of the cross section of the glassy scale with the repeated layers of fine ZrO_2 particles separated by thin layers of particle-free silica glass, indicating a flow of ZrO_2 particles.

We expect the viscosity of the BSZ liquid to change dramatically as the fluid boria component is lost and the remaining BSZ is enriched in silica. Very little data is available for the viscosity of borosilicate liquids (and no data exists for zirconia-containing borosilicate). However, we can take the known values for the viscosity of silica ($\eta_{SiO2} \sim 10^{10}$ Pa-s) and boria ($\eta_{B2O3} \sim 10$ Pa-s) at temperatures around 1500ºC, as we did in previous chapter, and combine that with a viscosity for one intermediate composition [13] to get a rough estimate for the change in the viscosity of the borosilicate (η_{BS}) with mole fraction boria (X_{B2O3}), which is approximately:

$$\log_{10} \eta_{BS} = 11 - 9X_{B2O3} \qquad (5.1)$$

For a 85vol%ZrB_2-15vol%SiC composite the composition of the fresh liquid oxide should have a boria to silica ratio $X_{B2O3} : X_{SiO2}$ of 0.79 : 0.21, thus the viscosity of the boria rich liquid can be roughly estimated to be around $\eta_{SiO2-B2O3} \sim 10^3$ Pa-s.

Eventually, as c. 95% of the boria has evaporated, the viscosity of the remaining liquid (η_{BS}) has increased to ca. 10^9 Pa-s.

If boria (boron oxide) would completely evaporate from the transient BSZ liquid of composition 71 mole% Boria + 18 mole% silica + 11 mole% zirconia, we would move into the two phase region where zircon ($ZrSiO_4$) precipitates and the final equilibrium phase assemblage would be a two phase mixture zircon and solid SiO_2 in the ratio of about 75 mole% zircon – 25 mole% SiO_2. (We observe zirconia, not zircon, also $ZrSiO_4$ is not very stable at these temperatures, so it is likely that it does not form). Assuming that evaporation of B_2O_3 stops due to the increase in viscosity of the liquid when about 10 mole% B_2O_3 remains in the liquid, the total composition moves to 58 mole% SiO_2, 36 mole% ZrO_2 and 6 mole% B_2O_3. The equilibrium phase assemblage at this composition is 66 mole% of a silica-rich liquid and 34 mole% solid zirconia (secondary). The composition of the silica-rich liquid is 10 mole% boria + 88 mole% silica + 2 mole% zirconia. The locations of these compositions on the ternary phase diagram are indicated by arrows and labels in Figure 5.9.

These considerations are in reasonable agreement with the observed volume fractions, estimated by stereological analysis of the glassy layer, which suggests about 75 vol.% (~70 mol.%) silica and about 25 vol.% (~30 mol.%) precipitated zirconia (as distinct from the primary zirconia). Because the microstructure of the secondary zirconia is different from the primary zirconia we can estimate the amount of secondary zirconia formed (the ZrO_2 islands) distinctively from the primary zirconia (the ZrO_2 layer under the SiO_2 rich glassy layer).

5.0 Conclusion

The formation of zirconium oxide (ZrO_2) deposits found in center of the convection cells, formed in silica rich surface layers during high temperature oxidation of ZrB_2-SiC material, are proposed to be the consequence of liquid transport. Fluid boria-silica-zirconia (BSZ) liquid is transported, due to a large volume increase, to the surface where the BSZ liquid flows laterally creating convection cell patterns when the boria (B_2O_3) evaporates, depositing ZrO_2 in the center of the cells and viscous silica (SiO_2) liquid which flows outward. These conclusions are based on chemical composition analysis; microstructural observations; and phase behavior predicted by calculated phase equilibrium diagrams for the binary ZrO_2-B_2O_3 and ternary B_2O_3-SiO_2-ZrO_2 systems, both reported here for the first time. The existence of a boria-silica-zirconia liquid is essential for the proposed convection mechanism of zirconia transport. The calculated phase diagram, for the isothermal section of the B_2O_3-SiO_2-ZrO_2 system at 1500^{o}C, shows equilibrium between a boria-silica-zirconia (BSZ) liquid solution and crystalline phases of zirconia (ZrO_2), where 11 mol% of dissolved ZrO_2 exists in the BSZ liquid, for an oxidized ZrB_2-15vol%SiC composite.

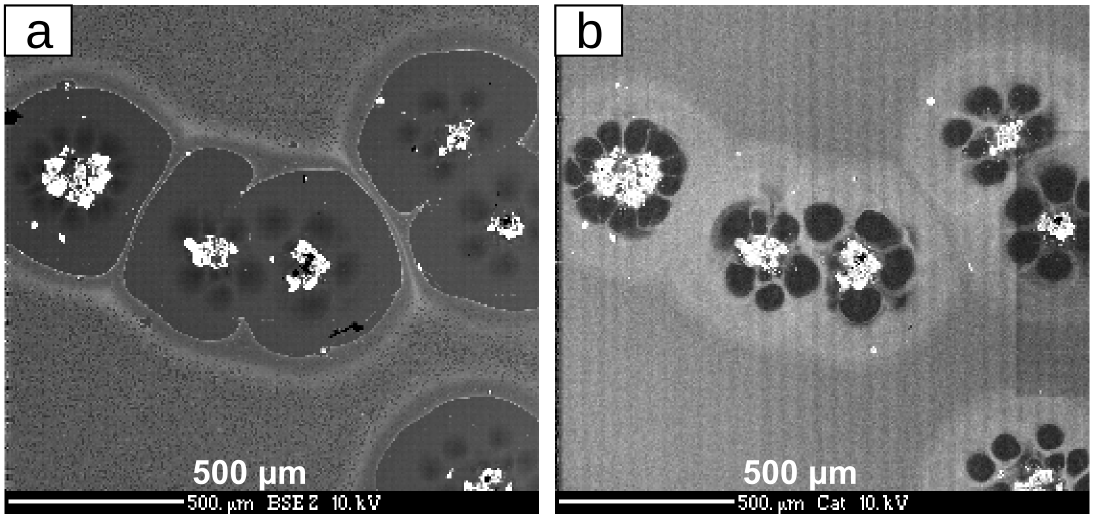

Figure 5.1: Surface of a ZrB_2-15 vol% SiC sample oxidized for 2 hours at 1550°C (a) Back Scattered Electron (BSE) image, showing zirconia in bright contrast (b) same area imaged by cathodoluminescence, showing petal-like lobes in dark contrast.

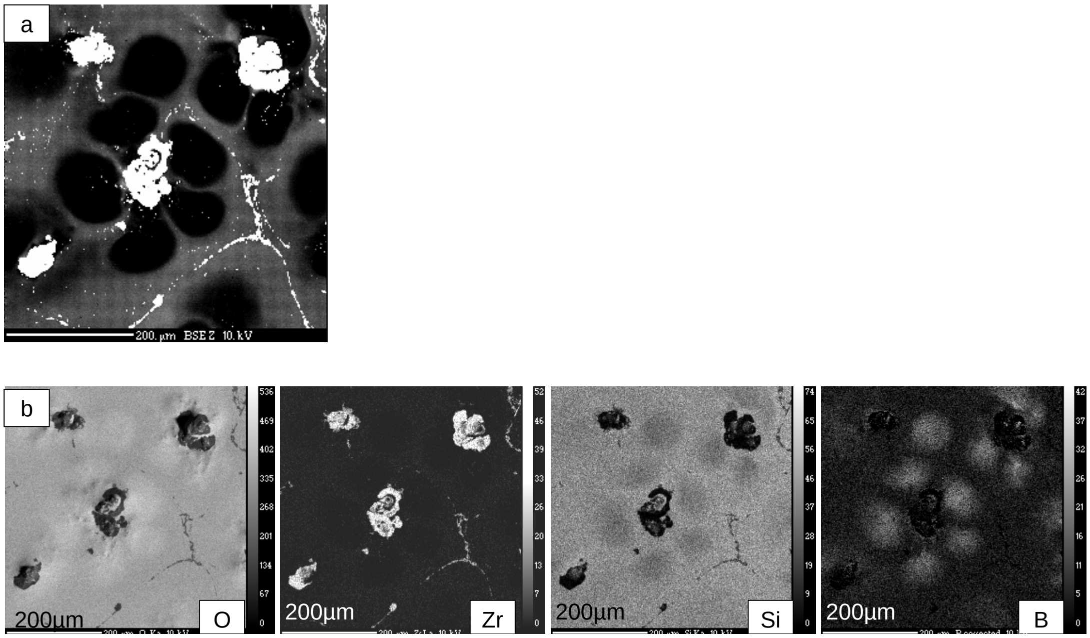

Figure 5.2: (a) A "soley" (flower pattern) in the surface of ZrB_2-15vol% SiC oxidized 4 hours at 1550^o C imaged in cathodoluminescence (b) same flower pattern imaged by electron probe microanalysis (left-to-right) in oxygen K_α x-rays, zirconium L_α x-rays, silicon K_α x-rays, boron K_α x-rays. The scale bars on the elemental maps in (b) represent the intensity of the corresponding element.

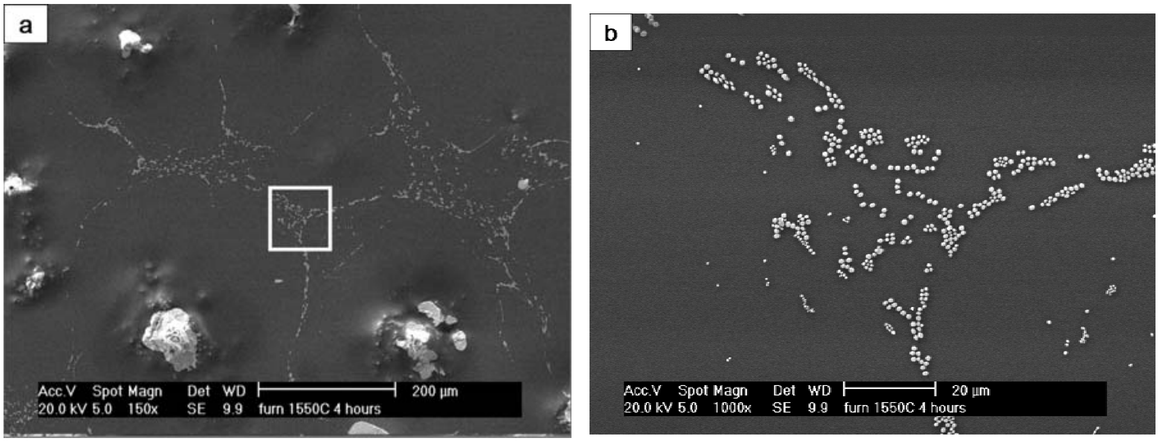

Figure 5.3: Surface of specimen oxidized at 1550ºC for four hours showing features suggesting flow along the surface (a) shows several convection cells, note the apparent flow patterns of the fine zirconia particles between the cells (b) Higher magnification of the small zirconia particles between the cells highlighted by the white box in Figure 5.3(a).

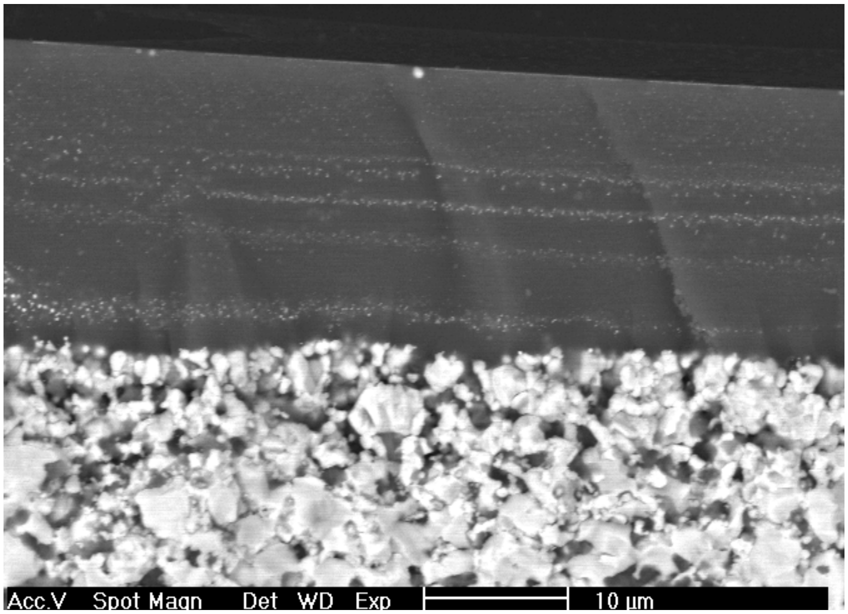

Figure 5.4: Fracture surface cross-section of sample, showing strata of small zirconia particles, suggesting layers of fine surface particles (as in Figure 5.3) repeatedly covered by liquid.

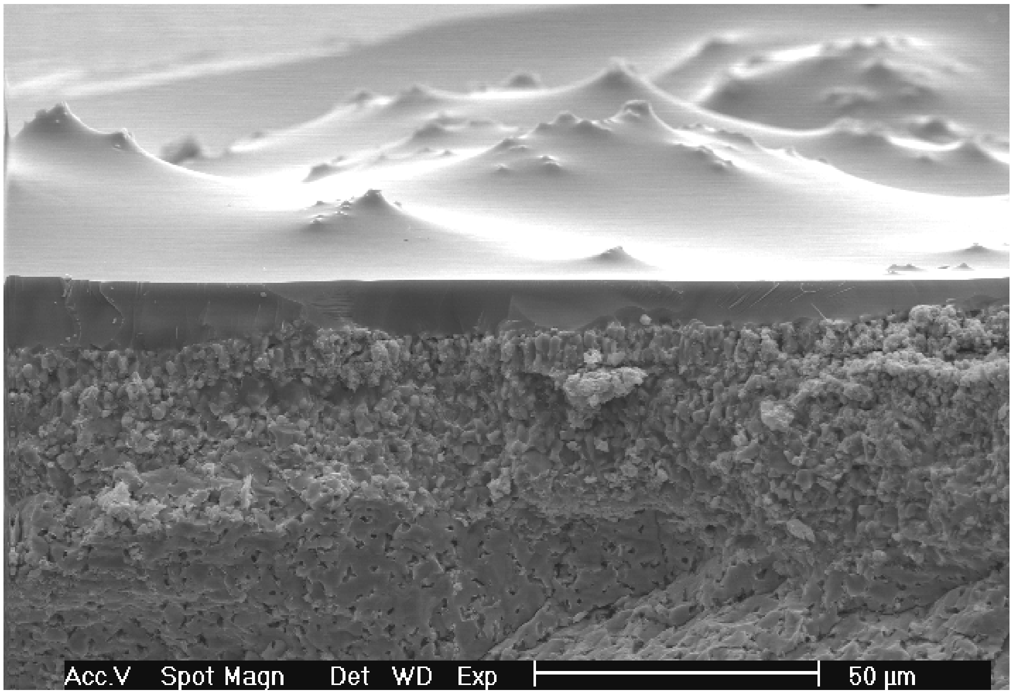

Figure 5.5: Fractured cross section of ZrB_2-15 vol% SiC specimen oxidized for 15 minutes at 1700°C in the ribbon apparatus, showing the (from the interior): unoxidized interior; SiC-depleted zone; a columnar zirconia layer; outer glassy layer.

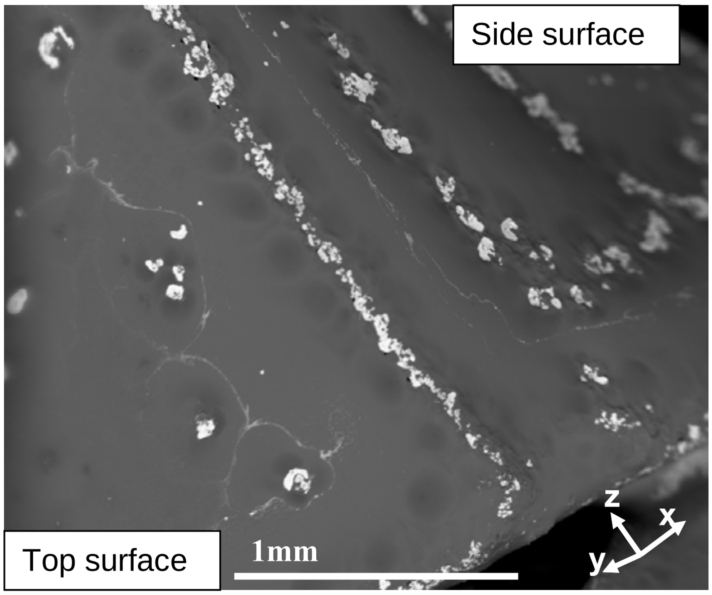

Figure 5.6: Corner of the surface of a ZrB_2-SiC composite oxidized for 3 hours at 1550°C in a conventional furnace. Convection cells decorate the side surface (x-z) and top surface (y-z) of the specimen. Note that the structure is similar on top and side, demonstrating that the direction of gravity does not affect shape of the convection cell features.

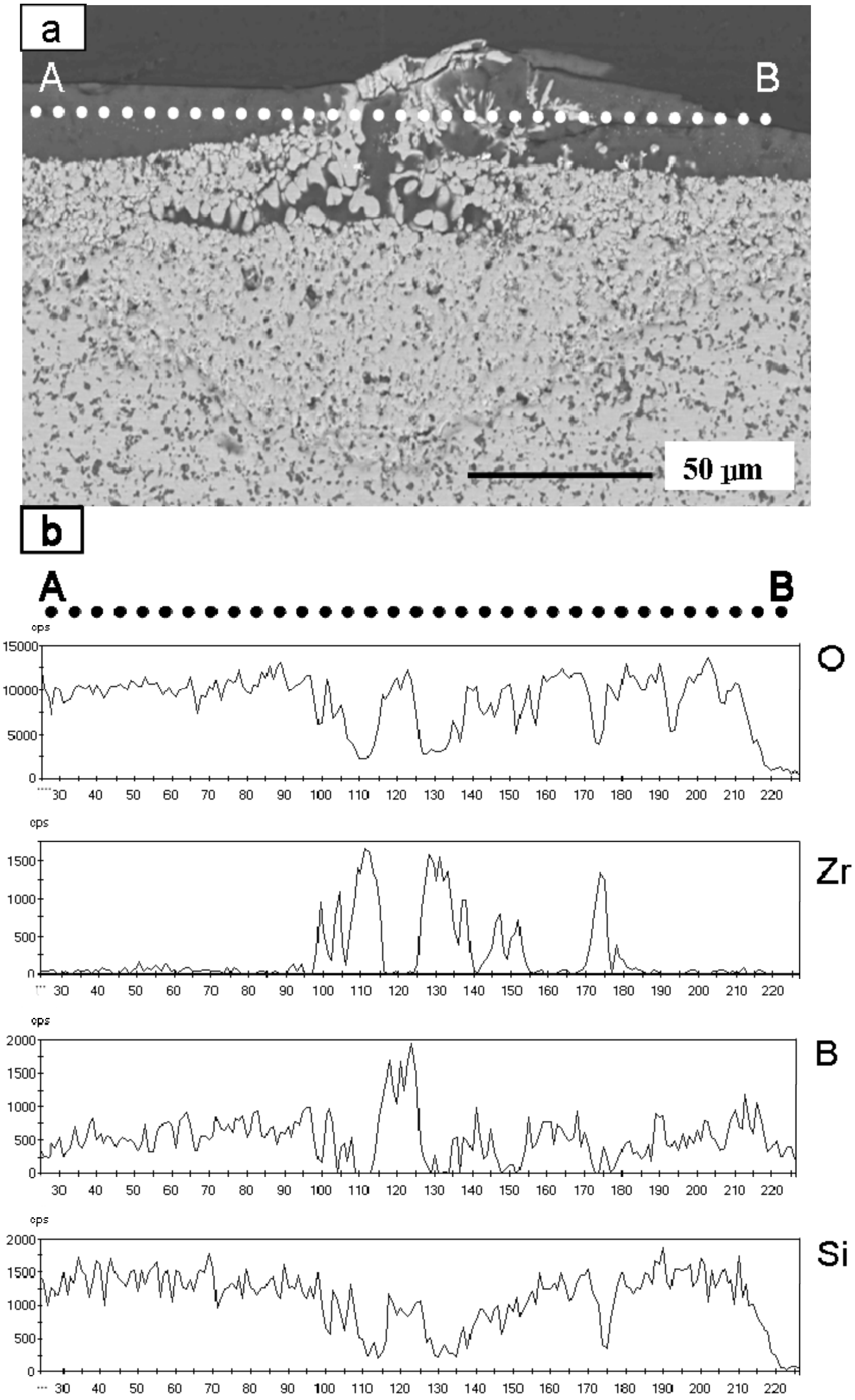

Figure 5.7: (a) BSE image of a cross-section of a cell on surface of a ZrB_2-15vol%SiC composite tested at 1550°C for 4 hrs. The line through the cell indicates where the EPMA line analyzes were done, the letter A indicates the start of the line scan and B the end, (b) graphs of the line analysis; the y-axis is the recorded intensity ((Cps) counts per second) and the x-axis is the distance (µm) from point A to B.

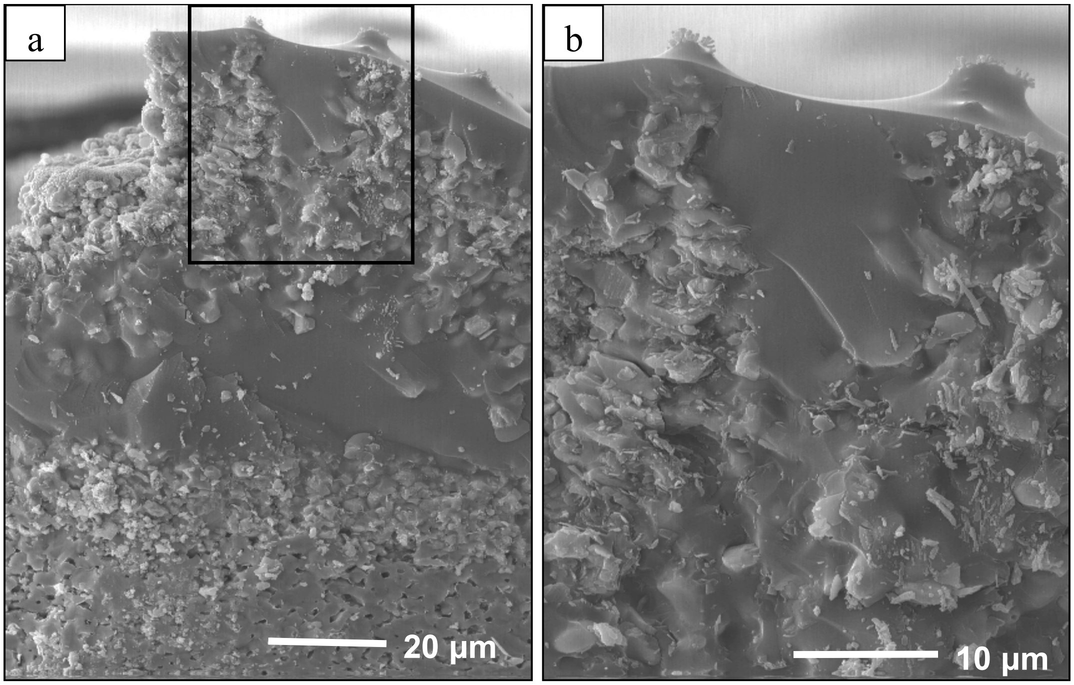

Figure 5.8: (a) Fracture surface of a ZrB_2-SiC oxidized at 1700^{o}C for 15 minutes in the ribbon apparatus, where the fracture plane has intersected two zirconia peaks (b) A higher magnification of the area highlighted with the black box in (a) showing the details of the zirconia peaks. Note their appearance as columns of discrete zirconia particles in a glassy matrix.

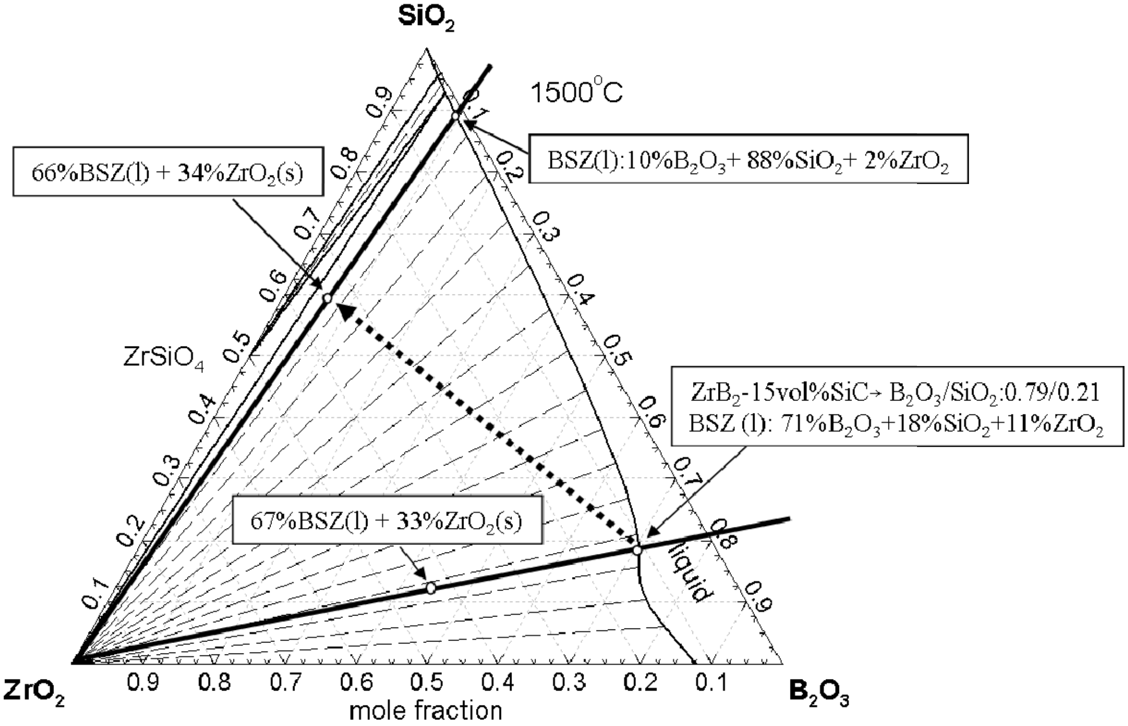

66%BSZ(l) + 34%ZrO_2(s)

BSZ(l):10%B_2O_3+ 88%SiO_2+ 2%ZrO_2

ZrB_2-15vol%SiC→ B_2O_3/SiO_2:0.79/0.21
BSZ (l): 71%B_2O_3+18%SiO_2+11%ZrO_2

67%BSZ(l) + 33%ZrO_2(s)

Figure 5.9: Calculated phase diagram for the 1500°C isothermal section of the ternary ZrO_2-SiO_2-B_2O_3, showing equilibrium between a boria-silica-zirconia (BSZ) liquid and crystalline phases of ZrO_2, $ZrSiO_4$, and SiO_2 (by A.N. Grundy).

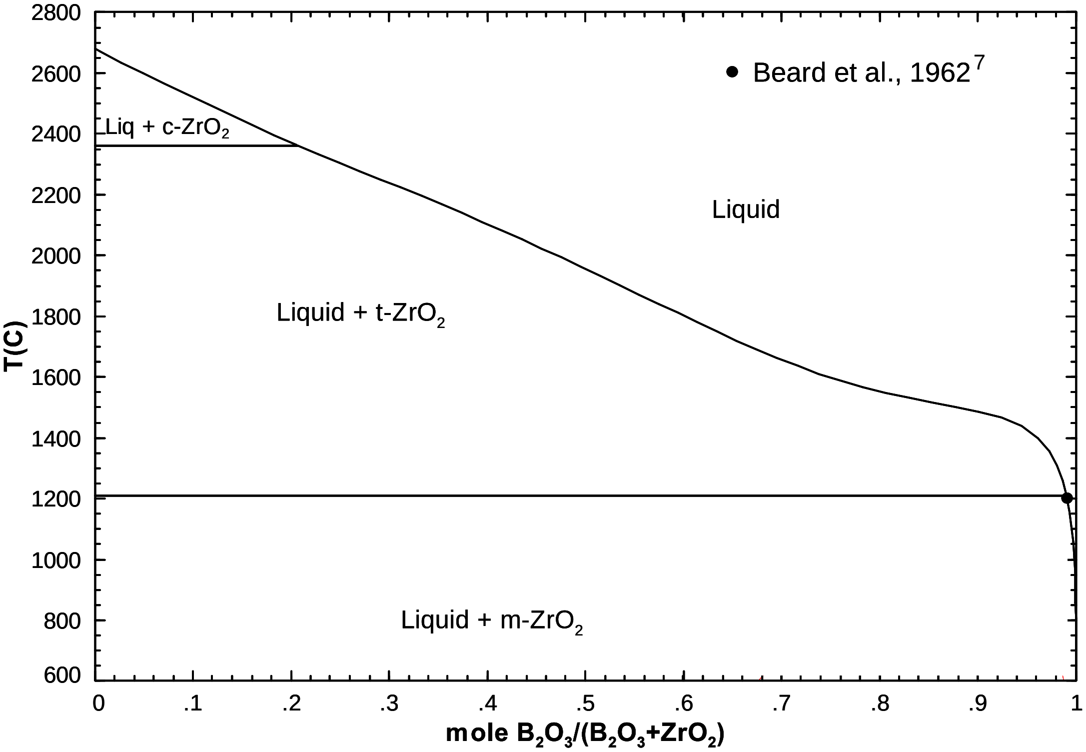

Figure 5.10: Calculated binary phase diagram for the system ZrO_2-B_2O_3, showing the solubility of zirconia (ZrO_2) in the boron oxide liquid as a function of temperature (by A.N. Grundy).

References

1. S.N. Karlsdottir, J. W. Halloran, and C.E. Henderson, “Convection patterns in liquid oxide films on zirconium diboride-silicon carbide composites oxidized at high temperature” (accepted by J. Am. Ceram. Soc., March 2007)

2. S.N. Karlsdottir and J. W. Halloran, “Rapid Oxdiation Characterization of Ultra-High Temperature Ceramics” (accepted by J. Am. Ceram. Soc., April 2007).

3. C.W. Bale, P. Chartrand, S.A. Degterov, G. Eriksson, K. Hack, R. Ben Mahfoud, J. Melanqon, A.D. Pelton and S. Petersen, “FactSage Thermochemical Software and Databases,” Calphad, 26 [2] 189-228 (2002).

4. A.D. Pelton and M. Blander, “Thermodynamic Analysis of Ordered Liquid Solutions by a Modified Quasichemical Approach - Application to Silicate Slags,” Metallurgical Transactions B, 17B 805-815 (1986).

5. S. A. Decterov, V. Swami and I.-H. Jung. “Thermodynamic Modeling of the B_2O_3, B_2O_3-SiO_2 and the B_2O_3-Al_2O_3 systems,” Int. Journal of Materials research, accepted, (2007).

6. W. C. Butterman and W. R. Foster. “Zircon stability and the zirconium oxide-silica phase diagram,” American Mineralogist, 52 [5-6] 880-885 (1967).

7. W. C. Beard, W. C. Butterman, D. E. Koopman, H. E. Wenden and W. R. Foster. “Research on phase equilibria between boron oxides and refractory oxides, including silicon and aluminum oxides,” Quarterly Progress Report No. 9, October 1, 1961-December 31, 1961, Technical Report, Ohio State Univ. Research Foundation, Columbus, OH, Jan 15 (1962).

8. W.C. Butterman, “Equilibrium Phase Relations among Oxides in the Systems GeO_2, GeO_2-B_2O_3, HfO_2-B_2O_3, ZrO_2-SiO_2-B_2O_3, and ZrO_2-SiO_2,” Ph.D. Dissertation, Ohio State University, (1965).

9. Q.N. Nguyen, E.J. Opila, and R.C. Robinson, “Oxidation of Ultra High Temperature Ceramics in Water Vapor”, NASA/TM-2004-212923 April (2004).

10. S. R. Levine, E.J. Opila, M. C. Halbig, J. D. Kiser, M. Singh and J. A. Salem. “Evaluation of Ultra-High Temperature Ceramics for Aeropropulsion Use,” J. Eur. Ceram. Soc., 22 2757-2767 (2002).

11. P.C. Setze, “A Review of the Physical and Thermodynamic Properties of Boric Oxide,” Lewis Flight Propulsion Laboratory, Cleveland, OH. NACA-RM-E57B14, April 24, (1957).

12. W.G. Fahrenholtz, “Thermodynamics of ZrB_2-SiC oxidation: the formation of a SiC-depleted region”, J. Am. Ceram. Soc. 90 [1] 142-148 (2007).

[13] R. Jabra, J. Phalippau, and J. Zarzicki, “Synthesis of binary glass-forming oxide glasses by hot-pressing” J. Non-crystalline Solids, 42 pp. 489-498 (1980).

CHAPTER 6

COMPARISON OF RIBBON METHOD TO CURRENT HIGH TEMPERATURE TESTING FACILITIES*

1.0 Introduction

In Chapter 3 the complex oxide scale known to form during oxidation of UHTC materials was shown to be easily reproduced by using the Ribbon Method. Here the applicability of Ribbon Method is verified further by comparing it to a conventional high temperature furnaces and arc jet facilities. Firstly, the ribbon method is compared to a high-temperature furnace by testing the same ZrB_2-SiC based composite with the two methods at same conditions. Secondly a ZrB_2-15vol%SiC-2vol%$MoSi_2$ specimens tested with the ribbon method are compared to ZrB_2-SiC based composites tested with Arc Jet facilities and high-temperature furnaces, previously reported in the literature.

---

* Parts of this chapter have been presented in the manuscript "Oxidation of ZrB_2-SiC: Comparison of Furnace Heated Coupons and Self-Heated Ribbon Specimens" by S.N. Karlsdottir, J.W. Halloran, F. Monteverde, and A. Bellosi accepted for publication in Proceedings of the International Conference on Advanced Ceramics and Composites, Daytona Beach FL, January 21-26, 2007 (accepted, May 2007). Results from Electron Microprobe Analysis presented here were done with help from Carl E. Henderson from the Department of Geological Sciences, University of Michigan, Ann Arbor, Michigan.

2.0 Oxidation of a ZrB_2-SiC-$MoSi_2$ composite: Comparison of Furnace Heated Coupon with Self-Heated Ribbon Specimen

2.1 Experimental Procedure

2.1.1 Material Fabrication

The UHTC material, ZrB_2-15vol%SiC-2vol%$MoSi_2$, tested was fabricated and provided by our collaborators at CNR-ISTEC mentioned in previous chapters. Details of the processing technique and material properties are presented in more detail in Chapter 3 section 2.1 and elsewhere[1].

The fabrication of the ribbon specimen was done in two steps. Firstly, the bulk material was cut with a wire-EDM machine into 2.25×2.0×25 mm bar. Secondly, about 100 μm of material was removed by diamond grinding to remove a heat-affected zone that can form during wire-EDM machining. The bar was then reduced in thickness in the center with a mechanical grinder (220 grit –diamond wheel) to make a ribbon, with a thickness of 450 μm. The coupon specimen was cut from bulk material with a wire-EDM by our collaborators at CNR-ISTEC to the dimension of 2.5 x 2.0 x 25 mm. Herein the ZrB_2-15vol% SiC-2vol% $MoSi_2$ specimen will be referred to as ZrB_2-SiC or ZrB_2-15vol%SiC specimen.

2.1.2 Oxidation Testing

For the comparison between furnace heated coupon and the ribbon specimen cyclic oxidation of the ZrB_2-SiC specimens were performed at 1600ºC in air.

The ribbon specimen was tested with the Ribbon Method (described in detail in Chapter 2) at the University of Michigan, for four cycles each for 5 min. at 1600ºC in stagnant ambient air, with average heating rate of 690ºC/min and a free cooling

(705ºC/sec). The fast cooling rate is due to the fast thermal response time of the specimen (3.0 ms at 1600ºC), which is depends on the thickness of the specimen ($t_{hot\text{-}zone} = 450$ μm) and its thermal diffusivity ($1.65\cdot10^{-5}$ m^2/s at 1600ºC). The fast heating rate minimizes the oxidation effect on the specimen prior to the hold at 1600ºC. The input power at peak temperature is about 90 W. Figure 6.1 shows the temperature and the current profile of the specimen tested in the apparatus. With time the thickness of the oxide scale of the specimen increases and the un-oxidized interior becomes smaller, so less current is needed to maintain the temperature of the hot-zone at 1600ºC.

The furnace heated coupon was tested by our collaborators Dr. Alida Bellosi and Dr. Frederic Montverde at CNR-ISTEC in Italy. The ZrB_2-SiC coupon was subjected to 4 cycled exposures at 1600°C, 5 min each. The coupon with dimensions of 2.5 x 2.0 x 25 mm was placed upon SiC supports, ensuring the minimal contact area between them. A bottom-loading furnace box, heated with $MoSi_2$ elements, and insulated with highly-porous Al_2O_3 fiber was used. Once slotted into the heated furnace chamber, a maximum time interval of 1 min was necessary to reach the set point of 1600°C.

For both the methods, prior to the testing the specimens were ultrasonically cleaned in acetone and dried. After oxidation, specimens were stored in moisture free desiccators to avoid any reaction of a B_2O_3 on the surface of the specimens. Cross-section of the oxidized specimen was prepared for microstructural analysis by non-aqueous polishing procedures down to 1μm finish.

The composition and morphology of the multilayer oxide scale formed on the ribbon specimen was characterized by Scanning Electron Microscopy (SEM), Energy Dispersive X-ray Spectroscopy (XEDS), Backscattering Electron Microscopy (BSE), and

Electron Microprobe Analyzer (EPMA). Detailed description of the procedure and standards used for the EPMA analysis is reported in Chapter 3. Microstructural and chemical composition analyses were done on the surface of the specimen and cross-section.

The composition and morphology of the multilayer oxide scale formed on the furnace coupon was characterized by our collaborators at CNR-ISTEC by Scanning Electron Microscopy (SEM), and Energy Dispersive X-ray Spectroscopy (XEDS). Micrographs of the tested furnace coupon reported here were provided by Dr. Alida Bellosi and her associates at CNR-ISTEC.

2.2 Results and Discussion

A multi-layer oxide scale was formed on the ZrB_2-SiC samples during the cyclic testing with the two methods.

Microstructural and elemental analysis revealed that the surface of the ribbon specimen was covered with silica (SiO_2) rich glass. The glass contained larger 50-70 µm ZrO_2 regions and small 2-5 µm dispersed zirconia (ZrO_2) particles that formed a flow pattern around the larger ZrO_2 regions. This was confirmed by XEDS analysis. These features resemble the convection cells discovered in furnace tested specimens and discussed in Chapter 4 and 5. This suggests that there existed a convective flow of the borosilicate liquid at the oxidation temperature (1600ºC) and that these ZrO_2 regions are in fact the ZrO_2 cores of the convection cells, herein called ZrO_2 islands. Figure 6.2(a) and (b) shows BSE and SEM image of the surface of the specimen. The existence of B_2O_3 in the glass could not be determined with the XEDS equipment used due to the low sensitivity of the equipment to light elements such as Boron (B). The BSE image (Fig.

6.2(a)) indicates though, with the dark contrast around the ZrO_2 islands, that there exist B_2O_3 rich areas around the islands. Previous elemental analysis (EPMA) of convection cells on furnace tested specimens showed that areas in dark contrasts around the ZrO_2 islands were richer in B_2O_3 compared to the surrounding glass.

The oxide scale formed on the ribbon specimen consists of three layers. This can be seen from the cross-section of the ribbon specimen shown in Figure 6.3. The outermost layer is the silica (SiO_2) rich glass layer mentioned above. The second layer is a porous ZrO_2 layer with small amount of glass embedded between the grains. The thickness of the SiO_2 and ZrO_2 layers were measured to be on the average 8 μm and 9 μm respectively. The cross-sectioning revealed enhanced oxidation, i.e. thicker ZrO_2, where the cross-section cut through a part of the convection cells; this is shown in Figure 6.4. The enhanced oxidation region under the convection cells is discussed and studied in Chapter 8.

The third layer of the oxide scale is SiC-depleted region; c.a. 10 μm in thickness. The SiC-depleted layer is situated below the ZrO_2 layer and above the un-reacted bulk material (ZrB_2-SiC). This was verified by elemental (EPMA) and microstructural analysis. The EPMA analyses were performed on the cross-section of the ribbon specimen shown in the BSE images in Figure 6.4 and Figure 6.5(a). The elements: silicon (Si), oxygen (O), zirconium (Zr), and boron (B) were mapped with EPMA to obtain information about the distribution of elements in the oxide scale; the maps are shown in Figure 6.5(b)-(e) and Figure 6.6(a)-(d). Additionally, molybdenum (Mo) was mapped, but the signal was low due to the small amount (2vol%). The EPMA mapping showed the distribution of Mo to be very similar to the distribution of Zr, i.e. Mo existed in the ZrO_2

layer, the SiC-depleted zone and the bulk material. Due to the small amount of Mo and no apparent significance of the Mo distribution the maps and the line analyses for it are not presented here. As mentioned earlier, Boron (B) is not detectable with the SEM/XEDS used, thus the EPMA analysis were important in supplying information on if there existed any borosilicate glass or boron oxide (B_2O_3) in the oxide scale. B_2O_3 was not detected in the SiO_2 rich scale or in the ZrO_2 region with the EPMA, this is likely due to the small amount of the B_2O_3 existing in the oxide scale which could not be detected with the scanning speed (20ms) used for the EPMA analysis. Small amount of B_2O_3 compared to SiO_2 in the borosilicate is expected due to the high temperature (1600ºC) that the specimen experienced. But as mentioned in previous chapters; B_2O_3 is believed to start volatilizing away from the borosilicate scale at higher temperatures. Carbon (C) was not mapped due to the cross-section had to be coated with C for the EPMA analysis; other coatings are not suitable due to the light elements that were being analyzed.

The elemental maps show clearly that the first two layers of the oxide scale consist of ZrO_2 and SiO_2 formed during oxidation. The enhanced oxidation region related to the convection cells can be easily identified from the local increased thickness of the ZrO_2 layer indicated from the Zr, O and B elemental maps in Figure 6.5 (a)-(d). For the third layer, the maps in Figure 6.6(b)-(e) show evidence of Zr, and B, but no Si. To gain more information about the distribution of the elements in the third layer, quantitative line analyses were done on the EPMA data. The line analysis is shown in Figure 6.7 where the x-ray intensity ((cps) counts per second) vs. location in the oxide scale (μm) is shown for O, B, Zr and Si. The start of the line is labeled with A (i.e. 0 μm) and the end with B (i.e. 63 μm). From Figure 6.7 we see that there exists some O in the third layer along with Zr and B but there are no traces of Si. These results indicate that the third layer is a SiC depleted region. SiC-depleted intermediate layers have been previously observed on similar materials oxidized under different regimes [1-5], in some cases the oxidation of SiC leaving carbon [6]. The existence of oxygen in the third layer of the oxide scale suggests that the SiC-depleted layer consists of some ZrO_2 as well as ZrB_2 bulk material. Fahrenholtz et al.[5] reported that an interface separating a layer where ZrO_2 is dominant from a layer in which ZrB_2 is dominant may be located in SiC-depleted layers formed in oxidized ZrB_2-SiC composites.

SEM image of the cross-section of the furnace coupon specimen is showed in Figure 6.8. Microstructural and chemical compositional analysis and imaging were performed and provided by our collaborators at CNR-ISTEC. Figure 6.8 illustrates the changes in the virgin microstructure after the repeated exposures at 1600°C in the furnace. On top of the exposed faces, a glassy SiO_2 rich scale has formed. The undulating trend of the thickness of the glassy layer indicates a laterally flow of the surface layer during oxidation. Underneath, a partly porous scale which separates the outermost glassy scale from the as-sintered virgin bulk is basically constituted of ZrO_2 grains embedded in a SiO_2-rich glassy phase.

In Figure 6.9(a)-(b) SEM images of the cross-sections of the ribbon specimen and the furnace coupon are compared. Both specimens have an outer SiO_2 rich surface layer and an underlying ZrO_2 layer of comparable thicknesses. The ribbon specimen has a total affected thickness of 27 μm and the furnace coupon 30 μm. Additionally a third layer, a SiC-depleted layer, was found in the ribbon specimen which was not observed in the furnace coupon.

2.3 Summary

The two testing methods are quite different. Firstly the size of the coupons (2.5 × 2.0 × 25 mm, V = 125.0 mm^3) tested in the conventional furnace are larger than the oxidized section of the ribbon specimen (0.45 × 2.25 × 6.7 mm, V = 6.8 mm^3) tested with the Ribbon Method in the apparatus. The volume of the furnace specimen is 18 times larger. Secondly, the furnace coupon is isothermally heated externally by convection in an enclosed environment, whereas the ribbon specimen is heated internally with a flowing current. The conditions are thus significantly different but the results from the micro-structural and compositional analysis show that the two facilities give very similar result. This indicates that the Ribbon Method is suitable and reliable for high-temperature oxidation of UHTC.

3.0 Comparison of Ribbon Method with Current High-Temperature Facilities

3.1 Ribbon Method vs. Arc Jet Facilities

3.1.1 Arc Jet Facilities

Arc-Jet heater facilities in USA are located in governmental research agencies and have been used for decades to evaluate materials for reentry vehicles, combustors, and hypersonic vehicle leading edges [7]. The Arc-Jet facilities are used to simulate aerodynamic heating that occurs on nose caps, wing leading edges and other areas of spacecrafts requiring thermal protection systems. The arc heaters produce a high-temperature gas stream by combined radiative, conductive and convective heat transfer from a high-voltage DC (Direct Current) electric arc discharge to a gas flowing through cooled column [3]. The Arc-Jet facilities in USA are located in the NASA Ames Arc Jet

Complex at NASA Ames Research Center, CA, and at the Aerospace Testing Alliance, Arnold Engineering Development Center, Arnold AFB, TN. The NASA Ames arc-jet facility called the Interactive Heating Facility (IHF) is the largest and most powerful arc jet facility operating within NASA. It has a 60 MW arc heater capable of producing enthalpies from 7 to 46 MJ/kg and high surface temperatures in the range of 1700-2500ºC for up to 30 min durations [3, 7-9]. Arc jet testing is expensive and time consuming due to the high power used during testing and the complicated application process needed to go through to get permission to use the facility [10].

3.1.2 Ribbon Specimens vs. Arc-Jet Coupon

Here a ZrB_2-30vol%SiC-2vol%WC specimen, tested with arc-jet heater in NASA Ames IHF, reported in the literature by Chamberlain et al.[1] is compared with a ZrB_2-15vol%SiC-2vol%$MoSi_2$ ribbon specimen tested with the Ribbon Method. The arc jet tested ZrB_2-SiC specimen was exposed to a heat flux of 350 W/cm^2 with a stagnation pressure of 0.07 atm and an exposure time of 600 sec. (10 min). The specimen was heated from room temperature up to 1700ºC in 30 sec. The surface temperature then increased slowly approaching 1800ºC at the end of the test. Chamberlain et al.[11] found that the surface layer was primarily composed of ZrO_2, with some voids in the layer (15 µm). These voids were reported to be more near the center of the specimen than near the edges. Microstructure and chemical composition analysis of the oxide scale revealed a three layer structure; a thin ZrO_2 surface layer (10 µm); a ZrO_2 + SiO_2 rich layer (~100 µm); and a SiC-depleted zone (~200 µm). Figure 6.10(b) shows an SEM image of the oxide scale of the arc-jet coupon. Chamberlain et al. detected some boron (B) in the ZrO_2

+ SiO_2 rich layer (2nd layer) which could indicate some amount of ZrB_2 still existing in this transitional region.

The ribbon specimen used for comparison was tested at 1700ºC in stagnant ambient air for 15 min with a heating rate of 480ºC/min. and a free cooling (~767ºC/sec) (described earlier in Chapter 3). The hot-zone of the specimen (the part of the specimen heated) experienced a heat flux of ca 220 W/cm^2, estimated from the power used for heating the specimen. Figure 6.10(a) shows the structure of the oxide scale of the ribbon specimen consisting of a three layer structure; thin SiO_2 rich surface layer + small ZrO_2 particulates (avg. 12 μm); a ZrO_2 + SiO_2 layer (avg. 90 μm); and a SiC-depleted zone (avg. 120 μm). The oxide scales of the arc-jet and the ribbon specimens are similar in composition and structure. Both have three layers, including ZrO_2 + SiO_2 rich layer and a SiC-depleted zone. Also the oxide thicknesses are comparable; the arc-jet coupon experienced shorter exposure time but higher temperature, c.a. 50-100ºC higher than the ribbon specimen, resulting in a thicker SiC-depleted zone and slightly thicker ZrO_2 + SiO_2 layer. Figure 6.10 compares the cross-sections of the two specimens. The main difference between the oxide scales lies in the surface layer of the two specimens, the difference is presumably due to the higher temperature exposure of the specimen in the arc-jet test, resulting in a complete volatilization of any SiO_2 formed. Presumably, any B_2O_3 (l) formed has volatilized away at these temperatures due to its high vapor pressure, and low melting temperature and viscosity [2-4]. This is consisted with the observations in Chapter 3 where it was suggested that the SiO_2 rich scale formed during oxidation starts volatilizing extensively at temperatures above 1700ºC, resulting in a porous ZrO_2 surface layer at higher temperatures (>1700ºC). The oxide scale of a ribbon specimen heated from room temperature to 1900ºC in 1 ½ min. reported in Chapter 3 also supports this where the surface layer consisted of porous ZrO_2.

3.2 Ribbon Method vs. Furnace Testing

Next, two ZrB_2-15vol%SiC-2vol%$MoSi_2$ ribbon specimens are compared to a ZrB_2-20vol%SiC composite tested at NASA Glenn with a high-temperature furnace [11]. The first ZrB_2-SiC-$MoSi_2$ specimen went through cyclic oxidation, three cycles; 1st cycle at avg. 1500ºC for 50 min., 2nd cycle at avg. 1690ºC for 28 min and the 3rd cycle at avg. 1650ºC for 16 min., the total exposure time being 94 min. The second ribbon specimen went through static oxidation and was tested at 1650ºC for 15 min., with a heating rate of 480ºC/min. and a free cooling (~767ºC/sec) (described earlier in Chapter 3). Levine et al.[11] at the NASA Glenn research center tested the ZrB_2-20vol%SiC specimen using a bottom loading furnace with Zirconia heating elements. It went through cyclic oxidation; ten 10 min. cycles at 1627ºC, thus experiencing total 100 min. of exposure. Figure 6.11(a)-(c) shows the cross-sectional view of the three samples showing the three layer structure of the oxide scale for all three specimens. The thickness of the oxide scale of the ribbon specimen that experienced the cyclic oxidation is comparable to the oxide scale thickness of the furnace heated specimen; see Figure 6.11(c) and (b). The oxide scale of the ribbon specimen tested at 1650ºC for 15 min. is on the other hand thinner than for the furnace tested specimen, which is what is expected for the shorter exposure time. The very thin SiO_2 surface layer on the cyclic ribbon specimen indicates that for the higher temperatures (≥1650ºC) the SiO_2 starts evaporating. The volatilization of SiO_2 at higher temperatures (~1700ºC) was also the result of the ZrB_2-SiC testing with the Ribbon Method in Chapter 3. From Figure 6.11(b) it can be seen that the SiO_2 outermost layer of the furnace specimen contains small ZrO_2 particulates near the underlying ZrO_2 columnar layer. The same is seen in the cyclic tested ribbon specimen and the ribbon specimen tested at 1700ºC mentioned earlier (in Chapter 3), where the thin SiO_2 surface layer is full of ZrO_2 particulates. This indicates that when the SiO_2 starts evaporating the ZrO_2 particulates are left behind forming a ZrO_2 surface layer seen in the arc-jet tested specimen and the ribbon specimen tested up to 1900ºC described in Chapter 3. The ZrO_2 particulates are shown in detail in Chapter 3 for the ribbon specimen tested at 1700ºC. The peculiar arrangement of these particulates is suggested here to be the results of a convective flow of the borosilicate liquid formed during oxidation [12-13], described in Chapter 4 and 5.

4.0 Conclusion

Here the Ribbon Method has been thoroughly compared to current UHTC high-temperature facilities used for oxidation testing. The heat transfer condition formed by the Ribbon Method is significantly different from both the furnace oxidation and the arc-jet testing. Nonetheless the micro-structural and compositional analyses show that the Ribbon Method gives similar result in terms of the oxide scale thickness, structure and composition of the ZrB_2-SiC based composites tested. As a result the Ribbon Method can be considered as a valuable addition to the current high temperature facilities available today for UHTC testing.

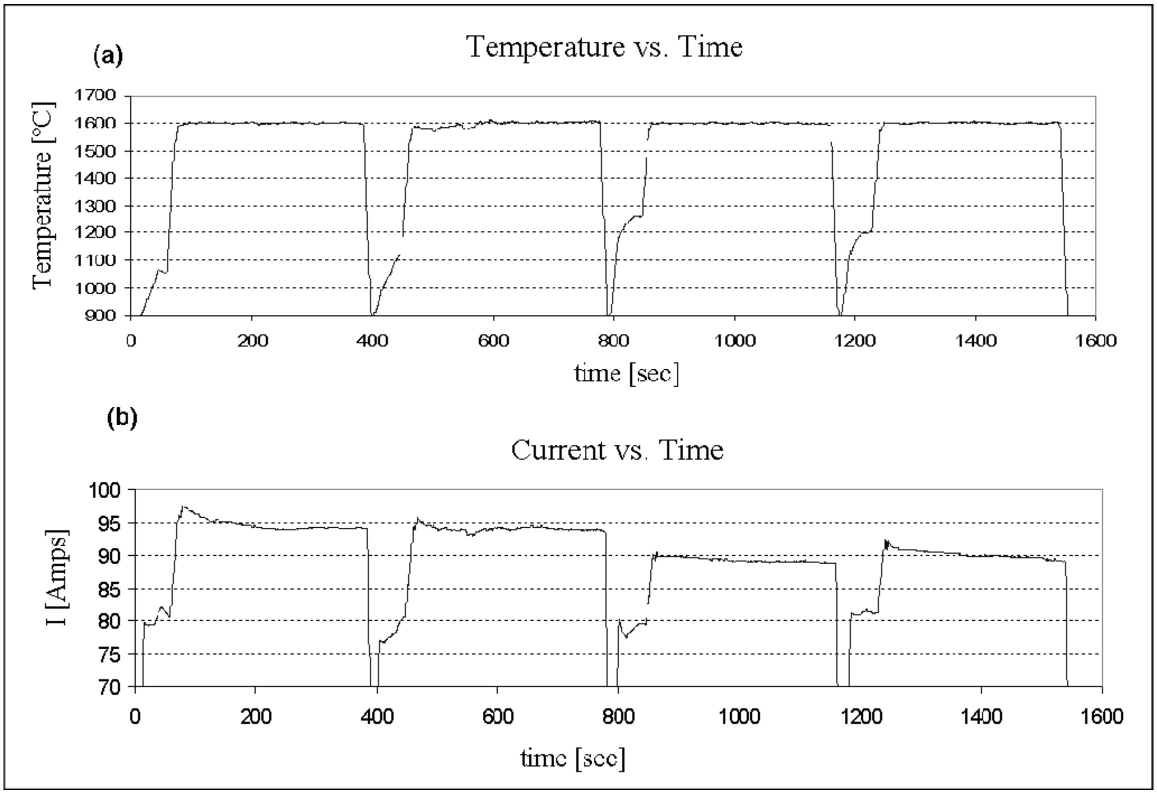

Figure 6.1: (a) Temperature profiles of the four cycles that the ribbon specimen underwent in the apparatus (b) Current profiles for the four cycles, showing the decreased current with time needed to reach the set temperature.

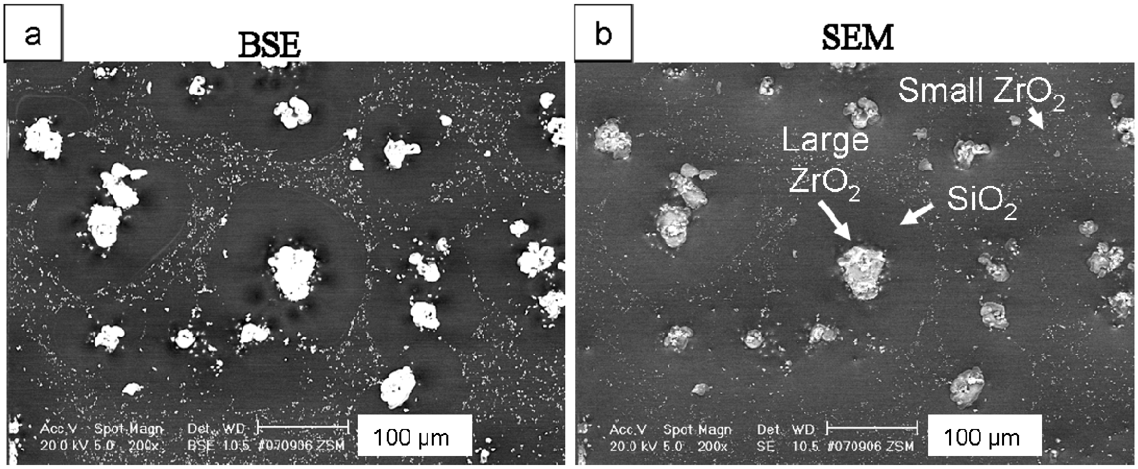

Figure 6.2: (a) BSE image of the surface of the ribbon specimen after the cycled oxidation, showing the white ZrO_2 cores in center of the convection cells; the small ZrO_2 particles around the convection cells; and the darker contrast inside the convection cells, indicating B_2O_3 rich regions (b) SEM of the same surface view with arrows indicating the convection cell features.

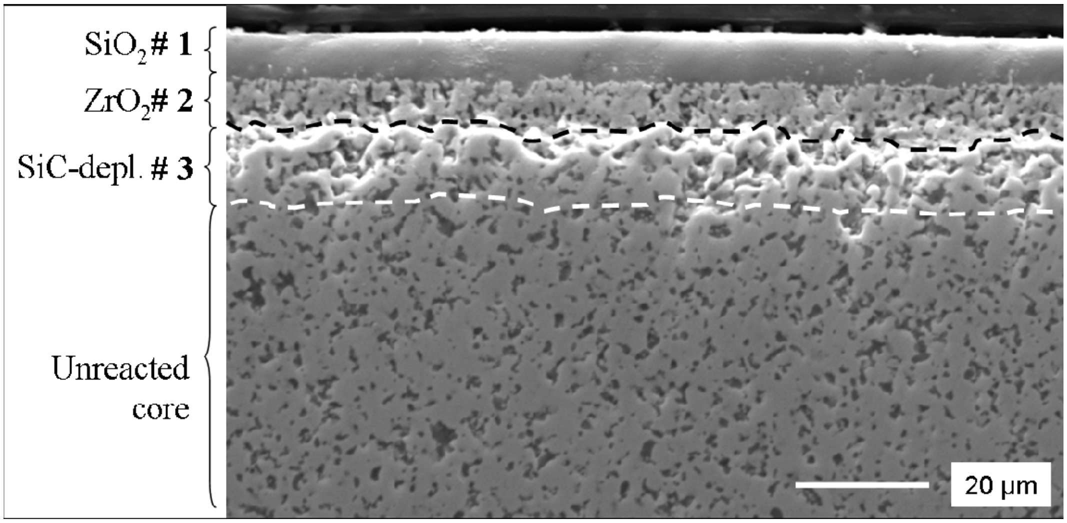

Figure 6.3: SEM image of the cross-section of the ribbon specimen showing the three layer structure of the oxide scale after four 5 min cycles at 1600°C.

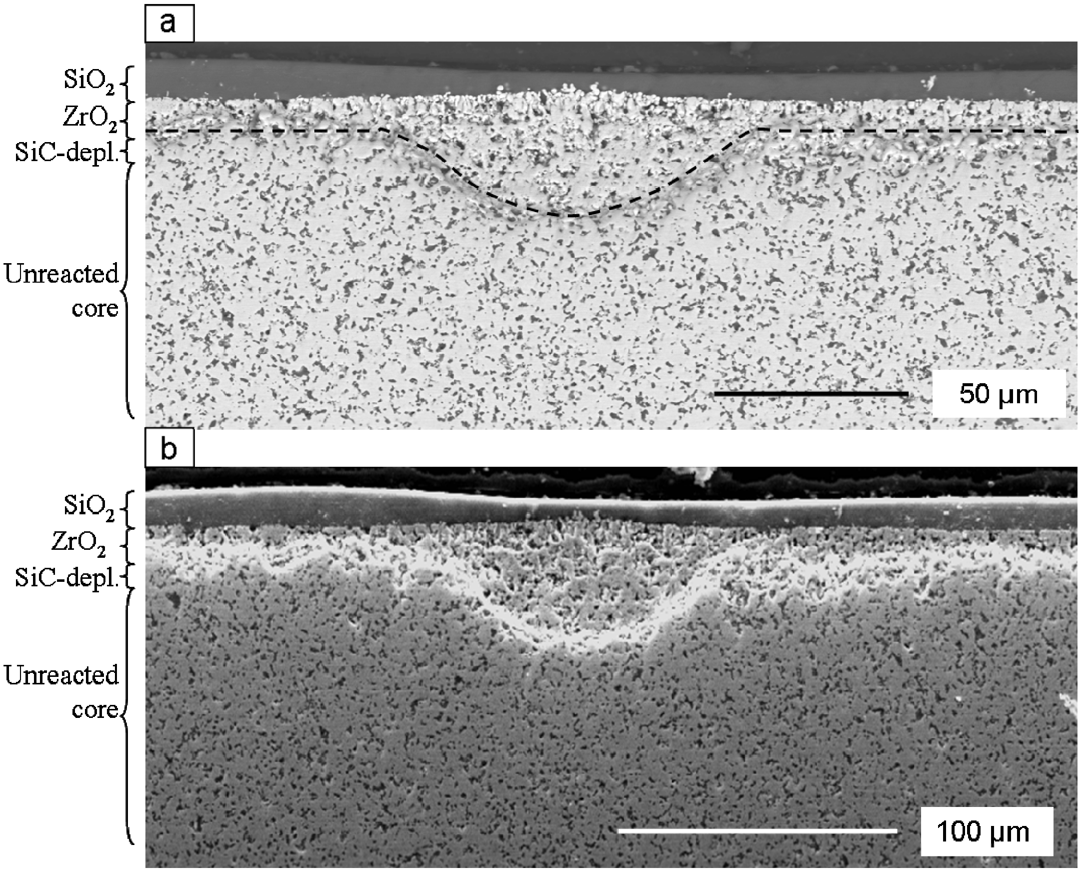

Figure 6.4: BSE image of a cross-section through a convection cell in the ribbon specimen showing a local enhanced oxidation zone indicated by an increased thickness of the ZrO_2 layer.

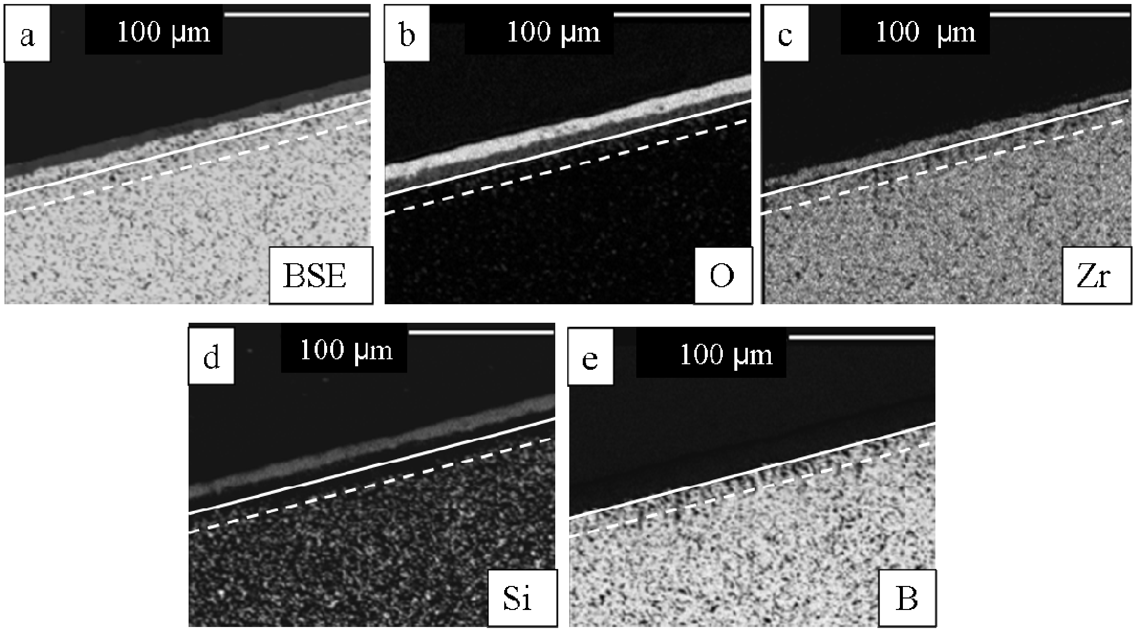

Figure 6.5: (a) BSE image of the cross-section of the ZrB_2-SiC ribbon specimen, (b) oxygen map (O) (c) zirconium map (Zr) (d) silicon map (Si) (e) boron map (B). The solid line outlines the interface between the ZrO_2 layer and the SiC depleted region and the slashed line outlines the interface between the SiC depleted and the un-reacted core.

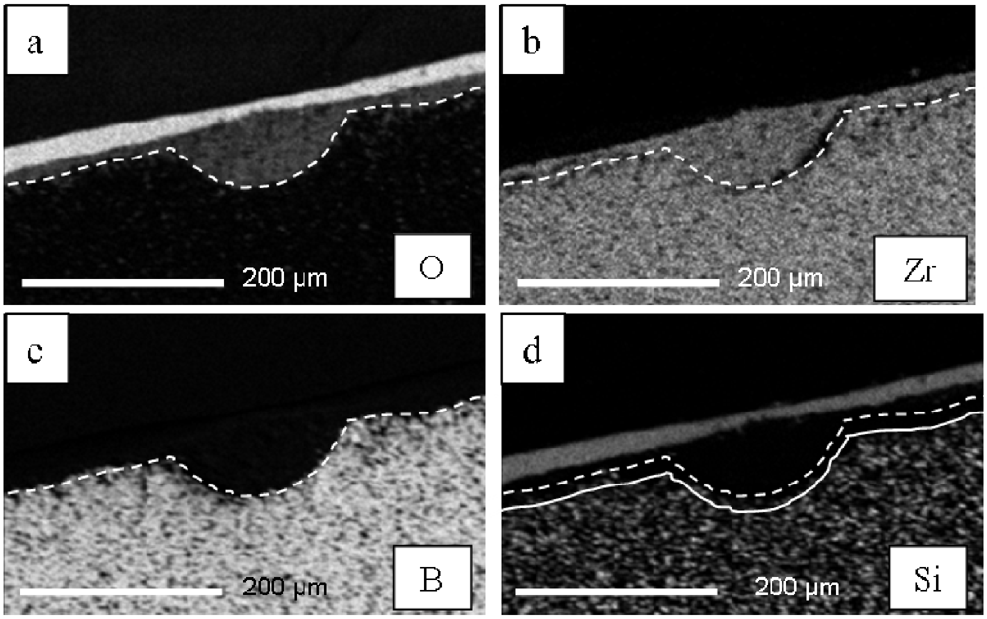

Figure 6.6: EPMA maps of the cross-section through the convection cell shown in Figure 6.4, (a) O map, (b) Zr map, (c) B map, and (d) Si map. The slashed line outlines the interface between the ZrO_2 layer and the SiC depleted region and the solid line in (d) outlines the interface between the SiC depleted layer and the un-reacted core.

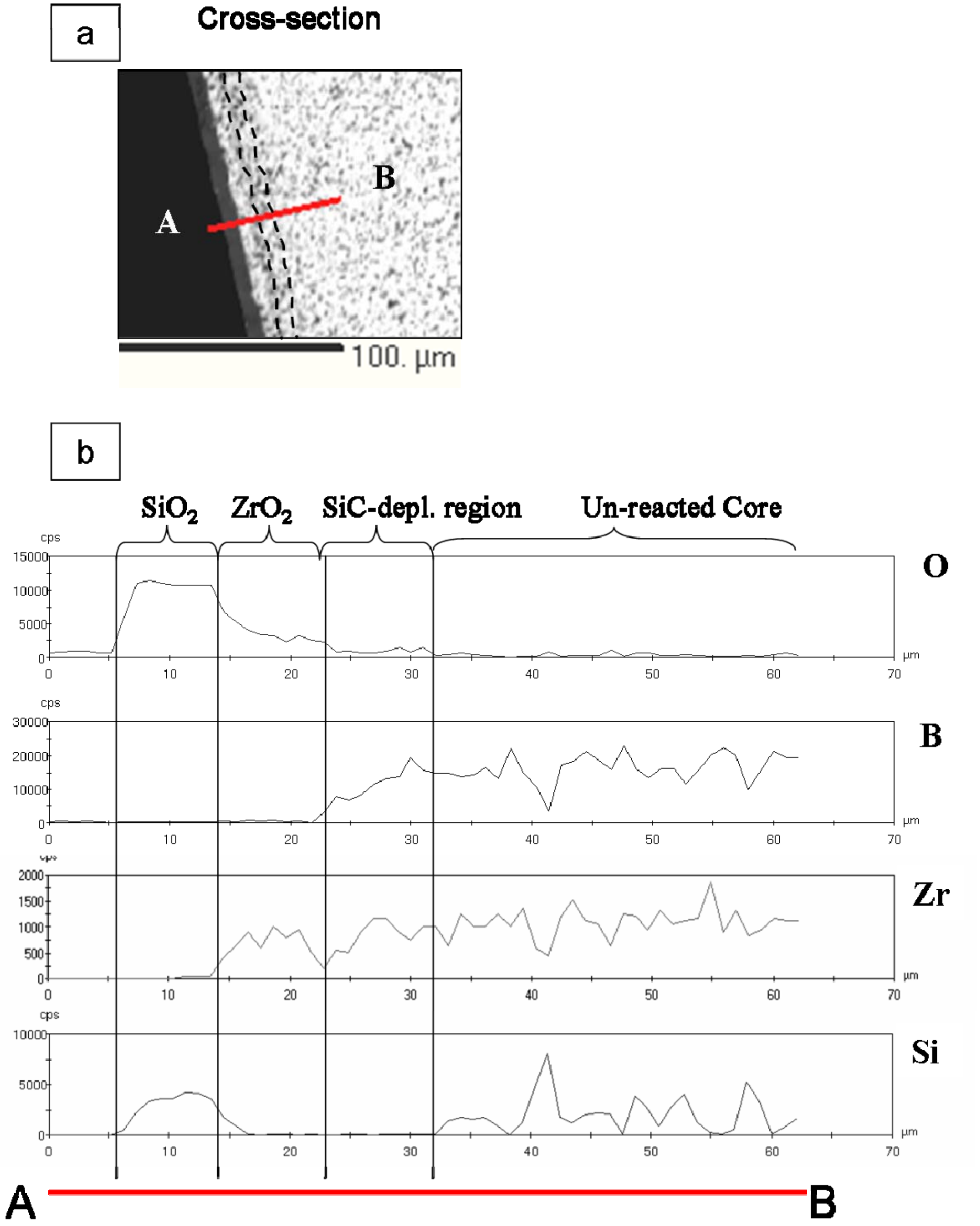

Figure 6.7: Line analysis of the EPMA maps (a) BSE image of the cross-section of the ribbon specimen showing the line where the intensity of the elements was recorded, A indicates the start of the line scan and B the end (b) Graphs of the recorded intensity (Cps) (counts per second) vs. distance (µm) of the line scan shown in (a).

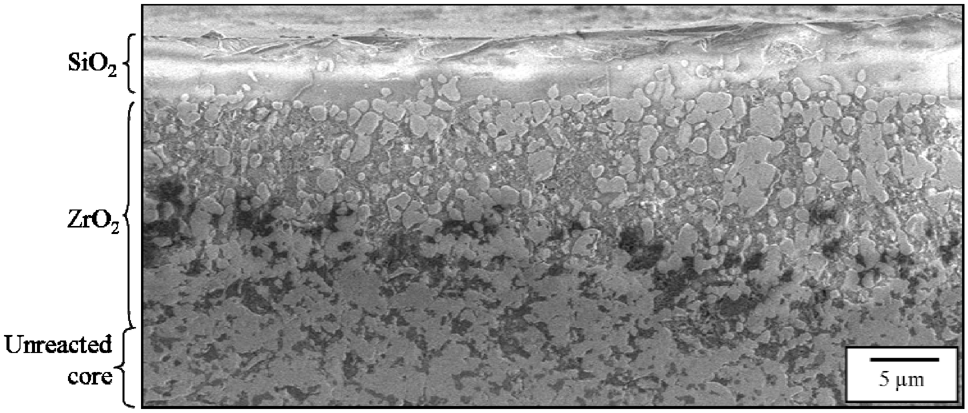

Figure 6.8: SEM micrograph of the cross-section of the furnace heated coupon showing the two layer structure of the oxide scale; SiO_2 rich surface layer and an underlying ZrO_2 rich region (provided by CNR-ISTEC).

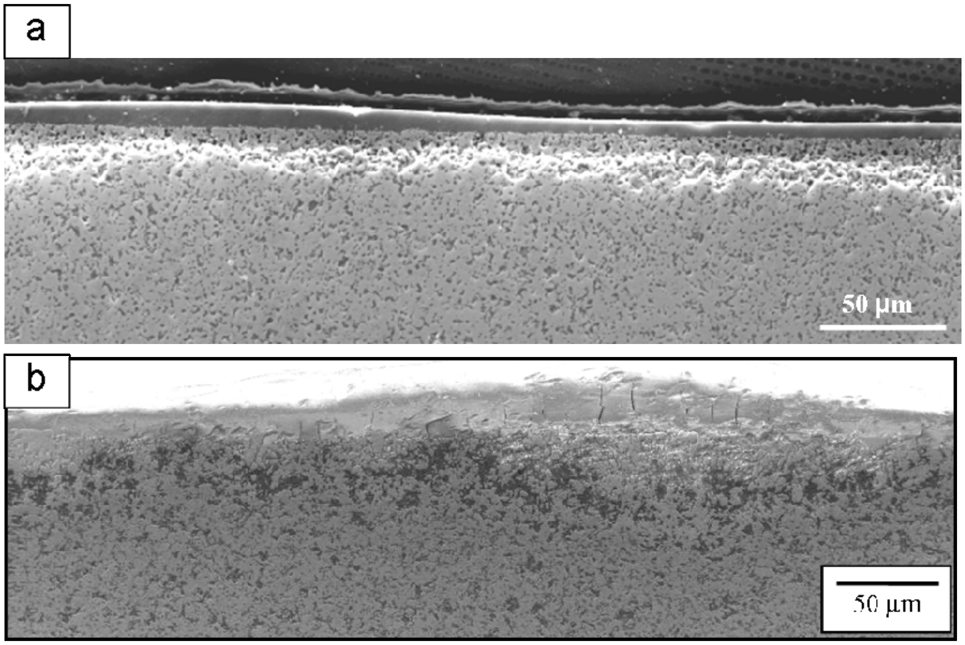

Figure 6.9: SEM micrographs of the cross-sections of (a) the ribbon specimen and (b) the furnace heated coupon (provided by CNR-ISTEC). Both specimens have an outer SiO_2 rich surface layer and an inner ZrO_2 rich layer. Additionally evidence of SiC-depleted zone was found for the ribbon specimen.

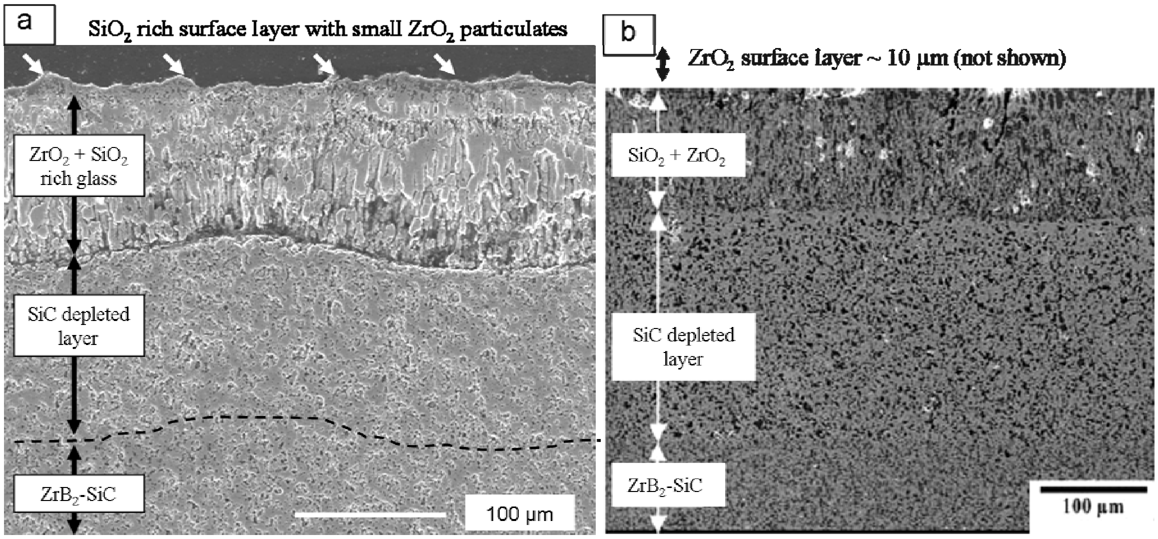

Figure 6.10: Cross-sections of (a) the ribbon specimen and (b) the arc-jet coupon[1], showing the similarity of the oxide scale structures of ZrB_2-SiC based specimens tested with the two different methods.

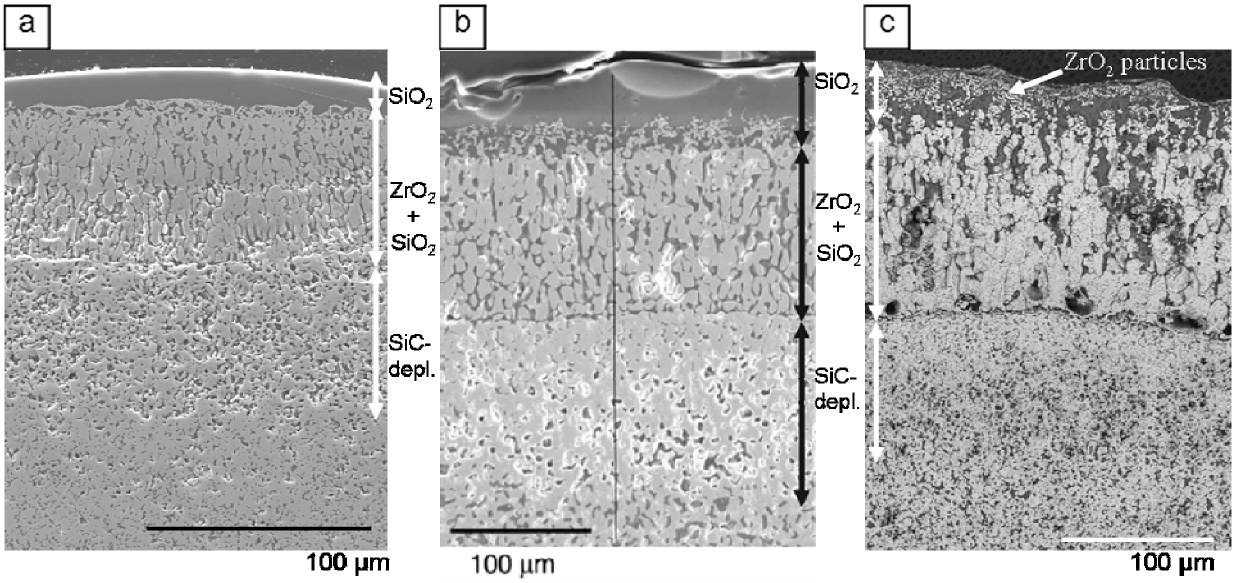

Figure 6.11: Cross-sections of the ribbon specimens (a, c) and the furnace tested specimen (b), showing the three layer structure of the oxide scale for all three specimens. The ribbon specimen in (a) was tested at 1650ºC for 15 min., the one in (c) experienced cyclic oxidation, 3 cycles; 1500ºC for 50 min., 1690ºC for 28 min, and 1650ºC for 16 min (total 94 min.). The furnace tested specimen shown in (b) was tested at 1627ºC for ten 10 min cycles (total 100 min.)[11].

References

1. A. Chamberlain, W. Fahrenholtz, G. Hilmas and D. Ellerby. "Oxidation of ZrB_2-SiC Ceramics under Atmospheric and Reentry Conditions," Refractories Applications Transactions, 1 [2] 1-8 (2005).

2. F. Monteverde, and A. Bellosi. "The Resistance to Oxidation of HfB_2-SiC Composite." J. Eur. Ceram. Soc. 25 1025-1031 (2005).

3. M. Gasch, D. Ellerby, E. Irby, S. Beckman, M. Gusman, & S. Johnson. "Processing, Properties and Arc Jet Oxidation of Hafnium Diboride/Silicon Carbide Ultra High Temperature Ceramics." Journal of Materials Science 39 5925-5937 (2004).

4. W. Fahrenholtz. "Thermodynamic Analysis of ZrB_2–SiC Oxidation: Formation of a SiC-Depleted Region." J. Am. Ceram. Soc., 90 [1] 143-148 (2007).

5. A. Rezaie, W.G. Fahrenholtz, and G.E. Hilmas, "Evolution of Structure during the Oxidation of Zirconium Diboride-Silicon Carbide in Air up to 1500C," J. Eur. Ceram. Soc. 27 [6] 2495-2501 (2007).

6. F. Monteverde "Beneficial effects of an ultra-fine SiC incorporation on the sinterability and mechanical properties of ZrB_2" Appl. Phys. A 82 329-337 (2006).

7. P.A. Montgomery, D.M. Smith, J.M. Sheeley, E.J. Felderman, and T. Budke, "The Quest for Higher Total Pressures: Justification and Current Development Efforts for a Higher Pressure Arc-Heated Facility," USAF Developmental Test and Evaluation Summit, Woodland Hills, CA. American Institute of Aeronautics and Astronautics, AIAA 2004-6815 (2004).

8. J.H. Grinstead, D.A. Stewart, and C.A. Smith, "High Enthalpy Test Methodologies for Thermal Protection Systems Development at NASA Ames Research Center," AIAA/CIRA 13th International Space Planes and Hypersonics Systems and Technologies, American Institute of Aeronautics and Astronautics AIAA 2005-3326 (2005).

9. National Aeronautics and Space Administration (NASA) website, Editor; Jonas Dio. http://www.nasa.gov/centers/ames/research/technology-onepagers/arcjetcomplex.html

10. Terrazas-Salinas and C. Cornelison. Test Planning Guide for ASF Facilities. A029-9701-XM3 Rev. B. Thermophysics Facilities Branch, Space Technology Division, NASA Ames Research Center, CA, March (1999).

11. S. R. Levine, E.J. Opila, M. C. Halbig, J. D. Kiser, M. Singh and J. A. Salem. "Evaluation of Ultra-High Temperature Ceramics for Aeropropulsion Use," J. Eur. Ceram. Soc., 22 2757-2767 (2002).

[12] S.N. Karlsdottir, J. W. Halloran, and C.E. Henderson, “Convection patterns in liquid oxide films on zirconium diboride-silicon carbide composites oxidized at high temperature,” Journal of American Ceramic Society, 90 [9] 2863-2867 (2007).

[13] S.N. Karlsdottir, J. W. Halloran, and A. N. Grundy, “Zirconia Transport by Liquid Convection During Oxidation of Zirconium Diboride-Silicon Carbide,” (accepted by J. Am. Ceram. Soc., July 2007).

CHAPTER 7

INTERPRETATION OF OXIDE SCALES OF ZIRCONIUM DIBORIDE- AND HAFNIUM DIBORIDE-SILICON CARBIDE COMPOSITES

1.0 Introduction

ZrB_2- and HfB_2-SiC composites oxidize to form a complex multi-layer oxide scale at temperatures above 1500ºC as shown in earlier chapters of this dissertation and in the UHTC literature[1]. Often the oxide scale features a silica-rich outer layer, which lies over a subscale of crystalline zirconia, sometimes with a columnar microstructure with silica between the zirconia grains. Depletion of SiC from the virgin material under the zirconia scale has also been observed and reported. While these features have been frequently observed, the mechanisms which form this complex scale are not understood in detail [1-2]. The interpretation of this complex oxide scale presents several puzzles. Zirconia appears often as a columnar subscale and as a non-columnar phase in the silica layer. Depletion of SiC underneath the zirconia scale suggests formation of SiO_2 liquid or SiO vapor under the zirconia, but most of the silica is found over the zirconia. Boron oxide (B_2O_3) is largely absent, due to evaporation at higher temperatures.

In previous chapters liquid flow of boria-silica-zirconia (BSZ) liquids is proposed to play an important role in the formation of these scales, based on distinctive microstructural features observed on the external oxide surface and in cross-section, illustrated schematically in Figure 7.1. These features, introduced as convection cells in earlier chapters, have not been discussed before in the literature. Close examination of cross-sectional micrographs from the literature suggest that they might have been observed, but not interpreted. In this chapter, interpretation of these oxide scale features on ZrB_2- and HfB_2-SiC composites and their possible significance will be discussed and analyzed.

2.0 Interpretation of Oxide Scale Features as Convection Cells

Figure 7.2 shows a backscattering electron (BSE) image of a surface of a ZrB_2-15vol%SiC-2vol%$MoSi_2$ specimen tested in a high-temperature box furnace (SentroTech Corporation, Berea, OH, USA) at 1600ºC for 30 min. The image shows how the surface is covered with convection cell pattern. The convection cells have ZrO_2 cores (or "islands") (white area) located in larger SiO_2 rich cells (grey area) with B_2O_3 rich patterns (dark contrast) surrounding the cores. The area around the convection cells consists of a SiO_2 rich glass (grey region) with small micron sized zirconia dispersoids (white dots). The B_2O_3 flower-like patterns are visible in backscattered electron images (BSE), but in stronger contrast when imaged by cathodoluminesence (CAL). The ZrO_2 cores are proposed in earlier chapters to have formed by precipitation during the evaporation of Boria (B_2O_3) from a boria-silica-zirconia (BSZ) liquid that rises through the outer SiO_2 rich borosilicate layer and flows laterally by viscous fingering forming the Boria rich regions around the ZrO_2 cores[3-4]. The driving force is proposed to be the large volume increase upon oxidation of the bulk material due to the formation of solid ZrO_2(s) and BSZ liquid[3]. The large volume increase can induce pressure and stresses when the oxide scale grows leading to a rupture in the "premature" (thin outer SiO_2-rich borosilicate layer and underlying ZrO_2) oxide scale, this is described in more detail in Chapter 4. As mentioned in Chapter 5 we make a distinction between the zirconia formed during oxidation; the "primary" zirconia, formed by the oxidation of ZrB_2 by oxygen diffusion through the SiO_2-rich borosilicate premature surface layer; and the "secondary" zirconia precipitated from the BSZ liquid. When the premature oxide scale ruptures the BSZ liquid flows to the external surface, the B_2O_3 starts evaporating and a secondary zirconia starts to precipitate, covering the surface with silica rich liquid and secondary zirconia near the site of B_2O_3 evaporation. The secondary zirconia precipitates can either remain at the location where they formed (the ZrO_2 islands), or be carried as dispersed particles by the flowing liquid, where they serve as remnant markers of the flow pattern in the SiO_2 rich glass after the liquid cools down.

The following images support the hypothesis of the large volume increase as the driving force for the liquid flow. Figure 7.3 shows a backscattering electron (BSE) image of a cross-section of a ZrB_2-15vol%SiC-2vol%$MoSi_2$ specimen showing deformations of the grown oxide scale due to the large volume increase. The specimen was tested at 1550ºC for 3 hrs. in a tube-furnace (Lindberg, Watertown, WI, USA) in ambient air, with a heating rate of 13ºC/min. and free cooling. The silica outer scale appears in the BSE image in darker contrast, while the zirconia subscale is in brighter contrast. The contrast between ZrO_2 and ZrB_2 is slight in this image. The higher magnifications, Fig. 7.3(b) and (c), show that the ZrO_2 scale is deformed; it appears to be lifted up, like a blister. Inside the blister is a glassy phase shown by EPMA maps and analysis to be rich in boria (B_2O_3), silica (SiO_2), and with some zirconia (ZrO_2). Figure 7.4(a)-(f) shows a BSE image of one of the deformations shown in Figure 7.3(a) and the corresponding EPMA maps of this area, showing the distribution of boron (B), silicon (Si), oxygen (O), molybdenum (Mo), and zirconium (Zr). Figure 7.5 shows the corresponding line analysis from these elemental maps, indicating that the glass inside the “blister” is rich in B_2O_3, and SiO_2, and has some ZrO_2. Based on the ternary phase diagram provided by our collaborator A.N. Grundy [4] (Figure 5.9 in Chapter 5), we presume this material is the glass formed by cooling of the BSZ liquid in equilibrium with $ZrO_2(s)$ at this temperature, where the BSZ liquid composition is; 71 mole% boria; 18 mole% silica; and 11 mole% zirconia. Similar oxide scales features of the same specimen are seen in Figure 7.6.

Figure 7.7 shows a secondary electron image of a polished cross-section of a convection cell (same area as shown in BSE images in Chapter 4 (Fig. 4.4) and 5 (Fig. 5.7)). The sample was oxidized for 4 hours at 1550ºC in a tube-furnace (Lindberg, Watertown, WI, USA) in ambient air, with a heating rate of 13ºC/min. and free cooling. The image shows the silica rich external scale, in dark grey contrast, covering a zirconia subscale (primary ZrO_2) in light grey contrast, over the un-oxidized ZrB_2-SiC substrate. The zirconia “island” impinging on the surface (secondary ZrO_2) is seen in cross-section to be a vertical feature containing region of glass in the middle which is shown by EPMA (see Figure 5.7 in Chapter 5). The glass contains B_2O_3, SiO_2 and perhaps some ZrO_2, it is also richer in boron (B) than the glass outside of the ZrO_2 “island”, suggesting this to be the glass of the B_2O_3 -rich BSZ liquid. Note the difference in the morphology of the primary zirconia in the inner scale from the secondary zirconia forming the ZrO_2 “island”. Note also that the interface between the primary zirconia scale and the unoxidized ZrB_2 –SiC substrate extends about 100 μm beneath the surface under the ZrO_2

"island" (the center of the convection cell) but only about 50 μm away from the center of the convection cell. Apparently this increased recession of the ZrB_2 –SiC substrate denotes faster oxidation at this location.

When interpreting the cross-sectional images of the deformations shown in Figure 7.3 one needs to consider that since the location of the plane-of-polish is not known, it is hard to infer if the features seen differ because of their location, or if they differ because they have not developed (immature or "before eruption") or have stopped operating ("extinct"). Figure 7.8 is an illustration of a convection cell intersected by several planes of cross-section for polish. Line "a" in Figure 7.8 intersects the center of a BSZ liquid pipe. This can create an image similar to Figure 7.7. If the plane of polish intersects the side of a convection cell (through a ZrO_2 "island" filled with liquid) i.e. line "b", it could create an image similar to Figure 7.3(c), while a plane of polish more remote from the pipe (line "c") could create an image similar to Figure 7.3(b).

3.0 Comparison with Literature

Microstructural features closely resembling the convection cells have been reported earlier in the literature but not interpreted as of any significance. Figure 7.9 compares previously published images of specimens tested at CNR-ISTEC with a specimen tested at University of Michigan (UM). Cross-sections of HfB_2-SiC-HfN and ZrB_2-HfB_2-SiC-HfN composites tested at 1450ºC for 20 hrs by Monteverde[5] at CNR-ISTEC are shown in Figure 7.9(a) and (b). The images show vertical zirconia features on top of an enhanced oxidation zone (increased thickness of ZrO_2 layer). Figure 7.9(c) shows a ZrB_2-15vol%SiC-2vol%$MoSi_2$ composite fabricated at CNR-ISTEC and oxidized at 1550ºC for 2 hrs at UM. The cross-sections shown in Figure 7.9 (a) and (b) closely resemble the cross-section of the convection cell shown in Figure 7.9 (c). Note the similarity in the morphology of the vertical zirconia feature of the specimens tested at CNR-ISTEC to the morphology of the ZrO_2 "island" of the specimen tested at UM (indicated by a arrow in Fig. 7.9). Also, all three specimens shown in Figure 7.9 have thicker ZrO_2 layer (enhanced oxidation zone) under the vertical ZrO_2 features. The similarity of these images indicate that the convection cells are seen in other boride-silicon carbide materials such as these $Hf(Zr)B_2$-SiC-HfN composites which have a different relative amount of in $Hf(Zr)O_2$, SiO_2, and B_2O_3 after oxidation.

Figure 7.10(a) shows similar features for a ZrB_2-30vol%SiC composite oxidized for 30 minutes at 1400ºC by Rezaie et al[6] at the University of Missouri-Rolla (UMR) previously reported in the literature. Figure 7.10(b) shows a cross-section of a ZrB_2-15vol%SiC-2vol%$MoSi_2$ composite (fabricated at CNR-ISTEC) tested for 1 hour at 1550^{o}C at UM. The cross-sections have very similar microstructural features; enhanced oxidation zone (thicker ZrO_2 layer) under a vertical zirconia feature. This indicates that convection cells were formed on the ZrB_2-30vol%SiC composite during oxidation. Figure 7.11 (a) shows a micrograph of the surface of the ZrB_2-SiC-$MoSi_2$ specimen tested for 1 hour at 1550^{o}C at UM. The image shows how the convection cells are spread over the surface, forming a pattern with small micron sized ZrO_2 particles located between the boundaries of the cells. Figure 7.11(b) shows the flow pattern of the zirconia particles in more detail. No micrographs of the surfaces of the specimens tested at CNR-ISTEC or UMR were reported, thus comparison of the surfaces to the UM specimen could not be done.

The features shown in previously published micrographs from CNR-ISTEC and UMR are suggested here to be in fact convection cells. These findings indicate that the convection cells do exist for other oxidized boride-silicon carbide materials but have not been brought to attention in the literature or interpreted as of significance for the oxidation behavior of these materials.

4.0 Discussion

4.1 Detection of Convection Cells

After finding microstructural features, in previous published micrographs of diboride-silicon carbide based composites, which closely resemble the features of our proposed convection cells the question arose; why were they not interpreted before as a significant part in the oxidation behavior of these materials? A possible reason could be that little attention has been devoted to analyzing the oxide surface. Generally when oxidation behavior of these materials are characterized the main emphasize is in measuring the thickness of the oxide scale formed and recording mass change with time. Also, the structure and the chemical composition of the oxide scale are usually analyzed in detail, but mainly in cross-section. Additionally, the cross-sections of the specimens are often mounted so the fragile oxide scale can be preserved. The surface after the mounting is then not accessible. This makes any connection of the cross-sectional features of the specimen to surface features difficult to comprehend. The large contrast between the ZrO_2, B_2O_3 and SiO_2 rich regions shown in Figure 7.2 can be obtained with backscattering electrons (BSE) and cathodoluminscence (CL) imaging modes which makes the detection of the convection cells easy during microstructural analysis. The secondary electron (SE) imaging mode commonly used in microstructural analysis does on the other hand not reveal the contrast of B_2O_3 region from SiO_2 rich regions. If that is the only imaging mode used then the detection of the convection cells becomes harder.

The convection cells have perhaps also not been reported earlier due the low probability of seeing them in cross-sections (cutting through them), especially if they are sparsely distributed. If we look at the cross-section of the emergent ZrO_2 "island" in the middle of the convection cell shown in Figure 7.7 we see that the ZrO_2 "island" is around 50 μm while the inner BSZ liquid "pipe" is only about 10 μm in diameter. During cross-section there will be a low probability of cutting through the BSZ liquid "pipe" due to the small size of the pipe. For example for a specimen tested at 1550ºC for 1 hr the average number of cells per square mm is 18 (quantification explained in Chapter 8), then for a top surface of 25 mm^2 and cylindrical shaped pipe only 0.14% of the total surface area will be covered with pipes. Here it has been assumed that all convection cells have pipes through them at the same time, which would not be the case if the transport of the BSZ liquid is episodic, as discussed in Chapter 8, thus it gives the upper limit of the probability of cutting through a pipe. This indicates that the pipes would then rarely (if ever) been observed in cross-sectional analysis so it could be easy to miss them.

4.2 Enhanced Oxidation Region

Now let us direct our attention to the local regions of enhances oxidation shown in Figure 7.7, 7.9 and 7.10. These are the areas with more diboride recession (deeper) and thicker oxide scales (thicker ZrO_2 layer) under the convection cell features. Why do these form? Our hypothesis is based on inward diffusion of oxygen. Let us assume that the rate of diboride oxidation is limited by inward oxygen transport as has been reported previously in the UHTC literature [6-8]. Areas of greater recession demand greater inward oxygen diffusion to leave a thicker scale. The driving force is similar, so the oxygen diffusivity must be locally higher. Here we can invoke the Stokes-Einstein relation[9] between diffusivity and viscosity, derived from studies of the Brownian motion of a solid sphere suspended in a fluid, where the particle's diffusivity is inversely proportional to the fluid viscosity i.e. $D \sim 1/\eta$, more specifically [9-11]:

$$D = \frac{k_B T}{6\pi\eta\ r} \tag{7.1}$$

where D is the diffusion coefficient, k_B is the Boltzmann constant, r is the radius of the slowest particle moving through the fluid (the hydrodynamic radius), and T is the absolute temperature. Another similar equation based on the theory of absolute reaction rates by Eyring[12] (1936) is sometimes preferred for silicate glasses to relate melt viscosities to the diffusion coefficients of oxygen in molten silicates [10, 12-13]:

$$D = \frac{k_B T}{\lambda\eta} \tag{7.2}$$

where λ is the mean jump distance of the diffusing particle (O^{-2}).

In the silica-rich scale, the viscosity at oxidation temperatures of 1500ºC is on the order of 10^{11} Poise (10^{10} Pa-s) [7]. With the presumed composition of BSZ liquid, we have estimated[a] based on limited data in the literature that the viscosity will be about 10^4 Poise (10^3 Pa-sec) [14-15]; this is a large viscosity difference, by about factor of 10^7. This implies that in the local regions of the BSZ liquid pipes, the diffusivity for inward diffusion of oxygen must be larger by a similar factor, about 10^7 times faster oxygen transport than in the silica scale remote from the pipe. When the convection cell forms (the deformation erupts) outward flow of material of low viscosity (BSZ liquid) occurs and a localized inward path for oxygen will be created. We illustrate this with Figure 7.12, a schematic of the synergy between oxygen transport in and liquid transport out, indicating increased oxygen diffusion inward in the BSE pipe (thick white arrow). Thus we expect a complex coupling of these phenomena.

Oxygen can diffuse through amorphous SiO_2 via two mechanisms: (1) so called network oxygen ions can diffuse through the SiO_4 tetrahedral network, and (2) interstitial (nominally molecular) oxygen can diffuse through the free volume of the silicate structure[16]. For the network oxygen ion diffusion the Eyring can be used to estimate the oxygen diffusion coefficient by using λ as the mean jump distance of the diffusing particle (O^{-2}) [10, 12-13]. The diffusion coefficient of interstitial oxygen diffusion (molecular) can be estimated by using the Stokes-Einstein relation with r (hydrodynamic radius) substituted by the O_2 bond length (1.21Å) [17]. The two mechanisms can operate simultaneously and most likely have different temperature dependencies. Thus oxidation at different temperatures could be governed by either mechanism[16]. The question of whether oxygen diffuses through silica as a molecule or ionically or perhaps both remains unclear, which has led to a broad range of reported diffusion coefficients [10-11, 13, 16-23].

Figure 7.13 shows the calculated diffusion coefficient of oxygen in a borosilicate melt vs. the viscosity, calculated with the Stokes-Einstein relation and the Eyring

---

[a] The viscosity of the borosilicate melt was estimated from a relationship extrapolated from data by Jabra et al. [14] introduced in Chapter 5.

equation. For the Stokes-Einstein relation the following parameter were used; T = 1550ºC, and r = 1.21 nm (where the O_2 bond length is used for the hydrodynamic radius of O_2[17]) and viscosity values are estimated by relationship extrapolated from data by Jabra et al. [14] (explained in detail in Chapter 5). The same viscosity values were used for the Eyring equation as well as T = 1550ºC, and λ = 0.159 nm, which is the Si-O distance in silica glass[13]. The diffusion coefficients calculated by the two equations differ on the order of about one magnitude. The difference is not large compared to the wide range of values reported in literature, also these values are comparable to measured and calculated values previously reported [10-11, 13, 16-24].

Figure 7.14 shows the diffusion coefficient of oxygen in a borosilicate melt vs. mol% of SiO_2 estimated by using the Stokes-Einstein relation with T = 1550ºC, r = 0.121 nm, and viscosity values estimated from data by Jabra et al.[14]. Figure 7.14 shows how the inward oxygen diffusion decreases with an increase in SiO_2 mol% in a B_2O_3-SiO_2 melt. This is indicated by the low diffusion coefficient of oxygen for a pure SiO_2 melt (100 mol% SiO_2; $D = 1.1 \cdot 10^{-21}\ m^2s^{-1}$) compared to a B_2O_3-rich melt (79 mol% B_2O_3-21mol% SiO_2; $D = 1.7 \cdot 10^{-14}\ m^2s^{-1}$); which is 10^7 times larger, as estimated from the large viscosity difference mentioned above. The calculated diffusion coefficients of oxygen in borosilicate melts (Figure 7.14) is smaller than the diffusion coefficient for oxygen in ZrO_2 (~$10^{-10}\ m^2 \cdot s^{-1}$ at 1500ºC) reported by Fox et al.[23] supporting our previous assumption that the borosilicate outer layer is the oxygen diffusion barrier (the rate controlling factor) during oxidation at these temperatures.

The local enhanced oxidation regions under the convection cells makes the oxidation of diboride-SiC composites at these temperatures a non-uniform process at a microscopic scale. Observations of apparently uniform oxidation behavior reported in the literature could result from the fine scale of the local events. Just like an intergranular corrosion may be quite homogenous on the macroscopic scale, it is though localized on a microscopic scale[25]. Perhaps in the early state of the oxidation uniform oxygen diffusion generates a pool of BSZ liquid. When the volume of the liquid and the pressure (by Pillings-Bedworth ratio) reaches a critical amount, it erupts. While it is erupting, oxygen can diffuse in by the same path, so it oxidizes faster under a cell creating the enhanced oxidation zone.

5.0 Summary

Oxide scale features previously published in the literature on ZrB_2- and HfB_2-SiC composites are suggested here to be in fact the proposed convection cells reported for the first time by the author and her associates[3]. These features are of great significance contributing to the formation of complex oxide scales of these materials. The flow of a B_2O_3 rich BSZ liquid to the surface, with the subsequent loss of B_2O_3 to evaporation, explains the formation of a glassy SiO_2 rich layer on the surface commonly reported in the literature. Also the outward flow of the BSZ liquid creates a localized inward path for oxygen due to lower viscosity that allows faster oxidation under the convection cell. The formation of a convection cell (eruption of the “premature” scale) creates a leak in the silica barrier, but the BSZ liquid eventually replenishes the silica scale, patching the leak creating a positive feedback.

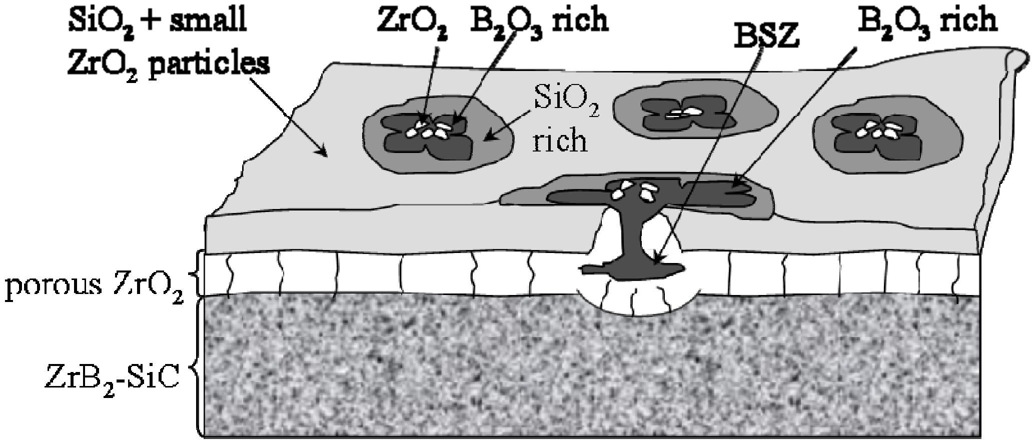

Figure 7.1: Schematic showing the features seen on surfaces and cross-sections of ZrB_2-SiC composites tested at temperatures between 1500-1600ºC showing the surface covered with cells that have ZrO_2 cores (white) located in larger SiO_2 cells (grey) with B_2O_3 rich patterns (black) surrounding the cores.

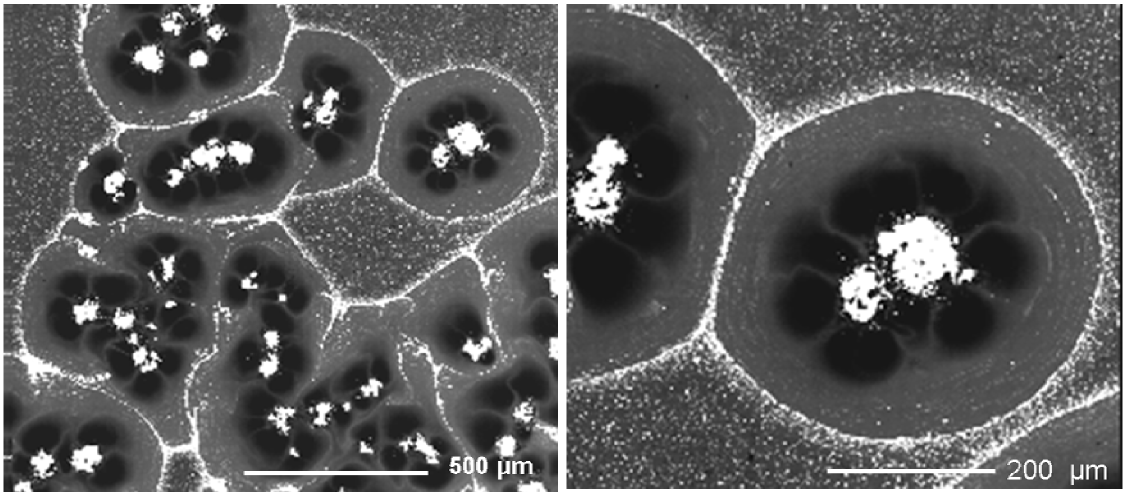

Figure 7.2: BSE images of the surface of a ZrB_2-15vol%SiC composite tested at 1600ºC for 30 min. (Left) showing the surface covered with convection cells that have ZrO_2 cores (white) located in larger SiO_2 cells (grey) with B_2O_3 rich patterns (black) surrounding the cores. (Right) Higher magnification of the convection cell.

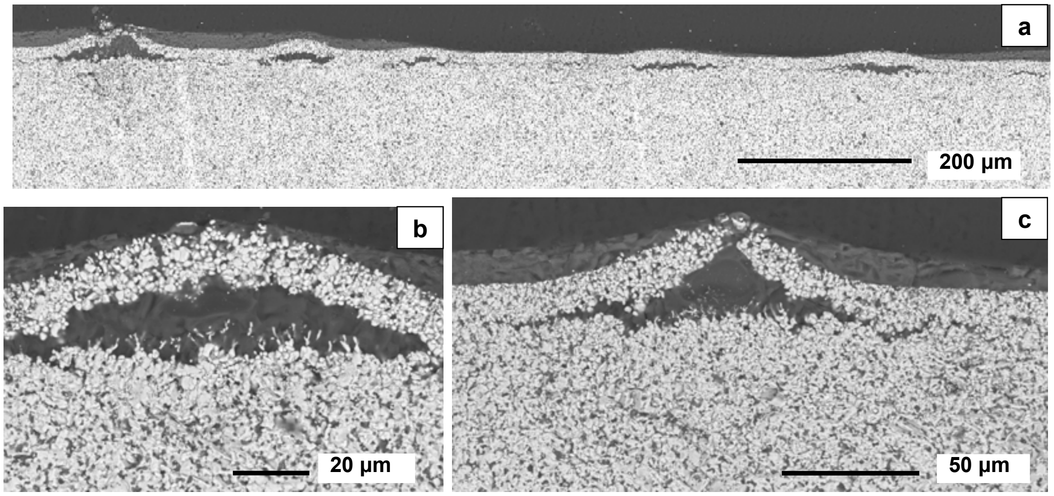

Figure 7.3: BSE images of cross-sections of a ZrB_2-15vol%SiC-2vol%$MoSi_2$ composite tested at 1550ºC, showing the built up of the BSZ liquid between the "premature" oxide scale (SiO_2 rich top layer and an under laying ZrO_2) and the bulk material .

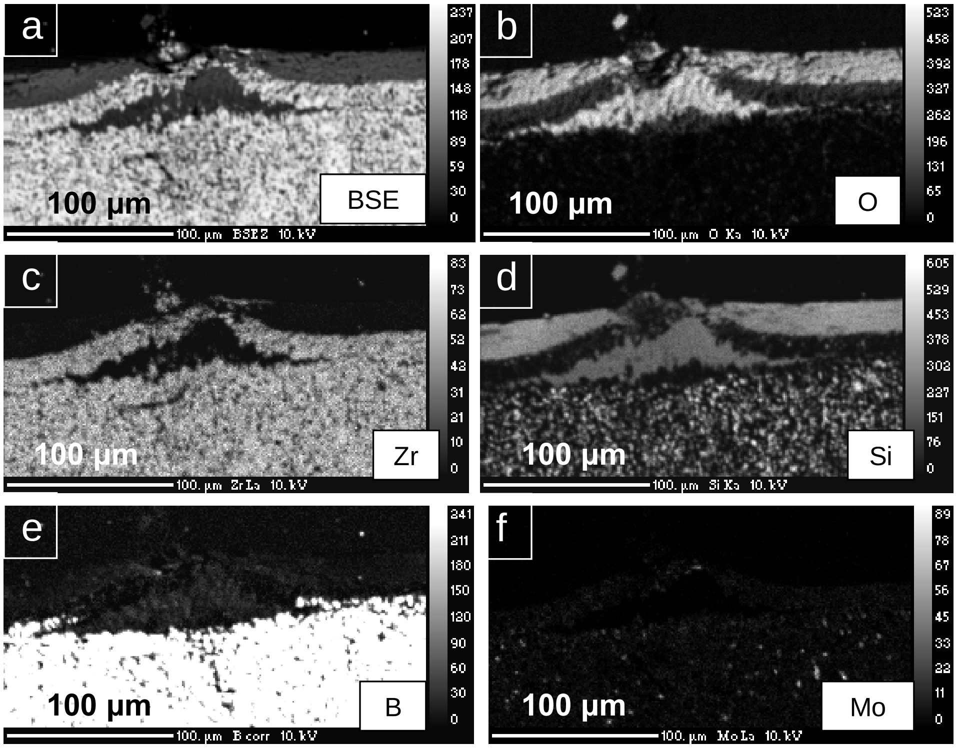

Figure 7.4: (a) BSE image of a deformation with glass inside located in the cross-section of the ZrB_2-SiC-$MoSi_2$ composite tested at 1550ºC for 3 hrs (b)-(f) The corresponding EPMA maps indicate the SiO_2 rich surface layer and the underlying ZrO_2 layer as well as the composition of the BSE glass inside the deformation.

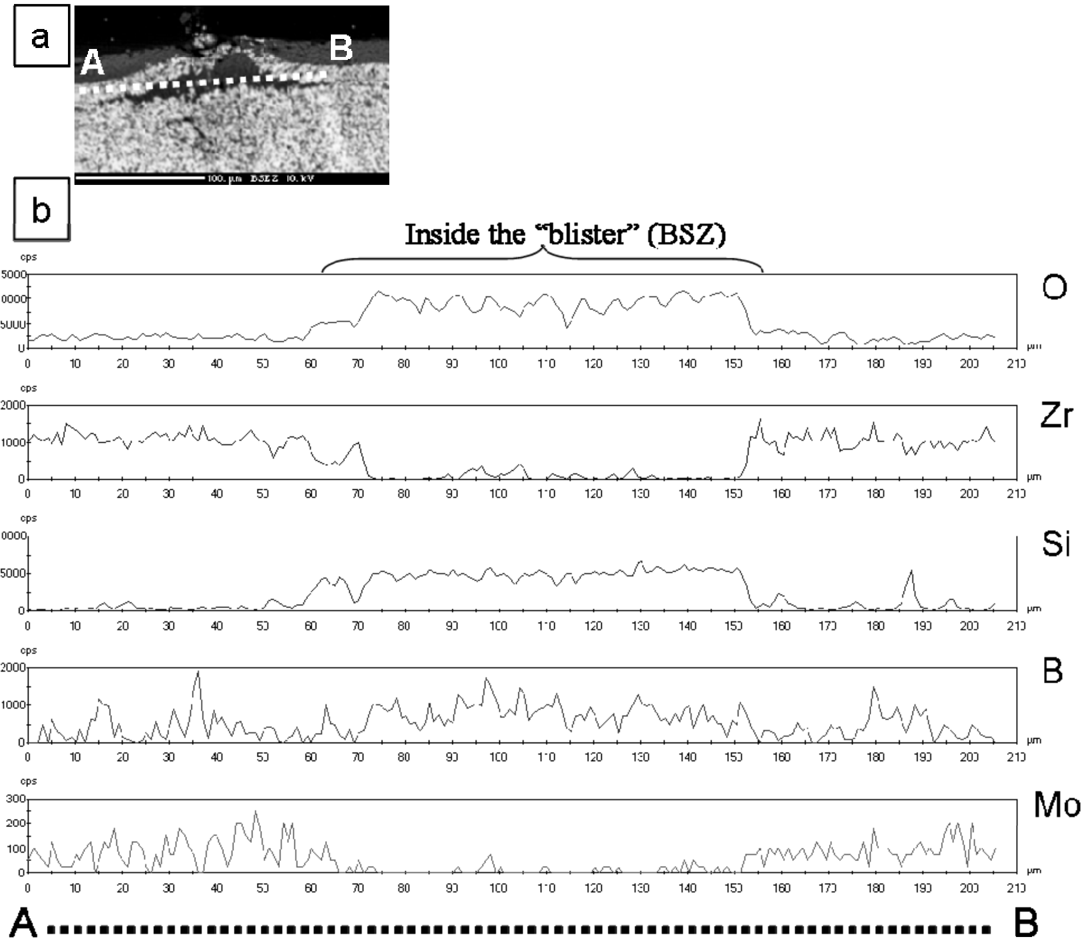

Figure 7.5: (a) BSE image of a cross-section of a cell on surface of a ZrB_2-15vol%SiC composite tested at 1550°C for 3 hrs. The red line through the "blister" (deformation) indicates where the EPMA line analyzes were done, the letter A indicates the start of the line scan and B the end (b) graphs of the recorded intensity ((Cps) counts per second) vs. distance (µm) of the line scan.

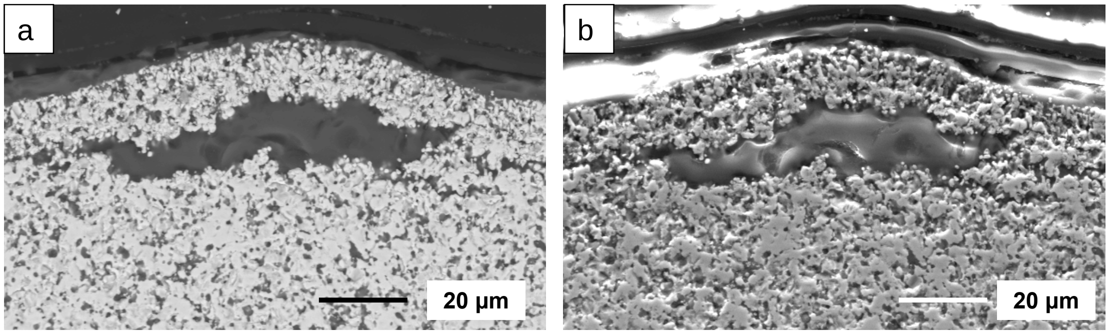

Figure 7.6: (a) BSE and (b) SEM images of a cross-section of a ZrB_2-SiC-$MoSi_2$ composite tested at 1550°C for 3 hrs, showing the built up of the BSZ liquid between the "premature" oxide scale (SiO_2 rich top layer and an under laying ZrO_2) and the bulk material.

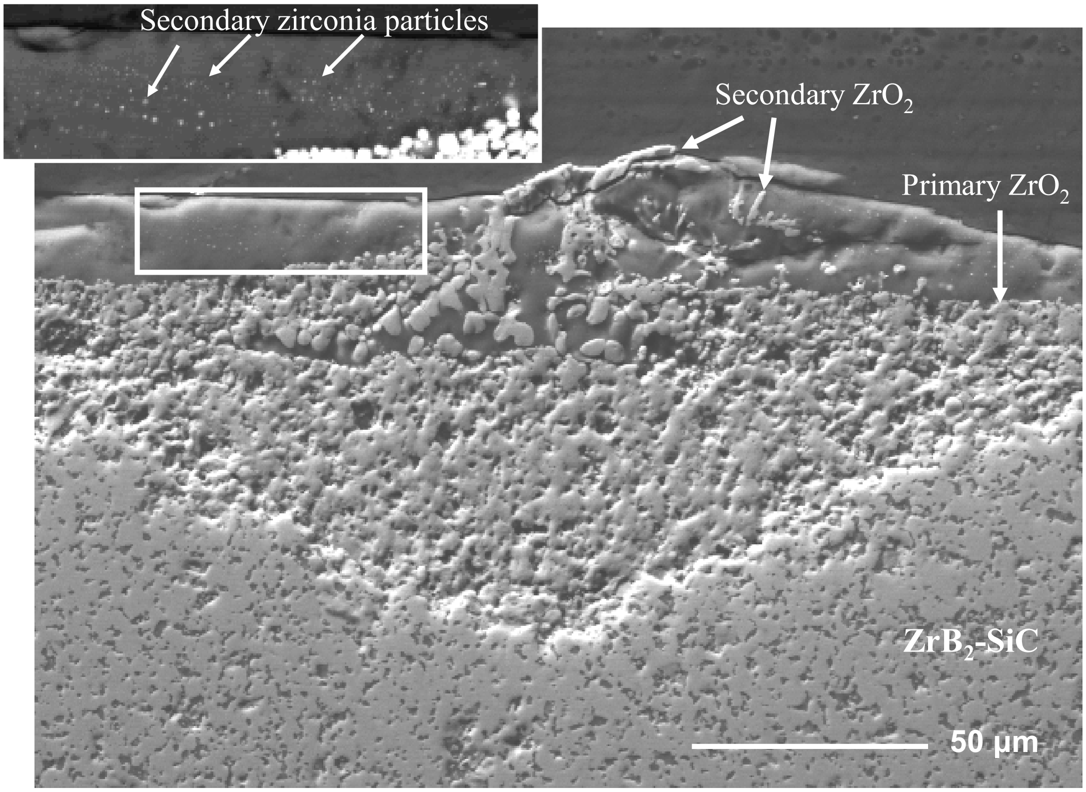

Figure 7.7: SEM image of a cross-section of a convection cell; ZrB_2-15vol%SiC composite tested at 1550ºC for 4 hrs, showing the inner structure of a convection cell.

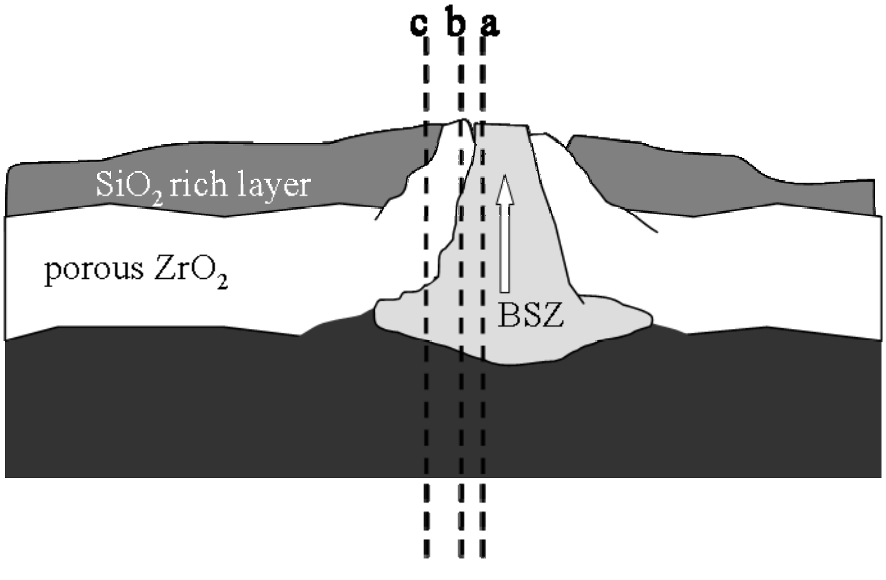

Figure 7.8: Schematic showing different planes of cross-sections possibly through a convection cell, showing the inner structure of the cell.

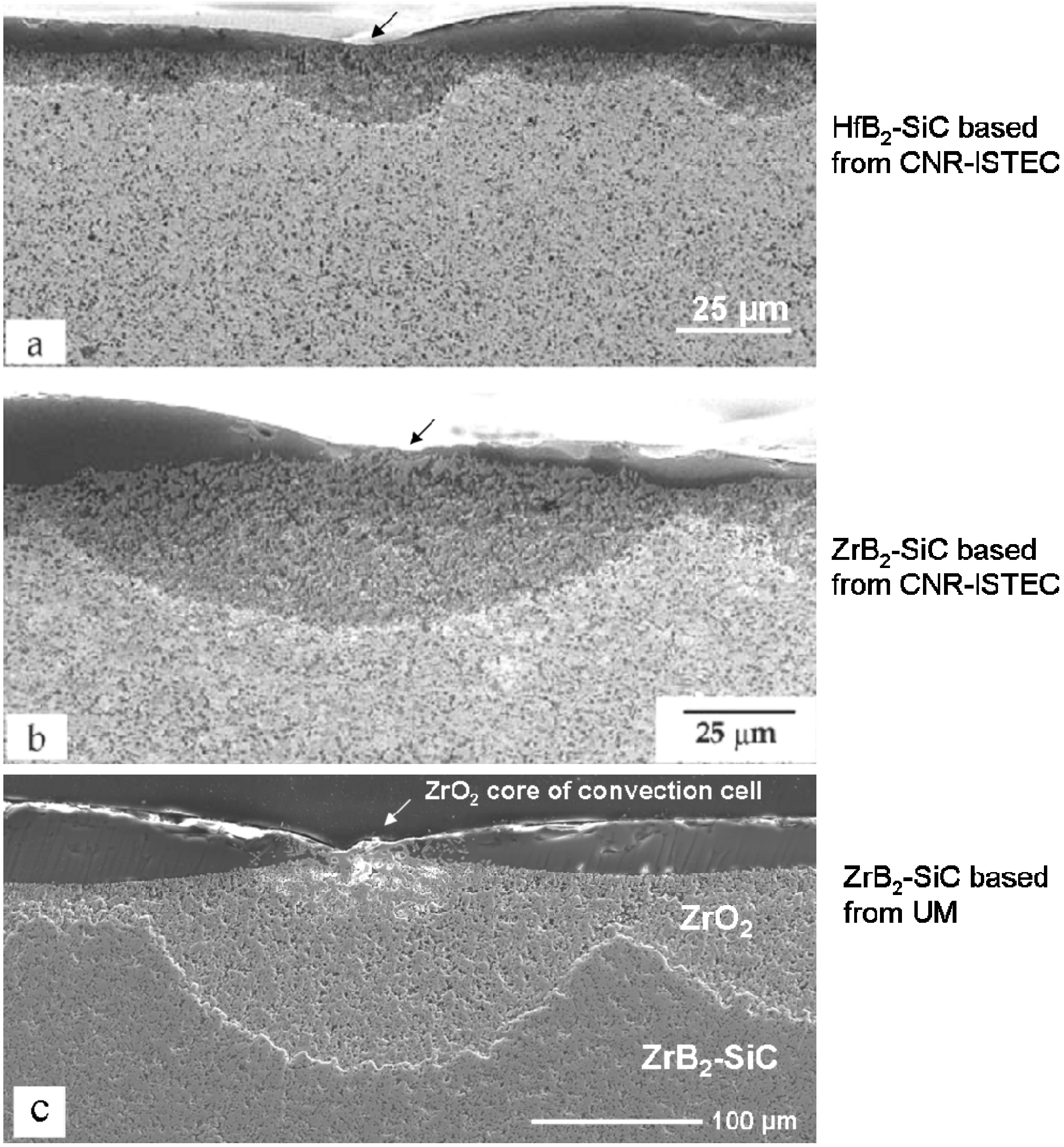

Figure 7.9: SEM images of the cross-sections of diboride/silicon carbide composites. (a) HfB_2-SiC-HfN and (b) ZrB_2-HfB_2-SiC-HfN composites tested at 1450°C for 20 hrs by Monteverde[5] and (c) a ZrB_2-SiC-$MoSi_2$ composite tested at 1550°C for 2 hrs.

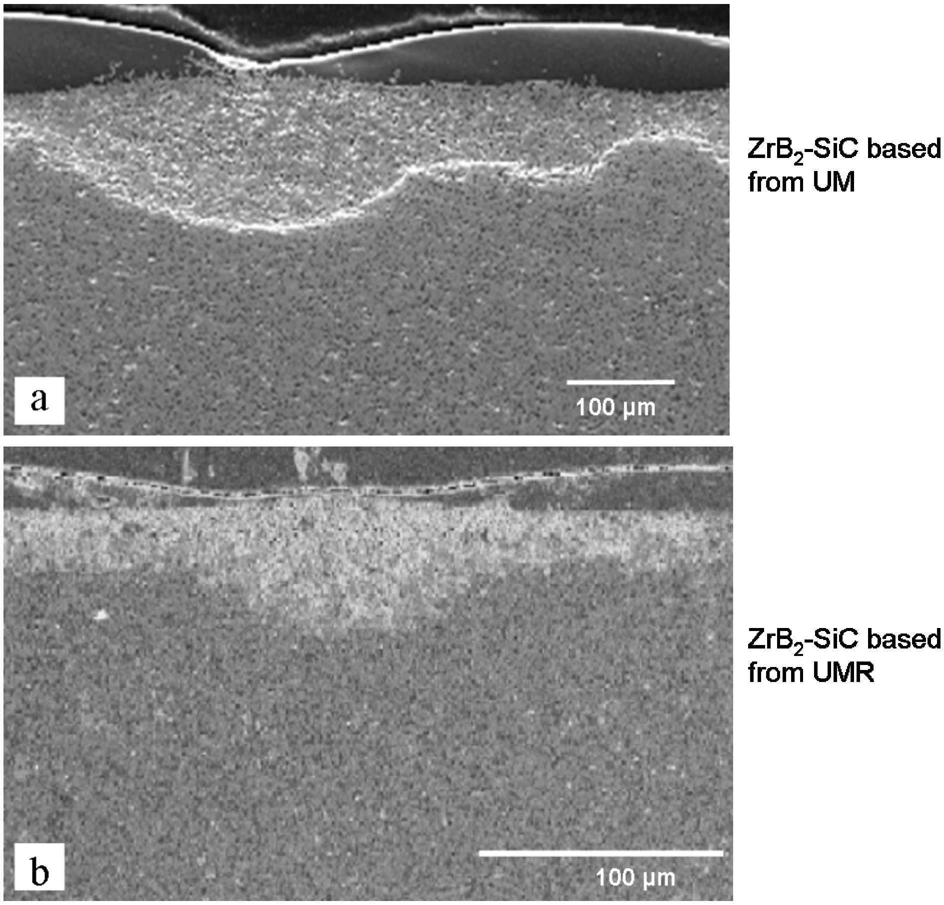

Figure 7.10: Cross-sections of ZrB_2-SiC composites (a) ZrB_2-SiC-$MoSi_2$ tested at 1550ºC for 1 hr and (b) ZrB_2-30vol%SiC tested at 1400ºC for 30 min by Rezaie et al [6].

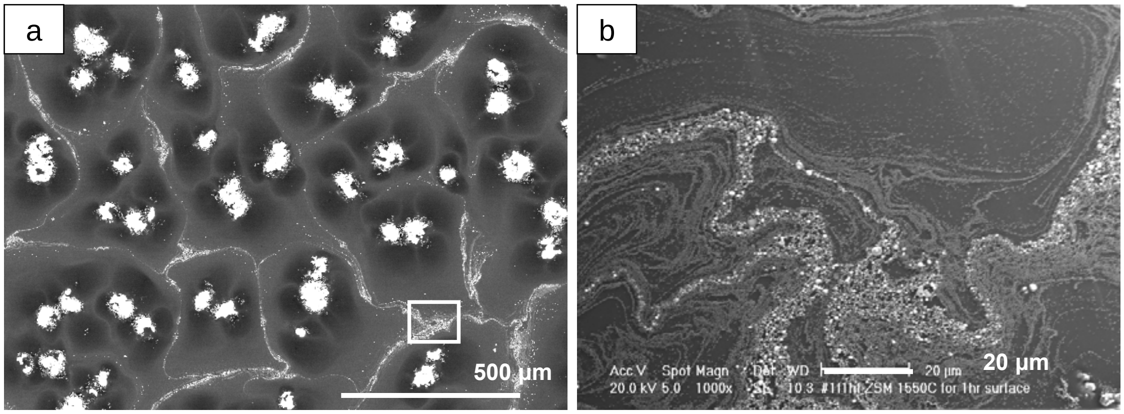

Figure 7.11: BSE images of the surface of a ZrB_2-SiC-$MoSi_2$ composite tested at 1550ºC for 1 hr (a) low magnification (b) high magnification of the area inside the white box in (a).

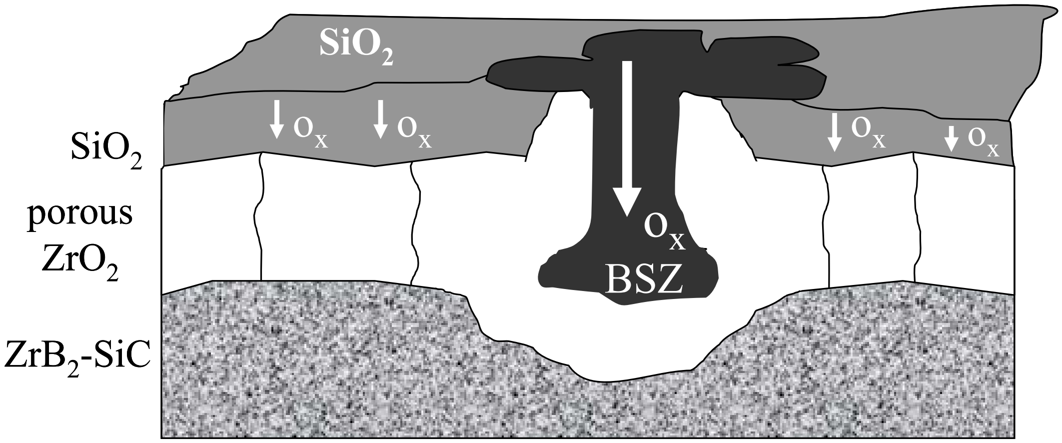

Figure 7.12: Schematic of the inward diffusion of oxygen through the cross-section of an oxide scale, showing the inner structure of a convection cell. The thick arrow through the BSZ pipe represents the increased oxygen diffusion rate through the pipe compared to the diffusion through the SiO_2 rich outer scale.

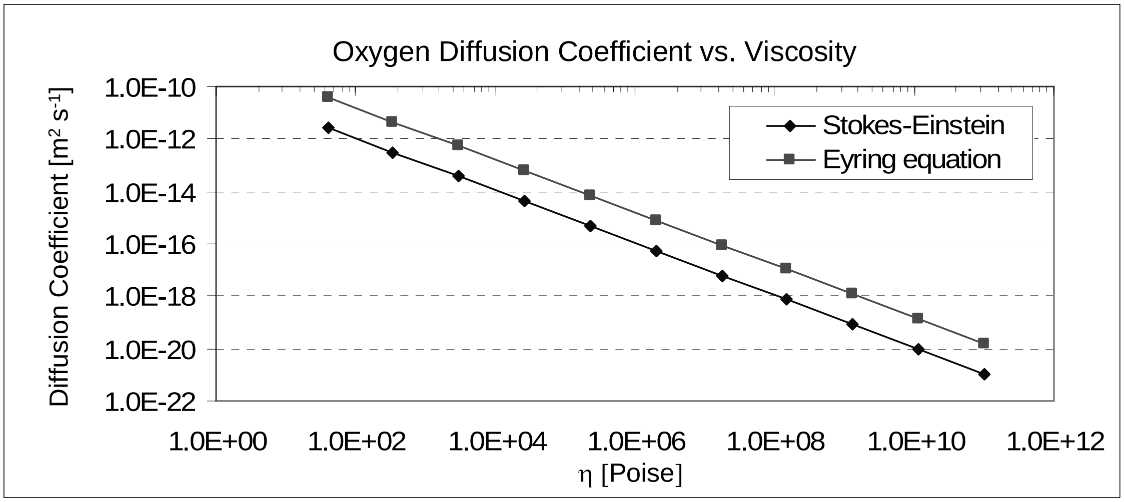

Figure 7.13: Diffusion coefficient of oxygen in a B_2O_3-SiO_2 melt at 1550ºC calculated by using the Stokes-Einstein relation (diamonds) and the Eyring equation (squares) vs. the shear viscosity (logarithmic scale).

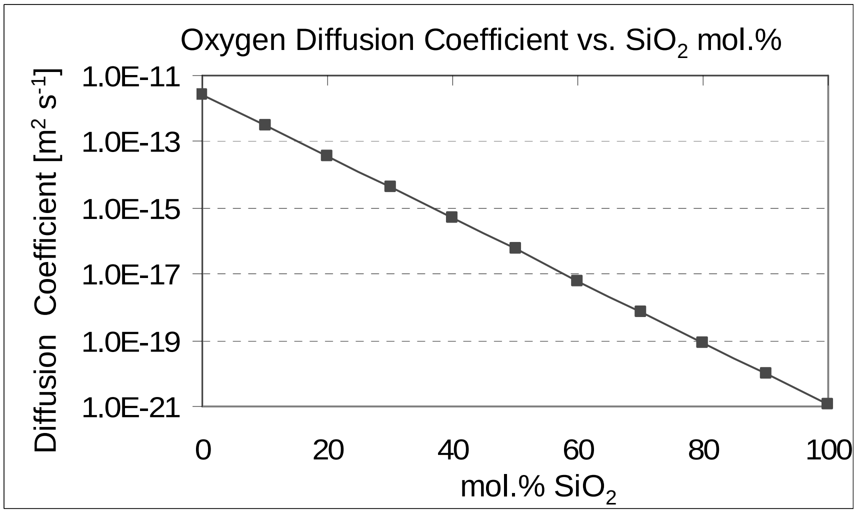

Figure 7.14: Diffusion coefficient of oxygen in a B_2O_3-SiO_2 melt vs. SiO_2 mol% calculated using the Stokes-Einstein relation.

Reference

[1] M. M. Opeka, I.G. Talmy, and J.A. Zaykoski, "Oxidation-Based Materials Selection for 2000ºC + Hypersonic Aerosurface: Theoretical Considerations and Historical Experience," J. of Mater. Sci., 39 [19] 5887-5904 (2004).

[2] A. Bongiorno, C.J. Först, R.K. Kalia, J. Li, J. Marschall, A. Nakano, M.M. Opeka, I.G. Talmy, P. Vashishta, and S. Yip. "A Perspective on Modeling Material in Extreme Environments: Oxidation of Ultra-High Temperature Ceramics." Materials Research Society Bulletin, 31 410-418 (2006).

[3] S.N. Karlsdottir, J. W. Halloran, and C.E. Henderson, "Convection patterns in liquid oxide films on zirconium diboride-silicon carbide composites oxidized at high temperature," Journal of American Ceramic Society, 90 [9] 2863-2867 (2007).

[4] S.N. Karlsdottir, J.W. Halloran, and A.N. Grundy, "Zirconia Transport by Liquid Convection during Oxidation of Zirconium Diboride-Silicon Carbide" (accepted by J. Am. Ceram. Soc., July 2007).

[5] F. Monteverde, "The Thermal Stability in Air of Hot Pressed Diboride Matrix Composites for Uses at Ultra-High Temperatures," Corrosion Science 47 2020-2033 (2005).

[6] A. Rezaie, W.G. Fahrenholtz, and G.E. Hilmas. "Evolution of structure during the oxidation of zirconium diboride–silicon carbide in air up to 1500ºC,"Journal of the European Ceramic Society, 27 [6] 2495-2501 (2007).

[7] F. Monteverde and A. Bellosi. "Oxidation of ZrB_2-Based Ceramics in Dry Air," Journal of the Electrochemical Society, 150 [11] B-552-B559 (2003).

[8] F. Monteverde, "Beneficial Effects of an Ultra-fine α-SiC Incorporation on the Sinterability and Mechanical Properties of ZrB_2," Appl. Phys. A, 82 329-337 (2006).

[9] A. Einstein, Investigations on the Theory of the Brownian Movement, reprinted by Dover Publications, New York. (1926).

[10] Y. Liang, F.M. Richter, A.M. Davis, and E.B. Watson, "Diffusion in Silicate Melts: I. Self Diffusion in CaO-Al_2O_3-SiO_2 at 1500ºC and 1 GPa," Geochimica et Cosmochimica Acta, Vol. 60, No. 22 4353-4367 (1996).

[11] E.M. Tanguep Njiokep, and H. Mehrer. “Diffusion of ^{22}Na and ^{45}Ca in Ionic Conduction in Two Standard Soda-Lime Glasses,” Solid State Ionics, 177 2839-2844 (2006).

[12] H. Eyring. “Viscosity, Plasticity, and Diffusion as examples of Absolute Reaction Rates,” J. Chem. Phys. 4 [4] 283-291 (1936).

[13] M.L. Ferreira Nascimento, and E.D. Zanotto. “Mechanisms and Dynamics of Crystal Growth, Viscous Flow, and Self-Diffusion in Silica Glass,” Physical Review, B 73 024209 (2006).

[14] R. Jabra, J. Phalippau, and J. Zarzicki, “Synthesis of binary glass-forming oxide glasses by hot-pressing” J. Non-crystalline Solids, 42 pp. 489-498 (1980).

[15] P.C. Setze, “A Review of the Physical and Thermodynamic Properties of Boric Oxide,” Lewis Flight Propulsion Laboratory, Cleveland, OH. NACA-RM-E57B14, April 24, (1957).

[16] C.E. Ramberg and W.L. Worrell. “Oxygen Transport in Silica at High Temperatures: Implications of Oxidation Kinetics,” J. Am. Ceram. Soc., 84 [11] 2607-2616 (2001).

[17] J. Read, K. Mutolo, M. Ervin, W. Behl, J. Wolfenstine, A. Driedger, and D. Foster. “Oxygen Transport Properties of Organic Electrolytes and Performance of Lithium/Oxygen Battery,” Journal of The Electrochemical Society, 150 [10] A1351-A1356 (2003).

[18] R.H. Doremus. “Transport of Oxygen in Silicate Glasses,” Journal of Non-Crystalline Solids, 349 242-247 (2004).

[19] Y. Zhang, E.M. Stolper, and G.J. Wasserburg. “Diffusion of a Multi-Species Component and its Role in Oxygen and Water Transport in Silicates,” Earth and Planetary Science Letters, 103 228-240 (1991).

[20] E.L. Williams. “Diffusion of Oxygen in Fused Silica,” Journal of the American Ceramic Society, 48 [4] 190-194 (1965).

[21] D. Tinker, C.E. Lesher, and I.D. Hutcheon. “Self-Diffusion of Si and O in diopside anorthite melt at high pressure,” Geochimica et Cosmochimica Acta, Vol. 67 No. 1 133-142 (2003).

[22] F.J. Norton. “Permeation of Gaseous Oxygen through Vitreous Silica,” Nature, 191 701 (1961).

[23] A.C. Fox, and T.W. Clyne. “Oxygen Transport by Gas Permeation through the Zirconia layer in Plasma Sprayed Thermal Barrier Coatings,” Surface and Coatings Technology, 184 311–321 (2004).

[24] J.D. Cawley, J.W. Halloran, and A.R. Cooper. “Oxygen-18 Tracer Study of the Passive Thermal Oxidation of Silicon,” Oxidation of Metals, 28 [1-2] 1-15 (1987).

[25] R. Telle, L. S. Sigl, and K. Takagi, “Transition Metal Boride Ceramics”; pp. 140-154 in Handbook of Ceramic Hard Materials, Vol. 1. Edited by R. Reidel R. Wiley-VCH, Germany, Weinheim, (2000).

CHAPTER 8

EVOLUTION OF CONVECTION CELL PATTERNS IN LIQUID OXIDE FILMS ON ZIRCONIUM DIBORIDE-SILICON CARBIDE COMPOSITES: EFFECT OF TIME, TEMPERATURE AND COMPOSITION

1.0 Introduction

In previous chapters the formation of convection cells and their significance in the oxidation behavior of ZrB_2-SiC composites was described and discussed. In this chapter the evolution of the convection cells with time, temperature and SiC concentration is investigated. Sets of oxidation tests were performed at temperatures between 1500 and 1600ºC for various dwelling times. The effect of SiC concentration on the oxide thickness and the population of convection cells was investigated by testing three different compositions; 15 vol%, 20 vol% and 30 vol% SiC- ZrB_2. Distribution, morphology and population of the convection cells are discussed and analyzed for the different oxidation conditions and SiC concentration. The microstructure and the chemical composition of the oxide scales is also analyzed for the different composition and oxidation conditions. The oxide thicknesses of specimens with different SiC concentration is then compared and the relationship between oxide thickness and the population of the density is discussed.

2.0 Experimental Procedure: Materials and Methods

To investigate the effect of dwelling time on the population and distribution of the convection cells ZrB_2-15vol%SiC-2vol%$MoSi_2$ (ZSM) composites provided by CNR-ISTEC and used in previous chapters were tested in a high-temperature box furnace (SentroTech Corporation, Berea, OH, USA) in ambient air at 1550ºC with different dwelling times, ranging from 0.5 hr. to 8 hrs. The heating and cooling rates used were 13ºC/min. Two ZSM composites were also tested for 0.5 hr. at 1500ºC and 1600ºC in the box furnace to study the effect of temperature on the convection cells for fixed time. Additionally, two ZrB_2-SiC based composites with different SiC concentration were tested to study the effect of SiC concentration on the convection cells. The two ZrB_2 based composites contained 20 and 30vol%SiC and were fabricated and provided by our collaborators Dr.William G. Fahrenholtz and Dr.Gregory E. Hilmas at the University of Missouri-Rolla (UMR). The ZrB_2-20vol%SiC (ZS20) composite contained around 2vol%WC that was incorporated during attrition milling step during fabrication of the material at UMR due to the use of WC milling media. The fabrication and materials are described in more detail elsewhere [1]. The ZrB_2-30vol%SiC (ZS30) composite was attrition milled at UMR with ZrO_2 milling media during fabrication; the presence of other phases than SiC and ZrB_2 was not observed indicating no contamination from the milling media. The fabrication and starting materials are described in detail elsewhere[2]. Figure 8.1 shows the microstructure of the three composites; ZSM, 20ZS, and 30ZS. The ZS20 and ZS30 were tested at the same conditions as the ZSM specimens at 1550ºC for 3, 4 and 8 hrs., the 20ZS was also tested at 1550ºC for 2 hrs.

The tested specimens were supported by the same material that was placed on a Al_2O_3 support in a Al_2O_3 crucible. Prior to testing ca. 200 μm were grinded off the surface of the specimens, with a fine diamond grid (Omni Brade, TBW Industries, Furlong, PA, USA) to remove any heat affected zone that could have formed during wire electrical discharge machining (w-EDM) (Ann Arbor Machine Model 1S15, Ann Arbor, MI, USA), that was used to cut the ZSM bulk material into thin sheets. The thin sheets of the ZSM were then cut with a diamond saw (IsoMet® 1000 diamond precision saw, Buehler, Lake Bluff, IL, USA) into small rectangular coupons with total surface area between 0.5-1 cm^2. The ZS20 and ZS30 composites were received from UMR as tests bars but were then grinded and cut with same tools as the ZSM to have the same surface finish of the specimens tested. Prior to testing the specimens were ultrasonically cleaned in acetone and dried at 100ºC.

Chemical composition and microstructural analysis were done on the surfaces and cross-sections of the tested specimens using Scanning Electron Microscopy (SEM), Backscattering Electron Microscopy (BSE), and Electron Microprobe Analyzer (EMPA). A Cameca SX100 was used for Electron Microprobe Analysis (EMPA), using well characterized mineral standards for quantitative analysis of boron, oxygen, zirconium, and silicon, and for imaging in the BSE and cathodoluminscence (CL) modes. The EPMA standards and technique that were used are described in more detail in Chapter 4 section 4.2. The cross-sections of the oxidized specimens was prepared for microstructural analysis by non-aqueous polishing procedures down to 1 μm finish. Specimens were coated with carbon before microstructural and elemental analysis.

3.0 Results: Evolution of Convection Cell Patterns with Time and Temperature

3.1 ZSM composite: Microstructure Analysis

3.1.1 Surface Analysis

Figure 8.2 shows the backscattered electron (BSE) micrographs of the surfaces of ZSM composites tested at 1550ºC for 0.5 hr.(ZSM-05; Fig. 8.2(a)) and 1 hr (ZSM-1; Fig. 8.2(b)). The micrographs show that the ZSM-1 has a larger number of convection cells that are more uniformly distributed on the surface than the ZSM-05. The ZSM-05 which has non-uniform distribution of the formed cells, has more closely packed cells on the right side of the specimen compared to left. The morphology and number of cells on these two specimens indicate that the population of the cells largely increases from 0.5 hr. to 1 hr. dwelling time at 1550ºC. Also, the distribution of the cells for the ZSM-05 specimen indicates that the cells form firstly rather sparsely on the surfaces but when the population increases they start to impinge and form convection cell pattern similar to the one seen on the ZSM-1 specimen.

Figure 8.3 shows backscattered electron (BSE) micrographs of the surfaces of ZSM composites tested at 1550ºC at various times; 1 hr., 2 hrs., 3 hrs., 4 hrs., 6 hrs., and 8 hrs (i.e. ZSM-1, ZSM-2 etc.). The images are taken at low magnifications (36-38X, 20KV, spot size: 5) to be able to compare the population of the convection cells between different dwelling times. The micrographs in Figure 8.3 indicate that the number of convection cells decrease with increasing dwelling time. This was explored in detail by quantifying the convection cells for each specimen. The number of convection cells per cubic mm (cell density: no./mm^2) was quantified visually by two investigators[a], who in a blinded fashion, counted separately the numbers of cells on the samples in 15 random fields (a square frame;1mm x 1mm) per sample at x36-38 microscopic magnification. The cell counts were then averaged for each sample. This kind of quantification by visual counting is commonly used for manual quantification of features using a microscope e.g. in cell staining [3-4]. Figure 8.4 shows the average densities calculated (no./mm^2) and the standard error (± standard deviation) for the different dwelling times. The graph shows that the data from both counts (investigator 1 and 2) reveal the same results; decrease in the number of cells with time and a population peak at ~1 hr. dwelling time (at 1550ºC). The micrographs shown in Figure 8.3 indicate that the distribution of the convection cells changes with dwelling time, i.e. from being uniformly distributed over the surface, for 1 hr. (ZSM-1), to being more locally clustered to together for 8 hrs. (ZSM-8). Interestingly, the surface of the ZSM-8 specimen was not smooth, it had a hilly appearance, were there were large areas dominated by SiO_2 “hills” and other regions dominated by clusters of convection cells.

Further quantitative analysis were done for the convection cells formed on the ZSM composites tested at 1550ºC with dwelling times from 1 hr. to 8 hrs. The number of B_2O_3 petals for each ZrO_2 flower (island) was quantified for each specimen. To visually quantify the number of petals the authors collaborator Jennifer Wecker calculated the average no. of petals per flower for each specimen. The averages were calculated by dividing the total no. of petals by the total no. of cells counted per field for each specimen. Fifteen random fields (a square frame;1mm x 1mm) were used per sample on

---

[a] The investigators were the author and her collaborator, Jennifer Wecker, an undergraduate student at UM.

micrographs with a x36-38 magnification. The results are shown in a graph in Figure 8.5. The graph indicates that the no. of petals per flower do not significantly change with increasing dwelling times (at 1550ºC) , i.e. the avg. no. of petals per flower for each dwelling time varies relatively little, from min. 2.64 ± 0.49 to max. 3.12 ± 0.79. The overall average of the no. of petals per flower is 2.83 ± 0.73. The relatively high error (standard deviation) could result from the dependence of the flower to the location (as indicated by the analysis of the no. cells (flowers/islands) per mm^2), which then affects the calculated avg. no. of petals per flower for each specimens.

The number of the petals per flower for the specimen tested for the shortest dwelling time, 0.5 hr (shown in Figure 8.2(a)), is not as straightforward to interpreted. For the newly formed convection cells shown in Figure 8.2(a) it is not quite clear if the larger isolated cells to left on the micrograph are many small cells pined together in a circle or if that is one isolated cell. The authors speculations are that these are in fact smaller ones pinned together, that will with time resemble the ones pinned together in the right corner of the micrograph. If that is true then the average no. of petals per flower for 0.5 hr. is similar to the specimens tested at longer dwelling times, ca. 3-4 flower petals per cell.

The size of the B_2O_3 petals, the SiO_2 "lagoons" and the ZrO_2 islands were also measured, and the average and standard error (± standard deviation) was calculated for the different dwelling times. The diameter of the B_2O_3 petals, the SiO_2 "lagoons" and the ZrO_2 islands were measured in x- and y-direction randomly. The values in x- and y-direction were very similar thus the measured size is the estimated diameter of the features. At least 20 values were used to calculate the average size for each dwelling time. The formation of these features (B_2O_3 petals, the SiO_2 "lagoons" (or cells) and the ZrO_2 islands) of the convection cells have been explained in detail in previous chapters (Chapter 4-5, 7). The size of the features was measured by the author for each specimen during microstructure analysis using SEM. The data was then compiled and averages and the standard errors were calculated by Jennifer Wecker. Figure 8.6 shows the average size of the ZrO_2 islands for the ZSM specimens tested at 1550ºC for different dwelling times, ranging from 0.5 hr. to 8 hrs. The size of the ZrO_2 islands seem overall to increase with longer dwelling time. There seems to be three different trends in the data; an evident increase from 0.5 hr. to 3 hrs., no significant increase between 3 hrs. and 6 hrs., and then from 6 hrs. (ZSM-6) to 8hrs. (ZSM-8) there is a rapid increase in the size of the ZrO_2 island. During microstructure analysis of the ZSM-8 specimen it became somewhat hard to distinguish one ZrO_2 island from another and some of them seem to have coalesced. Thus care was taken during measurements of the ZrO_2 islands for the ZSM-8 specimen, to make sure that the measured diameter was of one island but not two.

The increase in the size of the ZrO_2 could indicate that for the longer dwelling times, especially for 8 hrs., the ZrO_2 islands have grown in the SiO_2-B_2O_3 melt and then possibly coalesce together. Higher magnification of the ZrO_2 islands on the ZSM-8 specimen shows dendrites in the outer boundaries of the ZrO_2 islands, close to B_2O_3 petals, this is shown in Figure 8.7. Interestingly, similar dendrites but somewhat smaller are seen close to the B_2O_3 petals on the specimens tested for shorter dwelling times. This is shown in Figure 8.8 where dendrites are located on the edges of the ZrO_2 island on a ZSM specimen tested at 1550ºC for 2 hrs. Perhaps the ZrO_2 precipitates form as dendrites when there is super-saturation in the BSZ liquid when the B_2O_3 starts evaporating away from liquid. The dendrites then maybe coalescence together and form the grains that are the main constitutes of the ZrO_2 islands. Epassaka et al.[5] found that for ZrO_2 crystallites deposited by a chemical vapor deposition (CVD) under atmospheric pressure on a silicon substrate; at higher temperatures morphological instability were formed in the whiskers so they formed dendritic structure. They claimed that at higher substrate temperature, intermediate super-saturation favors the formation of the dendrites. Dendritic growth phenomena have also been seen for Cu–Hf–Ti–Ag–Ta bulk metallic glass composites (BMG) where Ta rich-dendrites form by precipitation during fabrication of the composite[6] and for AISI 304 stainless steel where precipitation of primary ferritic dendrites form during directional solidification[7]. For the precipitation of dendrites in under-cooled glass melts; at the beginning of spontaneous crystallization of an under-cooled melt the growth occurs in the preferred direction. Since conventional glass melts are very viscous the transport of new growth material by diffusion is too slow. Thus planes with the smallest rate of shifting at first cannot form and skeletons such as dendrites form [8]. For our case, when the B_2O_3 starts evaporating away from the BSZ liquid the viscosity of the liquid will increase due to the increase in the SiO_2 for the overall composition of the liquid. Perhaps this induces the dentritic form of the precipitated ZrO_2. Also, from the crystal growth theory it its known that in melts that are controlled by diffusion or heat-flow cellular morphologies such as dendrites form during crystal growth . Composition gradients and associated diffusion near crystal-melt interface are also known to affect crystal growth by causing the crystal to break up into a cellular morphology such as dendrites [9].

The size of the B_2O_3 petals, measured for each dwelling time at 1550ºC, are shown in Figure 8.9. The size of the B_2O_3 petals seem overall to increase with longer dwelling time just as the ZrO_2 islands, the increase is smaller though and there are more variation in this pattern then the pattern for the size of ZrO_2. This could perhaps be interpreted as evidence for correlation between the size of the B_2O_3 petals and the ZrO_2 islands, which would support our hypothesis about the composition dependence between B_2O_3 and ZrO_2 through the BSZ liquid formation. The size of the SiO_2 lagoons were also calculated and measured for dwelling times from 0.5 hr. to 6 hrs., this is shown in Figure 8.10. The size of the SiO_2 lagoons could not be measured for the 8 hrs. dwelling time (ZSM-8) due to the change in the convection cell distribution that resulted in no distinct boundaries of the SiO_2 lagoons. The changes from well defined SiO_2 lagoons (0.5 hr.) to almost no definite SiO_2 lagoon boundaries (8 hrs.), resulted in difficulties in measuring the sizes. Thus the data collected and the averages calculated for the SiO_2 lagoons are perhaps not very reliable. Overall though the conclusion can be drawn that the distinct boundaries of the SiO_2 lagoons changes with time, which suggest them to be dependent on the size and distribution of the ZrO_2 islands and their B_2O_3 petals.

Surface images of three ZSM specimens each tested at different temperature; 1500ºC, 1550ºC, and 1600ºC, for fixed time, 30 min, are shown in Figure 8.11. Convection cells were observed on all three specimens, which is evident from the surface images. By comparing the images it can be seen that, for this temperature range, the number of convection cells increase with increasing temperature. The images also suggest that when more convection cells form, they form until they cover the surface and then start to impinge together. The increased number of convection cells for higher temperatures is likely due to an increased evaporation rate of the B_2O_3 at increasing temperatures. When the B_2O_3 starts evaporating faster, ZrO_2 precipitates form faster which results in faster formation of the convection cells. These results are consistent with the observations seen from the fixed temperature experiment (ZSM tested at 1550ºC for different dwelling times; 30 min and 1 hr., see Figure 8.2) where the increased dwelling time produced more convection cells; the longer exposure time allowed more B_2O_3 evaporation and thus more ZrO_2 precipitation.

3.1.2 Cross-section Analysis

Figure 8.12 shows micrographs of cross-sections of ZSM specimens tested for 1 hr. (ZSM-1), 4 hrs. (ZSM-4), and 8hrs. (ZSM-8) at 1550ºC. The micrographs show the enhanced oxidation zones under the ZrO_2 islands discussed in Chapter 7. The overall thickness of the oxide layer increases with increasing dwelling time as expected, this is also demonstrated in Figure 8.13 which shows a graph of the measured total thickness of the oxide layer (B_2O_3-SiO_2 surface layer + ZrO_2) vs. dwelling time at 1550ºC. The graph also contains the calculated total thickness of the oxide layer which was calculated by adding the thicknesses of the B_2O_3-SiO_2 surface layer and the ZrO_2 layer that were measured individually. The calculated and the measured thickness agree quite well, were the calculated thickness is well within the standard deviation of the measured thickness. The oxide thickness increases rapidly first (between 0.5 hr. and 1 hr.) but then steadily increases with time. Figure 8.14 and 8.15 show graphs of the measured thickness of the SiO_2-rich surface layer and the ZrO_2 layer. The thickness for each layer was measured by averaging 20-30 values at various locations. Difficulties existed in measuring the average thickness due to the non-uniformity of the oxide layer, i.e. thicker oxide layer under the convection cells. The non-uniformity is easily seen from Figure 8.12. This made precise averaging hard to do and large standard deviation of the thickness resulted as can be seen from the graphs in Figure 8.13-15. The values of the averaged measured thicknesses should thus be taken with precaution.

For the ZSM specimens tested at 1550ºC for 6 hrs. and 8 hrs. microstructural analysis of the cross-sections revealed submerged ZrO_2 islands, completely covered with SiO_2 rich surface layer, this is shown in Figure 8.16(a) and (b). This indicates that there were convection cells formed at earlier stage in the oxidation, but were covered by the viscous SiO_2 liquid formed, presumably from other convection cells being formed. This perhaps explains why there is decrease in the number of convection cell with time, i.e. they become “extinct” and get covered by the flowing viscous liquid left behind when the B_2O_3 evaporates.

3.2 ZSM composite: X-ray Diffraction (XRD) Analysis

A X-ray diffractometer (Rigaku Miniflex, Rigaku Americas Corporation, TX, USA) was used for the XRD analysis of the surface of the specimens to get information about the phases and structure of the oxides formed, and to see if there had formed any zircon ($ZrSiO_4$). Theoretically, it can form as a stable compound in the ternary system ZrO_2-B_2O_3-SiO_2 when there is small amounts or no B_2O_3 as shown by the phase diagram in Figure 5.9 in Chapter 5. To analyze the diffraction patterns a XRD analysis software was used called JADE 7 (Materials Data, Inc., CA, USA) that uses the International Centre for Diffraction Data (ICDD) as the XRD pattern database. The software was used to identify the diffraction peaks recorded. The diffraction patterns of the ZSM specimens tested at 1550ºC for various dwelling times all showed a hump at low diffraction angles (2θ values between 15º and 28º) which is typically seen for amorphous glass, here it represents the amorphous borosilicate glass. For the analysis the XRD patterns were firstly smoothed and the background subtracted to get rid of noises (as a result from that the glass hump was removed). Figure 8.17 shows XRD patterns of the ZSM specimen tested at 1550ºC for 0.5 hr., 2 hrs., and 6 hrs. The main phases identified were ZrO_2 and ZrB_2, the corresponding diffraction peaks are indicated in Figure 8.16. The ZrB_2 peaks are only evident in the ZSM specimen tested for the shortest time 0.5 hr which has a thin glass layer on the surface that the X-rays can penetrate through. For the longer dwelling times the ZrB_2 peaks disappear due thicker borosilicate glass formed on the surfaces. No $ZrSiO_4$ peaks were observed in the XRD patterns recorded for the composites, this is not surprising since $ZrSiO_4$ has not been observed previously in the literature in borosilicate surface layers of similar ZrB_2-SiC composites tested at high temperatures. Zirconium oxide (ZrO_2) can form in three different structures; as monoclinic $\alpha-ZrO_2$ which is stable up to 1050ºC, tetragonal $\beta-ZrO_2$ stable above 1050ºC, and cubic $\gamma-ZrO_2$ structure which is only stable above 2300ºC[10]. Both monoclinic and tetragonal zirconia were identified in the diffraction patterns of the ZSM specimen tested for 0.5 hr., 2 hrs and 6 hrs. The corresponding diffraction peaks are shown in Figure 8.17. The diffraction patterns indicate that more tetragonal ZrO_2 forms for longer dwelling times at 1550ºC as expected. Also, the many monoclinic zirconia peaks in the diffraction patterns in the ZSM specimens tested for 2 and 6hrs. indicates that most of the tetragonal zirconia formed at the higher temperatures transformed to monoclinic zirconia during cooling.

4.0 Results: Effect of SiC Concentration on the Formation of Convection Cells

4.1 ZS20 and ZS30: Surface Analysis

The purpose of testing other ZrB_2-SiC composites with different SiC concentration was twofold: to verify that convection cells form in other ZrB_2-SiC materials than the ZrB_2-15vol%SiC-2vol%$MoSi_2$ (ZSM) composite and to study the effect of SiC concentration on the formation of convection cells. The ZS20 and ZS30 specimens tested at 1550ºC for 2, 3, 4 and 8 hrs. all had convection cells formed on the surfaces. This supports our hypothesis that the convection cells play an important part in the oxidation behavior of ZrB_2-SiC based composites. Interestingly the uniformity and the number of cells formed on the surfaces of these specimens were somewhat different from the convection cells formed on the ZrB_2-15vol%SiC-2vol%$MoSi_2$ (ZSM) composite. Firstly, in general they are fewer and not as uniform, secondly overall they seem less "evolved", e.g. for shorter dwelling times there are smaller ZrO_2 islands surrounded by B_2O_3 circles (instead of distinct petals). This was especially evident for the composite with the highest SiC content (ZS30). An example of this is shown in Figure 8.18 where backscattering electron images are shown of the surfaces of ZS20 and ZS30 specimens tested at 1550ºC for 4 hrs. and of a ZSM, for a comparison (tested at the same conditions). The micrographs also show that the ZSM specimen has a larger number of convection cells spread over the surface than the ZS20 and ZS30 specimens. The number of convection cells were quantified for the ZS20 and ZS30 specimens by visual counting, the same method described earlier for the ZSM tested composite. The overall results from the visual counting is shown in Figure 8.19. The graph in Figure 8.19 shows the "density" of the cells (no. of cells/mm^2) for the three specimen (ZS20, ZS30, and ZSM for comparison). The standard deviation (the error bars) for the ZS20 and ZS30 values are rather large, thus the values for the longer dwelling times, specially 8 hrs., do not differ much. Overall though the results indicate that with increasing amount of SiC there are fewer convection cells that form. The large standard deviation for the ZS20 and ZS30 composites (in Figure 8.19) results most likely from two reasons; firstly in general the cells formed on the ZS20 and ZS30 specimens were not uniformly distributed, secondly because there was limited material available for testing, the specimens that were tested were small, thus there were fewer fields to randomly count from (i.e. fewer data points to average). Figure 8.20 shows BSE images of the surface of the ZS20, ZS30 and ZSM specimens tested for 3 hrs. at 1550ºC. The images show the convection cells features formed for each composite; ZrO_2 islands surrounded by B_2O_3 rich regions and outer SiO_2 cells. The convection cell formed on the surface of the ZS30 (30vol%SiC) is clearly less "evolved" than for the lower SiC containing material; ZS20 (20vol% SiC) and ZSM (15vol% SiC). Some of the features of the convection cells formed on the ZS20 and ZS30 are very similar to what was observed on the ZSM specimens, especially for ZS20 which is closer in composition to ZSM than ZS30. These similarities are e.g. ZrO_2 dendrites close to the ZrO_2 islands as shown in Figure 8.21, which is a BSE image of the surface of a ZS20 specimen tested for 3 hrs at 1550ºC. Also, for the ZS20 tested for 2 hrs. at 1550ºC the convection cells were few but some had very similar morphology to the ZSM tested for 0.5 hr., an example is shown in Figure 8.22.

4.2 ZS20 and ZS30: Cross-sectional Analysis

The microstructural analysis of the cross-sections of the ZS20 and ZS30 tested specimens showed similar structures to the ZSM specimens, e.g. enhanced oxidation region where the cross-section cut through a convection cell. The only distinction was in the distribution of the convection cells; they were not as uniformly and closely packed/impinged, thus the cross-sectioning did not reveal as many convection-cell features as for the ZSM composites tested. Figure 8.23 shows a secondary electron image of cross-sections of ZS30 and ZS20 tested for 8 hrs. at 1550ºC. The images show cross-sections through the convection cells. The total oxide thickness of the ZS30 and ZS20 are compared to the results for the ZSM specimens in Figure 8.24. The total oxide thickness was calculated from the measured averages of the SiO_2-rich borosilicate surface layer and the underlying ZrO_2 layer. Figure 8.25 and 8.26 shows these measurements individually. The standard deviation is especially high for the ZS20 tested for 4 hrs., likely due to a non-uniform thickness of the SiO_2-rich borosilicate surface layer. Overall the thickness of the oxide scale decreases with increasing SiC content, indicating that larger SiC content increases the oxidation resistance of the composite.

5.0 Discussion and Conclusion

The results from Section 3.1 clearly show that the density (no.cells/mm^2) of convection cells for the ZSM composite tested at 1550ºC rapidly increases at the first stage of the oxidation but then decreases slowly with increasing time. If we compare the density (no.cells/mm^2) of cells for the ZSM composite at 1550ºC to the thickness of the SiO_2-rich surface layer we see the same trend, this is shown in Figure 8.27 (the data point are indicated by diamonds). This indicates that the convection cells are transient, i.e. they form and transport BSZ liquid to the surface but then with time the increasing amount of flowing viscous SiO_2-rich liquid submerges them and they become extinct. The “submerged” ZrO_2 islands shown in the cross-section of the ZSM-6 and -8 specimens in Figure 8.16 support this hypothesis. Perhaps the viscous SiO_2-rich layer is then thick enough to suppress the formation of new convection cells. This would suggest that the convection cell mechanisms is dominant in the early stage of the oxidation of these materials, supplying the SiO_2 to the surface, then when the surface layer becomes mainly viscous SiO_2 the replenishment of the SiO_2 by the formation of convection cells and their “volcanic” eruptions (due to the large volume increase) stops and they go “extinct”.

By increasing the temperature for the ZSM testing (from 1500 to 1600ºC) and holding the time fixed (0.5 hr.) the number of convection cells increase. This is likely due to the increased evaporation rate of B_2O_3 at higher temperatures, due to the higher vapor pressure, which speeds up the formation of the convection cells.

The results from Section 3.2 show that the convection cells do indeed form for other ZrB_2-SiC based material. This further supports our hypothesis that the formation of the convection cells are dependent on the formation of the transient BSZ liquid and the large volume increase for oxidized ZrB_2-SiC materials. Fewer convection cells (no. of cells per mm^2) form on the ZS20 and ZS30 composites compared to the ZSM, suggested here to be due to the difference in the BSZ liquid composition. The ZS20 and especially ZS30 have less B_2O_3 formed compared to ZSM thus there will be less ZrO_2 dissolved in the BSZ liquid, which should result in fewer ZrO_2 islands formed. This is supported by the ternary phase diagram for B_2O_3-SiO_2-ZrO_2 shown in Figure 5.9 in Chapter 5 and the observations from the microstructural analysis and the cell counting shown previously in Section 3.2. Table 8.1 shows the estimated amount of precipitated ZrO_2(s) for the three different ZrB_2-SiC compositions by using the ternary phase diagram. The ZrB_2-15vol%SiC composite (ZSM) is estimated to precipitate 22 mol.% more ZrO_2(s) than the ZrB_2-30vol%SiC (ZS30) when 90 mol% of the B_2O_3 has evaporated from the BSZ liquid. Table 8.1 shows how the solubility of the ZrO_2(s) in the BSZ liquid decreases with the increasing viscosity[b] and SiC vol% (i.e. increasing SiO_2 amount).

The cross-sectional analysis for all three compositions showed that the larger content of SiC results in more oxidation resistant composite, indicated by the decrease in total oxide scale thickness with increasing SiC content. The reason for the increased oxidation resistance of the higher SiC containing materials could be explained by less boron oxide content in the borosilicate surface layer. The increased SiO_2 content of the surface layer formed can suppress the evaporation of the B_2O_3 and hinder inward oxygen diffusion better at these temperatures.

The *formation* of the convection cells is not dependent on the thickness of the SiO_2-rich -B_2O_3 surface layer; the max. population of the convection cells for the three different ZrB_2-SiC composition do not form at one critical thickness, the graph in Figure 8.27 illustrates this. If this is true then it supports our previous conclusion that the convection cells are not driven by Bénard-Marangoni convection, i.e. dependant on the thickness of the liquid layer. On the other hand their *existence* is dependent on the

---

[b] The viscosity of the borosilicate melt was estimated from a relationship extrapolated from data by Jabra et al. introduced in Chapter 5.

thickness of the surface SiO_2-rich layer, as mentioned above, when it becomes thicker the convection cells are submerged by it and become extinct.

The overall effect of the convection cells on the oxidation resistance of ZrB_2-SiC is complicated because of their twofold role in oxygen diffusion as discussed in Chapter 7. Their formation is completely dependent on the formation of the BSZ liquid and its composition. The convection cells are shown to be an important part of the oxidation mechanism for boride-SiC based composites and to play an significant role in the formation of the complex oxide scale at these temperatures.

The B_2O_3 liquid plays a large role in the oxidation mechanism for boride-SiC based materials, just from looking at the starting composition of the material this should be expected. Nevertheless, the role of the B_2O_3 liquid has often been more or less forgotten in the boride-SiC UHTC literature. This could partially be due to expected volatility of the B_2O_3 liquid and the difficulty in detecting boron (B) in the oxide scale structure. Often the focus has then been on the other part of the borosilicate layer; the SiO_2 part which is more easily detected and at higher concentration. The focus for improving the oxidation resistance of boride-SiC composite has then been mainly on altering the SiO_2 glass formed with additives [10-13]. This has not been a great success, for example due to the limitation that the melting temperature of the formed surface layer imposes at higher temperatures [13]. Instead the author suggests that instead of focusing solely on the SiO_2 glass and improvement in the oxidation resistance by altering the SiO_2 glass, the focus should be more on the B_2O_3-SiO_2 glass, where perhaps e.g. Al_2O_3 additions would be of value.

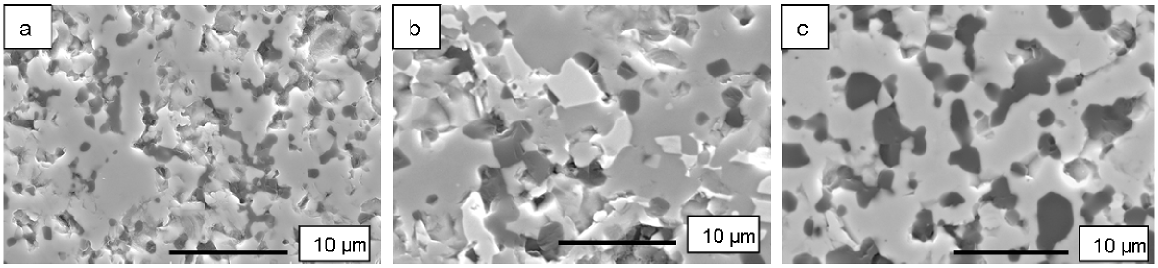

Figure 8.1: Secondary electron images of the microstructure of the three different composites tested (a) ZrB2-15vol%SiC-2vol%MoSi2 (ZSM), (b) ZrB2-20vol%SiC-2vol%WC (ZS20), and (c) ZrB2-30vol%SiC (ZS30).

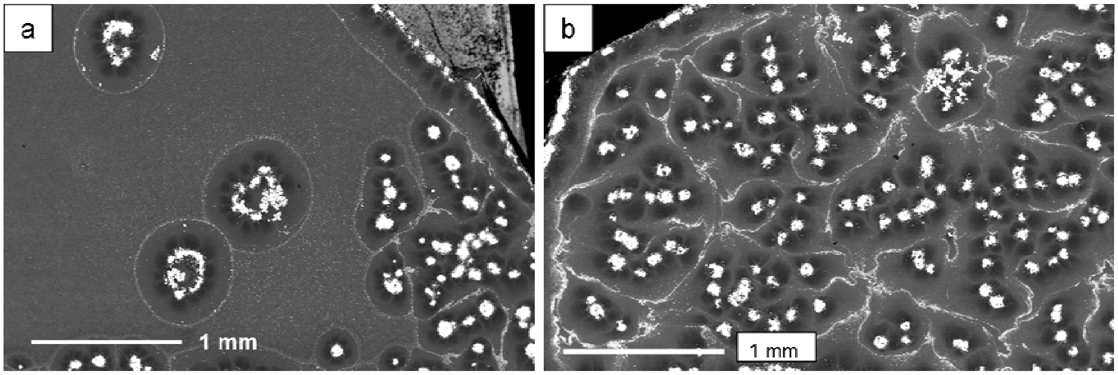

Figure 8.2: Backscattering electron images of the surface of (a) ZSM-0.5 and (b) ZSM-1 tested at 1550°C for 0.5 hr. and 1 hr. respectively.

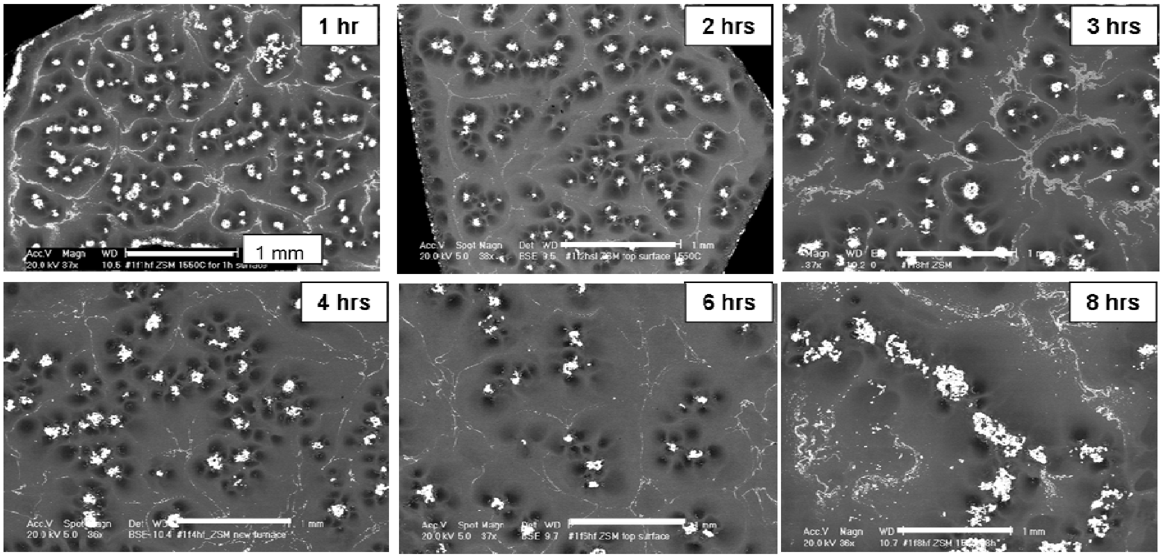

Figure 8.3: Backscattering electron images of surfaces of the ZSM composite tested at 1550ºC for various dwelling time. The dwelling times are shown in order, increasing from 1hr. (left top) to 8 hrs. (bottom right).

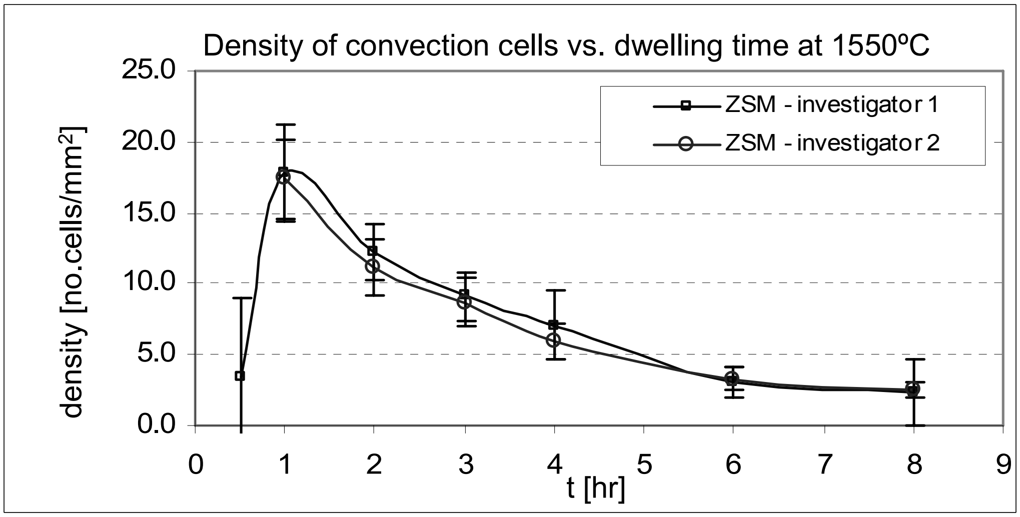

Figure 8.4: The calculated density of the convection cells (no. cells/mm^2) vs. the various dwelling times for a ZSM composite tested at 1550ºC.

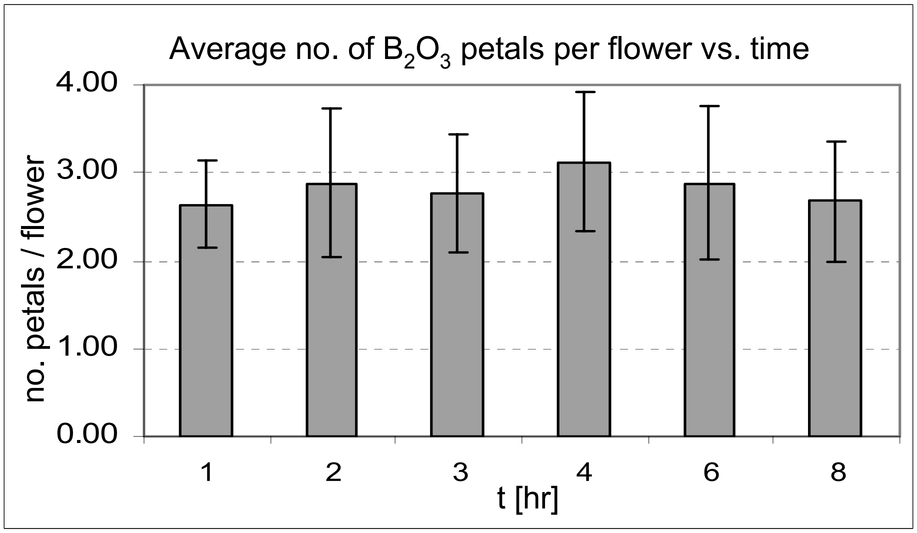

Figure 8.5: The average no. of petals per flower (i.e. per ZrO_2 island) for the ZSM composite tested at 1550°C for various dwelling times. Method 1 was used for quantifying the average no. of petals per flower.

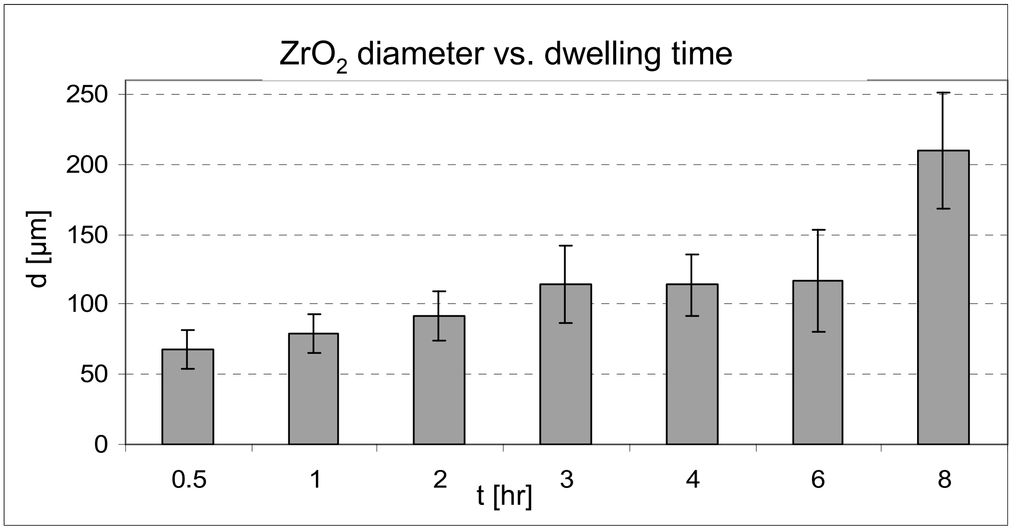

Figure 8.6: The average size of the ZrO_2 islands on the ZSM composites tested at 1550ºC for dwelling times ranging from 0.5 hr. to 8 hrs.

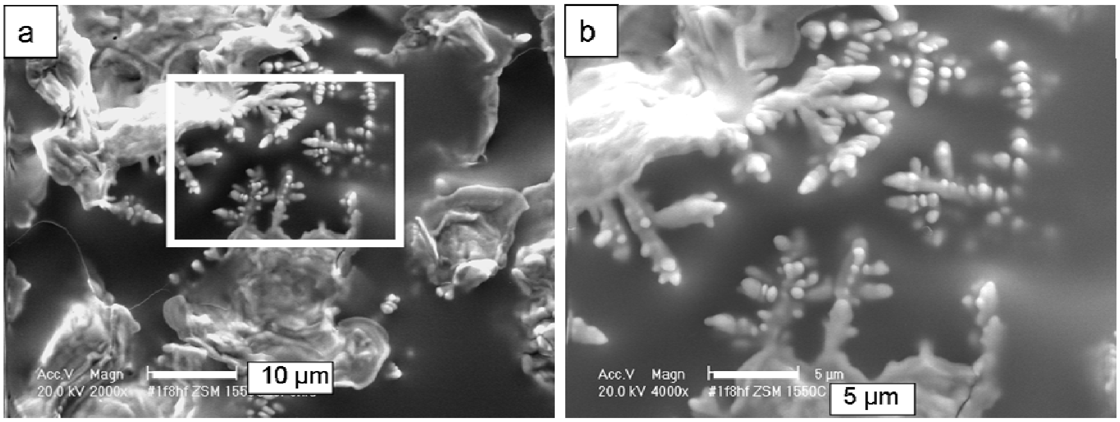

Figure 8.7: Secondary electron micrographs of the dendrite features observed connected to one of the ZrO_2 islands on the surface a ZSM composite tested at 1550ºC for 8 hrs. The right image is a higher magnification of the area inside the white box in the micrograph on the left side.

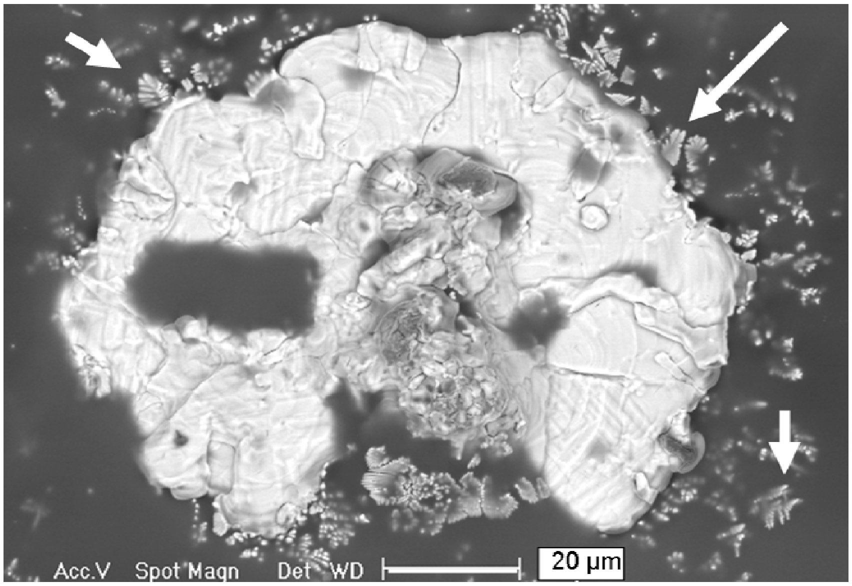

Figure 8.8: Secondary electron micrograph of a ZrO_2 islands on the surface a ZSM composite tested at 1550°C for 2 hrs showing some evidence of dentritic features to the sides close to the B_2O_3 petals.

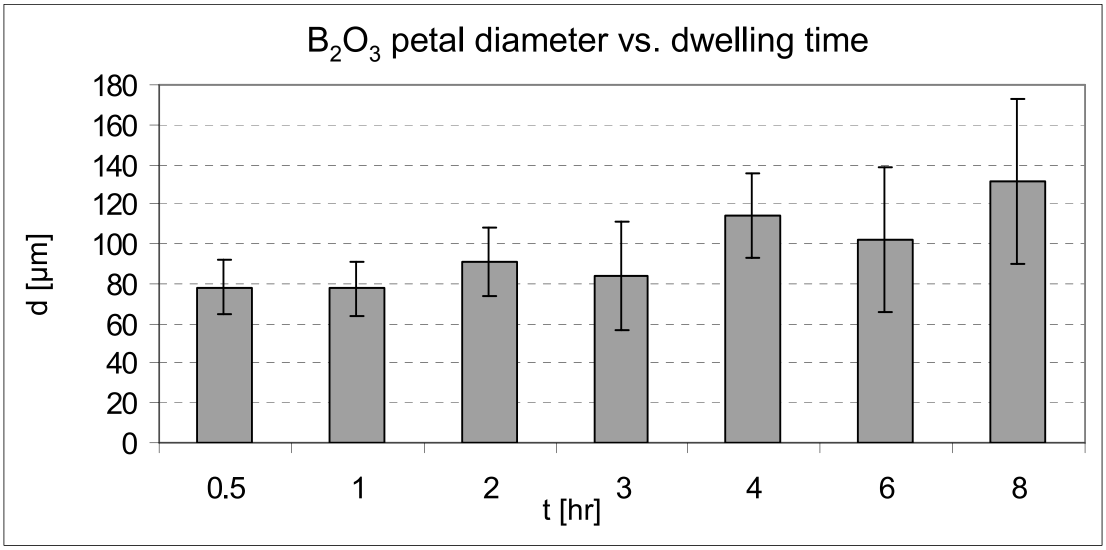

Figure 8.9: The average size of the B_2O_3 petals around the ZrO_2 islands (flower) on the ZSM composites tested at 1550°C for dwelling times ranging from 0.5 hr. to 8 hrs.

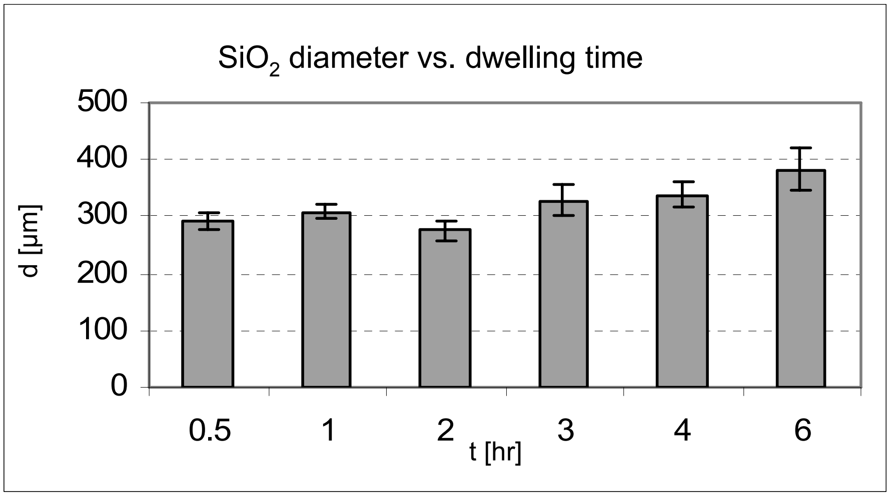

Figure 8.10: The average size of the SiO_2 “lagoons” around the ZrO_2 islands (flower) on the ZSM composites tested at 1550ºC for dwelling times ranging from 0.5 hr. to 8 hrs.

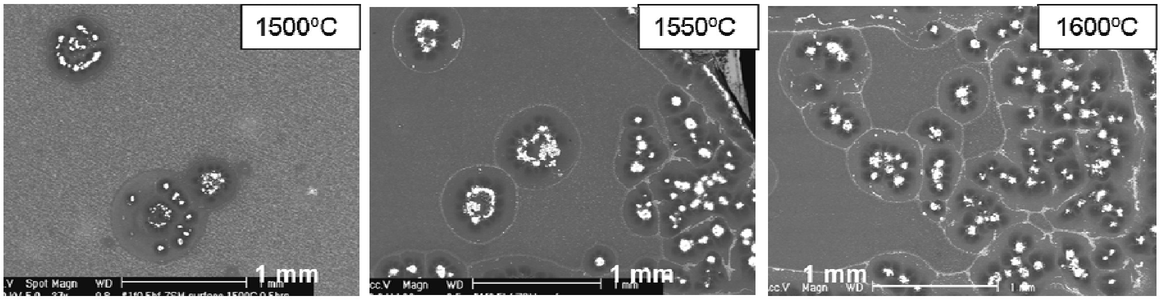

Figure 8.11: Backscattering electron images of the surface of ZSM composite tested for a fixed time, 0.5 hr., at different temperatures; (a) 1500ºC, (b) 1550ºC, and (c) 1600ºC respectively.

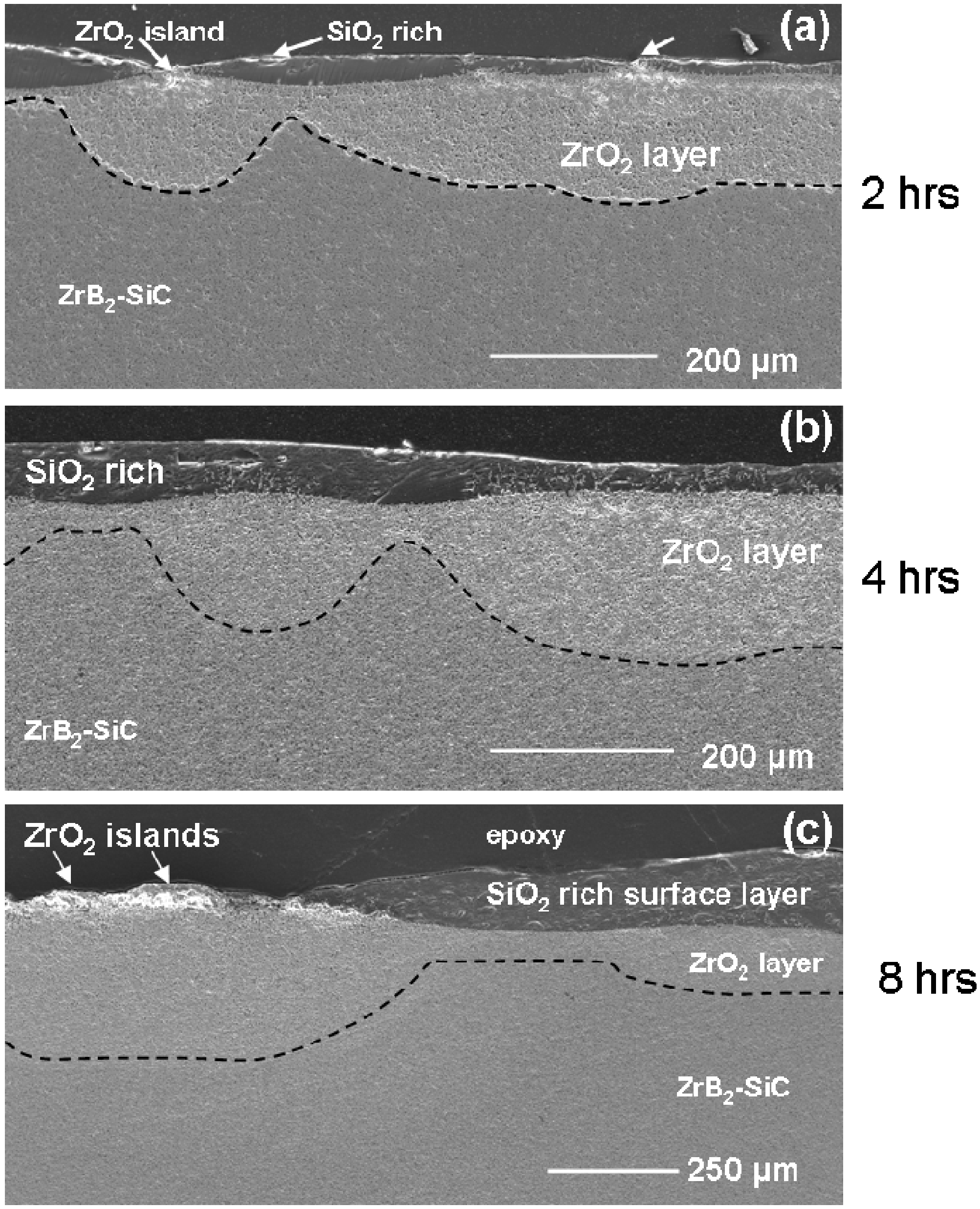

Figure 8.12: Secondary electron micrographs of the cross-sections of ZSM composites tested at 1550°C for (a) 2 hrs, (b) 4 hrs, and (c) 8 hrs, showing the large difference in the thickness of the oxide where the convection cells are located (ZrO_2 islands) compared to the area covered with SiO_2 rich surface layer. The interface between the ZrO_2 layer and the un-reacted bulk material is indicated with a broken line.

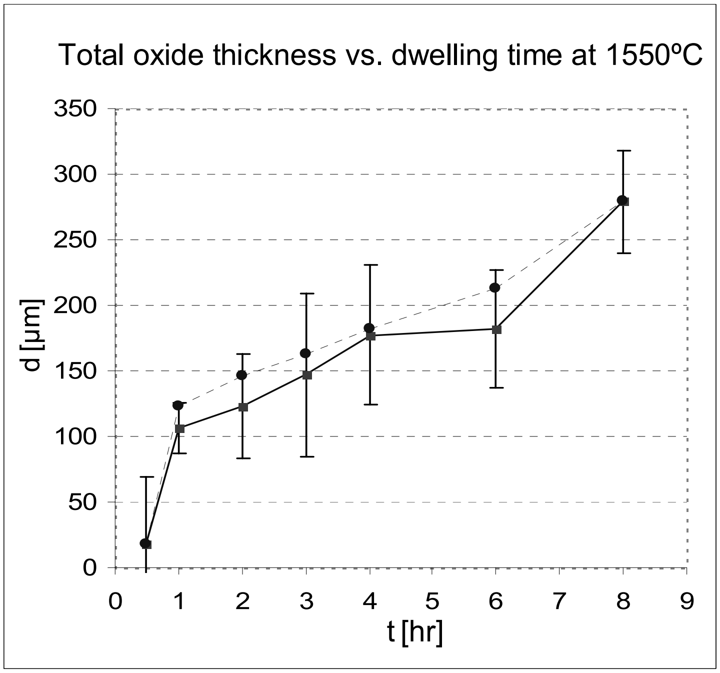

Figure 8.13: The calculated and measured total oxide thickness of the ZSM composites tested at various dwelling times from 0.5 hr. to 8 hrs. The broken line with the circles is the calculated data (sum of the measured thicknesses of the SiO_2 and ZrO_2 layers) whereas the solid line with the box are the measured ones with the corresponding error bars.

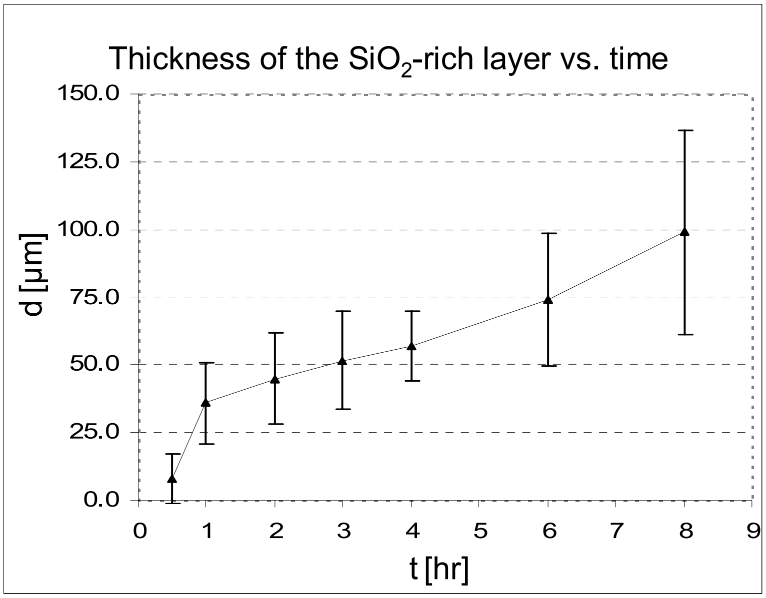

Figure 8.14: The measured thickness of the SiO_2 rich borosilicate surface layer of the ZSM composites tested at various dwelling times from 0.5 hr. to 8 hrs.

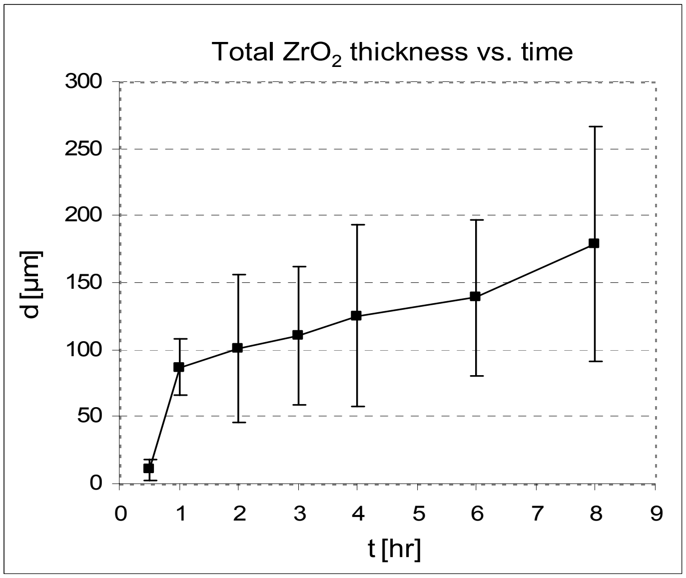

Figure 8.15: The measured thickness of the ZrO_2 layer (2nd layer) of the ZSM composites tested at various dwelling times from 0.5 hr. to 8 hrs.

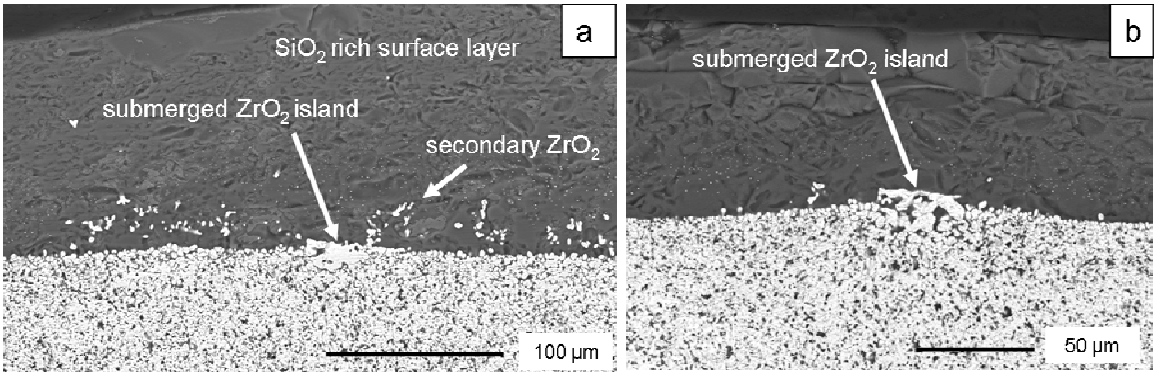

Figure 8.16: Backscattering electron images of cross-sections of ZSM specimens tested at 1550ºC for (a) 8hrs. and (b) 6 hrs. showing the SiO_2 rich surface layer (dark grey) and the underlying ZrO_2 (white contrast) layer of the oxide scale . The micrographs reveal submerged ZrO_2 islands, completely covered with SiO_2 rich surface layer.

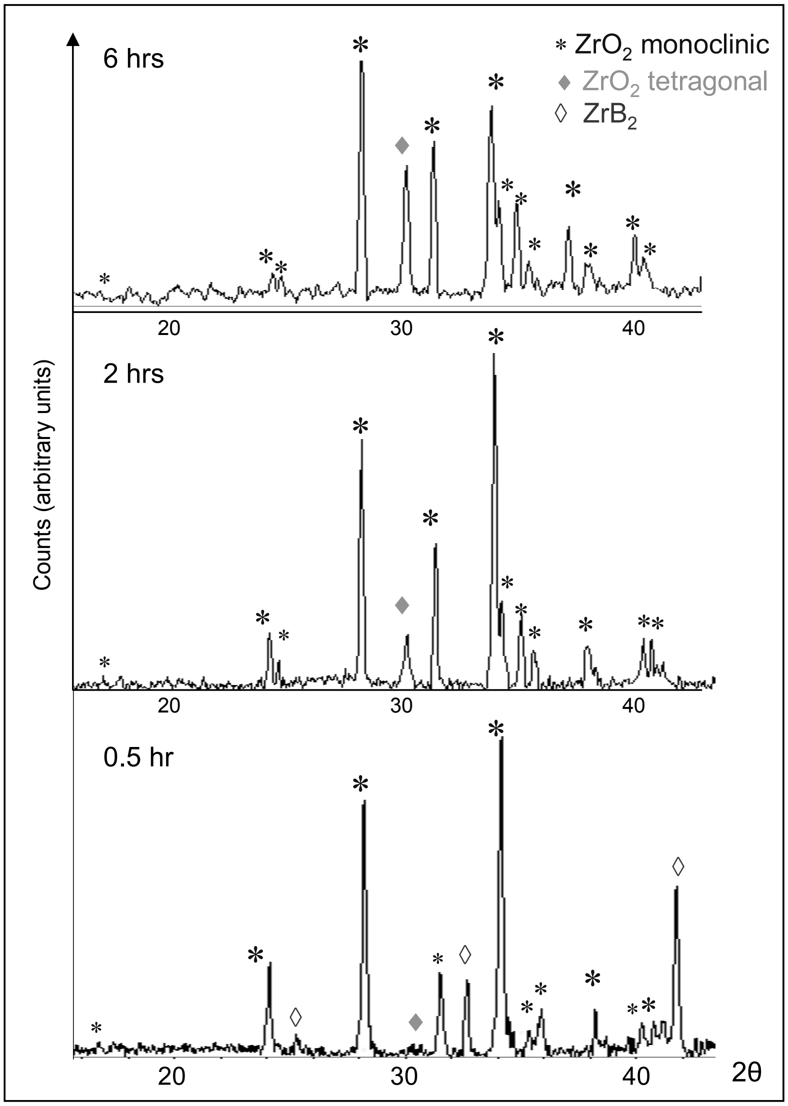

Figure 8.17: XRD patterns of the surface of ZSM specimens tested at 1550ºC for 0.5 hr. (bottom) , 2 hrs. , and 6 hrs. (top). The phases identified are shown with different markers; ZrB2 with open diamond, monoclinic $\alpha-ZrO_2$ with snowflake, and tetragonal $\beta-ZrO_2$ with closed diamond.

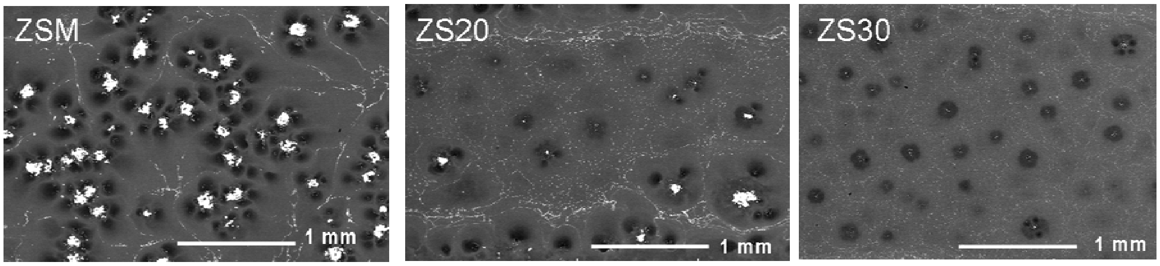

Figure 8.18: Backscattering electron images of the surfaces of the ZrB_2 composites containing different amount of SiC; ZrB_2-15vol%SiC (ZSM), ZrB_2-20vol%SiC (ZS20), and (c) ZrB_2-30vol%SiC (ZS30), all tested at 1550ºC 4 hrs.

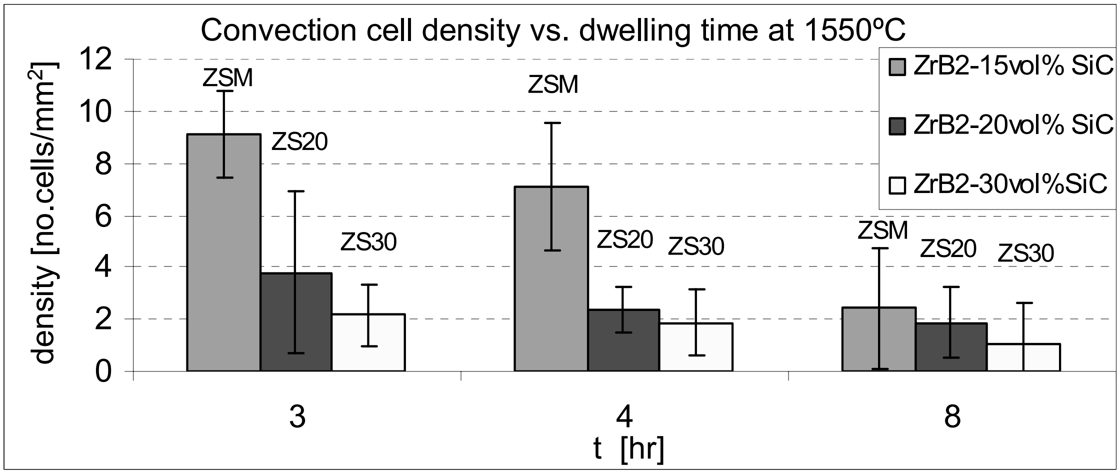

Figure 8.19: The density of convection cells (no. cells/mm^2) for the three composites containing different amount of SiC; ZSM, ZS20, and ZS30 tested at 1550ºC for 3, 4 and 8 hrs.

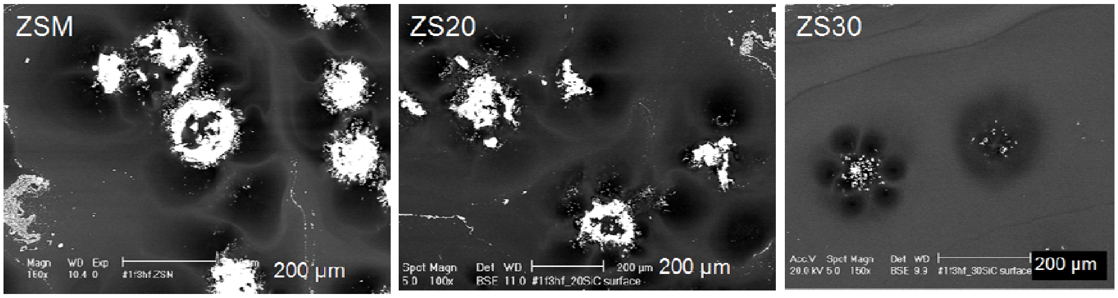

Figure 8.20: Backscattering electron images of the surfaces of the ZrB_2 composites containing different amount of SiC; ZrB_2-15vol%SiC (ZSM), ZrB_2-20vol%SiC (ZS20), and (c) ZrB_2-30vol%SiC (ZS30), all tested at 1550ºC for 3 hrs.

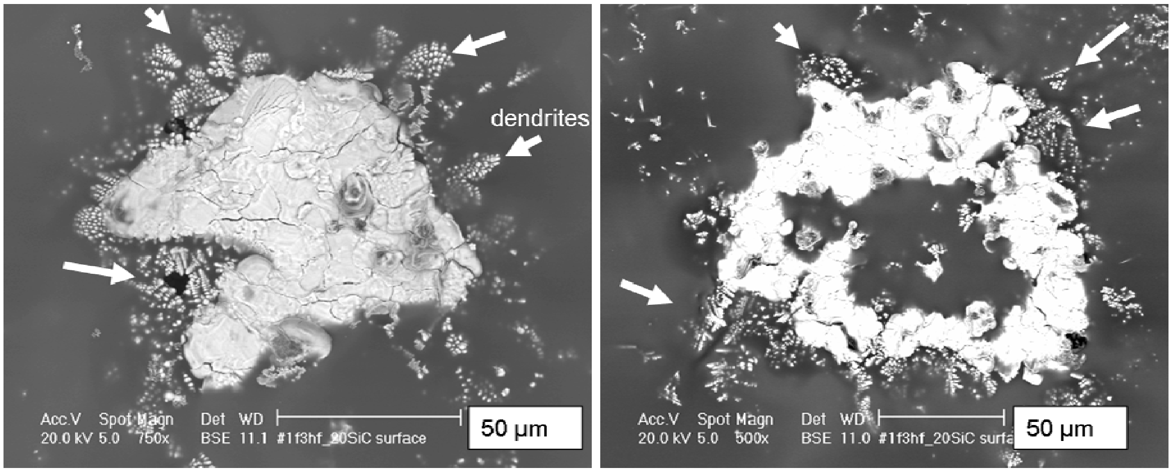

Figure 8.21: Secondary electron micrograph of a ZrO_2 islands on the surface a ZS20 composite tested at 1550°C for 3 hrs showing dendrite features similar to the ones that were observed on a ZSM composites.

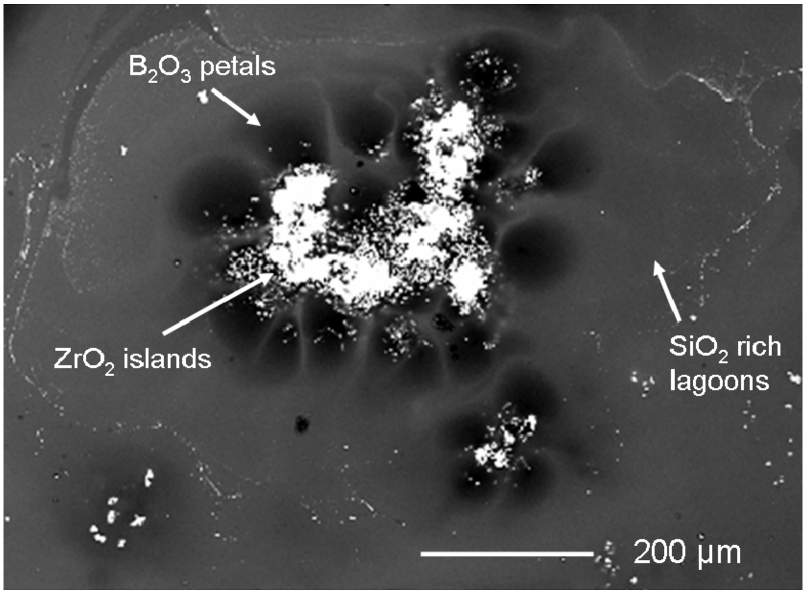

Figure 8.22: Backscattering electron image of the surfaces of a ZS20 composite tested at 1550°C for 2 hrs. showing convection cells formed during oxidation. The morphology of the convection cell resembles the morphology of convection cells formed on ZSM composites tested at similar conditions.

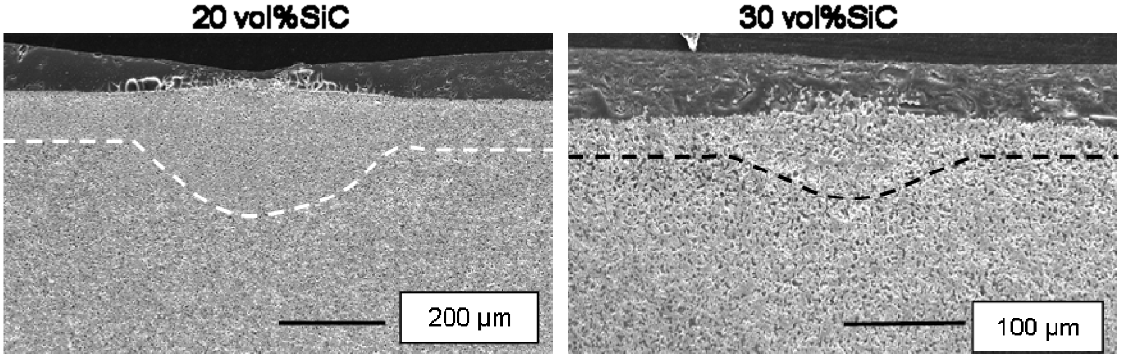

Figure 8.23: Secondary electron micrographs of the cross-sections of a ZS20 (left) and a ZS30 (right) composites tested at 1550ºC for 8 hrs. The interface between the ZrO_2 layer and the un-reacted bulk material is indicated with a broken line. The dark layer is the SiO_2 rich surface layer.

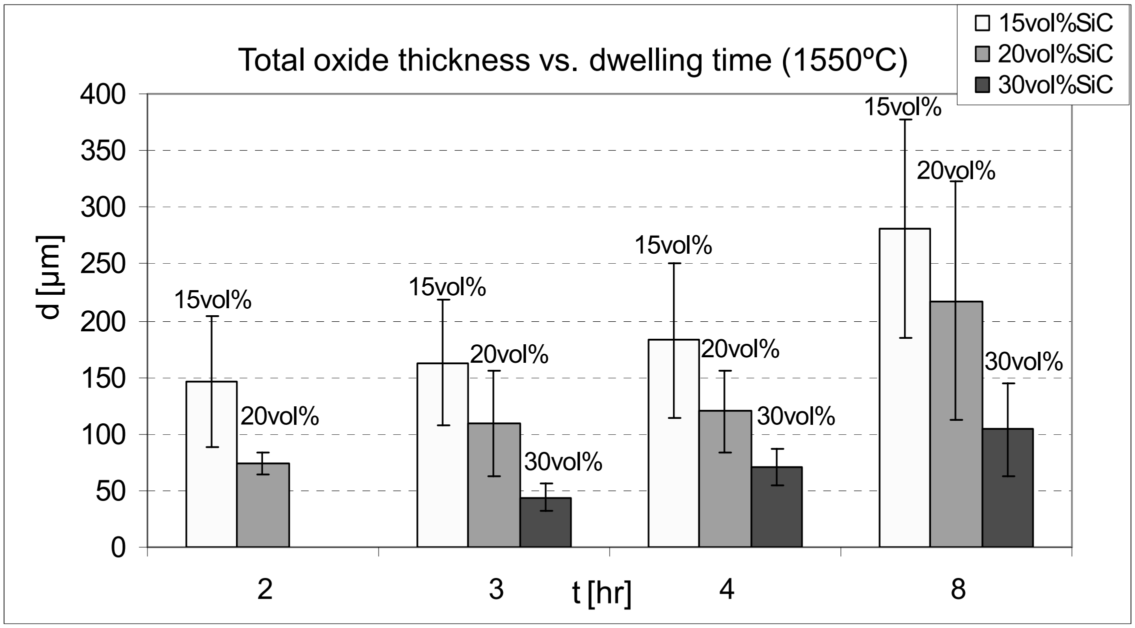

Figure 8.24: The total oxide thickness of the ZSM, ZS20 and ZS30 composites tested at various dwelling times. Calculated by adding the measured thicknesses of the SiO_2 –rich surface layer and the underlying ZrO_2 layer.

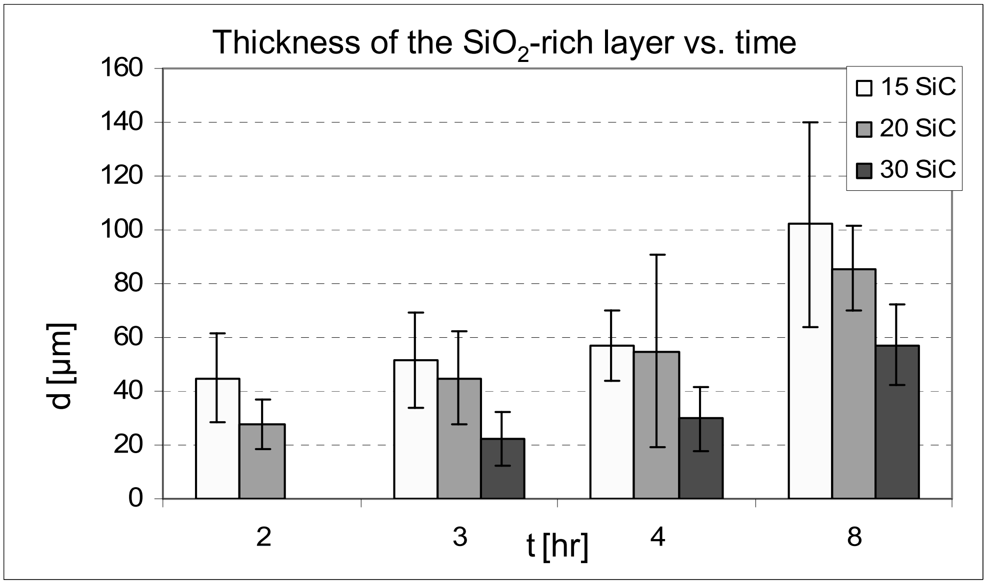

Figure 8.25: The measured thickness of the SiO_2 rich borosilicate surface layer of the ZSM, ZS20 and ZS30 composites tested at various dwelling times.

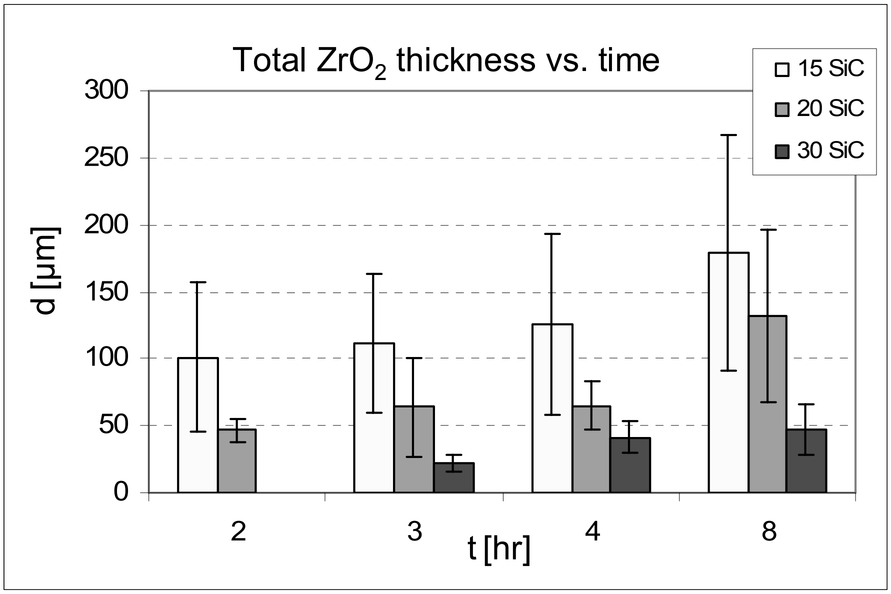

Figure 8.26: The measured thickness of the ZrO_2 layer (2nd layer) of the ZSM, ZS20 and ZS30 composites tested at various dwelling times.

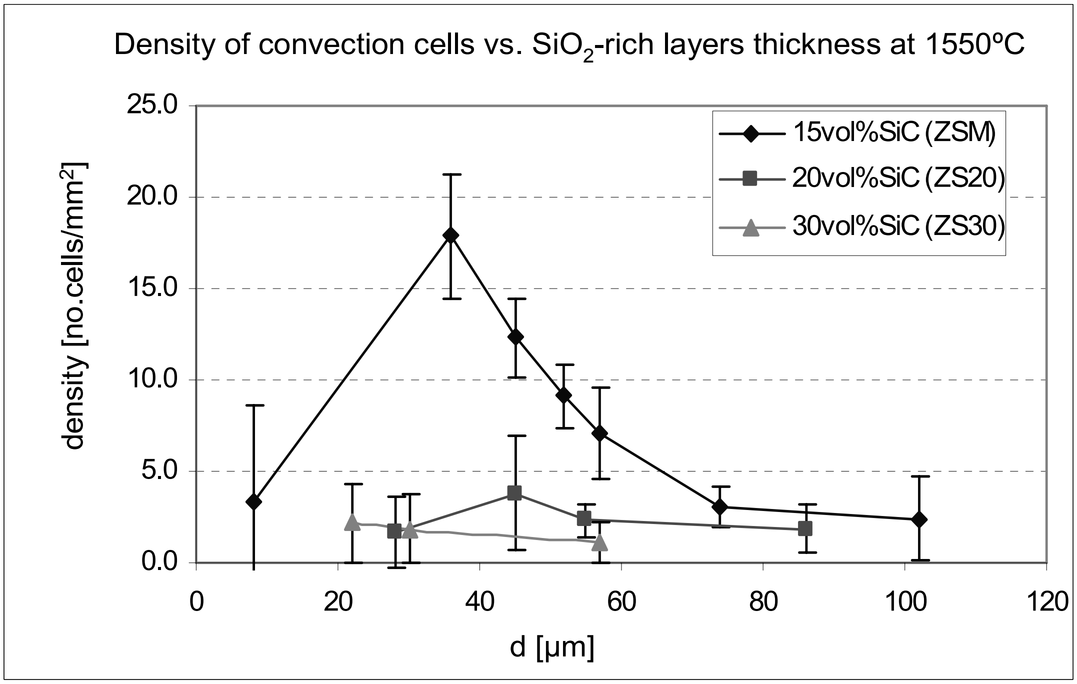

Figure 8.27: The density of convection cells (no. cells/mm^2) for the three composites containing different amount of SiC; ZSM, ZS20, and ZS30 tested at 1550ºC for various times vs. the measured thicknesses of the SiO$_2$-rich borosilicate surface layer.

SiC concentration [mol.%]	BSZ composition ZrO_2, SiO_2, B_2O_3 [mol.%]	Precipitated ZrO_2(s) [mol.% of total comp.]	Estimated viscosity [Pa·s]
15	11, 18, 71	34	$6.3 \cdot 10^2$
20	8, 25, 67	23	$5.0 \cdot 10^3$
30	6, 37, 57	12	$3.9 \cdot 10^4$

Table 8.1: The amount of precipitated secondary ZrO_2(s); BSZ liquid composition; and estimated viscosity, for the three ZrB_2-SiC composites estimated by using the ZrO_2-B_2O_3-SiO_2 ternary phase diagram from Chapter 5.

References

1. Chamberlain, W. Fahrenholtz, G. Hilmas and D. Ellerby. “Oxidation of ZrB_2-SiC Ceramics under Atmospheric and Reentry Conditions,” Refractories Applications Transactions, 1 [2] 1-8 (2005).

2. A. Rezaie, W.G. Fahrenholtz, and G.E. Hilmas. “Oxidation of Zirconium Diboride–Silicon Carbide at 1500ºC at a Low Partial Pressure of Oxygen,” J. Am. Ceram., Soc. 89 [10] 3240-3245 (2006).

3. A. Wackernagel, C. Massone, G. Hoefler, E. Steinbauer, H. Kerl, and P.Wolf. “Plasmacytoid Dendritic Cells are absent in Skin Lesions of Polymorphic Light Eruption,” Photodermatology, Photoimmunology and Photomedicine, 23 24–28 (2007).

4. H. Daims and M. Wagner. “Quantification of Uncultured Microorganisms by Fluorescence Microscopy and Digital Image Analysis,” Appl. Microbiol. Biotechnol., 75 237–248 (2007).

5. D.B. Epassaka, S. Ohshio, and H. Saitoh. “Morphological Instability of ZrO_2 Crystallites formed by CVD Technique Operated under Atmospheric Pressure,” Journal of Materials Science, 38 3239 – 3244 (2003).

6. Z. Bian, H. Kato, C.L. Qin, W. Zhang, A. Inoue. “Cu–Hf–Ti–Ag–Ta bulk metallic glass composites and their properties,” Acta Materialia, 53 2037–2048 (2005).

7. J.C. Ma, Y.S. Yang, W.H. Tong, Y. Fang, Y. Yu, Z.Q. Hu. “Microstructural evolution in AISI 304 Stainless Steel during Directional Solidification and subsequent Solid-State Transformation,” Materials Science and Engineering A, 444 64–68 (2007).

8. W. Vogel. Glass Chemistry, 2nd Edition. pp. 289-290 in Chapter 10.3 “Crystallization as a Defect in Glass,” Springer-Verlag, Berlin, Germany (1994).

9. R.J. Kirkpatrick. “ Crystal Growth from the Melt: A Review,” American Mineralogist, 60 798-614 (1975).

10. W. Jeitschko, R. Pöttgen, and R.-D. Hoffmann, “Structural Chemistry of Hard Materials”; pp. 32-35 in Handbook of Ceramic Hard Materials, Vol. 1. Edited by R. Reidel R. Wiley-VCH, Germany, Weinheim, (2000).

[11] I.G. Talmy, J.A. Zaykoski, M.M. Opeka, S. Dallek, "Oxidation of ZrB2 ceramics modified with SiC and Group IV-VI Transition Metal Diborides," Proceedings of the International Symposium on "High Temperature Corrosion and Materials Chemistry III," edited by M. McNallan and E. Opila, The Electrochemical Society, 12, p.144. (2001).

[12] I.G. Talmy, J.A. Zaykoski, M.M. Opeka, and A.H. Smith, "Properties of ceramics in the system ZrB_2-Ta_5Si_3," J. Mater. Res., 21 [10] 2593-2599 (2006).

[13] E.J. Opila, S.R. Levine and J. Lorincz. "Oxidation of ZrB_2-and HfB_2 based Ultra-High Temperature Ceramics: Effect of Ta Additions," Journal of Materials Science, 39 5969-5977 (2004).

CHAPTER 9

CONCLUSION

1.0 Summary

A novel method called the Ribbon Method was designed and built for testing ultra-high temperature ceramics (UHTC) at high temperature, rapidly at low cost. The method uses a miniaturized self-supported ribbon specimen which is resistively heated with a table-top apparatus to achieve very high temperatures. This method enables oxidation experiments to be performed at temperatures above 900ºC and as high as 2000ºC, with a power input of only around 100W and without creating a difficult-to-manage heat load in the surroundings due to the small size of the specimen. It also allows a large temperature-time-composition parameter space to be covered by rapidly producing a large set of post-oxidation samples for analysis. The Ribbon Method is a novel method for rapid oxidation characterization of UHTC at high temperatures and a valuable alternative to the current high temperature facilities for UHTC.

The complex oxide scale known to form during oxidation of UHTC materials was shown to be easily reproduced by using the Ribbon Method; verifying the applicability of the method as an alternative option for high temperature testing of UHTC materials. Sets of experiments were performed on a ZrB_2-15vol%SiC-2vol%$MoSi_2$ composite at temperatures from 1500-1900ºC in ambient air and pressure. A complex oxide scale was found to form for this material, consisting of an outer SiO_2-rich borosilicate layer with an underlying ZrO_2 layer at temperatures at and below 1700ºC. For more severe oxidation conditions, at temperatures above 1600ºC, a SiC-depleted layer was found to form underneath the ZrO_2 layer. The continuous SiO_2-rich borosilicate layer that forms during the oxidation of the ZrB_2-SiC-$MoSi_2$ composite acts as a protective barrier between 1500-1600ºC by hindering oxygen diffusion through the surface layer. It does not have the same effective role in limiting oxygen diffusion at temperatures above 1650ºC which is likely due to the higher vapor pressure, lower melting temperature and viscosity of the SiO_2 at higher temperatures (>1600ºC). The SiO_2-rich surface layer starts to volatilize extensively at higher temperatures (>1700ºC) resulting in a oxide scale with a less protective porous ZrO_2 surface layer which does decreases the oxidation resistance of the ZrB_2-SiC-$MoSi_2$ composite at these temperatures.

The Ribbon Method was also thoroughly compared to current UHTC high-temperature facilities used for oxidation testing. The heat transfer conditions applied with the Ribbon Method is significantly different from both the furnace oxidation and the arc-jet testing. Nonetheless the micro-structural and compositional analyses show that the Ribbon Method gives similar result in terms of the oxide scale thickness, structure and composition of the ZrB_2-SiC based composites tested. This comparison further verified that the Ribbon Method should be considered as a valuable addition to the current high temperature facilities available today for UHTC testing.

Patterns in the boro-silicate oxide surface layer on ZrB_2-SiC composites tested at temperatures between 1500-1600ºC were discovered, believed to be an evidence of liquid flow in oxide films that form during the oxidation of ZrB_2-SiC materials at high temperatures. These patterns called convection cells are formed when a fluid B_2O_3-rich borosilicate liquid containing dissolved ZrO_2, formed by oxidation, is transported to the surface where the B_2O_3 is lost by evaporation, depositing ZrO_2 in a viscous SiO_2-rich liquid, i.e. the convection cells. The driving force for the liquid transport is the large volume increase upon oxidation. The B_2O_3-rich patterns that form on the surface around the deposited ZrO_2 resembling flower patterns are suggested to form by a viscous fingering process as fluid B_2O_3-SiO_2-ZrO_2 liquid displaces the more viscous SiO_2-rich liquid. Liquid transport of the oxide liquid solution is claimed to play a significant role in the formation of oxide scales of ZrB_2-SiC composites and in more generally for boride-SiC based UTHC composites. Mass transport by liquid flow has not yet been reported for the high temperature oxidation of ZrB_2-SiC composites thus a novel mechanism for the high temperature oxidation of these materials is been presented here.

Interpretation of the oxide scales of ZrB_2- and HfB_2-SiC composites in terms of liquid flow mechanism was analyzed and discussed. Oxide scale features resembling the proposed convection cells were discovered in cross-sectional micrographs previously published in the literature. This suggests that convection cells might have been observed before for ZrB_2- and HfB_2-SiC systems but not interpreted as to be of significance. The convection cells are proposed here to be of great significance contributing to the formation of the complex oxide scales for these materials. The flow of a B_2O_3 rich borosilicate-zirconia (BSZ) liquid to the surface, with the subsequent loss of B_2O_3 to evaporation, explains the formation of a glassy SiO_2 rich layer on the surface commonly reported in the literature. Also the outward flow of the BSZ liquid creates a localized inward path for oxygen due to lower viscosity that allows faster oxidation under the convection cell. The formation of a convection cell (eruption of the “premature” scale) creates a leak in the silica barrier, but the BSZ liquid eventually replenishes the silica scale, patching the leak creating a positive feedback.

The evolution of the convection cells with time, temperature and SiC concentration was investigated. The effect of SiC concentration on the oxide thickness and the population of the convection cells was investigated by testing three different compositions; ZrB_2-15vol%SiC(ZSM), ZrB_2-20vol%SiC (ZS20) and ZrB_2-30vol%SiC(ZS30). The results indicated that the density (no.cells/mm^2) of convection cells for the ZSM composite tested at 1550ºC rapidly increases at the first stage of the oxidation but then decreases slowly with increasing time. The same trend was seen when the cell density (no.cells/mm^2) of the ZSM tested at 1550ºC was compared to the thickness of the SiO_2-rich borosilicate surface layer. This indicates that the convection cells are transient, i.e. they form when the BSZ liquid flows to the surface but then with time the increasing amount of flowing viscous SiO_2-rich liquid submerges them and they become extinct. When the viscous SiO_2-rich layer is then thick enough it suppresses the formation of new convection cells. The convection cell mechanisms is claimed to be dominant in the early stage of the oxidation of these materials, supplying the SiO_2 to the surface. When the surface layer becomes mainly viscous SiO_2 the replenishment of the SiO_2 by the formation of convection cells and their “volcanic” eruptions (due to the large volume increase) stops and they go extinct.

Increased testing temperature results in increasing number of convection cells. This is likely due to the increased evaporation rate of B_2O_3 at higher temperatures, due to the higher vapor pressure, which speeds up the formation of the convection cells at the early stage of oxidation.

Convection cells were formed on other ZrB_2-SiC composites with different SiC concentration (ZS20 and ZS30). This supports our hypothesis that the formation of the convection cells are dependant on the formation of the transient BSZ liquid and the large volume increase formed during oxidation of ZrB_2-SiC materials. The smaller number of convection cells formed on the ZS20 and ZS30 composites compared to the ZSM is suggested to be due to the difference in the BSZ liquid composition. The ZS20 and especially ZS30 have less B_2O_3 formed compared to ZSM thus there will be less ZrO_2 dissolved in the BSZ liquid, which result in fewer ZrO_2 islands formed.

The composites with more SiC vol.% are more oxidation resistant, indicated by the decrease in total oxide scale thickness with increasing SiC content. The reason for the increased oxidation resistance of the higher SiC containing materials is suggested here to be explained by less boron oxide content in the borosilicate surface layer. The increased SiO_2 content of the surface layer formed can suppress the evaporation of the B_2O_3 and hinder inward oxygen diffusion better at these temperatures.

The f*ormation* of the convection cells is not dependent on the thickness of the SiO_2-rich -B_2O_3 surface layer. On the other hand their *existence* is dependant on the thickness of the surface SiO_2-rich layer, as mentioned above when it becomes thicker the convection cells are submerges and become extinct. Their formation is completely dependant on the formation of the BSZ liquid and its composition. The convection cells are shown to be an important part of the oxidation mechanism for boride-SiC based composites and to play an significant role in the formation of the complex oxide scale at these temperatures.

The B_2O_3 liquid plays a large role in the oxidation mechanism for boride-SiC based materials, just from looking at the starting composition of the material this should be expected. Nevertheless, the role of the B_2O_3 liquid is most often more or less forgotten in the boride-SiC UHTC literature. This seems to be partially due to the expected volatility of the B_2O_3 liquid and the difficulty in detecting boron (B) in the oxide scale structure. Often the focus has then been on the other part of the borosilicate layer; the SiO_2 part which is more easily detected and more of. The focus for improving the oxidation resistance of boride-SiC composite has then been mainly on altering the SiO_2 glass formed with additives. This has not been a huge success e.g. due to the limitation that the melting temperature of the formed surface layer imposes at higher temperatures. Instead the author suggests that instead of focusing solely on the SiO_2 glass and improvement in the oxidation resistance by altering the SiO_2 glass, the focus should be on the B_2O_3-SiO_2 glass, where perhaps e.g. Al_2O_3 additions would be of value.

2.0 Future Work

Modifications to the apparatus for the Ribbon Method would be of great value to increase the parameter space for testing of UHTC. This could be done for example by modifying the apparatus to allow controlled atmospheric experiments. By designing a closed removable glass container that could encapsulate the ribbon specimens and its supports would allow the UTHC specimen to be tested at very high temperatures at different atmospheres (dry air vs. water-saturated air). This design could also allow variable pressures which would expand the parameter space further.

Testing of HfB_2-SiC and other compositional variations of diboride-SiC composites would be of great interest to explore further the effect of composition on the formation and evolution of the convection cells. The effect of additives such as Y_2O_3, Yb_2O_3 and Al_2O_2 should be explored by systematic testing of ZrB_2-SiC composite with and without the additives at temperatures around 1550ºC. This could give valuable information on how the glass composition effects the formation of the convection cells and the oxidation resistance of the composite. The effect of SiC particles, i.e. distribution and grain size, on the formation of the convection cells should be explored and would give further insight of the role of the SiC phase.

By using a focused ion beam (FIB) detailed cross-sectioning could be performed through convection cells at a particular location on the surface which would add further to our understanding of the convection cells. Transmission electron microscopy (TEM) could then be used in hand with the FIB to investigate the structure of the secondary ZrO_2 in the glass layer as well as give valuable information about the interfaces between the layers in the oxide scale.